Universitat Politécnica de Catalunya

Departament de Física i Enginyeria Nuclear

Tesi Doctoral en Física

MONTE CARLO STUDY OF QUANTUM PHASE TRANSITIONS AT ZERO TEMPERATURE

Directors:
Prof. Dr. Jordi Boronat,
Dr. G. E. Astrakharchik

Candidate:
O. N. Osychenko

Doctorat de Recerca en Física Computacional i Aplicada

23 de octubre de 2012

Contents

Introduction

Phase transition is a commont term for a wide range of phenomena generally described as a transition between different states of matter with the variation of one or more physical parameters of the system. The transition is accompanied by an abrupt change of some of its physical quantities or its derivatives, whereas the relevant physical magnitudes change continuously within a given phase. The simplest example of a phase transition is the melting of a crystal to form a fluid when its temperature is increased, which produces a discontinuous behavior of its density and some other physical properties. Historically, the first classification of the phase transitions was given by P. Ehrenfest [Ehr33] and relies on a definition of a phase as a state with the minimum thermodynamic free energy. The first-order transition in this framework is a transition with an abrupt change of the first derivative of the system's free energy with respect to a certain parameter. The second-order transitions are those when the first derivative has a cusp when the parameter is changed, that is when a finite discontinuity appears in the second derivative of the free energy. Ehrenfest's original proposal was later extended to the cases of infinite discontinuities of physical parameters. The higher-order transitions are defined similarly, as the ones possessing a discontinuity in n-th ($n > 1$) derivative of the free energy with respect to the parameter. Landau theory [LL80] describes the second-order phase transitions as a result of a symmetry breaking, with a rapid change of a so-called order parameter, characterizing the symmetry properties of a phase. Well-known examples of second-order phase transitions are the transitions between a normal fluid and a superfluid, with the superfluid fraction being the order parameter, or the ferromagnetic-paramagnetic transition with the magnetization as order parameter.

Quantum phase transitions are a broad subclass of these phenomena related to quantum matter, most generally described as a transition between phases at zero or low enough temperature, where quantum effects play an important role. The profound difference of quantum phase transitions from the classic phase transitions lay in the absence of entropy due to the Nernst heat theorem [Ner07]. A classical description of a zero-temperature system can prescribe only one phase (an ideal crystal), whilst a quantum system is capable to undergo a transition, but only with the change of a certain non-thermal parameter, as for instance its density. The role of entropy in classical systems is played in quantum phases by quantum fluctuations. One of the first experimental evidences of a quantum phase transition was the solidification to hcp solid ^{4}He at low temperatures with a growth of pressure, made by Keesom [Kee42]. The recent advances in methods of manipulation of ultracold matter, especially in the topics of cooling and trapping of atoms [Chu98, CT98, Phi98] and Feshbach resonances [TTHK99, CGJT10], demonstrated possibilities to produce systems with unique and highly tunable interparticle potentials [CTGO11]. The tunability of the interaction in terms of non-thermal parameters, which was achieved in a number of experiments, plays a key role for quantum phase transitions. One of the

first theoretical proposals for a quantum phase transition was the bosonic superfluid-Mott insulator transition, based on the Bose-Hubbard model [FWGF89, JBC+98], that was finally experimentally confirmed in the work of Greiner *et al.* [GME+02] and a number of subsequent experimental set-ups [OTF+01, TOPK06, TCF+11]. Recently, the phase diagram and essential thermodynamics of the three-dimensional Bose-Hubbard model was obtained in quantum Monte Carlo simulations by Capogrosso-Sansone *et al.* [CSPS07].

The energy of a quantum system, described by the Schrödinger equation in a state of a certain symmetry can be obtained with the help of Quantum Monte Carlo methods. From the equations of state, corresponding to different phases, one can find the pressure as a function of the relevant parameters. The double-tangent Maxwell construction, based on the equality of pressures and chemical potential along the transition line, allows to obtain the first-order transition point and the width of the transition zone.

Quantum Monte Carlo (QMC) techniques are *ab initio* quantum calculation algorithms that might provide deep insight into the design of quantum matter, with a capability to describe a multitude of relevant properties and phenomena of the system. Among them the possibility to locate quantum and temperature phase transitions, and to quantify correlations in the system (e.g. pair correction function, structure factors, and even non-local properties, such as superfluid fraction and Bose–Einstein condensate). Bose-Einstein condensation (BEC), i.e., a macroscopic occupation of the zero-momentum quantum state of a system, despite being proposed by A. Einstein and S. N. Bose in the mid-twenties of the previous century [Ein24], [Ein25], used to be considered for many decades more as a mathematical abstraction than an achievable state of matter. The superfluid properties of ^{4}He at low temperatures, found in the experiments of Kapitza, Allen and Misener [Kap38, AM38] are believed to be related to the presence of a Bose–Einstein condensate. The BEC-like phase transitions have also been observed in excitonic systems [LW93]. Long-lasting efforts of numerous experimental groups to actually observe a signature of a condensed phase in ultracold gases finally gave a positive result: in 1995 Bose-Einstein condensate was found by E. Cornell and C. Wieman [AEM+95] in gaseous ^{87}Rb and later the same year in the other alkali vapours of ^{23}Na (W. Ketterle *et al.* [DMA+95]) and ^{7}Li (R. Hulet *et al.* [BSTH95]). The experimental set-ups to produce a condensate are generally quite complex, partially due to the strict temperature requirements ($T \sim 10^{-7}$ K). From the theoretical sight, QMC simulations can yield accurate predictions about the properties of Bose–Einstein condensate, provided the interaction in the system is known.

Let us explain in more detail the techniques, challenges and results that we present in this thesis. We are usually concerned with the properties of a bulk system in its thermodynamic limit, but its QMC description of a bulk is generally performed with periodic boundary conditions (p.b.c.) applied to *finite* size system. Therefore any Quantum Monte Carlo method yields results with a certain error, related to the size of a simulated system and one has to study the limit $N_p \to \infty$, with N_p the number of particles. The properties of a system in the thermodynamic limit are therefore found out by extrapolating the data for limited system sizes to infinity. In the condensed systems that we consider, the conver-

gence in the energy goes as $1/N_p$. The dependence of a certain physical quantity is then found for a set of different numbers of particles, and the result is extrapolated to infinity. Nevertheless the lowest number of particles, for which the asymptotic $1/N_p$ behavior is reached within an acceptable precision is a priori unknown. In practice, a number of probe simulations is performed in order to observe the needed linear dependence, but sometimes the accessible system sizes are too small to obtain the thermodynamic limit correctly. In some cases this problem can be greatly relieved by using the Ewald summation technique. In the framework of the Ewald method the potential energy is calculated for the infinite system, consisting of periodically replicated copies of the original simulation box. Although the method makes the calculation more time-consuming, its use shows that in particular systems, especially when the long-range interactions are present, the $1/N_p$ dependence of the correction is substantially reduced, making the extrapolation to the thermodynamic limit possible.

The Ewald technique is a well-known simulation tool, often used with some modifications in a number of applications, involving molecular dynamics, Monte Carlo and other algorithms. Despite its popularity, the scope of its utilization is mostly limited to the summation of the Coulomb interactions, where its use is essential due to the long-range nature of the potential. Nonetheless, conceptually the Ewald technique may be applied to a broad variety of various pairwise potentials, for example, of the generic power-law type $1/|\boldsymbol{r}|^k$. In this Thesis we present a detailed step-by-step derivation of the Ewald sums for power-law interaction potentials and for all the terms we give explicit formulas, ready to be used straightforwardly in actual simulations. The derived expressions have been used in the simulations of systems consisting of Rydberg atoms and particles interacting via the Yukawa interaction potential.

The Yukawa potential has been used in the past as the simplest model interaction in atomic nuclei, in dusty plasmas and other systems, but recently this interaction appeared in the field of ultracold gases. In recent experiments [TVA+08, HTY+11] ultracold systems made up of two kinds of fermions, one heavy and another light, have been realized in actual setups, with an effective cooling achieved by means of an additional bosonic component. Theoretic treatment of quasi-two-dimensional systems with this kind of fermionic mixtures has been done in Ref. [PAP+07]. It is argued that the effective interaction potential between light-heavy pairs of fermions is of Yukawa (screened Coulomb) type, with a feasibility of reaching a gas-crystal phase transition in two-dimensional geometry. In the present Thesis we extend the study of crystallization to a fully three-dimensional case at zero temperature. A similar problem was pursued before [CCK76], but unfortunately this problem was not solved entirely, and an approximate Lindemann criterion was used instead of full scale quantum simulations. We find by means of the diffusion Monte Carlo method the exact phase diagram as a function of the relevant parameters, that is density and mass ratio between the two Fermi species. The obtained diagram provides valuable information on the minimum requirements for the mass ratio to achieve a phase transition in actual experiments. Thanks to advances in the field of optical lattices there arises a possibility to

produce particle mixtures with extremely high ratios of effective masses. In this Thesis we argue that certain existing setups, involving optical lattices, allow to increase the effective mass ratio enough for potentially reaching the crystallization.

In the last decade, there is a new wave of interest in ultracold systems consisting of Rydberg atoms, and a number of interesting experiments has been performed [HRB+07, LWK+09, HLW+11]. A Rydberg atom is a neutral atom with a single electron excited to a high orbital. The important properties of this quantum object are its simplicity and similarity to a hydrogen atom. Furthermore, its unique properties of possessing very strong and controllable interactions over long distances, together with the novel techniques of ultracold atom manipulation, attracted a great deal of attention due to a prospectively rich behavior of mixtures of excited and unexcited atoms. In a typical experiment a trapped cloud of cold atoms is exposed to a laser field, exciting a small fraction of atoms to a particular Rydberg state. These excited states interact in a much stronger way among themselves than with the unexcited background. The possibility of tuning, turning on, and off, the large magnitude of the forces, as well as a number of other advantageous properties, suggest its use as a quantum gate, that is, a basic element of quantum circuits. Currently, there is a wide range of proposals for physical systems to realize quantum information processing units: trapped ions [BW08], linear optics [KMN+07], superconductors [CW08], quantum dots [LWS+03], and so on. The one, based on systems made up of Rydberg atoms is unique in terms of the range and the amplitude of the interaction, the working frequency and other advantageous properties [SWM10]. The basic principles of a trapped Rydberg system as a quantum gate stem from the idea of a so-called Rydberg blockade, that is when a single excited atom shifts the energy levels of the nearby unexcited atoms out of the resonance with the driving laser pulse. Further excitations, injected into the cloud, can bring a macroscopic fraction of the cloud to a blockaded mode, allowing for a partial or complete saturation. In actual experiments, the fraction of unexcited atoms permits over 10^3 excitations before the suppression of the new ones appear [HRB+07, TFS+04, SRLA+04]. The actual physical phase of the excited atoms cannot be accessed directly in the reported experiments, although their arrangement is considered as a relevant information, both as a standalone physical problem and for the implementation of the quantum gate. A direct observation of a quantum phase transition and a presence of long-range ordering is argued to be a feasible task in similar systems [WLPB08, LWK+09]. In the field of quantum computations, Pohl *et al.* [PDL10] proposed that the presence of a crystal-like ordering could provide a better control over the quantum states. An insight to the spatial ordering in a cloud of Rydberg atoms may also shed light to the phenomenon of the so-called "antiblockade" [APPR07].

As mentioned before, the behavior of an ultracold mixture of excited Rydberg atoms and unexcited background is profoundly rich and complex. It can also depend substantially on particular experimental conditions, like the cloud geometry, laser field properties, etc. We perform a study of a model system, in which we neglect the interactions related to the unexcited background, and using the pairwise repulsive van der Waals $C_6/|\boldsymbol{r}|^6$ for the

excited atoms. The general aim of this study is to fully understand the phase diagram of the system. A perspective comparison with future experimental results can demonstrate, how well the properties of the system can be derived from this simple model. Since the number of Rydberg atoms, typically present in the current experimental works, is of the order of thousands or greater, in our simulations we look for all the relevant results in the thermodynamic limit. There is also a variety of possible crystal packings, which might be realized in the solid phase, hence we give a discussion on which of them are energetically preferable.

Another physically relevant system, considered in the Thesis, is bulk molecular *para*-hydrogen (p-H_2). This system in the quantum regime (at low temperature) was proposed theoretically as a possible candidate for superfluidity, but it crystallizes at the temperature substantially higher than transition temperature, making it impossible to observe a transition to the superfluid phase. In this work, our Group has studied a metastable non crystalline phase of bulk p-$H_2$by means of Quantum Monte Carlo methods in order to find out the temperature at which this system still contains a noticeable superfluid fraction. The ultimate goal that our Group pursued, was to frustrate the formation of the crystal in the simulated system and to calculate the temperature dependence of the one-body density matrix and of the superfluid fraction. I present the study of the limit of zero temperature using the diffusion Monte Carlo method. Results for the energy, condensate fraction, and structure of the metastable liquid phase at $T = 0$ are reported and compared with the ones of the stable solid phase. The simulation at zero temperature is used by our Group as a starting point for the simulation of the system at low temperatures by using Path Integral Monte Carlo technique.

The structure of the Thesis is as follows.

In Chapter 1 we discuss the analytical approaches and approximations used in the subsequent Chapters; also we describe the general concepts of the two-particle scattering problem as a tool to construct Jastrow terms in trial wave functions. Chapter 2 explains in details the Quantum Monte Carlo methods employed in our calculations from the theoretical and practical points of view. In Chapter 3 we explain the Ewald summation technique, applied to a power-law $1/|\boldsymbol{r}|^k$ interaction potential, and a generic approach to obtain the Ewald terms. The obtained expressions of this analytic work are implemented into simulations of different physically relevant systems (Rydberg atoms and Yukawa particles). Chapter 5 is devoted to the modelling of a system, governed by the model potential between Rydberg atoms $1/|\boldsymbol{r}|^6$. The phase diagram of the system is obtained for a relevant range of densities and temperatures, combining quantum simulations at low temperature and classical treatment at higher temperature. A special attention is paid to the classical description of this system, composed of Rydberg atoms, and its comparison to the quantum system. In Chapter 4 we present the simulation of a system with the Yukawa interaction potential. The following Chapter 6 presents the results of the Quantum Monte Carlo simulations of molecular para-hydrogen at zero and finite temperatures, performed in our Group. Conclusions are drawn in Chapter 7.

Chapter 1

Tools

1.1 Introduction

This Chapter is intended to provide theoretical basis for the following Chapters. The quantities characterizing properties of a quantum system (correlation functions, static structure factor, and so on) are introduced here and are later used in the subsequent chapters. We also discuss the two-body scattering problem in a three-dimensional system geometry that sheds light to the short-range properties of many-body systems. The two-body scattering solution can be used in the development of trial wave functions needed in the Quantum Monte Carlo algorithms.

The structure of the Chapter is the following.

In Section 1.2 we introduce experimentally relevant magnitudes and functions that are present in a quantum system. First of all, we consider the analytic forms of the first and second quantization (Secs. 1.2.1, 1.2.2). Special attention is given to the relation between correlation functions and mean values of quantum operators. Some correlation functions may be greatly simplified in case of a homogeneous system, which is presented in Section 1.2.2. The definitions and general comments on static structure factor and momentum distribution are drawn in Section 1.2.3.

Section 1.3 is devoted to the study of two-body scattering processes in three-dimensional geometry. The solutions of the two-body scattering problem are provided for a number of physically relevant interaction potentials. The main aim of this last Section is to give an efficient tool to construct two-body Jastrow terms of the trial wave function for Quantum Monte Carlo simulations (for details on QMC methodology see Chapter 2).

1.2 Correlation functions

1.2.1 Second quantization form

A quantum system of identical particles of variable number is generally described with the help of annihilation and creation operators. The commonly used notations for the auxiliary field operators are $\hat{\Psi}^\dagger(\mathbf{r})$ for an operator creating a particle in the position $\mathbf{r}$, and $\hat{\Psi}(\mathbf{r})$ for an operator destroying a particle in the same position. By means of the creation operator $\hat{a}_m$ for m-th state, that puts a particle to an orbital $\varphi_m(\mathbf{r})$, and the annihilation operator, $\hat{a}^\dagger_{\boldsymbol{m}}$, that removes a particle from the orbital $\varphi_m(\mathbf{r})$, these field operators can be easily represented in the following form:

$$\left\{ \begin{array}{rcl} \hat{\Psi}^\dagger(\mathbf{r}) & = & \sum\limits_{\boldsymbol{m}} \varphi^*_m(\mathbf{r})\, \hat{a}^\dagger_m \\ \hat{\Psi}(\mathbf{r}) & = & \sum\limits_{m} \varphi_m(\mathbf{r})\, \hat{a}_m \end{array} \right. , \tag{1.1}$$

If we consider a uniform gaseous system within a volume V, single particle states are evidently plain waves $\varphi_m(\mathbf{r}) = e^{\mathrm{i}\boldsymbol{k}_m\mathbf{r}}/\sqrt{V}$. Bosonic operators (1.1) obey commutation relation $[\Psi(\mathbf{r}), \Psi^\dagger(\mathbf{r}')] = \delta(\mathbf{r}-\mathbf{r}')$, $[\Psi(\mathbf{r}), \Psi(\mathbf{r}')] = 0$, while fermionic operators obey commutation relations.

First of all, let us discuss the relation between the correlation functions and the mean values of one- and two-body quantum mechanical operators. Let us consider the simplest case when the Hamiltonian of the system is a sum of only one-body and two-body operators

$$\hat{H} = \hat{F}^{(1)} + \hat{F}^{(2)}, \tag{1.2}$$

where the one-body operator $\hat{F}^{(1)}$ stands for a sum of the one-body terms, and the two-body operator $\hat{F}^{(2)}$ is a sum of corresponding two-body terms, depending on $\mathbf{r}_i$, $\mathbf{r}_j$:

$$\hat{F}^{(1)} = \sum_{i=1}^{N} \hat{f}^{(1)}_i \,, \tag{1.3}$$

$$\hat{F}^{(2)} = \frac{1}{2} \sum_{i\neq j}^{N} \hat{f}^{(2)}_{i,j} \,. \tag{1.4}$$

Obvious examples for one-body operators are an external potential field, depending only on the particles' coordinates: $f^{(1)}(\mathbf{r}) = V_{\text{ext}}(\mathbf{r})$, or the kinetic energy: $f^{(1)}(p) = p^2/2m$. The first operator is diagonal in coordinate space, while the second one is diagonal in momentum representation. A typical example of a two-body operator is a pairwise interaction potential, given in coordinate space: $f^{(2)}(\mathbf{r}_1, \mathbf{r}_2) = V_{\text{int}}(\mathbf{r}_1, \mathbf{r}_2)$.

The representation of one- and two-body operators $\hat{A}^{(1)}$ and $\hat{A}^{(2)}$ in terms of field operators (see (1.1)) is straightforward:

$$\hat{F}^{(1)} = \iint \hat{\Psi}^\dagger(\mathbf{r}) f^{(1)}(\mathbf{r}, \mathbf{r}') \hat{\Psi}(\mathbf{r}') \, \mathrm{d}\mathbf{r}\, \mathrm{d}\mathbf{r}' \tag{1.5}$$

$$\hat{F}^{(2)} = \frac{1}{2} \iint \hat{\Psi}^\dagger(\mathbf{r}) \hat{\Psi}^\dagger(\mathbf{r}') f^{(2)}(\mathbf{r}, \mathbf{r}') \hat{\Psi}(\mathbf{r}') \hat{\Psi}(\mathbf{r}) \, \mathrm{d}\mathbf{r}\, \mathrm{d}\mathbf{r}' \tag{1.6}$$

where the factor 1/2 is introduced to take into account the double summation.

Up to now, we did not restrict ourselves to local one-body operators (that is those satisfying the relation for the quantum averages $\langle \mathbf{r}|a^{(1)}|\mathbf{r}'\rangle = a^{(1)}(\mathbf{r})\delta(\mathbf{r}-\mathbf{r}')$), but we also consider non-local operators, that is, ones allowed to depend on two arguments $a^{(1)} = a^{(1)}(\mathbf{r},\mathbf{r}')$ in the corresponding integral of (1.1).

Correlation functions can be introduced in terms of the field operators in the following way:

$$C_1(\mathbf{r},\mathbf{r}') = \langle \hat{\Psi}^\dagger(\mathbf{r})\hat{\Psi}(\mathbf{r}')\rangle \,, \tag{1.7}$$

$$C_2(\mathbf{r},\mathbf{r}') = \langle \hat{\Psi}^\dagger(\mathbf{r})\hat{\Psi}^\dagger(\mathbf{r}')\hat{\Psi}(\mathbf{r}')\hat{\Psi}(\mathbf{r})\rangle \,, \tag{1.8}$$

Note that in one-body correlation function (1.7) we consider non-local dependence, and it has two arguments. At the same time we consider only local two-body operators, that is why we keep two arguments instead of four in (1.6).

The quantum averages of the operators $\hat{F}^{(1)}$ and $\hat{F}^{(2)}$ may be obtained from $\hat{f}^{(1)}$ and $\hat{f}^{(2)}$, when the correlation functions are known:

$$\langle \hat{F}^{(1)}\rangle = \int f^{(1)}(\mathbf{r})C_1(\mathbf{r},\mathbf{r})\,\mathrm{d}\mathbf{r} \tag{1.9}$$

$$\langle \hat{F}^{(2)}\rangle = \frac{1}{2}\iint f^{(2)}(\mathbf{r},\mathbf{r}')C_2(\mathbf{r},\mathbf{r}')\,\mathrm{d}\mathbf{r}\,\mathrm{d}\mathbf{r}' \,. \tag{1.10}$$

The correlations of the field operator between two distinct points $\mathbf{r}$ and $\mathbf{r}'$, are characterized by the one-body correlation function $C_1(\mathbf{r},\mathbf{r}')$. The diagonal component of (1.7) $\mathbf{r} = \mathbf{r}'$ yields the density of the particles $\rho(\mathbf{r}) = \langle \hat{\Psi}^\dagger(\mathbf{r})\hat{\Psi}(\mathbf{r})\rangle = C_1(\mathbf{r},\mathbf{r})$, hence the sum over the diagonal terms, i.e., the trace of the matrix C_1, is equal to the total number of particles $N = \operatorname{tr} C_1 = \int C_1(\mathbf{r},\mathbf{r})\,\mathrm{d}\mathbf{r}$. The two-body correlation function $C_2(\mathbf{r},\mathbf{r}')$ defines correspondingly the density correlations between the particles at positions $\mathbf{r}$ and $\mathbf{r}'$, respectively.

It is convenient to introduce dimensionless versions of these functions (1.7) and (1.8):

$$c_1(\mathbf{r},\mathbf{r}') = \frac{C_1(\mathbf{r},\mathbf{r}')}{\sqrt{\rho(\mathbf{r})}\sqrt{\rho(\mathbf{r}')}} \tag{1.11}$$

$$c_2(\mathbf{r},\mathbf{r}') = \frac{C_2(\mathbf{r},\mathbf{r}')}{\rho(\mathbf{r})\rho(\mathbf{r}')} \tag{1.12}$$

It can be seen that for bosons the range of any of the functions (1.11-1.12) is $[0,1]$, and the function can be interpreted as a probability to remove a particle from the position $\mathbf{r}$ and place it to the position $\mathbf{r}'$. The obvious relation $c_1(\mathbf{r},\mathbf{r}) = 1$ reflects the fact, that there is always a possibility to put the particle back to its initial location. If no Bose-Einstein condensate is present, the non-diagonal terms asymptotically vanish in the long range limit

$c_1(\mathbf{r},\mathbf{r}') \to 0, |\mathbf{r},\mathbf{r}'| \to \infty$. The function $c_2(\mathbf{r},\mathbf{r}')$ can be understood as a joint probability to find one particle in the point $\mathbf{r}$ and another one in the point $\mathbf{r}'$.

Additional information on correlation functions can be found in Refs [Fee67, Mah00, Gla63, NG99, GS03].

1.2.2 First quantization form

The physical meaning of the correlation function written in the form of the second quantization has been briefly discussed in Section 1.2.1. We will use the Monte Carlo methods in order to evaluate averages over the wave function $\psi(\mathbf{R})$ of the system. For that one needs to represent the averages as integrals of the operators over the wave function $\psi(\mathbf{R})$. We will look for the mean values of the operators in forms, similar to that of (1.9) and (1.10). In the first quantization the expectation value of a one-body operator reads as

$$\langle A^{(1)} \rangle = \frac{\int \psi^*(\mathbf{R}) A^{(1)} \psi(\mathbf{R}) \, \mathrm{d}\mathbf{R}}{\int |\psi(\mathbf{R})|^2 \, \mathrm{d}\mathbf{R}} = \frac{\sum_{i=1}^{N} \int \psi^*(\mathbf{r}_1, ..., \mathbf{r}_N) a_i^{(1)} \psi(\mathbf{r}_1, ..., \mathbf{r}_N) \, \mathrm{d}\mathbf{R}}{|\psi(\mathbf{R})|^2 \, \mathrm{d}\mathbf{R}} =$$
$$= N \frac{\int a^{(1)}(\mathbf{r}_1) |\psi(\mathbf{r}_1, ..., \mathbf{r}_N)|^2 \, \mathrm{d}\mathbf{R}}{\int |\psi(\mathbf{R})|^2 \, \mathrm{d}\mathbf{R}} = \int a^{(1)}(\mathbf{r}) C_1(\mathbf{r},\mathbf{r}) \, \mathrm{d}\mathbf{r}, \qquad (1.13)$$

with the notation $C_1(\mathbf{r},\mathbf{r}')$ used for the expression

$$C_1(\mathbf{r},\mathbf{r}') = N \frac{\int \psi^*(\mathbf{r}, \mathbf{r}_2, ..., \mathbf{r}_N) \psi(\mathbf{r}', \mathbf{r}_2, ..., \mathbf{r}_N) \, \mathrm{d}\mathbf{r}_2 ... \mathrm{d}\mathbf{r}_N}{\int \psi^*(\mathbf{r}_1, ..., \mathbf{r}_N) \psi(\mathbf{r}_1, ..., \mathbf{r}_N) \, \mathrm{d}\mathbf{r}_1 ... \mathrm{d}\mathbf{r}_N} \qquad (1.14)$$

An average of a two-body operator (1.10) can be expressed in terms of the two-body correlation function (1.8) in the following way:

$$\langle A^{(2)} \rangle = \frac{\int \psi^*(\mathbf{R}) A^{(2)}(\mathbf{R}) \psi(\mathbf{R}) \, \mathrm{d}\mathbf{R}}{\int |\psi(\mathbf{R})|^2 \, \mathrm{d}\mathbf{R}} = \frac{\frac{1}{2} \sum_{i \neq j}^{N} \int \psi^*(\mathbf{r}_1, ..., \mathbf{r}_N) a^{(2)}(\mathbf{r}_i, \mathbf{r}_j) \psi(\mathbf{r}_1, ..., \mathbf{r}_N) \, \mathrm{d}\mathbf{R}}{|\psi(\mathbf{R})|^2 \, dR} \qquad (1.15)$$
$$= \frac{N(N-1)}{2} \frac{\int a^{(2)}(\mathbf{r}_1, \mathbf{r}_2) |\psi(\mathbf{r}_1, ..., \mathbf{r}_N)|^2 \, \mathrm{d}\mathbf{R}}{\int |\psi^*(\mathbf{R})|^2 \, \mathrm{d}\mathbf{R}} = \frac{1}{2} \iint a^{(2)}(\mathbf{r}_1, \mathbf{r}_2) C_2(\mathbf{r}_1, \mathbf{r}_2) \, \mathrm{d}\mathbf{r}_1 \, \mathrm{d}\mathbf{r}_2, \qquad (1.16)$$

with the following expression for the first quantization form of the two-body correlation function

$$C_2(\mathbf{r}', \mathbf{r}'') = \frac{N(N-1) \int |\psi(\mathbf{r}', \mathbf{r}'', \mathbf{r}_3, ..., \mathbf{r}_N)|^2 \, \mathrm{d}\mathbf{r}_3 ... \mathrm{d}\mathbf{r}_N}{\int |\psi(\mathbf{r}_1, ..., \mathbf{r}_N)|^2 \, \mathrm{d}\mathbf{r}_1 ... \mathrm{d}\mathbf{r}_N} \qquad (1.17)$$

The situation can get easier if we stick to the case of a homogeneous system, as it possesses translational symmetry. In the case of one-body operator, the diagonal $\mathbf{r} = \mathbf{r}'$ element of Eq. (1.14) is just a constant, which value is fixed by the density $n = N/V$,

$C_1(\mathbf{r},\mathbf{r}) = n$. The non-diagonal elements of the normalized matrix of one-body operator in the first quantization (or simply *one-body density matrix*) read as

$$g_1(r) = \frac{N}{n}\frac{\int \psi^*(\mathbf{r},\mathbf{r}_2,...,\mathbf{r}_N)\psi(0,\mathbf{r}_2,...,\mathbf{r}_N)\ \mathrm{d}\mathbf{r}_2...\,\mathrm{d}\mathbf{r}_N}{\int |\psi(\mathbf{r}_1,...,\mathbf{r}_N)|^2\ \mathrm{d}\mathbf{r}_1...\,\mathrm{d}\mathbf{r}_N} \tag{1.18}$$

where $n = N/V$ is the average density of a homogeneous system. The normalized two-body density matrix, also called *pair distribution function* is represented by

$$g_2(r) = \frac{N(N-1)}{n^2}\frac{\int |\psi(\mathbf{r},0,\mathbf{r}_3,...,\mathbf{r}_N)|^2\ \mathrm{d}\mathbf{r}_3...\,\mathrm{d}\mathbf{r}_N}{\int |\psi(\mathbf{r}_1,...,\mathbf{r}_N)|^2\ \mathrm{d}\mathbf{r}_1...\,\mathrm{d}\mathbf{r}_N} \tag{1.19}$$

The basic properties of the pair distribution function in the zero temperature limit can be deduced in the following way. In a gas phase, density-density correlations vanish for large interparticle distances, which corresponds to $g_2(r) \to 1 - \frac{1}{N}$, hence in the thermodynamic limit $g_2(r)$ asymptotically tends to 1.

One faces the opposite situation at short distances, where the particle correlations are strong, and the value of $g_2(0)$ can vary depending on the interaction potential. For instance, in case of a repulsive potential $g_2(0) < 1$, on the contrary for a purely attractive potential $g_2(0) > 1$, and in the case of a hard-core interaction when the particles are not allowed to overlap, $g_2(0) = 0$, when $|\mathbf{r}| < R_{core}$.

Let us consider the expectation value of a two-body operator (1.10) and see how it can be simplified in a homogeneous system:

$$\left\langle A^{(2)} \right\rangle = \frac{n^2}{2}\iint g_2(\mathbf{r}_1,\mathbf{r}_2)\ a^{(2)}(|\mathbf{r}_1-\mathbf{r}_2|)\ \mathrm{d}\mathbf{r}_1\,\mathrm{d}\mathbf{r}_2 = \frac{nN}{2}\int g_2(r)\ a^{(2)}(r)\,dr \tag{1.20}$$

In the integration performed above we made use of the mentioned fact, that the operator depends only on the distance between particles, allowing to integrate one of the coordinates out.

In the simplest case of a contact delta-potential $V_{\mathrm{int}}(r) = g\delta(r)$ (g stands for a coupling constant, defining the interaction strength) the potential energy is simply proportional to the value of the pair distribution function at $\mathbf{r} = 0$:

$$\frac{E_{\mathrm{pot}}}{N} = \frac{1}{2}g\,n g_2(0) \tag{1.21}$$

1.2.3 Static structure factor

By virtue of the field operator (1.1) the momentum distribution $n_{\boldsymbol{k}}$ is represented as

$$n_{\boldsymbol{k}} = \langle \hat{\Psi}^\dagger_{\boldsymbol{k}}\hat{\Psi}_{\boldsymbol{k}}\rangle, \tag{1.22}$$

The field operator in momentum space $\hat{\Psi}_{\boldsymbol{k}}$ is in fact the Fourier transform of $\hat{\Psi}(\mathbf{r})$:

$$\begin{cases} \hat{\Psi}_{\boldsymbol{k}} &= \int e^{-\mathrm{i}\boldsymbol{k}\mathbf{r}}\hat{\Psi}(\mathbf{r})\frac{\mathrm{d}\mathbf{r}}{\sqrt{2\pi}^D} \\ \hat{\Psi}(\mathbf{r}) &= \int e^{\mathrm{i}\boldsymbol{k}\mathbf{r}}\hat{\Psi}_{\boldsymbol{m}}\frac{\mathrm{d}\mathbf{k}}{\sqrt{2\pi}^D} \end{cases} \tag{1.23}$$

where D stands for a dimensionality of the system. Applying the relation (1.23) to the equation (1.22) one finds the following form of the momentum distribution

$$n_{\boldsymbol{k}} = \frac{1}{2\pi}^{D} \iint e^{\mathrm{i}\boldsymbol{k}\boldsymbol{s}} C_1\left(\frac{\boldsymbol{s}}{2} + \mathbf{R}, \mathbf{R} - \frac{\boldsymbol{s}}{2}\right) \mathrm{d}\boldsymbol{s}\, \mathrm{d}\mathbf{R} \tag{1.24}$$

It can be noticed that in a homogeneous bulk system the center of mass motion can be integrated separately, as the dependence on the momentum is defined by the distance between the particles, not positions themselves. Performing this integration for a homogeneous system it yields

$$n_{\boldsymbol{k}} = n \int e^{-\mathrm{i}\boldsymbol{k}\mathbf{r}} g_1(\mathbf{r})\, \mathrm{d}\mathbf{r} \tag{1.25}$$

For example, for a fully Bose-condensed gas, the off-diagonal terms of one-body density matrix are constant, $g_1(\mathbf{r}) = n$, which results in a singular momentum distribution $n_{\boldsymbol{k}} = N\delta(\boldsymbol{k})$. In this case all particles are condensed in $\boldsymbol{k} = 0$ state.

Another useful quantity is the dynamic structure factor of the system, which characterizes a scattering process, corresponding to the exchange of energy $\hbar\omega$ and the momentum $\hbar k$ in the scattering event. The dynamic structure factor $S(k, \omega)$ can be expressed by virtue of the k-component of the density operator at zero temperature

$$\hat{\rho}_{\boldsymbol{k}} = \sum_{i=1}^{N} e^{-\mathrm{i}\boldsymbol{k}\mathbf{r}_i} \tag{1.26}$$

in the following form

$$S(\boldsymbol{k}, \omega) = \sum_i |\langle n|\hat{\rho}^\dagger_{\boldsymbol{k}} - \langle\hat{\rho}^\dagger_{\boldsymbol{k}}\rangle|0\rangle|^2 \delta(\hbar\omega - \hbar\omega_i)\,. \tag{1.27}$$

where ω_i is the frequency of the i-th stationary state. The static structure factor is proportional to the frequency integral of the dynamic structure factor, that is it characterizes the overall probability of scattering of a probe particle with the momentum transfer $\hbar k$. The separate integration over ω gives

$$S(\boldsymbol{k}) = \frac{\hbar}{N} \int_0^\infty S(\boldsymbol{k}, \omega)\, d\omega = \frac{1}{N}(\langle\hat{\rho}_{\boldsymbol{k}}\hat{\rho}_{-\boldsymbol{k}}\rangle - |\langle\hat{\rho}_{\boldsymbol{k}}\rangle|^2) \tag{1.28}$$

The latter expression (1.28) can be sampled directly in Quantum Monte Carlo simulations. The other way to write the static structure factor is to relate it to the two-body density matrix by means of the equations (1.8) and (1.26), having in mind the commutation properties of the field operator $\hat{\Psi}(r)$

$$S(k) = 1 + \iint \frac{1}{N} e^{\mathrm{i}(\mathbf{r}_2 - \mathbf{r}_1)\boldsymbol{k}} (C_2(\mathbf{r}_1, \mathbf{r}_2) - n(r_1)n(r_2))\, \mathrm{d}\mathbf{r}_1\, \mathrm{d}\mathbf{r}_2 \tag{1.29}$$

In case of a homogeneous system, the positions of the particles enter the two-body density matrix only as an interparticle distance $r = |\mathbf{r}_1 - \mathbf{r}_2|$, thus the static structure

factor can be rewritten in terms of the Fourier transform of the pair distribution (1.12) of the system:

$$S(k) = 1 + n \int e^{\mathrm{i}rk}(g_2(r) - 1)\ \mathrm{d}\mathbf{r} \tag{1.30}$$

The static structure factor can yield valuable information on the arrangement and the order of the system, and its value can be directly accessed in spectroscopy experiments.

1.3 Scattering problem

1.3.1 Introduction

The construction of a trial wave function for a many-body problem is in most cases a very complex task since the exact solution is generally unknown (rare exceptions for analytic solutions are the 1D gas of hard rods and hard points (Tonks-Girardeau gas), where the analytic solutions are known). A typical approach to develop a trial wave function therefore consists in matching long-range behavior with a two-body solution at short distances. In this Section, we will be concerned with the two-body scattering problems in three-dimensional systems, whose solutions are then used in many-body calculations presented in the following chapters.

1.3.2 Scattering problem in three-dimensional geometry

1.3.2.1 General approach

In this Section, we formulate a generic two-body scattering problem in a 3D geometry. For a three-dimensional system the low-density regime of interparticle interaction is supposed to be correctly described by two-body collisions.

Consider two particles with coordinates $\mathbf{r}_1$ and $\mathbf{r}_2$ and respective masses m_1 and m_2 staying close enough to see the process as a two-particle collision. We suppose that the system is not confined externally, hence the problem may be treated as translationary invariant, with the center of mass moving with a constant speed. Our purpose is to obtain the stationary solution $p(\mathbf{r}_1, \mathbf{r}_2)$ of the Schrödinger equation

$$\left[-\frac{\hbar^2}{2m_1}\Delta_{\mathbf{r}_1} - \frac{\hbar^2}{2m_2}\Delta_{\mathbf{r}_2} + V(|\mathbf{r}_1 - \mathbf{r}_2|)\right] p(\mathbf{r}_1, \mathbf{r}_2) = \mathcal{E}_{12}\, p(\mathbf{r}_1, \mathbf{r}_2)\ . \tag{1.31}$$

In the center of mass frame, the coordinate variables get separated, thus the representation of the Schrödinger equation for the motion of the center of mass $\mathcal{R} = (m_1\mathbf{r}_1 + m_2\mathbf{r}_2)/m_{\text{total}}$ gets simple

$$-\frac{\hbar^2}{2m_{\text{total}}}\Delta_{\mathcal{R}} f_{\mathcal{R}}(\mathcal{R}) = \mathcal{E}_{\mathcal{R}} f_{\mathcal{R}}(\mathcal{R})\ , \tag{1.32}$$

with $m_{\text{total}} = m_1 + m_2$ staying for the total mass. The solution of Eq. (1.32) is of a free wave form. Omitting the normalization, the solution reads $f_{\mathcal{R}}(\mathcal{R}) = \exp[\mathrm{i}\boldsymbol{k}_{\mathcal{R}}\mathcal{R}]$ with $\boldsymbol{k}_{\mathcal{R}}$, being the initial center of mass wave number of the system with the corresponding energy $\mathcal{E}_{\mathcal{R}} = \hbar^2 k_{\mathcal{R}}^2 / 2m_{\text{total}}$.

The equation for the position difference $\mathbf{r} = \mathbf{r}_1 - \mathbf{r}_2$ contains the pairwise interaction potential

$$\left(-\frac{\hbar^2}{2\mu}\Delta_{\mathbf{r}} + V(|\mathbf{r}|)\right) f(\mathbf{r}) = \mathcal{E} f(\mathbf{r}) \ , \tag{1.33}$$

with

$$\mu = \frac{m_1 m_2}{m_1 + m_2} \tag{1.34}$$

denoting the reduced mass. When one finds the solutions of Eqs (1.32-1.33), it is possible to obtain the needed solution of the scattering problem (1.31) as

$$\begin{cases} p(\mathbf{r}_1, \mathbf{r}_2) &= f_{\mathcal{R}}(\mathcal{R}) f(\mathbf{r}) \\ \mathcal{E}_{12} &= \mathcal{E} + \mathcal{E}_{\mathcal{R}} \end{cases} \tag{1.35}$$

We will assume that the energy of the incident particle E is small enough and the solution is spherically symmetric $f(\mathbf{r}) = f(|\mathbf{r}|)$. Under these prescriptions, and using the spherically symmetric representation of the Laplacian $\Delta = \frac{\partial^2}{\partial r^2} + \frac{2}{r}\frac{\partial}{\partial r}$, one can conveniently rewrite the equation (1.33), introducing the auxiliary function $w(r)$

$$f(r) \ = \ \frac{w(r)}{r} \tag{1.36}$$

in a way that its analytic form is similar to a one-dimensional Schrödinger equation:

$$-\frac{\hbar^2}{2\mu} w''(r) + V_{\text{int}}(r) w(r) = \mathcal{E} w(r) \tag{1.37}$$

with the additional requirement of the boundary condition

$$w(0) \ = \ 0 \ . \tag{1.38}$$

At distances, large compared to the range of the potential, one can neglect $V_{\text{int}}(\mathrm{r})$ term in Eq. (1.37) leaving with a free wave differential equation.

$$-\frac{\hbar^2}{2\mu} w''(r) = \mathcal{E} w(r) \tag{1.39}$$

The solution for this equation is a plane wave

$$w(r) = A \sin(k_s r + \delta(k_s)), \tag{1.40}$$

where

$$\hbar k_s = \sqrt{2\mu\mathcal{E}} \tag{1.41}$$

stands for the momentum of the incident particle and $\delta(k_s)$ is the scattering phase and A is an arbitrary constant.

Properties of the low-energy scattering depend on a single parameter, namely s-wave scattering length a_{3D}. Its value can be obtained from the phase shift $\delta(k_s)$ as the following limit

$$a_{3D} = -\lim_{k\to 0} \frac{\delta(k_s)}{k_s} \tag{1.42}$$

If we consider the asymptotic low-momentum limit $k \to 0$ (slow particles) the scattering solution (1.40) may be expanded

$$f(r) \to \text{const}\left(1 - \frac{a_{3D}}{r}\right) \tag{1.43}$$

and it is easy to see, that it has a node at a distance a_{3D}. The position of the first node of the positive energy scattered solution in the limit of low momenta can be seen as an equivalent definition of the scattering length in a three-dimensional system.

In low-density regime of weekly interacting gas the interparticle distance is large compared to the range of the potential. Under such conditions the exact shape of the interaction potential is not important and the description in terms of the s-wave scattering length is universal.

In the next several sections we will consider the scattering problem for a hard-sphere potential (1.3.2.2) as a simplest example, and afterwards the same problem for the Yukawa potential (1.3.2.3) and the common potential between Rydberg atoms (1.3.2.4) will be solved. We will obtain explicitly the expressions for the scattered functions, which are of great importance, since in many cases they can give a deep physical insight into properties of a many-body system. Indeed, under particular conditions the relation between the correlation functions and the scattered wave function $f(r)$ can be found. Another important point to mention is that often a many-body trial wave function is taken as a product of scattered functions $f(r)$. Hence, these calculations are of great importance for their further implementation of the Quantum Monte Carlo algorithms.

1.3.2.2 Scattering on hard sphere potential

As it was mentioned in Sec. 1.3.2.1, in the limit of low energy collisions the interaction potential is characterized exclusively by one parameter, the s-wave scattering length. It means that when $E \to 0$ the scattering on each potential possessing equal scattering lengths is the same, and it is said that the scattering becomes *universal*. If the scattering

is considered on some repulsive potential, then the easiest choice is the hard sphere (HS) potential:

$$V^{\mathrm{hs}}(r) = \begin{cases} +\infty, & r < a_{3D} \\ 0, & r \geq a_{3D} \end{cases} \tag{1.44}$$

This potential is controlled by a single parameter, which we denote a_{3D} in the definition (1.44). It is clear that we can treat this value as a range of the potential. Simultaneously it has a meaning of the scattering length, as it was presented in (1.42). It comes out in a natural way from the solution of the scattering problem, as by definition the s-wave scattering length is the position of the first node of the analytic continuation of a large-distance free wave solution. For the hard sphere potential this free-wave solution is valid for $r > a_{3D}$ with the position of the node given by $|\mathbf{r}| = a_{3D}$.

The Schrödinger equation (1.37) can be rewritten as (the reduced mass is $\mu = m/2$)

$$-\frac{\hbar^2}{m} w''(r) + V^{\mathrm{hs}}(r) w(r) = \mathcal{E} w(r) \tag{1.45}$$

A particle is unable to penetrate the potential wall of the hard core thus the solution tend to zero for distances below the size of the hard sphere. Notice that the energy in this case has only a kinetic component, and the interaction potential does not enter explicitly. Nevertheless it affects the boundary condition for the solution.

$$\begin{cases} w(r) = 0, & |r| < a_{3D} \\ w''(r) + \varkappa^2 w(r) = 0, & |r| \geq a_{3D} \end{cases} \tag{1.46}$$

with a convenient substitution for the frequency $\varkappa^2 = \frac{m\mathcal{E}}{\hbar^2}$. The solution of this differential equation (1.46) may be obtained easily. Joining together with (1.36) one gets:

$$f(r) = \begin{cases} 0, & |r| < a_{3D} \\ A \sin(k(r - a_{3D}))/r, & |r| \geq a_{3D} \end{cases}, \tag{1.47}$$

with A for an arbitrary constant. The phase shift is related linearly to the wave vector of the incident particle $\delta(k) = -\varkappa a_{3D}$ (1.42), showing explicitly that the range of the potential (1.44) has in fact the meaning of the three-dimensional scattering length as we said above in the same Section.

1.3.2.3 Scattering on Yukawa potential

The solution of the two-body scattering problem, as it was mentioned above, is used to construct the trial wave functions for subsequent use in the Quantum Monte Carlo simulations. The need of having correctly posed short-distance approximation for the trial wave stems from the fact that the majority of physically relevant pairwise interactions contain a repulsive core, that can vary in hardness. Since the diffusion Monte Carlo method is based on a sampling from the particle distribution $\psi_T \psi_0$, an inaccurate choice

of the trial wave function ψ_T for small r can result in a substantial growth of the overall error of the calculation. This can be manifested by a need of raising the number of walkers to reach a convergence as well as by a growth of a common statistical variance. On the other hand, the errors in the long-range part are usually easily "corrected" by the DMC algorithm, as this range is statistically well represented, and also the actual discrepancy of the trial wave and the ground state solution is relatively low.

The two-body scattering problem for the potential of Yukawa is solved in a similar manner, as was used in the solution for a system of hard spheres. The solution of the initial Schrödinger equation is considered spherically symmetric and therefore rewritten as a one-dimensional equation with a single argument, the interparticle distance $r = |\mathbf{r}_1 - \mathbf{r}_2|$. If we look for the solution in the form convenient for subsequent use as a Bijl-Jastrow term in Monte Carlo calculations, then in accordance with Eq. (1.37)

$$-\frac{\hbar^2}{m}w''(r) + V_0\frac{\exp(-2r)}{r}w(r) = \mathcal{E}w(r)\,. \tag{1.48}$$

The solution of the latter equation for short-range distances can be obtained by approximating $\exp(-2r)$ by 1. One possibility is to consider the scattering at a finite energy $\mathcal{E}$ and fix the value of $\mathcal{E}$ from continuous matching with the long-range behavior of Bijl-Jastrow term. Equation (1.48) can be solved by means of the hypergeometric functions. A less precise description can be obtained by setting $\mathcal{E} = 0$, still the obtained Bijl-Jastrow term is well suited for DMC calculation. The $\mathcal{E} = 0$ case

$$-\frac{\hbar^2}{m}w''(r) + \frac{\exp(-2r)}{r}w(r) = 0 \tag{1.49}$$

results in a more simple solution which is a linear combination of the modified Bessel functions of the first kind and the second kind with particular square root factors,

$$f(r) = C_i\frac{I_1(2\sqrt{r}/\varkappa)}{\varkappa\sqrt{r}} + C_k\frac{K_1(2\sqrt{r}/\varkappa)}{\varkappa\sqrt{r}} \tag{1.50}$$

with $\varkappa = \sqrt{\hbar^2/(mV_0)}$. The first component I_1 is finite for $\mathbf{r} = 0$, while the second one K_1 diverges for $\mathbf{r} = 0$. The arbitrary constant is irrelevant for the QMC algorithms that we use, therefore we stick to the following form of the two-body scattering solution

$$f(r) = \frac{I_1(2\sqrt{r}/\varkappa)}{\sqrt{r}} = \varkappa + \frac{\varkappa^3}{2}r + \frac{\varkappa^5}{12}r^2 + \mathcal{O}(r^3) \tag{1.51}$$

A more precise analytic solution can be found by using a higher-order expansion of the Yukawa factor $\exp(-2r)$, that is $\exp(-2r) \approx 1 - 2r$, however the use of a single first term of the expansion is usually enough for practical purposes.

The diffusion Monte Carlo study of Yukawa systems, made by Ceperley *et al.* [CCK78], was based on the following form of the Jastrow term of the trial wave function, typically used in the nuclear matter calculations

$$u(r) = Ae^{-Br}(1 - e^{-r/D})/r\,. \tag{1.52}$$

It can be shown that the expression $\exp(-u(r))$ can be made coincident in the leading terms with the expansion of the solution (1.51) of the two-body scattering problem:

$$\begin{aligned} e^{-u(r)} &= e^{-A/D} + \frac{A(1+2BD)e^{-A/D}}{2D^2}r + \\ &+ \frac{A(3D - 4D + 12ABD - 12BD^2 + 12AB^2D^2 - 12B^2D^3)e^{-A/D}}{24D^2}r^2 + \mathcal{O}(r^3) \end{aligned} \tag{1.53}$$

One can note that Jastrow term (1.54) coincides with the solution of the two-body scattering problem (1.50) for a particular choice of variational parameters A, B, D. Notice that the parameters A, B, D are subject to a variational optimization within a quantum Monte Carlo framework, although the trial wave function, constructed from a two-body scattering solution, is fixed for any given choice of the mass of the particle and of the interaction strength. However in practice it might be convenient to keep the functional form of the solution and to treat its characteristic coefficients as variational parameters. A typical Jastrow term of the trial wave function of this symmetrized functional form is given in Fig. (2.1) in the Section, devoted to the Monte Carlo methodology.

Worth noticing that in case of the Yukawa potential the pair distribution function at zero can be finite for $r = 0$, as it happens for the Coulomb potential. This can be easily confirmed if one takes a series expansion from Eq. (1.52). The typical value of the leading component A/D in the conditions of our problem is of the order of 10, therefore the zero value of the trial wave $\exp(-A/D)$ is very small and practically indistinguishable of zero, as one can see from Fig. (2.1).

1.3.2.4 Scattering on repulsive van der Waals

A similar derivation path can be applied to obtain the solution of the two-body scattering for the system of Rydberg atoms, interacting via the simple $1/\mathbf{r}^6$ interaction potential. The Schrödinger equation for the two-body Hamiltonian in the reduced units for this problem (see Sec. 5) in the system of the center of masses reads as

$$-w''(r) + \frac{C_6}{r^6}w(r) = Ew(r) \tag{1.54}$$

where we used a familiar substitution $f(r) = w(r)/r$. The finite low-energy solution of the latter equation has the following form (normalization is omitted):

$$f(r) = \frac{1}{\sqrt{r}}K\left(\frac{1}{4}, \frac{\sqrt{C_6}}{2r^2}\right) \tag{1.55}$$

where $K(\alpha, x)$ stands for the modified Bessel's function of the second kind. Its expansion in the series of r is given by

$$\frac{1}{\sqrt{r}} K\left(\frac{1}{4}, \frac{\sqrt{C_6}}{r^2}\right) = e^{-\frac{\sqrt{C_6}}{2r^2}} \left[\frac{\sqrt{2\pi}}{C_6^{1/4}}\sqrt{r} + \mathcal{O}(r^{5/2})\right] . \tag{1.56}$$

The short-range behavior of the function is dominated by the exponential term $e^{-\frac{\sqrt{C_6}}{2r^2}}$, which smoothly approaches zero as $r \to 0$. As in the case of the Yukawa potential, the interaction constant C_6 and the power (-2) can be conveniently treated as variational parameters, while keeping the overall functional form of the trial wave function intact. A typical form of a trial wave function and a pair distribution function for the system is presented in Fig. (1.1).

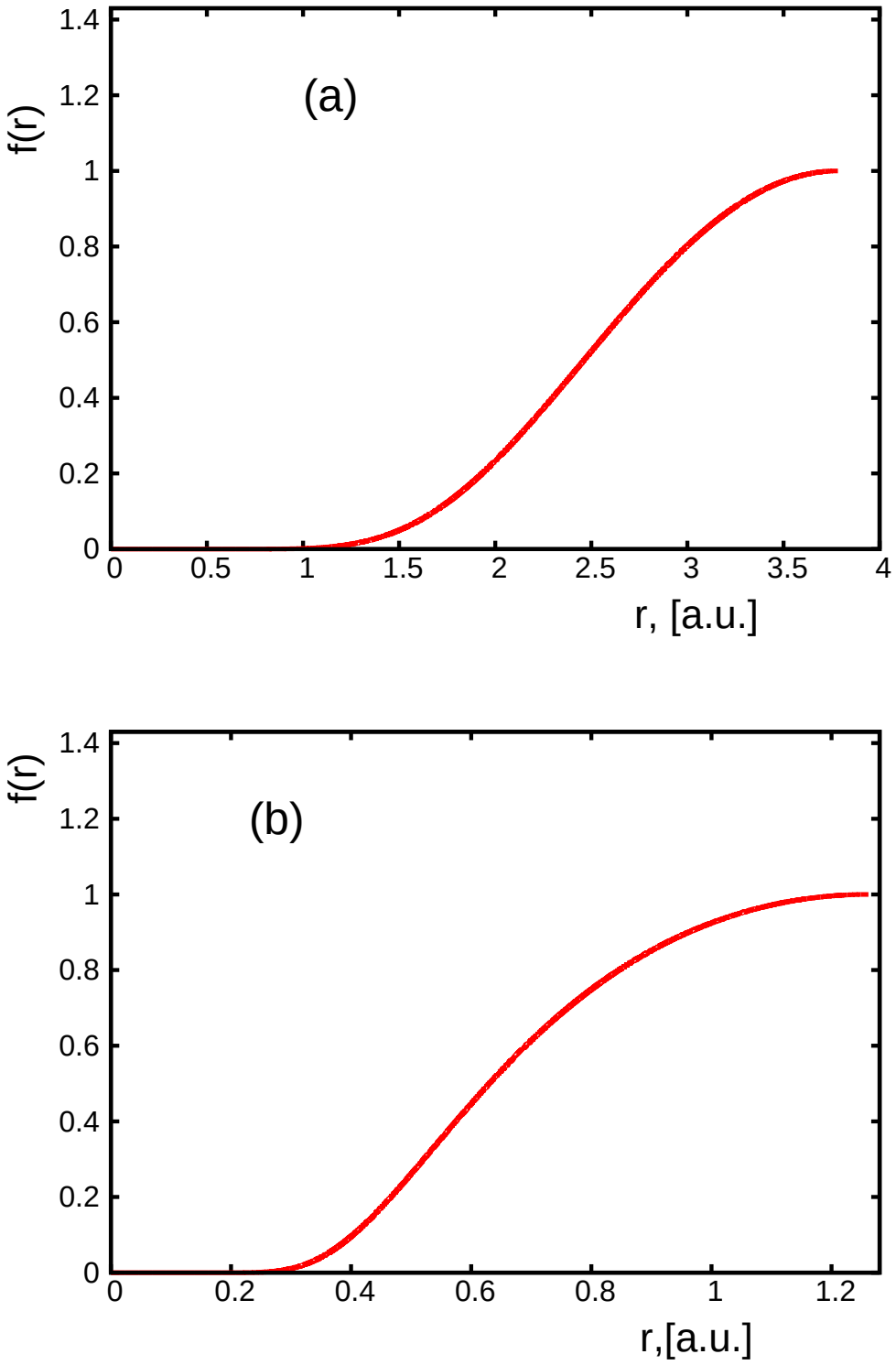

Figure 1.1: Typical forms of the trial wave functions for (a) Yukawa potential, and (b) model potential between Rydberg atoms.

Chapter 2

Quantum Monte Carlo methods

2.1 Introduction

Quantum Monte Carlo methods (QMC) are very efficient and multi-purpose tools for the investigation of quantum many-body systems (for a detailed review of the methods see, for instance, [Cep95], [Gua98]). The use of Quantum Monte Carlo techniques provides a deep insight into the microscopic behavior of quantum states of matter. QMC are essentially *ab initio* methods, relying on a microscopic description of a system and gathering valuable information on its properties of the system through a numerical simulation. In certain cases, it turns out that this technique is the only tool for studying complex problems with reasonable calculation costs. In fact, in order to have a model, accessible for being solved analytically in the exact way, a physicist usually faces the necessity to make some kinds of approximations, but this can be avoided to a big extent by virtue of Quantum Monte Carlo simulations. As an example, the applicability of perturbation theory is limited by a small value of the perturbation parameter, while the QMC methods do not present any restrictions of this kind. Quantum Monte Carlo technique allow to find the ground state solution of the many-body Schrödinger equation at zero temperature. As follows from the name, the Quantum Monte Carlo methods are based on stochastic numerical algorithms of different sorts, that by nature are especially advantageous when the system in question possesses multiple degrees of freedom. As for any other stochastic procedure, the QMC methods provide results with a certain statistical error that can be diminished by performing longer measurement series.

We are interested in studying the quantum properties of a given system. The quantum effects manifest the most when they are not disturbed by the thermal motion, that is at the lowest temperatures, when the system maintains in its ground state. For this case a possible method of choice to address the problem is the diffusion Monte Carlo (DMC) method. For a bosonic system this method allows to obtain the *exact* result for the energy of the ground state, as well as for any diagonal property of the state.

In this chapter first of all we discuss the variational Monte Carlo method as the simplest one. Then we will discuss the bosonic diffusion Monte Carlo method and give a detailed explanation on how trial wave functions are constructed. Finally, we will present the main ideas for the implementation of the sampling of the quantities of interest.

2.2 Variational Monte Carlo

2.2.1 General notes

The simplest of the Quantum Monte Carlo methods is the *variational* method (VMC). The general idea behind this technique is to find an approximate wave function ψ_T, called *trial wave function* (or, sometimes, *variational wave function*), and then by sampling from the probability distribution

$$p(\mathbf{r}) \;=\; |\psi_{\text{trial}}(\mathbf{r})|^2 \tag{2.1}$$

calculate averages of physical quantities. It can be shown that E_T, the expectation value of the Hamiltonian, is an upper bound to the ground-state energy E_0. By expanding the normalized trial wave function in the basis of the normalized eigenfunction of the Hamiltonian

$$\psi_T = \sum_{i=0}^{\infty} c_i \phi_i \tag{2.2}$$

$$\sum_{i=0}^{\infty} |c_i|^2 = 1\,, \tag{2.3}$$

one can rewrite the variational energy as

$$E_T \;=\; \frac{\langle\psi_T|\hat{H}|\psi_T\rangle}{\langle\psi_T|\psi_T\rangle} \tag{2.4}$$

$$\;=\; \langle\sum_{i=0}^{\infty} c_i\phi_i|\hat{H}|\sum_{j=0}^{\infty} c_j\phi_j\rangle = \sum_{i,j=0}^{\infty} c_i^* c_j \langle\phi_i|\hat{H}|\phi_j\rangle \tag{2.5}$$

$$\;=\; \sum_{i,j=0}^{\infty} c_i^* c_j \delta_{i,j} E_i = \sum_{i=0}^{\infty} E_i |c_i|^2 \geq E_0 \sum_{i=0}^{\infty} |c_i|^2 = E_0 \tag{2.6}$$

where E_i stands for a corresponding eigenvalue (energy of the i-th state). By minimizing the variational energy with respect to the parameters entering into it one can optimize the wave function within the given class of considered wave functions. The only situation when the zero variance can be reached is when the wave function is exactly known.

2.2.2 Usage of the VMC method

If the wave function, corresponding to the ground state, is exactly known the sampling by means of the Variational Monte Carlo method permits to evaluate exactly any static property of the system within some statistical errors. Such systems are scarce; the ground state of a system of hard rods [KMJ99] and the Tonks-Girardeau gas [Gir60] are among the most famous ones. The Variational Monte Carlo method in this case can provide the correlation functions, which could be not accessible directly through the wave function.

The Variational Monte Carlo approach provides not only a valuable description of the quantum systems, but it also can be used as a first step to deliver a good quality input for the diffusion Monte Carlo method. The efficiency and even applicability of this method depends substantially on the optimization of the trial wave function within a chosen class of functions.

2.2.3 Notes on algorithmic realization

Let us stick to a coordinate representation in the following description, since it is the easiest way to work with external or interparticle potentials. Consider a common $D-$dimensional Euclidian space with a system of N_p particles inside. The probability distribution function in this system will be a function of $N \cdot D$ variables $p(\mathbf{R}) = p(\mathbf{r}_1, ..., \mathbf{r}_{N_p})$. The mean value for an arbitrary operator $\hat{Z}$ is therefore calculated as an integral of $N \cdot D$ dimensions in the following form:

$$\langle Z \rangle = \frac{\int ... \int Z(\mathbf{r}_1, ..., \mathbf{r}_{N_p}) p(\mathbf{r}_1, ..., \mathbf{r}_{N_p}) d\mathbf{r}_1 ... d\mathbf{r}_{N_p}}{\int ... \int p(\mathbf{r}_1, ..., \mathbf{r}_{N_p}) d\mathbf{r}_1 ... d\mathbf{r}_{N_p}} \tag{2.7}$$

It is clear that the complexity of the estimation of this integral with conventional non-stochastic methods, based on a grid calculation, grows extremely fast with the number of particles, and already for a few dozens of particles its calculation is unreachable. On the other hand, the stochastic procedure on which the Monte Carlo methods are based is not affected strongly by the growth of the dimensionality of the problem. The basic idea of the variational technique is to generate configuration states $\mathbf{R}_1, ..., \mathbf{R}_m$ with the probability distribution $p(\mathbf{R})$ and by means of these states estimate the average value of the operator $\langle Z \rangle$,

$$\langle Z \rangle \approx \frac{1}{m} \sum_{j=1}^{m} Z(\mathbf{R}_j) \, . \tag{2.8}$$

Every state is obtained only from its preceding configuration, thus this set of states is indeed a Markovian chain. The Metropolis algorithm [MRR+53] despite its simplicity is a very efficient tool to produce the chain with the desired probability $p(\mathbf{R})$. The transition from the old $\mathbf{R}$ configuration to the new one $\mathbf{R}'$ is accepted with the probability $P(\mathbf{R} \to \mathbf{R}')$, expressed by the formula

$$P(\mathbf{R} \to \mathbf{R}') = \begin{cases} p(\mathbf{R}')/p(\mathbf{R}), & \text{if } p(\mathbf{R}') < p(\mathbf{R}) \\ 1, & \text{if } p(\mathbf{R}') \geq p(\mathbf{R}) \end{cases} \tag{2.9}$$

In a quantum system, the probability distribution is given by the square of the wave function. The way we construct the particular trial wave function for different quantum systems will be discussed in Sec. 2.4.

There are distinct approaches to perform transitions (or *trial moves*) between different particle configurations. A straightforward way for creating a new state is to move one

particle at once or all the particles at once $\mathbf{r}_i' = \mathbf{r}_i + \rho_\mathbf{i}, \mathbf{i} = \overline{\mathbf{1}, \mathbf{N_p}}$, where the displacements $\rho_\mathbf{i}$ are a set randomly chosen vectors with a certain upper bound $|\rho_\mathbf{i}| < \mathbf{U}$. The limiting amplitude U can be adjusted in order to have a desired acceptance rate. It is readily seen that for very small values of U the trial moves are accepted almost all the time, but the adjacent states are strongly correlated, that affects the variance of the overall statistics, and in the limit $U \to 0$ all the states are the same, making the whole calculation pointless. On the other hand, the steps of very large amplitude U are accepted only a small fraction of time, which also leads to a poor performance. The value of U can be optimized to ensure the maximum total displacement of the whole system by means of a set of benchmark calculations, but in practice a simple rule of thumb to have the acceptance rate of the trial moves in the range $0.5 - 0.65$ provides good enough results.

A generalization of these two strategies of particle displacements, when only a particular fraction of the points is shifted together, can bring even faster performance. The group of particles to move in one step can be chosen randomly. The advantage of this technique lies in the possibility of fine tuning the calculation parameters in order to achieve an optimal point in terms of the interplay between the correlation of the states and the acceptance rate.

2.3 Diffusion Monte Carlo technique

The diffusion Monte Carlo method (DMC) is a stochastic computational technique applied to systems at zero temperature, when all of the thermal motion can be neglected. The key point of the DMC method is to provide the solution of the time-dependent Schrödinger equation in imaginary time, which is known to exponentially decay to the ground state solution in the limit of long times. By means of the diffusion Monte Carlo method the equation of state for the system as well as diagonal properties can be calculated exactly with the only cost of controlled statistical noise.

2.3.1 Schrödinger equation

The wave function of a quantum system obeys the Schrödinger equation

$$\mathrm{i}\hbar\frac{\partial}{\partial t}\psi(\mathbf{R}, t) = \hat{H}\psi(\mathbf{R}, t)\,. \tag{2.10}$$

Our aim is to find the ground state properties of the system, rather than its actual time evolution. By substituting the time variable by an imaginary one $\tau = -it/\hbar$, one arrives to another representation of the Schrödinger equation

$$-\frac{\partial}{\partial \tau}\psi(\mathbf{R}, \tau) = (\hat{H} - E)\psi(\mathbf{R}, \tau), \tag{2.11}$$

where E stays for a constant energy shift close to expected ground state energy. The latter equation (2.11) has a formal solution $\psi(\mathbf{R}, \tau) = e^{-(\hat{H}-E)\tau}\psi(\mathbf{R}, 0)$. One can expand

this solution as the sum over the eigenstates of the Hamiltonian $\hat{H}\phi_n = E_n\phi_n$, with the eigenstates taken such that the eigenvalues are growing with ascending indexes, that is E_0 is the lowest among the eigenvalues. Performing the expansion,

$$\psi(\mathbf{R},\tau) = \sum_{i=0}^{\infty} a_i\phi_i(\mathbf{R})e^{-(E_i-E)\,\tau}\,. \tag{2.12}$$

It can be easily seen that the exponents in the sums behave differently (decay or grow) provided the sign of (E_i-E) is positive or negative. For large enough τ the only component of the sum (2.12) that survives is the one, corresponding to the ground state. All the other terms decay in time exponentially fast (we suppose the spectrum to be discreet):

$$\psi(\mathbf{R},\tau) \to a_0\ \phi_0(\mathbf{R})\ e^{-\tau(E_0-E)}, \qquad \text{if}\ \ \tau\to\infty \tag{2.13}$$

A general expression for the Hamiltonian of a many-body system of N_p particles, subjected to an external force field $V_{\text{ext}}(\mathbf{r}_i)$, depending on a particle's position, and interacting internally through a pairwise potential $V_{\text{int}}(|\mathbf{r}_i-\mathbf{r}_j|)$ can be given as

$$\hat{H} = -\frac{\hbar^2}{2m}\sum_{i=1}^{N_p}\Delta_i^2 + \sum_{i=1}^{N_p}V_{\text{ext}}(\mathbf{r}_i) + \sum_{i<j}^{N_p}V_{\text{int}}(|\mathbf{r}_i-\mathbf{r}_j|)\,. \tag{2.14}$$

We take a notation for the constant $D=\hbar^2/2m$, referring to D as a "diffusion" constant, the sense of which will be clarified later. The Schrödinger equation (2.11) reads as

$$-\frac{\partial}{\partial\tau}\psi(\mathbf{R},\tau) = -D\Delta_{\mathbf{R}}\psi(\mathbf{R},\tau) + (V_{\text{total}}(\mathbf{R})-E)\psi(\mathbf{R},\tau), \tag{2.15}$$

with the label $\mathbf{R}$ in the Laplacian denoting the differentiation with respect to each scalar component of the vector $\mathbf{R}$. For shortness, the summation over the internal and the external potentials is denominated by a single term $V_{\text{total}}(\mathbf{R}) = \sum V_{\text{ext}}(\mathbf{r}_i) + \sum V_{\text{int}}(|\mathbf{r}_{ij}|)$.

The last term in Eq. (2.15) $(V_{\text{total}}(\mathbf{R})-E)\psi(\mathbf{R},\tau)$ is diagonal, and it affects the normalization through a specific step, called *branching*. As we mentioned above, a key ingredient of the diffusion Monte Carlo technique is the use of a trial wave function which allows to radically reduce the calculation efforts needed to reach a required accuracy in the result. Hence, one gives an approximation of the true ground state solution $\psi_0(\mathbf{R},\tau)$ by a certain trial wave function $\psi_T(\mathbf{R},\tau)$, which is subject to a correction inside the algorithm by means of the branching. The whole approach, referred to as importance sampling, stems from an analog of the Schrödinger equation for the product of the true wave function and the trial wave function

$$f(\mathbf{R},\tau) = \psi_T(\mathbf{R})\psi(\mathbf{R},\tau)\,. \tag{2.16}$$

The expectation value of an operator Z over this product of the wave functions can be thought of as a mixed estimator $\langle Z\rangle = \int \psi_T Z\,\psi\ \mathrm{d}\mathbf{R}/\int\psi_T\psi\ \mathrm{d}\mathbf{R}$. Performing a substitution of f inside the Schrödinger equation (2.15) the following equality can be drawn

$$-\frac{\partial}{\partial\tau}f(\mathbf{R},\tau) = -D\Delta_{\mathbf{R}}f(\mathbf{R},\tau) + (E^{\text{local}}(\mathbf{R})-E)f(\mathbf{R},\tau) + D\nabla_{\mathbf{R}}(f(\mathbf{R},\tau)\mathbf{F}(\mathbf{R},\tau)) \tag{2.17}$$

where E^{local} is the so-called local energy, that is the expectation value of the Hamiltonian with respect to the trial wave function (a broad discussion on the calculation of the values is given in Section 2.5).

$$E^{\text{local}}(\mathbf{R}) = \frac{\hat{H}\psi_T(\mathbf{R})}{\psi_T(\mathbf{R})} = (V_{\text{total}}(\mathbf{R}) - E) - D\frac{\Delta_{\mathbf{R}}\psi_T(\mathbf{R})}{\psi_T(\mathbf{R})}\,. \tag{2.18}$$

The action of the Metropolis algorithm in the variational Monte Carlo method, that is the averaging of an operator over the probability distribution $p(\mathbf{R}) = |\psi_T(\mathbf{R})|^2$, is therefore the averaging of the local energy with respect to the set of N_c particle configurations

$$E = \frac{1}{N_c}\sum_{i=1}^{N_c} E^{\text{local}}(\mathbf{R}_i)\,. \tag{2.19}$$

Notice that the local energy is equal to the eigenvalue of the Hamiltonian, when the trial wave function coincides with the eigenfunction. It means that E^{local} is a constant ground state energy with zero variance if $\psi_T(\mathbf{R},\tau) = \psi_0(\mathbf{R},\tau)$. The deviations of the trial wave function from the exact solution result in a growth of variance in the local energy, which can serve as a quality criterion for the trial wave function. The notation $\mathbf{F}$ stands for the *drift force*, a vector value, equal to the gradient of the field defined by the trial wave function, multiplied by a convenient factor,

$$\mathbf{F} = \frac{2\nabla_{\mathbf{R}}\psi_T(\mathbf{R})}{\psi_T(\mathbf{R})}\,. \tag{2.20}$$

The drift force moves the walkers $\{\mathbf{R}_i\}$ towards the region where ψ_T is large.

Notice that the probability distribution function in a classical system is defined by a Boltzmann factor $f(\mathbf{R}) \sim \exp(-E_{\text{pot}}(\mathbf{R})/k_BT)$, with $E_{\text{pot}}(\mathbf{R})$ standing for the potential energy in the system. The force, produced by the field, is equal to its gradient with the negative sign, that is $\mathbf{F}(\mathbf{R}) = -\nabla E_{\text{pot}} = \nabla \ln p(\mathbf{R})$. Making a formal substitution of the trial wave function instead of the probability density $p(\mathbf{R}) = \psi_T^2(\mathbf{R})$, we can recover precisely the same form of the force, as in the definition (2.20).

2.3.2 The Green's function

The Schrödinger equation (2.15) can be resolved formally in the following way:

$$\langle \mathbf{R}|f(\tau)\rangle = \sum_{\mathbf{R}'}\langle \mathbf{R}|e^{-\tau(\hat{H}-E)}|\mathbf{R}'\rangle\langle \mathbf{R}'|f(0)\rangle, \tag{2.21}$$

where f stands for time-dependent wave function appearing in the equation.
The term $\langle \mathbf{R}|e^{-(\hat{H}-E)\tau}|\mathbf{R}'\rangle$ is the Green's function $G(\mathbf{R},\mathbf{R}',\tau)$ of the Hamiltonian, acting as a propagator of the system. The Schrödinger equation can be rewritten in the integral form in terms of $G(\mathbf{R},\mathbf{R}',\tau)$ as

$$f(\mathbf{R},\tau) = \int G(\mathbf{R},\mathbf{R}',\tau)f(\mathbf{R}',0)\,\mathbf{dR}' \tag{2.22}$$

The last integral equation is an analog of the traditional form of the Schrödinger equation (2.10) but it allows to obtain the solution $f(\mathbf{R}, \tau)$ by virtue of a multidimensional numerical integration, where the Monte Carlo methods are applicable. The exact form of the Green's function is not known, however it can be expanded in power series of τ, therefore with a certain approximation the solution can be reached in a number of integrations, depending on a the time-step size. Hence, the accuracy and the overall computational complexity to obtain the final solution depend on the time step. The solution of Eq. (2.22) after a single time step is then given by

$$f(\mathbf{R}, \tau + \Delta\tau) = \int G(\mathbf{R}, \mathbf{R}', \Delta\tau) f(\mathbf{R}', \tau)\, \mathbf{dR}' \tag{2.23}$$

As it was stated before, after a large enough number M of time steps the solution of Eq. (2.22) decays to the ground state, while all the other components of the solution exponentially disappear.

$$f(\mathbf{R}, M\Delta\tau) \to \psi_T(\mathbf{R})\phi_0(\mathbf{R}), \text{when } M \to \infty \tag{2.24}$$

It is natural to separate three different operators inside the Hamiltonian

$$\hat{H} = (-D\Delta) + D((\nabla_{\mathbf{R}}\mathbf{F}) + \mathbf{F}\nabla_{\mathbf{R}})) + (-E + E^{\text{local}}(\mathbf{R})), \tag{2.25}$$

that is

$$\hat{H} = \hat{H}_1 + \hat{H}_2 + \hat{H}_3\,, \tag{2.26}$$

and write down the Green's function for each of the operators $\hat{H}_i$,

$$G_i(\mathbf{R}, \mathbf{R}', \tau) = \langle \mathbf{R} | e^{-\tau \hat{H}_i} | \mathbf{R}' \rangle\,. \tag{2.27}$$

If components of an operator do not commute, its Green's function (or exponent of the operator) cannot be represented as a product of the Green's functions of the components. This is evidently the case for the components $\hat{H}_i$ of the Hamiltonian. Nonetheless, there is a possibility to use approximations of different orders of τ for $\exp(-\tau\hat{H})$. The first-order approximation for the exponential of $\hat{H}$ corresponds to

$$e^{-\tau\hat{H}} = e^{-\tau\hat{H}_1} e^{-\tau\hat{H}_2} e^{-\tau\hat{H}_3} + \mathcal{O}(\tau^2)\,. \tag{2.28}$$

The integration of this formula, when the term $\mathcal{O}(\tau^2)$ is neglected, yields the following expression for the Green's function

$$G(\mathbf{R}, \mathbf{R}', \tau) = \iint G_1(\mathbf{R}, \mathbf{R}_1, \tau) G_2(\mathbf{R}_1, \mathbf{R}_2, \tau) G_3(\mathbf{R}_2, \mathbf{R}', \tau)\ \mathrm{d}\mathbf{R}_1\, \mathrm{d}\mathbf{R}_2 \tag{2.29}$$

Notice that in accordance with (2.27) the Green's function G is a solution of the Bloch equation

$$\begin{cases} -\dfrac{\partial}{\partial\tau}G(\mathbf{R},\mathbf{R}',\tau) &= \hat{H}_i\, G(\mathbf{R},\mathbf{R}',\tau), \quad i=1,2,3 \\ G(\mathbf{R},\mathbf{R}',0) &= \delta(\mathbf{R}-\mathbf{R}') \end{cases} \tag{2.30}$$

The first (kinetic) component G_1 satisfies the equation

$$\frac{\partial G_1(\mathbf{R},\mathbf{R}',\tau)}{\partial\tau} = D\Delta G_1(\mathbf{R},\mathbf{R}',\tau) \tag{2.31}$$

which coincides formally with the diffusion equation. The diffusion constant of this equation is equal to D, and this is the reasoning of the name that we adopted for the constant. The last equation (2.31) can be easily solved in the momentum representation, as the kinetic energy operator is diagonal in this representation. Rewriting the solution again in the space coordinates, we get a well-known formula

$$G_1(\mathbf{R},\mathbf{R}',\tau) = \frac{1}{(4\pi\tau D)^{\frac{3N}{2}}} e^{-\frac{(\mathbf{R}-\mathbf{R}')^2}{4\tau D}} \tag{2.32}$$

The second term G_2, containing the drift force, satisfies the equation

$$\frac{\partial G_2(\mathbf{R},\mathbf{R}',\tau)}{\partial\tau} = D\nabla_{\mathbf{R}}(G_2(\mathbf{R},\mathbf{R}',\tau)\mathbf{F}) \tag{2.33}$$

is also easily resolved

$$G_2(\mathbf{R},\mathbf{R}',\tau) = \delta(\mathbf{R}-\mathbf{R}_c(\tau)), \tag{2.34}$$

where $\mathbf{R}_c(\tau)$ stands for the solution of the equation

$$\begin{cases} \dfrac{\mathrm{d}\mathbf{R}_c(\tau)}{\mathrm{d}\tau} &= DF(\mathbf{R}_c(\tau)), \\ \mathbf{R}_c(0) &= \mathbf{R}' \end{cases} \tag{2.35}$$

which defines the motion of the system, subjected to the drift force F.

The third equation from the set (2.30) is evident to solve:

$$G_3(\mathbf{R},\mathbf{R}',\tau) = \exp\{(E-E^{\mathrm{local}}(\mathbf{R}))\,\tau\}\ \delta(\mathbf{R}-\mathbf{R}') \tag{2.36}$$

which is generally referred to as the branching component, as it controls multiplication and annihilation of walkers in the algorithm.

2.3.3 The primitive (first-order) algorithm

If the wave function of the system $\psi(\mathbf{R},\tau)$ is real and positive, as it happens for the ground state of a Bose system, it can be treated as a population density distribution:

$$\psi(\mathbf{R},\tau) = C \sum_{i=1}^{N_{\text{walkers}}} \delta(\mathbf{R} - \mathbf{R_i}(\tau)), \tag{2.37}$$

with a constant $C > 0$ and $\mathbf{R_i}(\tau)$ are time-dependent positions of a single particle set, referred to as a *walker*. The formula (2.37) should be taken in a statistical sense, the average of any value A over the left hand side and right hand side distributions are equal to each other in the limit when size of the population N_W tends to infinity $\int A(\mathbf{R}) f(\mathbf{R},\tau)\,\mathrm{d}\mathbf{R} = \lim\limits_{N_w\to\infty} \int A(\mathbf{R}) \sum\limits_{i=1}^{N_w} C\delta(\mathbf{R} - \mathbf{R}_i(\tau))\,\mathrm{d}\mathbf{R}$. The walker resides in the coordinate space of $3N$ dimensions, and the infinitesimal probability $f(\mathbf{R},\tau)\,\mathbf{dR}$ is equal to the probability to encounter a walker in the infinitesimal range $\mathbf{dR}$ near the point $\mathbf{R}$ in the moment τ.

The algorithmic implementation of the time evolution of the system according to its Hamiltonian (2.25) is an evolution of a system of walkers upon the action of the elementary components of the Green's function, that is the transition matrices (2.32), (2.34) and (2.36).

The first function G_1 determines a diffusion of the whole system of walkers according to the equation

$$\mathbf{R}_1(\tau + \Delta\tau) = \mathbf{a} + \mathbf{R}(\tau), \tag{2.38}$$

where $\mathbf{a}$ stands for a displacement, taken randomly from the three-dimensional normal distribution $\exp\{-\mathbf{a}^2/(4\Delta\tau D)\}$.

The second function G_2 gives rise to the drift of the set of walkers towards areas in the configuration space where the trial wave function is large:

$$\mathbf{R}_2(\tau + \Delta\tau) = \mathbf{R}(\tau) + (D\Delta\tau)F(\mathbf{R})\,. \tag{2.39}$$

Notice that the Green's functions of the first two kinds (2.32),(2.34) have a normalization $\int G_{1,2}(\mathbf{R},\mathbf{R}',\tau)\ \mathrm{d}\mathbf{R} = \delta(\mathbf{R}')$, that is on each of the steps the number of walkers stays unchanged.

This is not the case for the third propagator, corresponding to the branching term,

$$f^{(3)}(\mathbf{R},\tau + \Delta\tau) = f(\mathbf{R},\tau)e^{-(E - E^{\text{local}}(\mathbf{R}))\,\Delta\tau}\,, \tag{2.40}$$

since the integral over its Green's function $G_3(\mathbf{R},\mathbf{R}',\tau)$ (2.36) is clearly not equal to unity. The most evident interpretation of the action of the third propagator is that each walker has a certain value attached to it, commonly thought as its "weight". This value is recalculated on each step for every walker. The formula (2.40) suggests that the walkers of less E^{local} are favored and the contrary are disfavored. A clear disadvantage of this scheme is that one would wish to have a better statistical representation for the favorable

areas of the configuration space, however the generation and elimination of walkers is not possible. The alternative and widely applied way to overcome the problem is that the value $c = \exp\{-(E - E^{\text{local}}(\mathbf{R}))\,\Delta\tau\}$ is treated as a number of exact copies of the walker. As one can see, this is a non-integer number that cannot be readily used for it. However, one can apply a randomization by throwing a random number from the uniform distribution [0, 1) and afterwards take $[c] + 1$ duplicates of the walker, if the number is within $[0, \{c\}]$, and $[c]$ is otherwise (the standard bracket notations [.] and {.} stand for the integer and the fractional parts, respectively). The relation $([c] + 1)\{c\} + [c](1 - \{c\}) = c$ ensures the correct mean action of the propagator.

The equation (2.40) also suggests that the branching can be effectively controlled by a dynamic choice of the reference energy E, that can be essential to avoid a collapse of the set of walkers as well as its undesirable expansion, that can make the simulation stall.

Looking closely one can notice that the diffusion and the drift steps represent only the sampling from the trial wave function. It means that being applied without the branching term, they are equivalent to the application of the variational Monte Carlo method (see [HJR94] and Section 2.2). The third branching step ensures that the system of walkers "prefers" the areas of higher ψ_0 (it is often called a *correction* of the trial wave function), and the overall sampling is taken from $\psi_T\psi_0$ rather than ψ_T^2. As it was commented above, if the trial wave function coincides with the ground-state solution (or, more generally, with an eigenfunction of the Hamiltonian), the local energy becomes equal to the eigenvalue, hence the branching factors are the same for all the walkers. The action of the branching step in this case does not affect the final result.

2.3.4 Second-order algorithm

In the previous section, we have described the simplest (first-order in τ) approximation (2.28) of the Green's function. The order of the application of the three propagators is clearly irrelevant, since overall results (for instance, the energy of the ground state) will depend linearly on the time step τ. To obtain the final result for a quantity of interest one should take a short enough τ to move the time-related error below the statistical noise or perform a series of simulations with distinct time steps, and then find a linearly extrapolated value. In practice the second approach is much more practical, since the time bias of the result can be very pronounced. However, a clear drawback is that the correctness of the linear dependence might be valid for undesirably small times. This is where the higher-order algorithms become useful.

The second-order in τ expansion of the exponent in the Green's function can be given in the form

$$e^{-\tau\hat{H}} = e^{-\tau\hat{H}_3/2}e^{-\tau\hat{H}_2/2}e^{-\tau\hat{H}_1}e^{-\tau\hat{H}_2/2}e^{-\tau\hat{H}_3/2} + \mathcal{O}(\tau^3) \tag{2.41}$$

which is not the only possible way of representation, but probably the most efficient for actual application[Chi90]. The final result for the equation of state of the system, yielded

by the formula (2.41), does not have linear in τ elements, thus for small enough time steps the dependence is quadratic. In this case one can again perform an extrapolation to $\tau \to 0$ via a series of measurements, or alternatively, find a time step short enough to guarantee the smallness of the time step-related error in accordance with a required accuracy level of the simulation. This accuracy is generally described by the statistical variance of the result. The choice between the two approaches must be taken regarding the interplay between the additional calculation costs, related to the extrapolation, and the slower evolution of the system in case of a shorter time step.

Let us explain the second-order algorithm, that relies on the expansion (2.41). Each propagation in time corresponds to a constant shift $\Delta\tau/2$ with respect to the current time. The state of a displaced walker is changed on every step from $\mathbf{R}_{i-1}$ to $\mathbf{R}_i$. The effect of the branching propagator is a corresponding multiplication or suppression of a walker in question. Since the walker is moved in a loop, the choice of the first step is arbitrary, and the list of the operations can by reordered.
The calculation procedure:
1) The first propagator, random Gaussian move (2.32):
$\mathbf{R} = \mathbf{R}_{i-1} + a$, a is taken from $\exp(-\mathbf{x^2}/\mathbf{\Delta}\tau)$
2) The second propagator, drift with $\mathbf{F}(\mathbf{R})$ (2.34):
$\mathbf{R}' = \mathbf{R} + \mathbf{F}(\mathbf{R})\,\Delta\tau/2$
$\mathbf{R}'' = \mathbf{R} + (\mathbf{F}(\mathbf{R}) + \mathbf{F}(\mathbf{R}')\,\Delta\tau/4$
$\mathbf{R}''' = \mathbf{R} + \mathbf{F}(\mathbf{R}'')\,\Delta\tau$
3) The branching propagator (2.36):
$\mathbf{R}'''$ unchanged.

2.4 Constructing the trial wave functions

2.4.1 Motivation

In this Section, the development of trial wave functions for bosonic systems is discussed from the technical point of view. The purpose of the following discussion is to present the theoretical basis of the construction of Nosanow-Jastrow trial wave function of a general kind in liquid and solid phases, its relation to the actual implementation, the technical issues that one faces, and their solutions.

2.4.2 Nosanow-Jastrow trial wave function

The natural way of constructing a bosonic trial wave function is to take it in the form of a product of one- and two-body correlation terms:

$$\Psi(\mathbf{r}_1, ..., \mathbf{r}_N) = \prod_{i=1}^{N_p} f_1(\mathbf{r}_i) \prod_{j<k}^{N_p} f_2(|\mathbf{r}_j - \mathbf{r}_k|)\,. \tag{2.42}$$

This form of the trial wave function is generally referred to as the Jastrow (or Bijl-Jastrow) trial wave function, first proposed by Bijl [Bij40] and then by Jastrow [Jas55]. The pairwise interaction of particles in the system is taken into account by the two-body Jastrow term $f_2(r)$. The pair correlation is clearly lost for large enough interparticle distances, that is this term must approach 1 asymptotically. The use of the periodic boundary conditions puts additional restrictions to $f_2(r)$. Namely, in order to avoid additional contributions to the kinetic energy from distances $r > d_{\text{plane}}$ (d_{plane} stands for a distance to the plane, closest to the center of the simulation cell), the Jastrow term should be constant in that region. For a rectangular simulation box it is one half of a minimum box dimension $d_{\text{plane}} = \min(L_x, L_y, L_z)/2$. For a calculation cell of the shape of truncated octahedron (see Appendix B) this distance is equal to

$$d_{\text{plane}} = \frac{3/4}{\sqrt{\frac{1}{1/L_x^2} + \frac{1}{1/L_y^2} + \frac{1}{1/L_z^2}}}\,. \tag{2.43}$$

The value of the Jastrow-Bijl term at distances larger than the cut-off one $r \geq L/2$ is not necessarily $f_2(L/2) = 1$, but, in principle, can be any arbitrary constant $f_2(L/2) = \text{const}$, $r \geq L/2$. Still, the unitary value might be convenient to use in the evaluation of the product of Bijl-Jastrow terms $\prod\limits_{i<j} f_2(\mathbf{r}_i - \mathbf{r}_j)$, which in code is usually implemented as evaluation of $\exp \sum\limits_{i<j} \ln f_2(\mathbf{r}_i - \mathbf{r}_j)$. With the choice $f_2(L/2) = 1$, $r \geq L/2$ the contributions of pairs with $|\mathbf{r}_i - \mathbf{r}_j| \geq L/2$ to the sum is zero.

The one-body Jastrow term $f_1(\mathbf{r})$ is introduced to take into account an external potential, present in the system. It can also define symmetry properties of the system, for example, the localization of the particles in crystalline nodes. The form of this one-body term is typically obtained from a solution of the Schrödinger equation for a single particle in the chosen potential.

For a quantum Monte Carlo simulation of a solid phase one might need to induce a corresponding crystalline symmetry to the trial wave function. This is done by "pegging" the particles to the nodes of a crystal through a multiplication of the Jastrow term by a particular factor, depending on the coordinates of the particles. A straightforward way to realize such a condition is to consider a one-body term

$$f_1(\mathbf{r}_i) = g(|\mathbf{r}_i - \xi_{\text{i}}|) \tag{2.44}$$

with the configuration $\{\xi_{\text{i}}\}$ standing for a set of crystal nodes' positions and $g(\mathbf{r})$ is a function, which localizes each particle $\mathbf{r}_i$ to the site ξ_{i}. This factor is generally referred to as Nosanow term [1], and a corresponding trial wave with a Jastrow two-body term

$$\Psi_{\text{NJ}}(\mathbf{r}_1, ..., \mathbf{r}_{N_p}) = \prod_{i<j} f_2(\mathbf{r}_{ij}) \prod_{k=1} g(|\mathbf{r}_i - \xi_{\text{i}}|) \tag{2.45}$$

[1] A not so brief explanation of the efficient construction of crystalline guiding wave functions can be found, for instance, in the recent work of Cazorla and collaborators [CACB09].

is called a Nosanow-Jastrow (NJ) trial wave function. The localization factor $g(\mathbf{r})$ is usually chosen as a Gaussian with a localization parameter $\gamma = 1/(2\sigma^2)$:

$$g(|\mathbf{r}_i - \xi_i|) = e^{-\gamma|\mathbf{r}_i - \xi_i|^2} . \tag{2.46}$$

since the Gaussian is a quantum mechanical solution for a 3D harmonic oscillator and usually is a good guess for describing a wave function close to a potential minimum. The parameter γ is determined through a variational optimization in VMC calculations.

Quantum Mechanics requires that the bosonic wave function is symmetric with respect to an exchange of equivalent particles, and that the Nosanow term does not satisfy this. Evidently, the analytical form of the symmetric trial wave function in this case becomes quite cumbersome for implementation and extremely expensive in terms of permanent calculation time, as it should in general contain a sum over all the permutations of the lattice nodes in the system. Nonetheless, the results of the quantum Monte Carlo simulations when the Nosanow-Jastrow term is used are for practical purposes indistinguishable from that of the symmetrized trial wave function [CB08b, CACB09], as far as the energetic properties of a crystal are concerned, and the exchange energy is usually negligible. In this Thesis we will use this form of the NJ trial wave function throughout all the quantum Monte Carlo calculations of solid phases. However, the physical quantities, related to Bose statistics, may not be treated with the NJ trial wave function, since any particle exchange is suppressed.

The quantum Monte Carlo technique requires knowledge of not only the trial wave function itself, but also of its first two derivatives. In the case of the DMC method the second derivative enters in the calculation of energy, which is needed for the branching term. Hence the second derivative of the trial wave function is required not also for evaluating averages of the observables, but even for the time evolution of the system.

The actual implementation can be substantially improved, if one takes into account that the trial wave function appears in the implementation of the method in three distinct combinations, which can be presented as functions and can be tabulated.

A. The logarithm of the Jastrow term (needed in Metropolis algorithm in VMC simulations and also for estimations of the non-local quantities, for instance the one-body density matrix)

$$w(r) = \ln f(r) \tag{2.47}$$

B. The logarithmic derivative of the trial wave function, which is required in the calculation of the drift force (2.20))

$$\mathbf{F}(r) = \frac{\mathrm{d} \ln f(r)}{\mathrm{d}r} = \frac{f'(r)}{f(r)} \tag{2.48}$$

C. The second derivative of the Jastrow term appears only in a linear combination with the drift force in the calculation of the kinetic energy. The following representation takes

place:

$$E^{\text{local}}(r) = -\frac{f''(r)}{f(r)} + \left(\frac{f'(r)}{f(r)}\right)^2 + \frac{mV_{\text{int}}(r)}{\hbar^2} - \frac{d-1}{r}\frac{f'(r)}{f(r)}, \tag{2.49}$$

with d stands for for a dimensionality of the problem.

2.4.3 Explicit expressions for wave functions

2.4.3.1 Trial wave function for hard sphere potential

The problem of scattering on a simple hard sphere potential, Yukawa potential and common potential between Rydberg atoms was discussed in Sec. 1.3.2.2. The hard sphere and the considered model potential of Rydberg atoms make the wave function vanish when two particles meet each other, which means that three-body collisions are greatly suppressed. The same is true for a Yukawa potential at low density due to its similarity to the Coulomb potential. If three-body correlations are neglected, at small interparticle distances the two-body Jastrow term $f_2(r)$ can be conveniently approximated by the solution $f(r)$ of the two-body scattering problem, that is by the wave function of a system of two particles. At large distances, the pair wave correlation function asymptotically tends to a constant, as the particles lose correlation.

Taking these facts into account we introduce the trial function in the following way [GBC99] (here we use a dimensionless notation in which the distances r are mesured in units of the hard sphere radius a_{3D} and the energy E is measured in units of $\hbar^2/(ma_{3D}^2)$)

$$f_2(r) = \begin{cases} \dfrac{A\sin(\sqrt{2E}(r-1))}{r}, & |r| \le R_m \\ 1 - B\exp\left\{-\dfrac{r}{\alpha}\right\}, & |r| > R_m \end{cases} \tag{2.50}$$

The Jastrow term has to be smooth at the matching point R_m, that is

A. the function $f_2(r)$ itself must be continuous:

$$\frac{A\sin(\sqrt{2E}(R_m-1))}{R_m} = 1 - B\exp\left\{-\frac{R_m}{\alpha}\right\} \tag{2.51}$$

B. derivative $f_2'(r)$ must be continuous

$$\frac{A\sqrt{2E}\cos(\sqrt{2E}(R_m-1))}{R_m} - \frac{A\sin(\sqrt{E}(R_m-1))}{R_m^2} = \frac{B}{\alpha}\exp\left\{-\frac{R_m}{\alpha}\right\} \tag{2.52}$$

C. the local energy $f_2(r)^{-1}(-\hbar^2\Delta_1/2m - \hbar^2\Delta_1/2m + V_{\text{int}}(\mathbf{r}_i - \mathbf{r}_j))f_2(r)$ must be continuous

$$2E = \frac{\left(\dfrac{1}{\alpha^2} - \dfrac{2}{R_m\alpha}\right)B\exp\left(-\dfrac{R_m}{\alpha}\right)}{1 - B\exp\left(-\dfrac{R_m}{\alpha}\right)} \tag{2.53}$$

The solution of this system is

$$\begin{cases} A = \dfrac{R}{\sin(u(1-1/R))} \dfrac{\xi^2 - 2\xi}{\xi^2 - 2\xi + u^2}, \\ B = \dfrac{u^2 \exp(\xi)}{\xi^2 - 2\xi + u^2}, \end{cases} \tag{2.54}$$

where we used the notation $u = \sqrt{2E}R$ and $\xi = R/\alpha$. The value of ξ is obtained from the equation

$$1 - \frac{1}{R} = \frac{1}{u} \arctan \frac{u(\xi - 2)}{u^2 + \xi - 2} \tag{2.55}$$

There are three conditions for the determination of five unknown parameters, consequently two parameters are left free. The usual way to define them is to minimize the variational energy in variational Monte Carlo which yields an optimized trial wave function.

2.4.3.2 Trial wave function for Yukawa potential

The construction of a trial wave function for a Yukawa system can be done in different ways. The first one, widely employed in our calculations, is a use of the solution of a two-body scattering problem, that yields a satisfactory short-range approximation for the trial wave function, which is valid for a dilute system. At large distances the trial wave function is intended to arrive smoothly to unity at the half size of the simulation box (see Sec. (1.3)). If the Jastrow term is chosen in a form $f(\mathbf{r}) = e^{-u(\mathbf{r})}$ [RC67], this can be achieved by a symmetrization of the trial wave function with respect to the inversion $r \to (L - r)$ as

$$u(r) := u_1(r) + u_1(L - r) - u_1(L/2) \tag{2.56}$$

that brings the logarithm of the Jastrow term and its first derivative in the point $L/2$ to zero.

According to Eq. (1.51), the solution of the two-body scattering problems reads as

$$u_1(r) = \ln \left(\frac{I_1(\text{const}\sqrt{r})}{\sqrt{r}} \right) = \ln \sqrt{A} + \frac{A}{2} r - \frac{A^2}{24} r^2 + \mathcal{O}(r^3) \tag{2.57}$$

where A is a constant, subject to optimization. This solution formally coincides with the scattering solution provided $A = V_0$ (V_0 stands for the interaction strength constant of the original two-body scattering problem (1.49)). An optimal value of A should therefore be close to V_0.

The most productive way to generate trial wave functions in the case of the Yukawa potential appeared to be the hypernetted chain method [CP79], based on an iterative solution of a set of Euler–Lagrange equations

$$\frac{\delta}{\delta u_n(\mathbf{r}_1, ..., \mathbf{r}_n)} \frac{\langle \psi | H | \psi \rangle}{\langle \psi | \psi \rangle} = 0, \; i = 1, .., N. \tag{2.58}$$

	E/N
VMC Jastrow TWF	19.862(3)
VMC HNC TWF	19.634(3)
DMC result	19.595(3)

Table 2.1: The energy per particle without size correction for different trial waves compared to the exact DMC result.

The more detailed explanation of the method is given in Section 2.4.3.4.

A comparison of two-body correlation factors from Eq. (2.57) and the HNC solution is given in Fig. (2.1). The particular conditions of the data correspond to VMC and DMC calculations with 64 particles in the truncated octahedron cell, $\Lambda = 0.46$, $\rho = 0.024$ (for details on the used model and involved parameters see Section 4).

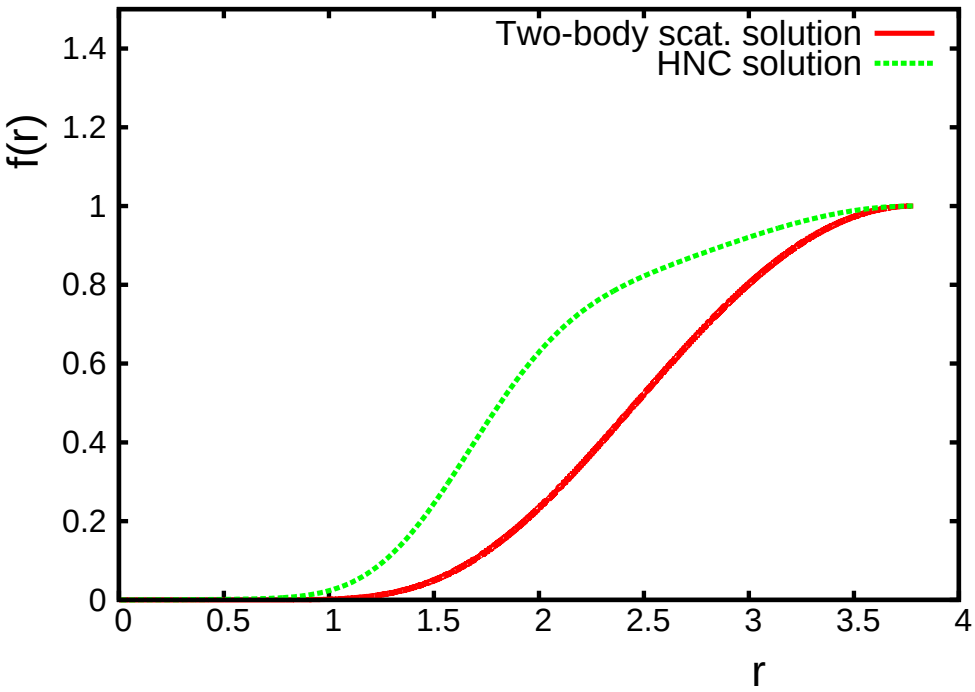

Figure 2.1: Two-body correlation factor for a system, interacting via a repulsive Yukawa potential in the liquid phase, in the Jastrow parameter-optimized model (red solid line) and the HNC one (green dashed line). The particular conditions of the data correspond to a DMC calculation with 64 particles in the truncated octahedron cell, $\Lambda = 0.46$, $\rho = 0.024$.

HNC $f(r)$ leads to better estimates of the energy; a simple comparison is shown in Table (2.1) (the conditions of the simulation are the same as in the figures above, no finite size correction added).

2.4.3.3 Trial wave function for repulsive van der Waals

In our simulations of the bulk system with the pairwise van der Waals interaction $1/|\mathbf{r}|^6$ at zero temperature we use the short-range approximation of the two-body scattering problem, as it was solved in Sec. (1.3). The technical procedure to obtain the functional forms of the solution follows the derivation, used in the case of the Yukawa potential. The final result for the Jastrow factor reads as a logarithm of the first term in the expansion (1.55):

$$u_1(r) = \frac{\sqrt{C_6}}{2r^2} - \ln \frac{\sqrt{2\pi}}{C_6^{1/4}} - \frac{\ln r}{2} \tag{2.59}$$

$$u(r) = u_1(r) + u_1(L-r) - 2u_1(L/2)\,. \tag{2.60}$$

In this equation the factor C_6 comes from the interaction strength and is constant. Nonetheless, it can be treated as a parameter and variated in order to optimize the trial wave function by minimizing the VMC energy. Typical forms of the guiding wave functions and pair distributions are presented in Fig. 2.2.

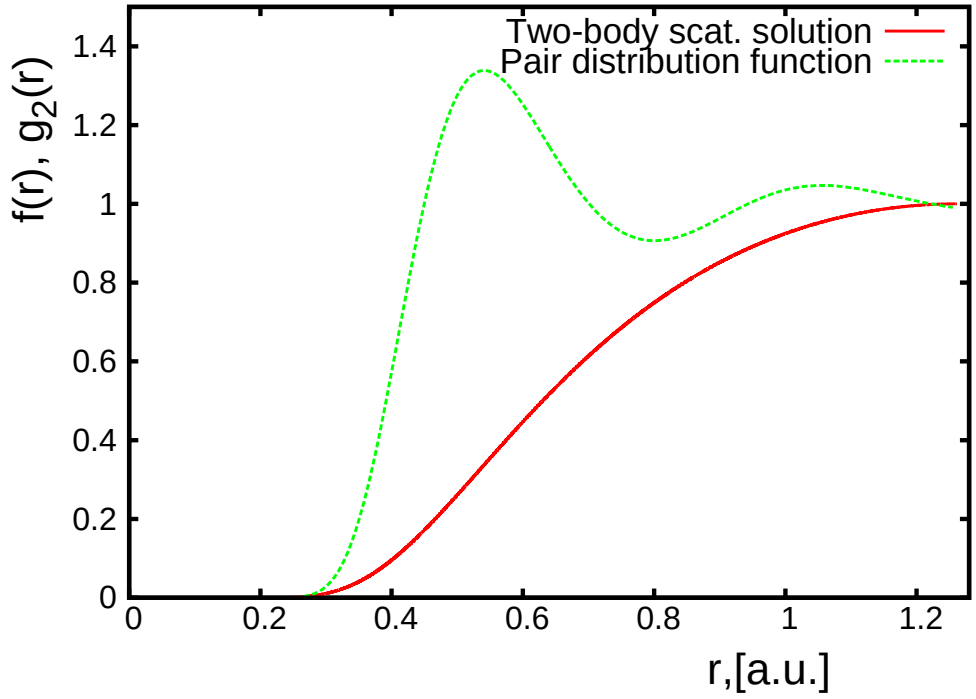

Figure 2.2: A typical two-body correlation factor and pair distribution function for a system, interacting via a repulsive van der Waals $1/r^6$ potential in the liquid phase. The particular conditions of the data correspond to a DMC calculation with 108 particles in the cubic cell, $\rho = 6.7$.

A similar result is provided by the *cusp condition* demand, when the leading term of the guiding wave function is sought in a suitable exponential form $f(r) = \exp(-a/r^b)$,

with parameters a, b. After a substitution of this functional form into Eq. (1.54)) one finds that the equation can be satisfied only when $b = 2$, while a is still arbitrary. It is easily seen, that this procedure yields the leading term of the two-body scattering solution.

2.4.3.4 Hypernetted chain method

The hypernetted chain method is a technique to solve many-body problems in homogeneous and inhomogeneous media [Kro98],[vGd59]. In this scheme, the static structure factor $S(k)$ that minimizes the variational energy in the subspace of Jastrow wave functions has the form

$$S(k) = \frac{t(k)}{\sqrt{t^2(k) + 2t(k)V_{ph}(k)}} \ , \tag{2.61}$$

with $t(k) = \hbar^2 k^2/2m$ and $V_{ph}(k)$ the so-called particle-hole interaction. Its Fourier transform $FT[V_{ph}(k)] = \tilde{V}_{ph}(r)$ satisfies the following equation in coordinate space

$$\tilde{V}_{ph}(r) = g(r)V(r) + \frac{\hbar^2}{m} |\nabla\sqrt{g(r)}|^2 + (g(r)-1)\omega_I(r) \ , \tag{2.62}$$

where $V(r)$ and $g(r)$ are the bare two-body potential and the pair distribution function (the Fourier transform of $S(k)$), respectively. Finally, in momentum space the induced interaction $\omega_I(k)$ becomes

$$\omega_I(k) = -\frac{1}{2}\, t(k) \frac{[2S(k)+1][Sk)-1]^2}{S^2(k)} \ . \tag{2.63}$$

In this way, Eqs. (2.61), (2.62) and (2.63) form a set of nonlinear coupled equations that have to be solved iteratively. The Fourier transform of the resulting $S(k)$ provides $g(r)$ and, in this scheme, the optimal two-body Jastrow factor results from the corresponding HNC/0 equation

$$f_2(r) = \sqrt{g(r)} e^{-N(r)/2} \ , \tag{2.64}$$

where $N(r)$ is the sum of nodal diagrams, related to $S(k)$ in momentum space by the expression $N(k) = (S(k) - 1)^2/S(k)$.

2.5 Estimators for physical quantities

2.5.1 Local energy

The general form of a Hamiltonian of a system of N interacting bosons in an external field is (2.14):

$$\hat{H} = -\frac{\hbar^2}{2m} \sum_{i=1}^{N} \Delta_{\mathbf{r}_i} + \sum_{i=1}^{N} V_{\text{ext}}(\mathbf{r}) + \sum_{j<k}^{N} V_{\text{int}}(|\mathbf{r}_j - \mathbf{r}_k|), \tag{2.65}$$

where m is mass of a particle, $V_{\rm ext}(\mathbf{r})$ is the external field, $V_{\rm int}(|\mathbf{r}|)$ is the two-body particle-particle interaction potential. Given the many-body wave function $\Psi(\mathbf{r}_1,...,\mathbf{r}_N)$ the local energy is defined according to (2.18):

$$E^{\rm loc}(\mathbf{r}_1,...,\mathbf{r}_N) = \frac{\hat{H}\Psi(\mathbf{r}_1,...,\mathbf{r}_N)}{\Psi(\mathbf{r}_1,...,\mathbf{r}_N)} \tag{2.66}$$

The external field and particle-particle interaction are diagonal in this representation and are calculated trivially as a summation over particles and pairs of the second and third terms of (2.65). Calculation of the kinetic energy, first term of (2.65) is more involved, as the Laplacian operator is not diagonal.

2.5.1.1 Local kinetic energy

In this Section, we will find the expression of the local kinetic energy

$$T^{\rm loc}(\mathbf{r}_1,...,\mathbf{r}_N) = -\frac{\hbar^2}{2m}\frac{\Delta\Psi(\mathbf{r}_1,...,\mathbf{r}_N)}{\Psi(\mathbf{r}_1,...,\mathbf{r}_N)} \tag{2.67}$$

Let us calculate the second derivative in two steps, as the first derivative is important for the calculation of the drift force. We consider the Jastrow form (2.42) of the trial wave function and will express the final results in terms of one- and two-body terms f_1 and f_2. The gradient of the many-body trial wave function is given by

$$\nabla_i\Psi(\mathbf{r}_1,...,\mathbf{r}_N) = \Psi(\mathbf{r}_1,...,\mathbf{r}_N)\left(\frac{f_1'(\mathbf{r}_i)}{f_1(\mathbf{r}_i)}\frac{\mathbf{r}_i}{r_i} + \sum_{k\neq i}^{N}\frac{f_2'(|\mathbf{r}_i-\mathbf{r}_k|)}{f_2(|\mathbf{r}_i-\mathbf{r}_k|)}\frac{\mathbf{r}_i-\mathbf{r}_k}{|\mathbf{r}_i-\mathbf{r}_k|}\right) \tag{2.68}$$

The full expression for the Laplacian is

$$\begin{aligned}\Delta_{\mathbf{r}_i}\Psi(\mathbf{r}_1,...,\mathbf{r}_N) \quad = \quad & \Psi(\mathbf{r}_1,...,\mathbf{r}_N)\left(\frac{f_1'(\mathbf{r}_i)}{f_1(\mathbf{r}_i)}\frac{\mathbf{r}_i}{r_i} + \sum_{k\neq i}^{N}\frac{f_2'(|\mathbf{r}_i-\mathbf{r}_k|)}{f_2(|\mathbf{r}_i-\mathbf{r}_k|)}\frac{\mathbf{r}_i-\mathbf{r}_k}{|\mathbf{r}_i-\mathbf{r}_k|}\right)^2 + \\ & + \Psi(\mathbf{r}_1,...,\mathbf{r}_N)\left(\frac{f_1''(\mathbf{r}_i)}{f_1(\mathbf{r}_i)} - \left(\frac{f_1'(\mathbf{r}_i)}{f_1(\mathbf{r}_i)}\right)^2 + \sum_{k\neq i}^{N}\left[\frac{f_2''(|\mathbf{r}_i-\mathbf{r}_k|)}{f_2(|\mathbf{r}_i-\mathbf{r}_k|)} - \left(\frac{f_2'(|\mathbf{r}_i-\mathbf{r}_k|)}{f_2(|\mathbf{r}_i-\mathbf{r}_k|)}\right)^2\right]\right).\end{aligned} \tag{2.69}$$

The kinetic energy can be written in a compact form

$$T^{\rm loc}(\mathbf{r}_1,...,\mathbf{r}_N) = -\frac{\hbar^2}{2m}\left\{\sum_{i=1}^{N}\mathcal{E}_1^{\rm loc}(\mathbf{r}_i) + 2\sum_{j<k}^{N}\mathcal{E}_2^{\rm loc}(|\mathbf{r}_j-\mathbf{r}_k|) - \frac{1}{4}\sum_{i=1}^{N}|\mathbf{F}_i(\mathbf{r}_1,...,\mathbf{r}_N)|^2\right\}, \tag{2.70}$$

where we introduced notation for the one- and two-body contribution to the local energy (see, also, (2.49))

$$\mathcal{E}_1^{\rm loc}(\mathbf{r}) = -\frac{f_1''(\mathbf{r})}{f_1(\mathbf{r})} + \left(\frac{f_1'(\mathbf{r})}{f_1(\mathbf{r})}\right)^2 \tag{2.71}$$

$$\mathcal{E}_2^{\rm loc}(r) = -\frac{f_2''(r)}{f_2(r)} + \left(\frac{f_2'(r)}{f_2(r)}\right)^2 \tag{2.72}$$

and introduced the drift force (see (2.48))

$$\mathbf{F}_i(\mathbf{r}_1,...,\mathbf{r}_N) = 2\left(\frac{f_1'(\mathbf{r}_i)}{f_1(\mathbf{r}_i)}\frac{\mathbf{r}_i}{r_i} + \sum_{k\neq i}^{N}\frac{f_2'(|\mathbf{r}_i-\mathbf{r}_k|)}{f_2(|\mathbf{r}_i-\mathbf{r}_k|)}\frac{\mathbf{r}_i-\mathbf{r}_k}{|\mathbf{r}_i-\mathbf{r}_k|}\right) \tag{2.73}$$

2.5.1.2 Exponentiation

It is convenient (see Eq.2.47) to do the exponentiation of the one- and two- body terms $u_1(\mathbf{r}) = \ln f_1(\mathbf{r})$, $u_2(r) = \ln f_2(r)$. The point is that numerically a better precision is achieved by working with numbers of the same order. The formula for the kinetic energy becomes more simple

$$T^{\rm loc}(\mathbf{r}_1,...,\mathbf{r}_N) = -\frac{\hbar^2}{2m}\left\{\sum_{i=1}^{N}u_1''(\mathbf{r}_i) + 2\sum_{j<k}^{N}u_2''(|\mathbf{r}_j-\mathbf{r}_k|) + \frac{1}{4}\sum_{i=1}^{N}|\mathbf{F}_i(\mathbf{r}_1,...,\mathbf{r}_N)|^2\right\} \tag{2.74}$$

with

$$\mathbf{F}_i(\mathbf{r}_1,...,\mathbf{r}_N) = 2u_1'(\mathbf{r}_i)\frac{\mathbf{r}_i}{r_i} + \sum_{k\neq i}^{N}u_2'(|\mathbf{r}_i-\mathbf{r}_k|)\frac{\mathbf{r}_i-\mathbf{r}_k}{|\mathbf{r}_i-\mathbf{r}_k|} \tag{2.75}$$

2.5.2 Static structure factor

The static structure factor $S(\boldsymbol{k})$ is the correlation function of the momentum distribution between elements $-\boldsymbol{k}$ and $\boldsymbol{k}$ (1.28):

$$NS(\boldsymbol{k}) = \langle\rho_{-\boldsymbol{k}}\rho_{\boldsymbol{k}}\rangle - |\langle\rho_{\boldsymbol{k}}\rangle|^2, \tag{2.76}$$

Using the properties of the Fourier component $\rho_{-\boldsymbol{k}} = (\rho_{\boldsymbol{k}})^*$ it can be rewritten in a different way

$$NS(\boldsymbol{k}) = \langle|\rho_{\boldsymbol{k}}|^2\rangle - |\langle\rho_{\boldsymbol{k}}\rangle|^2\,. \tag{2.77}$$

The density distribution in coordinate space is the sum of δ-functions located at the positions of the particles:

$$n(\mathbf{r}) = \frac{1}{V}\sum_{i=1}^{N}\delta(\mathbf{r}-\mathbf{r}_i)\,. \tag{2.78}$$

By means of its momentum space representation (i.e. its Fourier transform)

$$\rho_{\boldsymbol{k}} = \sum_{i=1}^{N} e^{-i\boldsymbol{k}\mathbf{r}_i} = \sum_{i=1}^{N} \cos \boldsymbol{k}\mathbf{r}_i - i \sum_{i=1}^{N} \sin \boldsymbol{k}\mathbf{r}_i \tag{2.79}$$

we obtain a simple expression for the static structure factor

$$NS(\boldsymbol{k}) = \left\langle \left(\sum_{i=1}^{N} \cos \boldsymbol{k}\mathbf{r}_i \right)^2 + \left(\sum_{i=1}^{N} \sin \boldsymbol{k}\mathbf{r}_i \right)^2 \right\rangle - \left| \left\langle \sum_{i=1}^{N} \cos \boldsymbol{k}\mathbf{r}_i \right\rangle \right|^2 - \left| \left\langle \sum_{i=1}^{N} \sin \boldsymbol{k}\mathbf{r}_i \right\rangle \right|^2 . \tag{2.80}$$

In a homogeneous system the two last terms in (2.81) are vanishing, that is

$$NS(\boldsymbol{k}) = \left\langle \left(\sum_{i=1}^{N} \cos \boldsymbol{k}\mathbf{r}_i \right)^2 + \left(\sum_{i=1}^{N} \sin \boldsymbol{k}\mathbf{r}_i \right)^2 \right\rangle . \tag{2.81}$$

If periodic boundary conditions are used, the values of momenta are quantized and depend on the size of the box

$$k_{n_{x,y,z}} = \frac{2\pi}{L} n_{x,y,z} . \tag{2.82}$$

2.5.3 Calculation of one-body density matrix

The one-body density matrix (OBDM) g_1 of a homogeneous system described by the many-body wave function $\psi(\mathbf{r}_1, ..., \mathbf{r}_N)$ according to (1.18) is equal to

$$g_1(|\mathbf{r}\,' - \mathbf{r}\,''|) = N \frac{\int ... \int \psi^*(\mathbf{r}\,', \mathbf{r}_2, ..., \mathbf{r}_N) \psi(\mathbf{r}\,'', \mathbf{r}_2, ..., \mathbf{r}_N)\, d\mathbf{r}_2 ... d\mathbf{r}_N}{\int ... \int |\psi(\mathbf{r}_1, ..., \mathbf{r}_N)|^2\, d\mathbf{r}_1 ... d\mathbf{r}_N} . \tag{2.83}$$

Since in DMC one does not sample directly the ground-state probability distribution ϕ_0^2, but instead the mixed probability $\psi_T \phi_0$ (2.16) one obtains the *mixed* one-body density matrix as the output

$$g_1^{mixed}(\mathbf{r}) = N \frac{\int ... \int \psi_T^*(\mathbf{r}_1 + \mathbf{r}, \mathbf{r}_2, ..., \mathbf{r}_N) \phi_0(\mathbf{r}_1, \mathbf{r}_2, ..., \mathbf{r}_N)\, d\mathbf{r}_2 ... d\mathbf{r}_N}{\int ... \int \psi_T^*(\mathbf{r}_1, ..., \mathbf{r}_N) \phi_0(\mathbf{r}_1, ..., \mathbf{r}_N)\, d\mathbf{r}_1 ... d\mathbf{r}_N}, \tag{2.84}$$

This formula can be rewritten in a way convenient for the Monte Carlo sampling:

$$g_1^{mixed}(r) = n \frac{\int ... \int [\psi_T^*(\mathbf{r}_1 + \mathbf{r}, \mathbf{r}_2, ..., \mathbf{r}_N)(\psi_T^*(\mathbf{r}_1, \mathbf{r}_2, ..., \mathbf{r}_N))^{-1}] f(\mathbf{r}_1, ..., \mathbf{r}_N) d\mathbf{r}_1 ... d\mathbf{r}_N}{\int ... \int f(\mathbf{r}_1, ..., \mathbf{r}_N) d\mathbf{r}_1 ... d\mathbf{r}_N}, \tag{2.85}$$

where we have used the asymptotic formula (2.24) and have taken into account that in a homogeneous system g_q depends only on the module of the relative distance. If the trial wave function is chosen as a product of pair functions (2.42) then using the notation (2.47)

$u(|\mathbf{r}_i - \mathbf{r}_j|) = \ln f_2(|\mathbf{r}_i - \mathbf{r}_j|))$ and $f_1 \equiv 1$ one has $\psi_T(\mathbf{r}_1, ..., \mathbf{r}_N) = \prod_{i<j} \exp\{u(|\mathbf{r}_i - \mathbf{r}_j|)\}$. Then the ratio of the trial wave function appearing in (2.85) becomes

$$\frac{\psi_T(\mathbf{r}_1 + \mathbf{r}, ..., \mathbf{r}_N)}{\psi_T(\mathbf{r}_1, ..., \mathbf{r}_N)} = \exp\left\{\sum_{j>1} u(|\mathbf{r}_1 + \mathbf{r} - \mathbf{r}_j|) - u(|\mathbf{r}_1 - \mathbf{r}_j|)\right\} \tag{2.86}$$

In order to gain better statistics it is convenient to average over all possible pairs of particles

$$\begin{aligned} g_1^{mixed}(r) &= \frac{1}{N}\sum_{i=1}^{N} \frac{\psi_T(\mathbf{r}_1, ..., \mathbf{r}_i + \mathbf{r}, ..., \mathbf{r}_N)}{\psi_T(\mathbf{r}_1, ..., \mathbf{r}_N)} \\ &= \frac{1}{N}\sum_{i=1}^{N} \exp\left\{\sum_{j\neq i}^{N} u(|\mathbf{r}_i + \mathbf{r} - \mathbf{r}_j|) - u(|\mathbf{r}_i - \mathbf{r}_j|)\right\} \end{aligned} \tag{2.87}$$

The asymptotic limit of the OBDM gives the Bose-Einstein condensate density

$$\lim_{r\to\infty} g_1(r) = \frac{N_0}{V} \tag{2.88}$$

and the condensate fraction is obtained by calculating the asymptotic ratio

$$\lim_{r\to\infty} \frac{g_1(r)}{n} = \frac{N_0}{N} \tag{2.89}$$

2.5.4 Two-body density matrix

The two-body density matrix (TBDM) $\langle\hat{\Psi}^\dagger(\mathbf{r}_1')\hat{\Psi}^\dagger(\mathbf{r}_2')\hat{\Psi}(\mathbf{r}_2)\hat{\Psi}(\mathbf{r}_1)\rangle$, depends on 4 vector arguments corresponding to destroying two particles at positions $\mathbf{r}_1$ and $\mathbf{r}_2$ and inserting them at positions $\mathbf{r}_1'$ and $\mathbf{r}_2'$. The diagonal element $\mathbf{r}_1 = \mathbf{r}_1'$ and $\mathbf{r}_2 = \mathbf{r}_2'$ (see Eq. (1.8)) is called the pair distribution function. Generally, it depends on two vector arguments $\mathbf{r}_1$ and $\mathbf{r}_2$. In a translationally invariant system (e.g. in a homogeneous gas) it is a function of $(\mathbf{r}_1 - \mathbf{r}_2)$, that is a function of the distance between a pair of particles and two angles. We consider spherically averaged pair distribution function

$$g_2(|\mathbf{r}_2 - \mathbf{r}_1|) = \frac{N(N-1)}{n^2} \frac{\int |\psi(\mathbf{R})|^2 \, \mathrm{d}\mathbf{r}_3 ... \, \mathrm{d}\mathbf{r}_N}{\int |\psi(\mathbf{R})|^2 \, \mathrm{d}\mathbf{R}} \, . \tag{2.90}$$

Let us explain now how this formula is implemented in Monte Carlo calculation. We make summation over all pairs of particles:

$$g_2(r) = \frac{N(N-1)}{n^2 L^3} \frac{\int \delta(\mathbf{r}_1 - \mathbf{r}_2 - \mathbf{r})|\psi(\mathbf{R})|^2 \, \mathrm{d}\mathbf{R}}{\int |\psi(\mathbf{R})|^2 \, \mathrm{d}\mathbf{R}} = \frac{2}{nN} \frac{\int \sum_{i<j} \delta(r_{ij} - r)|\psi(\mathbf{R})|^2 \, \mathrm{d}\mathbf{R}}{\int |\psi(\mathbf{R})|^2 \, \mathrm{d}\mathbf{R}} \tag{2.91}$$

If we do a discretization of the coordinate space with spacing h and introduce function $\vartheta_h(z)$ which is one if $z < h$ and zero otherwise (the distribution is obviously symmetric) one obtains the following expressions:

- In one-dimensional system:

$$g_2^{1D}(z) = \left\langle \frac{2}{2hnN} \sum_{i<j} \vartheta_h(|z_{ij} - z|)| \right\rangle \tag{2.92}$$

  In an uncorrelated system $\vartheta_h(|z|) = 2h/L$ is constant and $g_2(z) = 1 - 1/N$. The form of the pair distribution function depends on a dimensionality of the problem.

- In a three-dimensional system the expression is

$$g_2^{3D}(r) = \left\langle \frac{2}{4\pi z^2 hnN} \sum_{i<j} \vartheta_h(|r_{ij} - r|)| \right\rangle . \tag{2.93}$$

  Notice that the distance r enters explicitly in the expression of the pair distribution function, leading to larger numerical variance at small distances.

2.5.5 Pure estimators and extrapolation technique

In a VMC calculation one obtains a *variational* esimator for a given quantity (let it be denoted by an operator $\hat{A}$), which corresponds to an average over the trial wave function ψ_T:

$$\langle \hat{A} \rangle_{\text{var}} = \frac{\langle \psi_T | \hat{A} | \psi_T \rangle}{\langle \psi_T | \psi_T \rangle} \tag{2.94}$$

Instead, the DMC method asymptotically provides a more precise *mixed* estimator given by

$$\langle \hat{A} \rangle_{\text{mix}} = \frac{\langle \phi_0 | \hat{A} | \psi_T \rangle}{\langle \phi_0 | \psi_T \rangle} \tag{2.95}$$

Nonetheless, this type of average can differ from the inbiased ("pure") ground state average, which corresponds to the true quantum-mechanical equilibrium value at zero temperature

$$\langle \hat{A} \rangle_{\text{pure}} = \frac{\langle \phi_0 | \hat{A} | \phi_0 \rangle}{\langle \phi_0 | \phi_0 \rangle} \tag{2.96}$$

The DMC method gives an exact result for the energy, as the mixed average of the local energy $E_{\text{loc}} = \psi_T^{-1} \hat{H} \psi_T$ coincides with the pure estimator. This can be easily seen by noticing that when $\langle \phi_0$ acts on $\hat{H}$, it gives exactly the ground state energy.

From now on, we will demonstrate that averages of local diagonal operators can be calculated in a "pure" way. This means that the pair distribution function, potential energy and static structure factor can be estimated exactly. Local quantities are diagonal

in coordinate space $\langle \mathbf{R}|\hat{A}|\mathbf{R}'\rangle = A(\mathbf{R})\langle \mathbf{R}|\mathbf{R}'\rangle$. The "pure" average can be related to the mixed one in the following way

$$\langle \hat{A}\rangle_{\text{pure}} = \frac{\langle \phi_0|A(\mathbf{R})\frac{\phi_0(\mathbf{R})}{\psi_T(\mathbf{R})}|\psi_T\rangle}{\langle \phi_0|\frac{\phi_0(\mathbf{R})}{\psi_T(\mathbf{R})}|\psi_T\rangle} = \frac{\langle A(\mathbf{R})P(\mathbf{R})\rangle_{\text{mix}}}{\langle P(\mathbf{R})\rangle_{\text{mix}}}, \tag{2.97}$$

where $P(\mathbf{R})$ is defined as

$$P(\mathbf{R}) = \frac{\phi_0(\mathbf{R})}{\psi_T(\mathbf{R})}\langle \phi_0|\psi_T\rangle\,. \tag{2.98}$$

The asymptotic number of offsprings of a walker can give $\phi_0(\mathbf{R})/\psi_T(\mathbf{R})$ [LKC74]. By "tagging" walkers one can identify, at any time, what is the parent walker. This forward walking method [BRL91, RBHL86, RR90, Run92] permits to sample pure averages.

A more simple algorithm was devised by J. Boronat and J. Casulleras [CB95a], in which the explicit history should not be recorded and one operates with the actual values of an observable. This method is used in our calculations.

Eq. (2.98) gives the number of descendants of a walker $\mathbf{R}$ for large times $\tau \to \infty$. Practically it is enough to wait a sufficiently large, but a finite time T. One makes measurements of a local quantity for all of the walkers, but calculates the average after the time T, so that each walker was replicated according to the weight $P(\mathbf{R})$.

An important example of a non-local quantity, for which no "pure" is known, is one-body density matrix (see Eq. (2.85)); this quantity deserves a special attention. We will explain an extrapolation technique, which can be applied for finding averages of non-local operators. It is also worth noticing that extrapolation can be used in estimating diagonal quantities, for example, pair correlation function.

Adopting the notation $\delta\psi$ for the difference between the trial wave function and ground-state wave function

$$\phi_0 = \psi_T + \delta\psi\,, \tag{2.99}$$

the ground-state average can be written as

$$\langle \hat{A}\rangle_{\text{pure}} = \langle \phi_0|\hat{A}|\phi_0\rangle = \langle \psi_T|\hat{A}|\psi_T\rangle + 2\langle \phi_0|\hat{A}|\delta\psi\rangle + \langle \delta\psi|\hat{A}|\delta\psi\rangle \tag{2.100}$$

If $\delta\psi$ is small the second order term $\langle \delta\psi|\hat{A}|\delta\psi\rangle$ can be neglected. After substitution $\langle \phi_0|\hat{A}|\delta\psi\rangle = \langle \psi_T|\hat{A}|\phi_0\rangle - \langle \psi_T|\hat{A}|\psi_T\rangle$ the extrapolation formula turns into

$$\langle \hat{A}\rangle_{pure} \approx 2\langle \hat{A}\rangle_{\text{mix}} - \langle \hat{A}\rangle_{\text{var}}\,. \tag{2.101}$$

It is possible to write another extrapolation formula of the same order of accuracy:

$$\langle \hat{A}\rangle_{\text{pure}} \approx \frac{\langle \hat{A}\rangle^2_{\text{mix}}}{\langle \hat{A}\rangle_{\text{var}}}\,. \tag{2.102}$$

An applicability condition for the extrapolation method is that the expressions (2.101) and (2.102) yield the same final result. Nevertheless, in certain situations the use of the second formula can be advantageous, as it does not change the sign of the function, which is not always true in the case of the first formula, when the function is very close to 0. This can be useful in an estimation of essentially positive non-local quantities, for instance, the one-body density matrix.

Chapter 3

Ewald method for polytropic potentials

3.1 Introduction

The behavior of many-body systems is often governed by the long-range Coulomb potential between charged particles. Numerical simulations of such systems are usually performed by considering a finite number of particles in a cell with periodic boundary conditions. The correct estimation of the potential energy in such systems requires of a summation over all images created by the periodic boundary conditions. For long-range interaction potentials such direct summation either converges slowly or it is conditionally convergent, making its evaluation computationally cumbersome. Instead, the performance of the calculation can be greatly improved by using Ewald summation methods [Ewa21]. In these methods, the slowly convergent tail of the sum in the potential energy is represented by a rapidly convergent sum in momentum space. The method is named after Paul Peter Ewald who in his pioneering work dated almost a century ago calculated the electrostatic energy in ionic crystals (a detailed derivation for the Ewald sums for the Coulomb potential can be found in the work of de Leeuw *et al.* [dLPS80]). An alternative approach to deal with long-range systems is proposed by Smith [Smi94]. In his method, the Hamiltonian and equations of motion are derived using constraints on the velocities of particles. Instead, in the following we will stick to a standard model for the Hamiltonian and will consider ways to improve the convergence in the potential energy.

For a good performance in simulations of large N-particle systems, a number of modified summation methods has been developed. Historically, the first efforts to enhance the Ewald method consisted in looking for appropriate truncation schemes, but all of them were strongly dependent on the system properties, in particular on the system size. Tabulations of precalculated terms in both real space and momentum space sums [SD76], as well as polynomial approximations of the involved functions [dLB47, BST66, Han73], were also proposed to look for a balance between calculation time and truncation errors. Nevertheless, these approximate methods suffer from error accumulation in simulations of large systems, and do not allow for reducing the overall $\mathcal{O}(N^2)$ complexity of the original Ewald summation. The work of Perram *et al.* [PPdL88] was the first to give a way to optimize the splitting of the interparticle potential between the long-range and short-range parts to yield a total complexity of $\mathcal{O}(N^{3/2})$. A special modification of the Ewald method called

Wolf summation [WKPE99, EGA10], based on a damping of the Fourier-transformed part of the sum, was posteriorly developed in order to render the original Ewald summation more efficient for non-periodic systems and large model sizes. The Ewald technique was also applied to develop the method of evaluation of electrostatic potential near the surfaces of ionic crystals [Par75, Par76].

Another way for improving the Ewald method is to perform fast Fourier transform (FFT) of a reciprocal space sum on a mesh. The oldest algorithm of this kind is the so-called Particle-Particle Particle-Mesh (P^3M) method, invented and improved to the complexity $\mathcal{O}(N)$ in calculation of forces by Hockney and coauthors in the 70's [HE88, HGE73]. The P^3M technique is based on a distribution of the charge density on a grid using a certain smooth assignment function and then the discrete Poisson equation is solved using FFT. This algorithm appeared to be less complex to yield $\mathcal{O}(N \ln N)$ with an appropriate choice of the free parameters. The P^3M algorithm was recently improved by Ballenegger *et al.* [BCLH08] for calculation of energies, bringing, as claimed, the maximal precision in the energy by an optimization of the "influence" function (a substitution of the potential in the Fourier-transformed Poisson's equation). For a comprehensive introduction to Ewald- and mesh-based techniques we recommend to refer to the cited work of Ballenegger and coauthors where special attention is paid to the estimation of both sum truncation-imposed and grid-imposed errors. The extension of this method, called Particle Mesh Ewald [DYP93] (PME), makes use of the analytical form of the sum in the reciprocal space and evaluates potentials via FFT instead of interpolating them as P^3M does. Although PME is slightly more complex than the P^3M algorithm, it is still $\mathcal{O}(N \ln N)$ and allows to reduce significantly the memory expenses. Later Particle Mesh Ewald method was reformulated by Essmann *et al.* [EPB+95], making use of cardinal B-splines to interpolate structure factors. This approach, called Smooth Particle-Mesh Ewald (SPME) substantially improved the accuracy of PME with a comparable computational cost, as it still scales as $\mathcal{O}(N \ln N)$. SPME is also claimed to be applicable to potentials of the polytropic form $1/|\boldsymbol{r}|^k$. In general, the conventional FFT-based approaches suffer from the severe fallback of requiring equidistant particle positions. The invention of the variant of Fourier transform for nonequispaced nodes (NFFT) opened a path to overcome this shortcoming, while keeping the introduced errors below the specified target levels. The nonequispaced fast Fourier transform is currently considered as a promising means to improve the Ewald summation performance, with open code implementations available [KKP]. The early variants of the NFFT algorithms are reviewed in the work of A. F. Ware [War98]; a general approach to the fast summation methods based on NFFT can be found in the article of G. Steidl [Ste98].

The most recent family of algorithms based on the Ewald approach are the tree-based algorithms, with the fast multipole method (FMM) being the most known and widely used among them. The algorithm, developed primarily by L. Greengard and V. Rokhlin [GR87], is based on the idea of keeping the direct summation of potentials or forces for the nearby atoms and approximating the interactions of the distant atoms by their multipole ex-

pansions. FMM offers the asymptotically fastest performance among the Ewald-related algorithms, being linear in N in most cases and not worse than $\mathcal{O}(N \ln N)$ with explicitly controlled accuracy. The FMM technique is naturally applicable to inhomogeneous and non-periodic systems, being also easy to parallelise since it is an entirely real-space summation. Since then the algorithm was significantly improved in efficiency, mostly by introducing new diagonal forms of translation operators [GR97]. However, FMM has an intrinsic shortcoming, when applied to molecular dynamics calculations, as the energy conservation it brings is poor; the method *per se* is also rather cumbersome in implementation. Another group of methods, based on the multigrid methods of solving elliptic (in this particular case – Poisson's) equations [BLdL98], was developed a decade ago [SD01]. These methods allow to preserve the scaling $\mathcal{O}(N)$ and parallelization advantages of tree-based methods, as well as the applicability in simulations without PBC, being on the other hand satisfactorily energy-conserving and additionally accelerated on all length scales. An efficient realization of the multigrid method and its analysis may be found in the work of Sagui *et al.* [SPD04]. An advanced mesh Ewald technique, claimed to reduce significantly the computational costs of charge spreading in multigrid-based methods, was recently proposed by Y. Shan and coworkers [SKE+05].

A detailed comparison of the optimized $\mathcal{O}(N^{3/2})$ pure Ewald technique, FFT-based summations, and multipole-based methods was made by H. G. Petersen [Pet95] for systems with approximately uniform charge distributions, taking into account a possible parallel implementation. According to Petersen, the method of choice with a number of particles below 10^4 is the conventional Ewald summation, PME is preferable in the range $N \sim 10^4 - 10^5$, and the fast multipole method should overperform them with $N > 10^5$. A more recent and ample review of FMM, P^{3}M and pure Ewald methods by Pollock and Glosli [PG96], based partially on their own calculations, implies that P^{3}M is faster than the Ewald summation already for 500 particles, although it is stressed that the other factors as the ease of the coding, the system geometry, as well as the code optimization can change the choice. We would also suggest a thorough survey of different Ewald summation techniques given in the work of Toukmaji and Board [TJ96].

An approach, alternative to using cubic periodic boundary conditions in a calculation of long-range interactions, called Isotropic Periodic Sum (IPS), was recently proposed by Wu and Brooks [WB05]. The main goal of their approach is to deal with long-range interactions, avoiding artificial correlations and anisotropy bias induced by a PBC-based summation in a cubic box. In this technique, only the interactions of a particle A with the others within a certain radius $\boldsymbol{r}_c$ are taken into account (as in a plain cut-off scheme), and this spherical simulation zone is repeated in an infinite number of shifts by vectors $\boldsymbol{r}_{\mathrm{sh}}$, such that $|\boldsymbol{r}_{\mathrm{sh}}| = 2N|\boldsymbol{r}_c|$. Therefore, the particle A interacts not only with B (within the sphere radius), but also with all the images of B, occupying homogeneously the shells of radii $2N|\boldsymbol{r}_c|$, centered in B. The subsequent integration and summation over the shells allows to obtain explicit expressions of forces and energies for a number of interactions of most physical interest, like electrostatic, Lennard–Jones and exponential potentials. The

method is known to yield a performance close to the one shown by the Ewald summation, but without imposing unwanted symmetry effects.

Since its proposal, the Ewald method has been applied to a large number of physical problems, although mostly to systems with the Coulomb $1/|\boldsymbol{r}|$ interaction potential. In a recent work by R. E. Johnson and S. Ranganathan [JR07], a generalized approach to Ewald summation is stated to obtain potential energy and forces for systems with a power-law, Yukawa potential and electronic bilayer systems. The Ewald method for two-dimensional systems with electrostatic interactions was developed by Parry [Par75], but his technique appeared to be computationally inefficient. Spohr *et al.*. [Spo97] studied a slab geometry by treating the simulation cell as a fully three-dimensional one with the conventional Ewald summation. Later on, a significant advance was made by Yeh and Berkowitz [YB99], as the authors managed to obtain the explicit correction term for the rigorous three-dimensional Ewald summation, that brings the results for a slab system in a satisfactory agreement with the 2D summation. The 2D Ewald technique was also applied by Wen Yang *et al.* [YJ06] to calculate the energy of Coulomb particles in a slab system with a uniformly charged surface. One of the first two-dimensional variants of the Ewald summation was presented in [GZW97], applied to the quasi-2D Stockmayer model with the potential $1/|\boldsymbol{r}|^3$. Recent applications to dipolar bosons in a 2D geometry have been made by C. Mora *et al.* [MPW07] and Xin Lu *et al.* [MPLW08]. On the other hand, the explicit forms of the Ewald sums for Yukawa interactions have been also reported: in 3D geometry, with partial periodic boundary conditions [SC00, Maz07a], and in 2D geometry [Maz07b]. The general approach to the Ewald summation in quasi-two-dimensional systems with power-law potentials and results for several values of power factor are given in [Maz10]. The Ewald method can also be useful even applied to fast decaying power-law potentials. For instance, the Ewald formalism was developed in [KI89] for the dispersion interaction $1/|\boldsymbol{r}|^6$ and later for the Lennard-Jones potential by W.-Z. Ou-Yang *et al.* [OYLS+05]. Also, Shirts *et al.* in their recent work [SMCP07] argue the need for taking into account the effects of cutoffs in molecular dispersion interactions due to a Lennard-Jones potential, especially in non-isotropic and inhomogeneous media. The authors developed two formalisms for the estimation of these cutoff errors in binding free energy of macromolecular systems, which can in principle be extended to the other observables. However, it is claimed that the adequate implementation of the Ewald summation for this kind of systems may render their corrections unnecessary by mostly eliminating the cutoff-dependent behavior.

In this Chapter, we report explicit expressions of the Ewald sums for the general case of particles interacting via a $1/|\boldsymbol{r}|^k$ polytropic potential and in 3D, 2D, and 1D geometries [OAB12]. The closed derivation of these sums is given, with special attention being paid to conditionally convergent potentials. One of the difficulties of the derivation is that different terms have to be considered in the cases of short-range, long-range or "marginal" potentials. In the case of a short-range interaction, the original slowly convergent sum is represented as a linear combination of two rapidly convergent ones. For a long-range interaction, the condition of charge neutrality in the simulation cell is shown to be necessary

to make the energy absolutely convergent within the considered scheme. The introduction of a uniform neutralizing charged background (*jellium*), as a particular case of a charge-neutral system, is also discussed. The explicit forms of the Ewald sums are reported for a jellium system and for an arbitrary polytropic potential. We explicitly calculate the expressions for physically relevant interactions as Coulomb, dipole-dipole, and Lennard-Jones potentials. Finally, we have extended the Ewald sums to the case of a noncubic simulation cell, that could be useful in simulations of hexagonal closed packed (hcp) and two-dimensional triangular solids. In addition, the general derivation path given in this work may be used to obtain the forms of Ewald sums for other interaction potentials.

The computational efficiency is another important issue of the practical implementation of the method. In fact, one needs to choose correctly a free parameter, appearing in the integral representation of the sums, and to decide which number of terms should be kept in spatial and momentum sums in order to reach the required accuracy. The choice of these three parameters affects the difference between the calculated result and the exact one as well as the calculation complexity. Therefore, a certain optimization of the parameters is always required. In this Chapter, this optimization process is formalized and it is shown that following the described procedure the overall computation time is significantly reduced. The accuracy of the result is shown to be kept under control, with the only cost of a preliminary benchmark calculation.

The rest of the chapter is organized as follows. In Section 3.2, we formulate the problem, develop the general Ewald approach and report explicit expressions for the Ewald sums for a polytropic potential in a three-dimensional cubic simulation cell. Sections 3.3 and 3.4 contain derivations of the Ewald sums in two-dimensional and one-dimensional geometries, respectively. In Section 3.5, the case of a simulation cell with different side lengths is considered for three- and two-dimensional systems. The final general expressions and their particularization to the most physically relevant cases are presented in Section 3.7. The practical algorithm for the parameter optimization and an actual application of the Ewald method is discussed in Section 3.8. Summary and conclusions are drawn in Section 3.9.

3.2 Ewald method in 3D geometry

3.2.1 Basic assumptions and initial sums

We consider a system of N particles inside a cubic simulation cell of size L with periodic boundary conditions. Thus, each particle with coordinates $\boldsymbol{r}$ in the initial cell has an infinite number of images $\boldsymbol{r} + \boldsymbol{n}L$ in the adjacent cells. The total potential energy is estimated by

$$U = \frac{1}{2} {\sum_{\boldsymbol{n}\in\mathbb{Z}^3}}' \left[\sum_{i=1}^{N} \sum_{j=1}^{N} \phi(\boldsymbol{r}_{ij} + \boldsymbol{n}L) \right] \tag{3.1}$$

where $\phi(\boldsymbol{r})$ is the interparticle potential, $\boldsymbol{r}_{ij} \equiv \boldsymbol{r}_i - \boldsymbol{r}_j$, and the prime in the first sum means that the summation over an integer vector $\boldsymbol{n}$ must be done omitting the term $\boldsymbol{n} = \boldsymbol{0}$ when $i = j$.

3.2.2 Analytic derivation

In many physical situations, the interaction potential between two particles i and j has the power-law form $q_i q_j/|\boldsymbol{r}|^k$ with positive k and q_i, q_j being the generalized charges of the particles. This sort of interaction is generally referred to as *polytropic* potential.

First, let us consider the case of short-range potentials, $k \leq 3$. As we will see later, the potentials corresponding to $k > 3$ give a similar result. For $k \leq 3$, the right-hand part of Eq. (3.1) diverges and it can be made convergent only if the restriction of charge neutrality is required, i.e., when $\sum_{i=1}^{N} q_i = 0$. It has also been shown [FF96] that for a pure electrostatic interaction the total energy (3.1) can be conditionally convergent even in a neutral simulation cell because of a higher multipole contribution. The energy and forces are therefore dependent on the order of summation, which can also be implicitly set by a choice of a convergence factor. The ambiguity usually appears in a form of a constant or a position-dependent term, vanishing in the limit $L \to \infty$. Hence, the preference in one or another factor should be dictated either by physical properties of a particular system or by arguments regarding rates of convergence to the thermodynamic limit. For a general discussion on the convergence issues appearing in periodic boundary conditions, see Ref. [MP95]. The main idea of the Ewald summation technique in the approach proposed by de Leeuw, Perram, and Smith [dLPS80] is to multiply each component of the sum by the dimensionless factor e^{-sn^2}, with $s > 0$ being a dimensionless regularizing parameter, making the sum absolutely convergent. Then, the limit $s \to 0$ is taken, so that the singularity in the initial sum (3.1) can be explicitly separated into a term depending only on s, that finally can be cancelled due to the charge neutrality condition. We take a similar multiplier $c(\boldsymbol{n}, \boldsymbol{r}, s) = e^{-s|\boldsymbol{n}+\boldsymbol{r}|^2}$ yielding the same rate of convergence (since $0 \leq r \leq 1$ in units of L). As the sum, multiplied by c, is invariant to an arbitrary substitution $\boldsymbol{r} \to \boldsymbol{n}+\boldsymbol{r}$, the chosen convergence factor allows to preserve the periodicity of the potential in order to avoid any possible artefacts in the final results.

For the sake of clearness of the derivation, it is convenient to use reduced length units, that is to use the size of the box L as unity of length and substitute r_{ij} by $r_{ij}L$. From now on, and for simplicity, we use the notation $\boldsymbol{r}$ for $\boldsymbol{r}_{ij}$ and, in case of possible ambiguity, we will stick to the standard notation $\boldsymbol{r}_{ij}$. Also, we rewrite the potential energy by splitting the total sum (3.1) into two terms: I_{01} (the sum of the interactions between a particle with all the *other* particles in the box), and I_{00} (the sum of the interaction of a particle with *its own* images, comprised of the components $i = j$ in Eq. (3.1)). Explicitly,

$$U = \frac{1}{L^k}(I_{01} + I_{00}) \ , \tag{3.2}$$

with

$$I_{01} = \sum_{\boldsymbol{n}\in\mathbb{Z}^3}\left[\sum_{1\le i<j\le N}\frac{q_iq_je^{-s|\boldsymbol{r}_{ij}+\boldsymbol{n}|^2}}{|\boldsymbol{r}_{ij}+\boldsymbol{n}|^k}\right] \tag{3.3}$$

$$I_{00} = \frac{1}{2}\sum_{\boldsymbol{n}\in\mathbb{Z}^3\setminus\boldsymbol{0}}\frac{e^{-sn^2}}{n^k}\sum_{i=1}^{N}q_i^2\ , \tag{3.4}$$

where the shorthand notation $n=|\boldsymbol{n}|$ is used.

First, let us focus on the I_{01} term, which we rewrite as

$$I_{01} = \sum_{1\le i<j\le N} q_iq_j\psi(\boldsymbol{r},s)\ , \tag{3.5}$$

where we have defined the "screened" interaction potential $\psi(\boldsymbol{r},s)=\sum_{\boldsymbol{n}}e^{-s|\boldsymbol{r}+\boldsymbol{n}|^2}/|\boldsymbol{r}+\boldsymbol{n}|^k$, extended from a single cell to the whole coordinate space. Since the total potential energy consists of a sum of pair interaction components, we may consider a single pair without any loss of generality.

Let us apply the equation

$$x^{-2s} = \frac{1}{\Gamma(s)}\int_0^\infty t^{s-1}e^{-tx^2}\,\mathrm{d}t\ , \tag{3.6}$$

representing the definition of the gamma-function, to the polytropic potential $|\boldsymbol{r}+\boldsymbol{n}|^{-k}$. Then the function ψ may be represented in an integral form,

$$\psi(\boldsymbol{r},s) = \frac{1}{\Gamma(k/2)}\int_0^\infty t^{\frac{k}{2}-1}\sum_{\boldsymbol{n}}e^{-t|\boldsymbol{r}+\boldsymbol{n}|^2}e^{-s|\boldsymbol{r}+\boldsymbol{n}|^2}\,\mathrm{d}t\ . \tag{3.7}$$

We expect that the integral (3.7) contains a singularity that will be located in the vicinity of zero. Therefore, we split this integral into two domains $[0,\alpha^2]$ and $[\alpha^2,\infty)$, the corresponding integrals being denoted as ψ_{fin} and ψ_{inf}, where α is some arbitrary positive constant,

$$\psi(\boldsymbol{r},s) = \psi_{\mathrm{fin}}(\boldsymbol{r},s)+\psi_{\mathrm{inf}}(\boldsymbol{r},s)\ . \tag{3.8}$$

In the following, we analyze the two terms of the previous sum (3.8).

1. The explicit analytical form of the term $\psi_{\mathrm{inf}}(\boldsymbol{r},s)$ can be found

$$\psi_{\mathrm{inf}}(\boldsymbol{r},s) = \frac{1}{\Gamma(\frac{k}{2})}\sum_{\boldsymbol{n}}\int_{\alpha^2}^\infty t^{\frac{k}{2}-1}e^{-t|\boldsymbol{r}+\boldsymbol{n}|^2-s|\boldsymbol{r}+\boldsymbol{n}|^2}\,\mathrm{d}t = \sum_{\boldsymbol{n}}\frac{e^{-s|\boldsymbol{r}+\boldsymbol{n}|^2}}{|\boldsymbol{r}+\boldsymbol{n}|^k}\frac{\Gamma(\frac{k}{2},\alpha^2|\boldsymbol{r}+\boldsymbol{n}|^2)}{\Gamma(\frac{k}{2})}\ , \tag{3.9}$$

where $\Gamma(a,z)$ is the incomplete gamma function. From the large distance asymptotic expansion of this function, one obtains that the above lattice sum is absolutely and uniformly convergent if $s\ge 0$ and $\alpha>0$. Therefore, one may simply take the limit of vanishing screening $s\to 0$,

$$\psi_{\mathrm{inf}}(\boldsymbol{r},s)\xrightarrow{s\to 0}\frac{1}{\Gamma(\frac{k}{2})}\sum_{\boldsymbol{n}}\frac{\Gamma(\frac{k}{2},\alpha^2|\boldsymbol{r}+\boldsymbol{n}|^2)}{|\boldsymbol{r}+\boldsymbol{n}|^k}\ . \tag{3.10}$$

2. The calculation of $\psi_{\text{fin}}(\boldsymbol{r}, s)$ is done by making a separate analysis of the $\boldsymbol{n} = \boldsymbol{0}$ case,

$$\psi_{\text{fin}}(\boldsymbol{r}, s) = \psi_{\text{fin}}^{\boldsymbol{m}\neq\boldsymbol{0}}(\boldsymbol{r}, s) + \psi_{\text{fin}}^{\boldsymbol{m}=\boldsymbol{0}}(\boldsymbol{r}, s) \ . \tag{3.11}$$

Explicitly,

$$\psi_{\text{fin}}^{\boldsymbol{m}\neq\boldsymbol{0}}(\boldsymbol{r}, s) = \frac{\pi^{\frac{3}{2}}}{\Gamma(\frac{k}{2})} \sum_{\boldsymbol{m}\neq\boldsymbol{0}} \int_0^{\alpha^2} \frac{t^{\frac{k}{2}-1}}{(t+s)^{\frac{3}{2}}} \exp\left[\frac{-\pi^2 m^2}{t+s} + 2\pi \mathrm{i} \boldsymbol{m}\boldsymbol{r}\right] \mathrm{d}t \tag{3.12}$$

$$\psi_{\text{fin}}^{\boldsymbol{m}=\boldsymbol{0}}(\boldsymbol{r}, s) = \frac{\pi^{\frac{3}{2}}}{\Gamma(\frac{k}{2})} \int_0^{\alpha^2} \frac{t^{\frac{k}{2}-1}}{(t+s)^{\frac{3}{2}}} \mathrm{d}t \ , \tag{3.13}$$

where we have used the Jacobi transformation [Jac21, WW]

$$\sum_{\boldsymbol{n}} e^{-s|\boldsymbol{n}+\boldsymbol{r}|^2} = \left(\frac{\pi}{s}\right)^{3/2} \sum_{\boldsymbol{m}} \exp[-\pi^2 m^2/s + 2\pi \mathrm{i} \boldsymbol{m}\boldsymbol{r}] \ \text{ for } \ \boldsymbol{n}, \boldsymbol{m} \in \mathbb{Z}^3 \ , \tag{3.14}$$

applied to

$$\exp[-s|\boldsymbol{n}+\boldsymbol{r}|^2 - t|\boldsymbol{n}+\boldsymbol{r}|^2] = \exp[-(s+t)|\boldsymbol{n}+\boldsymbol{r}|^2]. \tag{3.15}$$

We evaluate the integral $\psi_{\text{fin}}^{\boldsymbol{m}\neq\boldsymbol{0}}(\boldsymbol{r}, s)$ by the following analysis. Consider separately the following factor of the integrated expression from (3.12)

$$M = \frac{\exp\left[-\frac{\pi^2 n^2}{t+s}\right]}{(t+s)^{\frac{3}{2}}}. \tag{3.16}$$

It is clearly continuous and bounded on $(0, +\infty)$ as a function of $(t+s)$, also notice that $t^{k/2-1}$ is absolutely integrable on $(0, \alpha^2)$ for $k > 0$. In accordance with the standard convergence test for improper integrals, the integral $\psi_{\text{fin}}^{\boldsymbol{m}\neq\boldsymbol{0}}(\boldsymbol{r}, s)$ converges absolutely and uniformly with s being considered as a parameter. Then, the limit $s \to 0$ may be carried out and the integral becomes

$$\psi_{\text{fin}}^{\boldsymbol{m}\neq\boldsymbol{0}}(\boldsymbol{r}, s) = \frac{\pi^{\frac{3}{2}}}{\Gamma(\frac{k}{2})} \sum_{\boldsymbol{m}\neq\boldsymbol{0}} e^{2\pi \mathrm{i} \boldsymbol{m}\boldsymbol{r}} \int_0^{\alpha^2} t^{\frac{k-5}{2}} \exp\left[-\frac{\pi^2 m^2}{t}\right] \mathrm{d}t \tag{3.17}$$

$$= \sum_{\boldsymbol{m}\neq\boldsymbol{0}} \frac{\pi^{\frac{3}{2}} \cos(2\pi \boldsymbol{m}\boldsymbol{r})}{\Gamma(\frac{k}{2})} \alpha^{k-3} E_{\frac{k-1}{2}}\left(\frac{\pi^2 m^2}{\alpha^2}\right) \ . \tag{3.18}$$

The function $E_n(z)$ is the exponential integral function, and we have cancelled the imaginary part of the sum (3.17) by grouping the pairs with $\boldsymbol{n}$ and $-\boldsymbol{n}$.

Now, we analyze the second term of $\psi_{\text{fin}}(\boldsymbol{r}, s)$,

$$\psi_{\text{fin}}^{\boldsymbol{m}=\boldsymbol{0}}(\boldsymbol{r}, s) = \frac{\pi^{\frac{3}{2}}}{\Gamma(\frac{k}{2})} \int_0^{\alpha^2} \frac{t^{\frac{k}{2}-1}}{(t+s)^{\frac{3}{2}}} \mathrm{d}t \ . \tag{3.19}$$

In terms of a new variable $v = s/(t+s)$,

$$\psi_{\text{fin}}^{\boldsymbol{m}=\boldsymbol{0}}(\boldsymbol{r},s) = \frac{\pi^{\frac{3}{2}}}{\Gamma(\frac{k}{2})}\int_{s/(\alpha^2+s)}^{1}\frac{(1-v)^{\frac{k}{2}-1}}{v^{\frac{k-1}{2}}}s^{(k-3)/2}\,\mathrm{d}v\ . \tag{3.20}$$

The integration of $\psi_{\text{fin}}^{\boldsymbol{m}=\boldsymbol{0}}(\boldsymbol{r},s)$ for a $1/|r|^k$ interaction has to be carefully analyzed as a function of k: $1 \leq k < 3$, long-range potential; $k = 3$, marginal case; and $k > 3$, short-range potential.

(a) Suppose $1 \leq k < 3$. The resulting integral,

$$\psi_{\text{fin}}^{\boldsymbol{m}=\boldsymbol{0}}(\boldsymbol{r},s) = \psi_{\text{fin}}^{\boldsymbol{m}=\boldsymbol{0}}(\boldsymbol{r},s) = \frac{\pi^{\frac{3}{2}}}{\Gamma(\frac{k}{2})}\int_{s/(\alpha^2+s)}^{1}\frac{(1-v)^{\frac{k}{2}-1}}{v^{\frac{k-1}{2}}}s^{(k-3)/2}\,\mathrm{d}v \tag{3.21}$$

may be given explicitly in terms of incomplete beta- and incomplete gamma-functions. Expanding the resulting function for small s,

$$\psi_{\text{fin}}^{\boldsymbol{m}=\boldsymbol{0}}(\boldsymbol{r},s) = s^{\frac{k-3}{2}}2\pi\Gamma\left[\frac{3-k}{2}\right] + \frac{2\pi^{\frac{3}{2}}\alpha^{k-3}}{(k-3)\Gamma\left[\frac{k}{2}\right]} + \mathcal{O}(s) \tag{3.22}$$

It is easily seen, that the only divergent term in the expansion (3.22) is the first one, which we define as

$$S(s) = s^{\frac{k-3}{2}}2\pi\Gamma\left[\frac{3-k}{2}\right]\ . \tag{3.23}$$

We remind that the choice of a convergence factor (that explicitly affects the summation order) may in principle lead to additional contributions in the total energy if the convergence of the sum is conditional (like for a charge-neutral cell of Coulomb particles with non-zero total dipole moment). In the original derivation of de Leeuw *et al.* [dLPS80], the factor $\exp(-sn^2)$ results in an additional dipole-like component in $\psi_{\text{fin}}^{\boldsymbol{m}=\boldsymbol{0}}$, which breaks the periodicity of the potential and therefore complicates its use in simulations with periodic boundary conditions. Moreover, this procedure [dLPS80] yields a nonvanishing dipole term exclusively for $k = 1$ in 3D geometry, with the rest of the sums remaining unchanged. From our point of view, this discontinuity points out to an nonphysical character of the dipole term appearing in the case of the Coulomb potential. Nevertheless, in a number of studies [FF96, MP95] it is considered as a first order correction when the convergence to the thermodynamic limit is analyzed. The mere fact that the results for the two different convergence multipliers coincide when $k > 1$ is a consequence of the absolute convergence of the higher multipole contributions in this case.

(b) Suppose $k = 3$. In this marginal case, the expression (3.21) may be integrated directly to yield the following logarithmic dependence

$$\psi_{\text{fin}}^{\boldsymbol{m}=\boldsymbol{0}}(\boldsymbol{r}, s) = \frac{\pi^{\frac{3}{2}}}{\Gamma(\frac{3}{2})}\left(\frac{-2\alpha s - 2\alpha^3}{(\alpha^2+s)^{\frac{3}{2}}} + \ln(s + 2\alpha^2 + 2\alpha\sqrt{s+\alpha^2}) - \ln s\right) \tag{3.24}$$

that close to $s = 0$ expands as

$$\psi_{\text{fin}}^{\boldsymbol{m}=\boldsymbol{0}}(\boldsymbol{r}, s) = -2\pi \ln\, s - 4\pi + 4\pi \ln(2\alpha) + \mathcal{O}(s \ln s) \tag{3.25}$$

with the diverging term

$$S(s) = -2\pi \ln\, s\ . \tag{3.26}$$

(c) Consider the remaining option $k > 3$. In this case, $(1-v)^{\frac{k}{2}-1}$ is bounded from above and $(k-1)/2 > 1$. It means that the integral converges absolutely and the only finite contribution to the integral comes from the first (constant) term of the integral expansion for small s,

$$\psi_{\text{fin}}^{\boldsymbol{m}=\boldsymbol{0}}(\boldsymbol{r}, s) = \frac{2\pi^{\frac{3}{2}}\alpha^{k-3}}{(k-3)\Gamma\left[\frac{k}{2}\right]} \tag{3.27}$$

The second term of the total potential energy, I_{00} (3.2) can be derived in a similar form to the first one. The procedure to find the form of $\psi(\boldsymbol{r}, s)$ is repeated here with $\boldsymbol{r}_{ij} = 0$, hence the results are obtained straightforwardly via (3.10), (3.18), (3.25) and (3.27),

$$\begin{aligned} I_{00} = \quad & \sum_{i=1}^{N} q_i^2 \left[\frac{1}{\Gamma(\frac{k}{2})}\sum_{\boldsymbol{n}} \frac{\Gamma(\frac{k}{2}, \alpha^2 n^2)}{n^k} + \sum_{\boldsymbol{m}\neq\boldsymbol{0}} \frac{\pi^{\frac{3}{2}}}{\Gamma(\frac{k}{2})}\alpha^{k-3} E_{\frac{k-1}{2}}\left(\frac{\pi^2 m^2}{\alpha^2}\right)\right. \\ & \left. - \frac{\alpha^k}{\Gamma(\frac{k}{2}+1)} + \psi_{\text{fin}}^{\boldsymbol{m}=\boldsymbol{0}}(\boldsymbol{r}, s)\right]\ , \end{aligned} \tag{3.28}$$

with the term $\psi_{\text{fin}}^{\boldsymbol{m}=\boldsymbol{0}}(\boldsymbol{r}, s)$ depending on the potential parameter k via (3.22), (3.25) or (3.27).

Putting all together, the potential energy can be written in a more compact form as,

$$\begin{aligned} U = \quad & \frac{1}{L^k}(I_{01} + I_{00}) \\ = \quad & \frac{1}{L^k}\sum_{i<j} q_i q_j \psi(r_{ij}/L) + \frac{1}{2L^k}\sum_{i=1}^{N} q_i^2\, \xi + \frac{1}{L^k}\sum_{i<j} q_i q_j S(s) + \frac{1}{2L^k}\sum_i q_i^2 S(s)\ , \end{aligned} \tag{3.29}$$

with the generalized potential,

$$\psi(\boldsymbol{r}) = \sum_{\boldsymbol{n}} R(\boldsymbol{n}, \boldsymbol{r}) + \sum_{\boldsymbol{m}\neq 0} K(\boldsymbol{m}, \boldsymbol{r}) + C_1\ . \tag{3.30}$$

A constant shift in the definition of ψ is introduced to satisfy by the property $\int_{\text{cell}} \psi \, \mathrm{d}\boldsymbol{r} = 0$, convenient for a proper treatment of the background contributions (see Appendix A). The functions entering in Eq. (3.30) are defined as

$$R(\boldsymbol{n}, \boldsymbol{r}) = \frac{\Gamma(\frac{k}{2}, \alpha^2|\boldsymbol{r}+\boldsymbol{n}|^2)}{\Gamma(\frac{k}{2})|\boldsymbol{r}+\boldsymbol{n}|^k} \tag{3.31}$$

$$K(\boldsymbol{m}, \boldsymbol{r}) = \varkappa(\boldsymbol{m}) \cos(2\pi \boldsymbol{m}\boldsymbol{r}) \ , \tag{3.32}$$

$$\tag{3.33}$$

with

$$\varkappa(\boldsymbol{m}) = \frac{\pi^{\frac{3}{2}}\alpha^{k-3}}{\Gamma(\frac{k}{2})} E_{\frac{k-1}{2}}\left(\frac{\pi^2 m^2}{\alpha^2}\right) \ . \tag{3.34}$$

The explicit form of the function $S(s)$ depends on the k value,

$$S(s) = \begin{cases} s^{\frac{k-3}{2}} 2\pi\Gamma\left[\frac{3-k}{2}\right] & \text{if } k \leq 3 \text{ (singular term)} \\ -2\pi \ln s & \text{if } k = 3 \text{ (singular term)} \\ 0 & \text{if } k > 3 \end{cases} \ , \tag{3.35}$$

and the term ξ depends only on the choice of α,

$$\xi = \sum_{\boldsymbol{n}\neq 0} \rho(\boldsymbol{n}) + \sum_{\boldsymbol{m}\neq 0} \varkappa(\boldsymbol{m}) + C_1 + C_2 \ , \tag{3.36}$$

with

$$\rho(\boldsymbol{n}) = \frac{\Gamma(\frac{k}{2}, \alpha^2 n^2)}{\Gamma(\frac{k}{2}) n^k} \ , \tag{3.37}$$

and $\varkappa(\boldsymbol{n})$ defined in Eq. (3.34). The constants C_1 and C_2 are explicitly,

$$C_1 = \begin{cases} \frac{2\pi^{\frac{3}{2}}\alpha^{k-3}}{(k-3)\Gamma\left[\frac{k}{2}\right]} & \text{if } k \neq 3 \\ -4\pi + 4\pi \ln(2\alpha) & \text{if } k = 3 \end{cases} \tag{3.38}$$

$$C_2 = -\frac{\alpha^k}{\Gamma(\frac{k}{2}+1)} \tag{3.39}$$

$$\tag{3.40}$$

3.2.3 Removing singularities for $k \leq 3$

The diverging part U_s (containing a singularity) of the total potential energy equals to

$$U_s = \frac{1}{L^k} \sum_{i<j} q_i q_j S(s) + \frac{1}{2L^k} \sum_i q_i^2 S(s) = \frac{1}{2L} \left(\sum_i q_i\right)^2 S(s) \tag{3.41}$$

and vanishes, if the charge neutrality condition $\sum_i q_i = 0$ is taken.

Consider now a charge-neutral system with a neutralizing background consisting of a large number of identical uniformly distributed particles of the opposite charge (the "jellium" model). We denote the numbers of negatively charged particles q_- and positively charged (background) particles q_+ as N_- and N_+, respectively. By imposing charge neutrality, $q_+ = -[N_-/N_+]q_-$, with N the total number of particles, $N = N_- + N_+$.

The potential energy for the jellium model can be written as

$$U = \frac{1}{L^k} \sum_{i<j} q_i q_j \psi(r_{ij}/L) + \frac{N_- q_-^2 + N_+ q_+^2}{2L^k} \xi \ . \tag{3.42}$$

The second term in Eq. (3.42) has a component proportional to $N_+ q_+^2$. Note that the negative charges q_- and their number N_- is defined by the problem and therefore fixed. Hence, in the limit $N_+ \to \infty$, this term cancels $N_+ q_+^2 = (N_-^2 q_-^2)/N_+ \to 0$, and therefore this background contribution may be eliminated to yield

$$\frac{N_- q_-^2 + N_+ q_+^2}{2L^k} \xi = \frac{N_- q_-^2}{2L^k} \xi \ . \tag{3.43}$$

Concerning the first term of Eq. (3.42), let us split it into three pieces,

$$\frac{1}{L} \sum_{1 \le i < j \le N} q_i q_j \psi(\boldsymbol{r}) = \frac{1}{L} (S_{--} + 2S_{-+} + S_{++}) \ , \tag{3.44}$$

where the first sum corresponds to the interaction between the negative charges

$$S_{--} = \sum_{1 \le i < j \le N_-} q_i q_j \psi(\boldsymbol{r}) \ , \tag{3.45}$$

the second sum is the interaction of the negatively charged particles with the positive charges of the background

$$S_{-+} = \sum_{i=1}^{N_-} \sum_{j=1+N_-}^{N_+ + N_-} q_i q_j \psi(\boldsymbol{r}) \ , \tag{3.46}$$

and the third one is the interaction between the background charges

$$S_{++} = \sum_{1+N_- \le i < j \le N_+ + N_-} q_i q_j \psi(\boldsymbol{r}) \ . \tag{3.47}$$

The last two terms S_{-+} and S_{++} are easily shown to be zero in the limit $N_+ \to \infty$ as a consequence of the zero value of the integral of ψ over the simulation cell (see Appendix A).

With the above considerations we can finally write the expression for the potential energy within the jellium model as

$$U^{\text{jel}} = \frac{q_-^2}{L^k} \sum_{i<j} \psi(r_{ij}/L) + \frac{N q_-^2}{2L^k} \xi \tag{3.48}$$

In the more general case of different charges in a charge-neutral simulation cell (with a long-range potential) or a system with an arbitrary short-range potential the potential energy is given by

$$U^{\text{gen}} = \frac{1}{L^k}\sum_{i<j} q_i q_j \psi(r_{ij}/L) + \frac{\sum_{i=1}^{N} q_i^2}{2L^k}\xi \ . \tag{3.49}$$

A certain analytical conversion of the sum in the reciprocal space is also possible in order to sum it up faster. Expanding the sum that defines $K(\boldsymbol{m}, \boldsymbol{r})$ (3.32), one can simplify it in the following way,

$$\begin{aligned}
\sum_{i<j} q_i q_j \sum_{\boldsymbol{m}\neq 0} K(\boldsymbol{m}, \boldsymbol{r}) &= \sum_{\boldsymbol{m}\neq 0} \varkappa(\boldsymbol{m}) \sum_{i<j} q_i q_j \cos(2\pi \boldsymbol{m}\boldsymbol{r}) \\
&= \frac{1}{2}\sum_{\boldsymbol{m}\neq 0} \varkappa(\boldsymbol{m}) \sum_{i,j} q_i q_j \left[\cos(2\pi \boldsymbol{m}\boldsymbol{r}_i)\cos(2\pi \boldsymbol{m}\boldsymbol{r}_j) + \sin(2\pi \boldsymbol{m}\boldsymbol{r}_i)\sin(2\pi \boldsymbol{m}\boldsymbol{r}_j)\right] \\
&\quad -\frac{1}{2}\sum_i q_i^2 \sum_{\boldsymbol{m}\neq 0} \varkappa(\boldsymbol{m}) \\
&= \frac{1}{2}\sum_{\boldsymbol{m}\neq 0} \varkappa(\boldsymbol{m}) \left|\sum_j q_j \exp(2\pi \mathrm{i} \boldsymbol{m}\boldsymbol{r}_j)\right|^2 - \frac{1}{2}\sum_i q_i^2 \sum_{\boldsymbol{m}\neq 0} \varkappa(\boldsymbol{m})
\end{aligned} \tag{3.50}$$

In this form, the sum over all pairs of particles in the reciprocal space is represented as a single sum over particles and thus it scales as $\mathcal{O}(N)$ instead of $\mathcal{O}(N^2)$. Notice that the number of prefactors $\varkappa(\boldsymbol{m})$ and exponents in the sum depends on a chosen cutoff, which in general also might depend on N, making the overall complexity of the k-space grow. Naïve schemes with α and the cutoff not depending on N do not take into account the interplay between the r-space and k-space sum complexities, thus leaving at least $\mathcal{O}(N^2)$ in one of them. Nevertheless, as we show later, optimization with α and cutoff depending on N gives a best total complexity of $\mathcal{O}(N^{3/2})$. An alternative method to sum up the momentum space part is to use Fast Fourier transform-based techniques (like PME), which is fast as $\mathcal{O}(N \ln N)$.

The last term in Eq. (3.50) cancels the $\varkappa(\boldsymbol{m})$ component of ξ. Introduce the notation,

$$\tilde{\psi}(\boldsymbol{r}) = \sum_{\boldsymbol{n}} R(\boldsymbol{n}, \boldsymbol{r}) + C_1 \tag{3.51}$$

$$\tilde{\xi} = \sum_{\boldsymbol{n}\neq \boldsymbol{0}} \rho(\boldsymbol{n}) + C_1 + C_2 \tag{3.52}$$

$$\tilde{S}_{\text{equal}}(\boldsymbol{m}) = q_- \sum_j \exp(2\pi \mathrm{i} \boldsymbol{m}\boldsymbol{r}_j/L) \tag{3.53}$$

$$\tilde{S}_q(\boldsymbol{m}) = \sum_j q_j \exp(2\pi \mathrm{i} \boldsymbol{m}\boldsymbol{r}_j/L) \ , \tag{3.54}$$

where $\tilde{S}_{\text{equal}}$ is used when the system of equally charged particles q_- is considered. Within this notation the potential energy may be rewritten in the following forms, which are more

efficient for numerical implementation,

$$U^{\text{jel}} = \frac{q_-^2}{L^k}\sum_{i<j}\tilde{\psi}(r_{ij}/L) + \frac{1}{2L^k}\sum_{\boldsymbol{m}\neq 0}\varkappa(\boldsymbol{m})|\tilde{S}_{\text{equal}}(\boldsymbol{m})|^2 + \frac{Nq_-^2}{2L^k}\tilde{\xi} \tag{3.55}$$

$$U^{\text{gen}} = \frac{1}{L^k}\sum_{i<j}q_iq_j\tilde{\psi}(r_{ij}/L) + \frac{1}{2L^k}\sum_{\boldsymbol{m}\neq 0}\varkappa(\boldsymbol{m})|\tilde{S}_q(\boldsymbol{m})|^2 + \frac{\sum_{i=1}^N q_i^2}{2L^k}\tilde{\xi}\ , \tag{3.56}$$

with $\boldsymbol{r}_i$, r_{ij} in the original length units.

3.2.4 Short-range potentials and the marginal case

In case of a short-range interaction ($k > 3$), the potential energy does not diverge, which is clear from the form of the singular term $S(s)$(see Eq. 3.35). Hence, there is no need to add a neutralizing background and, even more, the background must be necessarily excluded since it leads to a divergence in the energy. This is easily seen by considering the potential energy of the background separately

$$U_{bg} = C\int_0^{\text{cell}}\frac{\mathrm{d}\boldsymbol{r}}{|\boldsymbol{r}|^k}\ , \tag{3.57}$$

that contains a singularity in zero. The expression for the potential energy is simply equal to Eq. (3.49),

$$U = \frac{1}{L^k}\sum_{i<j}q_iq_j\psi(r_{ij}/L) + \frac{\sum_{i=1}^N q_i^2}{2L^k}\xi\ . \tag{3.58}$$

When $k = 3$ (marginal case), both ultraviolet (coming from short-range contributions) and infrared (coming from long-range contributions) divergences arise in zero for the background as well as in the vicinity of infinity (the logarithmic divergence in the energy of negative charges). The only coherent model here is a plain "quasi-neutral" gas consisting of a mixture of a finite number of charges per box with the constraint $\sum q_i = 0$, i.e., with the positive background excluded.

3.3 Ewald method in 2D geometry

3.3.1 General notes for lower dimensions

The Ewald sums can be extended to two-dimensional (2D) systems interacting through polytropic potentials. The difference with the 3D case comes from a different form of the Jacobi imaginary transformation for the Jacobi θ-functions [its 3D form is given in Eq. (3.14)].

The "third" Jacobi θ-function $\theta_3(z,\tau)$ is defined as

$$\theta_3(z|\tau) = \sum_{m=-\infty}^{+\infty} e^{\mathrm{i}\pi\tau m^2}e^{2miz}\ , \tag{3.59}$$

and satisfies the Jacobi imaginary transformation,

$$\theta_3(z|\tau) = (-\mathrm{i}\tau)^{-1/2} e^{\mathrm{i}\tau' 2z^2/\pi}\, \theta_3(z\tau'|\tau') \ , \tag{3.60}$$

with $\tau' = -1/\tau$. Under the change of variables, $z = \pi r$ and $\tau = \mathrm{i}\pi/s$, the θ-function becomes a Gaussian, which is the relevant function for performing the Ewald sums,

$$\sum_{n=-\infty}^{+\infty} e^{-s(r+n)^2} = (\pi/s)^{1/2} \sum_{m=-\infty}^{+\infty} e^{-\pi^2 m^2/s} e^{2\pi \mathrm{i} m r} \ . \tag{3.61}$$

This expression will be used later, in the derivation of the Ewald sum in one-dimensional systems. Equation (3.61) may be easily generalized to the 2D geometry,

$$\sum_{\boldsymbol{n}} e^{-s|\boldsymbol{r}+\boldsymbol{n}|^2} = (\pi/s) \sum_{\boldsymbol{m}} e^{-\pi^2 m^2/s} e^{2\pi \mathrm{i} \boldsymbol{m}\boldsymbol{r}} \ . \tag{3.62}$$

Comparing this result for 2D with its 1D (3.61) and 3D(3.14) counterparts one finds that the dimensionality D affects only the constant multiplier as $(\pi/s)^{D/2}$.

3.3.2 Analytic derivation

The analytical derivation of the Ewald sum in 2D proceeds similarly to the one already presented for 3D. Equations from (3.2) to (3.11) are also valid here because their derivation is done without explicit reference to the dimensionality of the problem. In particular, the integral $\psi_{\mathrm{inf}}(\boldsymbol{r}, s)$ converges absolutely and to the same value

$$\psi_{\mathrm{inf}}(\boldsymbol{r}, s) \xrightarrow{s\to 0} \frac{1}{\Gamma(\frac{k}{2})} \sum_{\boldsymbol{n}} \frac{\Gamma(\frac{k}{2}, \alpha^2|\boldsymbol{r}+\boldsymbol{n}|^2)}{|\boldsymbol{r}+\boldsymbol{n}|^k} \ . \tag{3.63}$$

We make the same decomposition of the integral $\psi_{\mathrm{fin}}(\boldsymbol{r}, s)$ as in 3D,

$$\psi_{\mathrm{fin}}(\boldsymbol{r}, s) = \psi_{\mathrm{fin}}^{\boldsymbol{m}\neq\boldsymbol{0}}(\boldsymbol{r}, s) + \psi_{\mathrm{fin}}^{\boldsymbol{m}=\boldsymbol{0}}(\boldsymbol{r}, s) \ , \tag{3.64}$$

with

$$\psi_{\mathrm{fin}}^{\boldsymbol{m}\neq\boldsymbol{0}}(\boldsymbol{r}, s) = \frac{\pi}{\Gamma(\frac{k}{2})} \sum_{\boldsymbol{m}\neq\boldsymbol{0}} \int_0^{\alpha^2} \frac{t^{\frac{k}{2}-1}}{(t+s)} \exp\left[\frac{-\pi^2 m^2}{t+s} + 2\pi \mathrm{i} \boldsymbol{m}\boldsymbol{r}\right] \mathrm{d}t \tag{3.65}$$

$$\psi_{\mathrm{fin}}^{\boldsymbol{m}=\boldsymbol{0}}(\boldsymbol{r}, s) = \frac{\pi}{\Gamma(\frac{k}{2})} \int_0^{\alpha^2} \frac{t^{\frac{k}{2}-1}}{(t+s)} \mathrm{d}t \ , \tag{3.66}$$

where the two-dimensional variant of the Jacobi transformation (3.62) is used. The difference between the pair of equations (3.65, 3.66) and their three-dimensional analogues (3.12, 3.13) relies in a substitution of the 3D factor $(\pi/(t+s))^{3/2}$ by the 2D one $\pi/(t+s)$.

First, we consider the term $\psi_{\text{fin}}^{\boldsymbol{m}\neq\boldsymbol{0}}(\boldsymbol{r},s)$. Following the same analysis as for its 3D counterpart, it can be shown that this parametric integral also converges absolutely. It yields

$$\begin{aligned}\psi_{\text{fin}}^{\boldsymbol{m}\neq\boldsymbol{0}}(\boldsymbol{r},s) = & \quad \frac{\pi}{\Gamma(\frac{k}{2})}\sum_{\boldsymbol{m}\neq\boldsymbol{0}} e^{2\pi \mathrm{i}\boldsymbol{m}\boldsymbol{r}}\int_0^{\alpha^2} t^{\frac{k}{2}-2}\exp\left[-\frac{\pi^2 m^2}{t}\right]\mathrm{d}t \\ = & \quad \sum_{\boldsymbol{m}\neq\boldsymbol{0}}\frac{\pi\cos(2\pi\boldsymbol{m}\boldsymbol{r})}{\Gamma(\frac{k}{2})}\alpha^{k-2}E_{\frac{k}{2}}\left(\frac{\pi^2 m^2}{\alpha^2}\right) . \end{aligned} \tag{3.67}$$

The modification of the integral $\psi_{\text{fin}}^{\boldsymbol{m}=\boldsymbol{0}}$ is less straightforward, since it requires specific integrations and expansions in the series for small s. Namely, we have to evaluate the integral

$$\psi_{\text{fin}}^{\boldsymbol{m}=\boldsymbol{0}} = \frac{\pi}{\Gamma(\frac{k}{2})}\int_{s/(\alpha^2+s)}^1 \frac{(1-v)^{\frac{k}{2}-1}}{v^{\frac{k}{2}}}s^{k/2-1}\,\mathrm{d}v \tag{3.68}$$

which is the 2D equivalent of Eq. (3.20).

In the following, we consider separately the cases of long-range potential ($1 \leq k < 2$), marginal interaction ($k = 2$) and short-range potential ($k > 2$).

1. $1 \leq k < 2$. As in 3D, the integral can be found analytically via the incomplete beta- and incomplete gamma-function with known series expansions for small s. Omitting these unnecessary intermediate expressions, we give the final expansion for $\psi_{\text{fin}}^{\boldsymbol{m}=\boldsymbol{0}}$,

$$\psi_{\text{fin}}^{\boldsymbol{m}=\boldsymbol{0}} = s^{\frac{k-2}{2}}\frac{\pi^2}{\sin\left(\frac{k\pi}{2}\right)\Gamma\left(\frac{k}{2}\right)} + \frac{2\pi\alpha^{k-2}}{(k-2)\Gamma\left[\frac{k}{2}\right]} + \mathcal{O}(s^{k/2}) . \tag{3.69}$$

   The first term of the expansion,

$$S(s) = s^{\frac{k-2}{2}}\frac{\pi^2}{\sin\left(\frac{k\pi}{2}\right)\Gamma\left(\frac{k}{2}\right)} , \tag{3.70}$$

   clearly diverges when $s \to 0$. Similarly to the 3D case, this term is cancelled in a charge-neutral cell and hence,

$$\psi_{\text{fin}}^{\boldsymbol{m}=\boldsymbol{0}} = \frac{2\pi\alpha^{k-2}}{(k-2)\Gamma\left[\frac{k}{2}\right]} \tag{3.71}$$

2. $k = 2$. The integration of Eq. (3.68) is performed to yield in the limit $s \to 0$ a marginal logarithmic dependence,

$$\psi_{\text{fin}}^{\boldsymbol{m}=\boldsymbol{0}} = -\pi\ln s + 2\pi\ln\alpha + \mathcal{O}(s\ln s) . \tag{3.72}$$

   As for the 3D geometry, the jellium model is inapplicable in this particular case since the energy of the continuous background diverges. Nonetheless the diverging component

$$S(s) = -\pi\ln s \tag{3.73}$$

can be removed if we consider a charge-neutral system with a finite number of charges. In this case,

$$\psi_{\text{fin}}^{\boldsymbol{m}=\boldsymbol{0}} = 2\pi \ln \alpha \ . \tag{3.74}$$

3. $k > 2$. The integral (3.68) can be evaluated by taking $s = 0$, since its convergence is absolute,

$$\psi_{\text{fin}}^{\boldsymbol{m}=\boldsymbol{0}} \xrightarrow{s\to 0} \frac{2\pi\alpha^{k-2}}{(k-2)\Gamma\left[\frac{k}{2}\right]} \tag{3.75}$$

The second potential energy component, I_{00} (3.2), is calculated as in the 3D case. The result for 2D is

$$\begin{aligned} I_{00}(s) &= \sum_{i=1}^{N} q_i^2 (\psi_{\text{fin}}^{\boldsymbol{m}\neq\boldsymbol{0}}(\boldsymbol{0}, s) + \psi_{\text{inf}}(\boldsymbol{0}, s) - \psi_{\text{inf}}^{\boldsymbol{n}=\boldsymbol{0}}(\boldsymbol{0}, s)) \qquad (3.76) \\ &= \sum_{i=1}^{N} q_i^2 \left[\sum_{\boldsymbol{n}} \frac{\Gamma(\frac{k}{2}, \alpha^2 n^2)}{\Gamma(\frac{k}{2}) n^k} + \sum_{\boldsymbol{m}\neq\boldsymbol{0}} \frac{\pi\alpha^{k-2}}{\Gamma(\frac{k}{2})} E_{\frac{k}{2}}\left(\frac{\pi^2 m^2}{\alpha^2}\right) - \frac{\alpha^k}{\Gamma(\frac{k}{2}+1)} + \psi_{\text{fin}}^{\boldsymbol{m}=\boldsymbol{0}} \right] . \end{aligned}$$

3.3.3 Final expressions

With respect to the 3D case, the changes in the 2D Ewald sum appear in those terms in which the Jacobi transformation is used, that is in $\varkappa(\boldsymbol{n})$ and C_1,

$$\begin{aligned} \varkappa(\boldsymbol{m}) &= \frac{\pi\alpha^{k-2}}{\Gamma(\frac{k}{2})} E_{\frac{k}{2}}\left(\frac{\pi^2 m^2}{\alpha^2}\right) \qquad (3.77) \\ C_1 &= \psi_{\text{fin}}^{\boldsymbol{m}=\boldsymbol{0}} \qquad (3.78) \end{aligned}$$

The other terms, namely $R(\boldsymbol{r}, \boldsymbol{n})$, $\rho(\boldsymbol{n})$ and C_2, are not affected by dimensionality and may be taken directly from the previous section.

Within the jellium model for a long-range potential ($k < 2$), the Ewald sum is given by

$$U^{\text{jel}} = \frac{q_-^2}{L^k} \sum_{i<j} \psi(r_{ij}/L) + \frac{N q_-^2}{2L^k} \xi \ . \tag{3.79}$$

A more general form, applicable to any system with a short-range potential ($k > 2$), a charge-neutral system with long-range interaction ($k < 2$), or a marginal ($k = 2$) potential is expressed as

$$U^{\text{gen}} = \frac{1}{L^k} \sum_{i<j} q_i q_j \psi(r_{ij}/L) + \frac{\xi}{2L^k} \sum_{i=1}^{N} q_i^2 \ . \tag{3.80}$$

In the same way as for the 3D systems we can modify the sum in the reciprocal space, and with the same notations (3.51) – (3.54) (ρ, R and the constants C_1, C_2 are the new

ones, corresponding to 2D case) the potential energy may be given by

$$U^{\text{jel}} = \frac{q_-^2}{L^k}\sum_{i<j}\tilde{\psi}(r_{ij}/L) + \frac{1}{2L^k}\sum_{\boldsymbol{m}\neq 0}\varkappa(\boldsymbol{m})|\tilde{S}_{\text{equal}}|^2 + \frac{Nq_-^2}{2L^k}\tilde{\xi} \tag{3.81}$$

$$U^{\text{gen}} = \frac{1}{L^k}\sum_{i<j}q_iq_j\tilde{\psi}(r_{ij}/L) + \frac{1}{2L^k}\sum_{\boldsymbol{m}\neq 0}\varkappa(\boldsymbol{m})|\tilde{S}_q|^2 + \frac{\sum q_i^2}{2L^k}\tilde{\xi}\ . \tag{3.82}$$

3.4 Ewald method in 1D geometry

As it has been commented before for the 2D case, the differences due to dimensionality are caused by the form of the Jacobi imaginary transformation. In the derivation for 1D, one needs the following ones

$$x^{-2s} = \frac{1}{\Gamma(s)}\int_0^\infty t^{s-1}e^{-tx^2}\,\mathrm{d}t \tag{3.83}$$

$$\sum_{n=-\infty}^{+\infty} e^{-sn^2} = (\pi/s)^{1/2}\sum_{m=-\infty}^{+\infty} e^{-\pi^2m^2/s} \tag{3.84}$$

$$\sum_{n=-\infty}^{+\infty} e^{-s(r+n)^2} = (\pi/s)^{1/2}\sum_{m=-\infty}^{+\infty} e^{-\pi^2m^2/s}e^{2\pi\mathrm{i}mr}\ . \tag{3.85}$$

Similarly to what discussed in the previous section, the only terms to be changed are those where the Jacobi transformation is used, namely $\psi_{\text{fin}}^{m\neq 0}$ (in I_{01} in a radial-dependent form, in I_{00} for $r=0$). The difference arises from a different power exponent $(1/2)$ in (3.84) and (3.85), that is in (3.18) k has to be substituted by $k+2$ (and $\pi^{3/2}$ – by $\pi^{1/2}$, respectively), yielding

$$\psi_{\text{fin}}^{m\neq 0} = \sum_{n\neq 0}\frac{\pi^{1/2}e^{2\pi\mathrm{i}mr}}{\Gamma(\frac{k}{2})}\alpha^{k-1}E_{\frac{k+1}{2}}\left(\frac{\pi^2m^2}{\alpha^2}\right)\ . \tag{3.86}$$

As far as the term $\psi_{\text{fin}}^{m=0}$ is concerned, we should perform a simple integration and do a series expansion for small s,

$$\psi_{\text{fin}}^{m=0} = \frac{\pi^{1/2}}{\Gamma(\frac{k}{2})}\int_{s/(\alpha^2+s)}^1 \frac{(1-v)^{\frac{k-1}{2}}}{v^{\frac{k+1}{2}}}\,\mathrm{d}v \tag{3.87}$$

The estimation of this integral depends on the k value. In the following, we detail this analysis.

1. $k=1$, the marginal case,

$$\psi_{\text{fin}}^{m=0} = \frac{\pi^{1/2}}{\Gamma(\frac{k}{2})}(-\ln s - 2 + 2\ln(2\alpha)) + \mathcal{O}(s)\ . \tag{3.88}$$

As before, we keep only the constant term, considering the diverging term absent due to the charge neutrality condition. Therefore, with $\Gamma(1/2)=\sqrt{\pi}$ one has

$$\psi_{\text{fin}}^{m=0} = -2 + 2\ln(2\alpha) \tag{3.89}$$

2. $k > 1$, the short-range potential,

$$\psi_{\rm fin}^{m=0} = \frac{\pi^{1/2}}{\Gamma(\frac{k}{2})} \cdot \frac{2\alpha^{k-1}}{k-1} + \mathcal{O}(s) + \mathcal{O}(s^{(k-1)/2} \ln s) \ . \tag{3.90}$$

In the limit $s \to 0$, it yields

$$\psi_{\rm fin}^{m=0} = \frac{2\pi^{1/2}\alpha^{k-1}}{(k-1)\Gamma(\frac{k}{2})} \tag{3.91}$$

resembling the 3D result (3.27), with the change $k \to k+2$ (except in the Γ term) and $\pi^{3/2} \to \pi^{1/2}$.

The final result for the one-dimensional Ewald summation reads

$$\psi(\boldsymbol{r}) = \sum_n R(n,r) + \sum_{m\neq 0} K(m,r)) + C_1 \tag{3.92}$$

$$\xi = \sum_{n\neq 0} \rho(n) + \sum_{m\neq 0} \varkappa(m) + C_1 + C_2 \ , \tag{3.93}$$

where $C_1 = \psi_{fin}^{m=0}$ is taken from the expressions (3.89) (if $k=1$) or (3.91) (if $k>1$).

For $k = 1$, the only consistent system is the charge-neutral one with a finite number of particles. In this case and for a short-range potential ($k > 1$) one the potential energy is given by

$$U^{\rm gen} = \frac{1}{L}\sum_{i<j} q_i q_j \psi(r_{ij}/L) + \frac{\sum_{i=1}^N q_i^2}{2L^k}\xi \ . \tag{3.94}$$

Although the Ewald method is applicable to one-dimensional problems, there is a direct way to calculate the sums for polytropic potentials

$$U = \frac{1}{L^k}\sum_{n=-\infty}^{n=+\infty} \frac{1}{|r+n|^k} \ . \tag{3.95}$$

For $k > 1$, this sum can be represented as a linear combination of the Hurwitz zeta functions,

$$\frac{1}{L^k}\sum_{n=-\infty}^{+\infty} \frac{1}{|r+n|^k} = \frac{1}{L^k}(H_k(r) + H_k(1-r)) \ . \tag{3.96}$$

In particular, for $k = 2$ the sum converts into a familiar expression used in the Calogero-Sutherland model [Sut71, AGLS06],

$$\frac{1}{L^2}\sum_{n=-\infty}^{+\infty} \frac{1}{|r+n|^2} = \frac{\pi^2}{L^2 \sin^2(\pi r)} \ . \tag{3.97}$$

Notice that the sum (3.96) may be expressed in terms of trigonometric functions only for even values of k via $(k-2)$ times differentiation of Eq. (3.97). Anyway, the possibility to find exact expressions for infinite sums in 1D suggests that the use of the Ewald method might not be needed, but we keep it as a possibly useful mathematical relation and for completeness.

3.5 Generalizations to non-cubic simulation cells

3.5.1 3D case

A special and interesting situation arises if we consider a simulation cell in a more general way, as a rectangular box with different side lengths (L_x, L_y, L_z in the corresponding dimensions). The need to deal with a box of unequal size lengths may occur in the simulation of a solid with a noncubic lattice (the simplest examples include a hexagonal closed packed crystal in 3D geometry), since the lattice vectors $\boldsymbol{n}$ in the sum over images on (3.1) are no longer orthogonal. Focusing our analysis to a 3D geometry, the potential energy is now given by

$$U = \frac{1}{2} {\sum_{\boldsymbol{n_a} \in \mathbb{Z}^3}}' \left[\sum_{i=1}^{N} \sum_{j=1}^{N} \phi(\boldsymbol{r}_{ij} + L_0 \boldsymbol{n}_r) \right] , \tag{3.98}$$

with $\boldsymbol{n}_r = (\boldsymbol{n}_x L_x + \boldsymbol{n}_y L_y + \boldsymbol{n}_z L_z)/L_0$, $\boldsymbol{n}_{x,y,z}$ being integer vectors along the corresponding axis x, y, z. We have introduced the geometric average $L_0 = (L_x L_y L_z)^{1/3}$ and we will use reduced L_0 units for r_{ij}, and hence r_{ij} will be adimensional. Repeating the standard procedure, we multiply the potential energy by a Gaussian term $\exp(-s|\boldsymbol{n}_r + \boldsymbol{r}|^2)$ and, at the end, we take the limit $s \to 0$, separating the converging part, if present. We group separately the interaction with images of other particles I_{01} and the interaction of a particle with its own images I_{00},

$$U = \frac{1}{L_0^k} (I_{01} + I_{00}) , \tag{3.99}$$

where

$$I_{01} = \sum_{\boldsymbol{n} \in \mathbb{Z}^3} \left[\sum_{1 \le i < j \le N} \frac{q_i q_j e^{-s|\boldsymbol{n}_r + \boldsymbol{r}_{ij}|^2}}{|\boldsymbol{r}_{ij} + \boldsymbol{n}_r|^k} \right] \tag{3.100}$$

$$I_{00} = \frac{1}{2} \sum_{\boldsymbol{n} \in \mathbb{Z}^3 \setminus \boldsymbol{0}} \frac{e^{-s|\boldsymbol{n}_r^2|}}{|\boldsymbol{n}_r|^k} \sum_{i=1}^{N} q_i^2 . \tag{3.101}$$

Comparing the relations (3.99) – (3.101) to the cubic case (3.2) – (3.4), one notices that these relations remain unchanged if $\boldsymbol{n}$ is formally substituted by $\boldsymbol{n}_r$, and the constant coefficient $1/L^k$ is replaced by $1/L_0^k$. Therefore, all the results found without the Jacobi transformation (3.14) remain the same with $\boldsymbol{n}_r$ instead of $\boldsymbol{n}$. In particular, Eq. (3.10) transforms into the following

$$\psi_{\text{inf}} = \frac{1}{\Gamma(\frac{k}{2})} \sum_{\boldsymbol{n}} \frac{\Gamma(\frac{k}{2}, \alpha^2 |\boldsymbol{r} + \boldsymbol{n}_r|^2)}{|\boldsymbol{r} + \boldsymbol{n}_r|^k} . \tag{3.102}$$

The Jacobi transformation (3.14) in a noncubic box has the following form

$$\begin{aligned}\sum_{\boldsymbol{n}_r} e^{-s|\boldsymbol{n}_r+\boldsymbol{r}|^2} &= \prod_{i=x,y,z}\sum_{n_i} e^{-s(n_iL_i/L_0+r_i)^2} \\ &= \left[\prod_{i=x,y,z}\left(\frac{\pi}{s(L_i/L_0)^2}\right)^{1/2}\right]\prod_{i=x,y,z}\sum_{m_i}\exp\left(-\frac{\pi^2 m_i^2}{s(L_i/L_0)^2}\right)\exp(2\pi\mathrm{i}m_i r_i L_0/L_i) \\ &= (\pi/s)^{3/2}\sum_{\boldsymbol{m}_k}\exp(-\pi^2|\boldsymbol{m}_k|^2/s)\exp(2\pi\mathrm{i}\boldsymbol{m}_k\boldsymbol{r})\ , \end{aligned} \tag{3.103}$$

with $\boldsymbol{m}_k = \boldsymbol{m}_x L_0/L_x + \boldsymbol{m}_y L_0/L_y + \boldsymbol{m}_z L_0/L_z$ the normalized displacement vector in momentum space. The last equation is obtained from the original expression (3.14) by a formal substitution of the vector $\boldsymbol{m}$ by $\boldsymbol{m}_k$.

In order to calculate ψ_{fin} we first modify Eq. (3.15),

$$\exp[-s|\boldsymbol{n}_r+\boldsymbol{r}|^2 - t|\boldsymbol{n}_r+\boldsymbol{r}|^2] = \exp\left[-(s+t)|\boldsymbol{n}_r+\boldsymbol{r}|^2\right]\ , \tag{3.104}$$

then insert it into the relation (3.103), and finally separate the summand $\boldsymbol{n}=\boldsymbol{0}$,

$$\begin{aligned}\psi_{\text{fin}} &= \frac{\pi^{\frac{3}{2}}}{\Gamma(\frac{k}{2})}\sum_{\boldsymbol{m}_k\neq\boldsymbol{0}}\int_0^{\alpha^2}\frac{t^{\frac{k}{2}-1}}{(t+s)^{\frac{3}{2}}}\exp\left[\frac{-\pi^2\boldsymbol{m}_k^2}{t+s}+2\pi\mathrm{i}\boldsymbol{m}_k\boldsymbol{r}\right]\mathrm{d}t + \frac{\pi^{\frac{3}{2}}}{\Gamma(\frac{k}{2})}\int_0^{\alpha^2}\frac{t^{\frac{k}{2}-1}}{(t+s)^{\frac{3}{2}}}\,\mathrm{d}t \\ &= \psi_{\text{fin}}^{\boldsymbol{m}\neq\boldsymbol{0}} + \psi_{\text{fin}}^{\boldsymbol{m}=\boldsymbol{0}}\ . \end{aligned} \tag{3.105}$$

The subsequent derivation follows exactly the derivation for a cubic box, with the change of $\boldsymbol{n}$ by $\boldsymbol{n}_r$ and $\boldsymbol{m}$ by $\boldsymbol{m}_k$ for sums in the real and momentum spaces, respectively. The final result for a 3D system in a noncubic box can be summarized as follows

$$\psi(\boldsymbol{r}) = \sum_{\boldsymbol{n}_r}\frac{\Gamma(k/2,\alpha^2|\boldsymbol{n}_r+\boldsymbol{r}|^2)}{\Gamma(k/2)|\boldsymbol{n}_r+\boldsymbol{r}|^k} + \sum_{\boldsymbol{m}_k\neq\boldsymbol{0}}\frac{\pi^{\frac{3}{2}}\alpha^{k-3}\cos(2\pi\boldsymbol{m}_k\boldsymbol{r})}{\Gamma(k/2)}E_{\frac{k-1}{2}}\left(\frac{\pi^2|\boldsymbol{m}_k|^2}{\alpha^2}\right) + C_1 \tag{3.106}$$

$$\xi = \sum_{\boldsymbol{n}_r\neq\boldsymbol{0}}\frac{\Gamma(k/2,\alpha^2|\boldsymbol{n}_r|^2)}{\Gamma(k/2)|\boldsymbol{n}_r|^k} + \sum_{\boldsymbol{m}_k\neq\boldsymbol{0}}\frac{\pi^{\frac{3}{2}}\alpha^{k-3}}{\Gamma(k/2)}E_{\frac{k-1}{2}}\left(\frac{\pi^2|\boldsymbol{m}_k|^2}{\alpha^2}\right) + C_1 + C_2 \tag{3.107}$$

$$U = \frac{q_-^2}{L_0^k}\sum_{i<j}\psi(r_{ij}/L_0) + \frac{Nq_-^2}{2L_0^k}\xi \tag{3.108}$$

with the constants C_1 and C_2 defined in (3.38) and (3.39). As it was done in the cubic box, the potential energy may also be given with the momentum space sum (linear in N). Applying the definitions, similar to Eqs (3.51) – (3.54),

$$\tilde{\psi}(\boldsymbol{r}) = \sum_{\boldsymbol{n}_r} R(\boldsymbol{n}_r,\boldsymbol{r}) + C_1 \tag{3.109}$$

$$\tilde{\xi} = \sum_{\boldsymbol{n}_r\neq\boldsymbol{0}}\rho(\boldsymbol{n}_r) + C_1 + C_2 \tag{3.110}$$

$$\tilde{S}_{\text{equal}}(\boldsymbol{m}_k) = q_-\sum_j \exp(2\pi\mathrm{i}\boldsymbol{m}_k\boldsymbol{r}_j/L) \tag{3.111}$$

$$\tilde{S}_q(\boldsymbol{m}_k) = \sum_j q_j\exp(2\pi\mathrm{i}\boldsymbol{m}_k\boldsymbol{r}_j/L)\ , \tag{3.112}$$

the potential energy for a one-component jellium model converts into

$$U^{\text{jel}} = \frac{q_-^2}{L_0^k}\sum_{i<j}\tilde{\psi}(r_{ij}/L_0) + \frac{1}{2L_0^k}\sum_{\boldsymbol{m}_k\neq 0}\varkappa(\boldsymbol{m}_k)|\tilde{S}_{\text{equal}}(\boldsymbol{m}_k)|^2 + \frac{Nq_-^2}{2L_0^k}\tilde{\xi}\ , \tag{3.113}$$

with a natural extension to the general case

$$U^{\text{gen}} = \frac{1}{L_0^k}\sum_{i<j}q_iq_j\tilde{\psi}(r_{ij}/L_0) + \frac{1}{2L_0^k}\sum_{\boldsymbol{m}_k\neq 0}\varkappa(\boldsymbol{m}_k)|\tilde{S}_q(\boldsymbol{m}_k)|^2 + \frac{\sum q_i^2}{2L_0^k}\tilde{\xi}\ . \tag{3.114}$$

Note that the formulas are derived for an orthogonal basis set. Still many triclinic lattices can be sampled in a similar form. In such cases the crystal is constructed not by translating the smallest-volume unit cell along non-orthogonal vectors but rather by translating a pseudo-unit cell of size $L_x \times L_y \times L_z$ containing more atoms along orthogonal directions. For example hcp crystal can be summed in this way. Nonetheless, as the pseudo-elementary cell technique may be inconvenient in application to triclinic lattices, we would suggest the reader to rely on a reciprocal lattice technique (see [AM76]).

3.5.2 2D case

The generalization of the formulas found in a square 2D geometry to a rectangular simulation box comes in a similar manner. It is sufficient to take the resulting expressions for the two-dimensional problem (3.63) and (3.67), and to perform the necessary substitutions $\boldsymbol{n} \to \boldsymbol{n}_r$ and $\boldsymbol{n} \to \boldsymbol{m}_k$,

$$\psi(\boldsymbol{r}) = \sum_{\boldsymbol{n}_r}\frac{\Gamma(k/2,\alpha^2|\boldsymbol{n}_r+\boldsymbol{r}|^2)}{\Gamma(k/2)|\boldsymbol{n}_r+\boldsymbol{r}|^k} + \sum_{\boldsymbol{m}_k\neq\boldsymbol{0}}\frac{\pi\alpha^{k-2}\cos(2\pi\boldsymbol{m}_k\boldsymbol{r})}{\Gamma(k/2)}E_{\frac{k}{2}}\left(\frac{\pi^2|\boldsymbol{m}_k|^2}{\alpha^2}\right) + \psi_{\text{fin}}^{\boldsymbol{n}=\boldsymbol{0}} \tag{3.115}$$

$$\xi = \sum_{\boldsymbol{n}_r\neq\boldsymbol{0}}\frac{\Gamma(k/2,\alpha^2|\boldsymbol{n}_r|^2)}{\Gamma(k/2)|\boldsymbol{n}_r|^k} + \sum_{\boldsymbol{m}_k\neq\boldsymbol{0}}\frac{\pi\alpha^{k-2}}{\Gamma(k/2)}E_{\frac{k}{2}}\left(\frac{\pi^2|\boldsymbol{m}_k|^2}{\alpha^2}\right) + \psi_{\text{fin}}^{\boldsymbol{m}=\boldsymbol{0}} - \frac{\alpha^k}{\Gamma(\frac{k}{2}+1)}\ , \tag{3.116}$$

where $\psi_{\text{fin}}^{\boldsymbol{m}=\boldsymbol{0}}$ is given by the expressions (3.71), (3.74) or (3.75).

For a long-range interaction within the jellium model, the potential energy becomes

$$U^{\text{jel}} = \frac{q_-^2}{L_0^k}\sum_{i<j}\psi(r_{ij}/L_0) + \frac{Nq_-^2}{2L_0^k}\xi \tag{3.117}$$

with the notation

$$L_0 = (L_xL_y)^{1/2} \tag{3.118}$$

$$\boldsymbol{n}_r = \boldsymbol{n}_xL_x/L_0 + \boldsymbol{n}_yL_y/L_0 \tag{3.119}$$

$$\boldsymbol{m}_k = \boldsymbol{m}_xL_0/L_x + \boldsymbol{m}_yL_0/L_y\ . \tag{3.120}$$

For a multicomponent gas (quasi-neutral in case of a long-range potential), the potential energy is

$$U^{\text{gen}} = \frac{1}{L_0^k}\sum_{i<j} q_i q_j \psi(r_{ij}/L_0) + \frac{\sum q_i^2}{2L_0^k}\xi \ . \tag{3.121}$$

Finally, the usual modification to calculate the momentum space sum linearly in N is given by

$$U^{\text{jel}} = \frac{q_-^2}{L_0^k}\sum_{i<j}\tilde{\psi}(r_{ij}/L_0) + \frac{1}{2L_0^k}\sum_{\boldsymbol{m}_k\neq 0}\varkappa(\boldsymbol{m}_k)|\tilde{S}_{\text{equal}}(\boldsymbol{m}_k)|^2 + \frac{Nq_-^2}{2L_0^k}\tilde{\xi} \tag{3.122}$$

$$U^{\text{gen}} = \frac{1}{L_0^k}\sum_{i<j} q_i q_j\tilde{\psi}(r_{ij}/L_0) + \frac{1}{2L_0^k}\sum_{\boldsymbol{m}_k\neq 0}\varkappa(\boldsymbol{m}_k)|\tilde{S}_q(\boldsymbol{m}_k)|^2 + \frac{\sum q_i^2}{2L_0^k}\tilde{\xi} \ , \tag{3.123}$$

with $\tilde{\psi}$, $\tilde{\xi}$, $\tilde{S}_{\text{equal}}$, $\tilde{S}_q$ defined by (3.109) – (3.112) in their corresponding two-dimensional variants.

Some of non-orthogonal lattices can be sampled using the concept of pseudo-unit cell. For example a triangular lattice is constructed by translation of a single atom along two vectors with 60° angle between them. The same filling can be obtained by translation of a rectangular pseudoelementary cell with two atoms which can be readily calculated with the presented formulas.

3.6 Ewald method for Yukawa potential

As it was mentioned above, the Ewald summation technique can be applied to interaction potentials of a more generic kind, than polytropic ones, for example to the Yukawa class of interaction $E_p(\boldsymbol{r}_i - \boldsymbol{r}_j = \exp(-a|\boldsymbol{r}|)/r$. The interaction potential of this form widely appeared in nuclear physics as a primitive model potential inside nuclei and in simulations of plasmas, where it is used instead of the Coulomb potential to reflect the screening properties of plasma, and in the other applications.

The derivation of Ewald sums in the style of de Leeuw et al. [dLPS80], that we applied in 3, cannot be used directly with the Yukawa term $\exp(-a|\boldsymbol{r}|)/r$, but its certain modification may actually be used. Let us briefly explain how it can be done, having in mind the general line of derivation, given in the chapters above.

Consider the pairwise potential $E_p(\boldsymbol{r}) = \exp(-a|\boldsymbol{r}|)/\boldsymbol{r}$, with a for a positive constant, defining a screening size. We can repeat all the procedure of obtaining the form of $\rho(\boldsymbol{r})$ term (real-term component of the Ewald sum) unchanged for Coulomb potential with the coefficient $\exp(-a|\boldsymbol{r}|)$. Therefore this term is obtained straightforwardly as

$$\rho(\boldsymbol{n}) = \exp(-a|\boldsymbol{n}|)\text{erfc}(\alpha|\boldsymbol{n}|)/|\boldsymbol{n}| \tag{3.124}$$

The other component $\xi(\boldsymbol{m})$ cannot be found directly in this manner, since the Jacobi

transform, relying on a multidimensional variant of the Poisson formula [SW71]

$$\sum_{\boldsymbol{n}} f(\boldsymbol{r}+\boldsymbol{n}) = \sum_{\boldsymbol{m}} F[f](\boldsymbol{m}) e^{2\pi \mathrm{i} \boldsymbol{r}\boldsymbol{m}} \tag{3.125}$$

with $f(\boldsymbol{u}) = \exp(-\boldsymbol{u}^2 - a|\boldsymbol{u}|)$, requires for an analytical form of 3D Fourier transform $F[f]$, which is unknown for $a > 0$. Nevertheless, it can be found computationally with an arbitrary precision, thus allowing to discover all the components of $\psi(\boldsymbol{r})$ and ξ. As the summation in the Fourier space is a summation of cosines with the factors $\varkappa(\boldsymbol{m})$, depending only on the magnitude of the wave vector $|\boldsymbol{m}|$, the latter factors can be precalculated and taken from a one-dimensional array.

The other approach to the derivation of Ewald sums was presented in a number of works [SC00, Maz07a, Maz07b] and based on a traditional treatment of the Ewald technique for Coulomb systems. The first step of the approach it to consider the charge distribution as $\delta(\boldsymbol{r}) = (\delta(\boldsymbol{r}) - d(\boldsymbol{r})) + d(\boldsymbol{r}) = d_1(\boldsymbol{r}) + d_2(\boldsymbol{r})$, where $d(\boldsymbol{r})$ stands for a charge density, represented by a function, well localized around the point charge with suitable mathematical properties, normally it is a Gaussian. This background $\rho(\boldsymbol{r})$ has to obey the condition, that the integral charge below the Gaussian is equal to the point charge, that is the background is neutralizing. The variance of the Gaussian is taken as an arbitrary parameter and is a subject of optimization in the following treatment. The charge density profiles are then treated separately, making use of the fact, that the Yukawa potential is a Green's function of a Helmholtz equation of a certain form. The final solution reduces to finding the Green's functions for two Helmholtz equations for charge densities $d_1(\boldsymbol{r})$ and $d_2(\boldsymbol{r})$, which is a relatively simple analytical problem. The periodic (Ewald) form Yukawa potential is then equal to the sum of these Green's functions.

The final expressions of the Ewald sum for the Yukawa potential in our previous notations $\{\rho(\boldsymbol{n}), \varkappa(\boldsymbol{m}), \xi, C_1, C_2\}$ can be written in the following form:

$$\rho(\boldsymbol{n}) = \frac{\operatorname{erfc}(\alpha|\boldsymbol{n}| + a/(2\alpha))e^{a|\boldsymbol{n}|} + \operatorname{erfc}(\alpha|\boldsymbol{n}| - a/(2\alpha))e^{-a|\boldsymbol{n}|}}{2|\boldsymbol{n}|} \tag{3.126}$$

$$\varkappa(\boldsymbol{m}) = \pi \frac{\exp(-\frac{\pi^2\boldsymbol{m}^2 + a^2/4}{\alpha^2})}{\pi^2\boldsymbol{m}^2 + a^2/4} \tag{3.127}$$

$$C_1 = 4\pi \frac{\exp(-\frac{a^2}{4\alpha^2})}{a^2} \tag{3.128}$$

$$C_2 = -\frac{2\alpha}{\sqrt{\pi}} \exp\left(-\frac{a^2}{4\alpha^2}\right) + a \operatorname{erfc}\left(\frac{a}{2\alpha}\right) \tag{3.129}$$

where a is dimensionless, when $\boldsymbol{r}$ is given in the units of L. Notice that the limit $a \to 0$, corresponding to a Coulomb system, yields incorrect results in the constants C_1 and C_2. This may be seen as a reflection of the fact that the initial sum over $\boldsymbol{n}$ for a Yukawa system with any finite parameter a is absolutely convergent, which is not the case for a system of Coulomb charges, thus here the continuous passage to the limit $a \to 0$ is an incorrect operation.

3.7 Summary of the analytic results

In the previous sections, we have derived general expressions of the Ewald sums for polytropic $1/|\boldsymbol{r}|^k$ potentials in three- two- and one-dimensional systems. For integer values of k, the polytropic potential reduces to a power-law interaction, which comprises realizations of high physical relevance. Integer power-law potentials include

- $k = 1$ – Coulomb $1/|\boldsymbol{r}|$ interaction;
- $k = 2$ – Calogero-Sutherland $1/|\boldsymbol{r}|^2$ interaction;
- $k = 3$ – isotropic $1/|\boldsymbol{r}|^3$ component of dipole-dipole interaction (one-dimensional systems; two-dimensional system of dipole oriented perpendicularly to the plane);
- $k = 4,\ 5,\ 6$ – interaction between different Rydberg atoms;
- $k = 6,\ 12$ – van der Waals interaction.

The expressions for the potential energy for both the jellium model and the general case of a charge-neutral simulation cell are the following

$$U^{\text{gen}} = \frac{1}{L_0^k}\sum_{i<j} q_i q_j \psi(r_{ij}/L_0) + \frac{\sum q_i^2}{2L_0^k}\xi \tag{3.130}$$

$$U^{\text{jel}} = \frac{q_-^2}{L_0^k}\sum_{i<j} \psi(r_{ij}/L_0) + \frac{Nq_-^2}{2L_0^k}\xi \tag{3.131}$$

$$\psi(\boldsymbol{r}) = \sum_{\boldsymbol{n}} R(\boldsymbol{n}_r, \boldsymbol{r}) + \sum_{\boldsymbol{m}\neq 0} K(\boldsymbol{m}_k, \boldsymbol{r}) + C_1 \tag{3.132}$$

$$\xi = \sum_{\boldsymbol{n}\neq 0} \rho(\boldsymbol{n}_r) + \sum_{\boldsymbol{m}\neq 0} \varkappa(\boldsymbol{m}_k) + C_1 + C_2 \tag{3.133}$$

$$R(\boldsymbol{n}, \boldsymbol{r}) = \rho(\boldsymbol{n} + \boldsymbol{r}) \tag{3.134}$$

$$K(\boldsymbol{n}, \boldsymbol{r}) = \varkappa(\boldsymbol{m})\cos(2\pi \boldsymbol{m}\boldsymbol{r}) \tag{3.135}$$

$$C_1^{\text{3D}} = \begin{cases} \frac{2\pi^{\frac{3}{2}}\alpha^{k-3}}{(k-3)\Gamma\left[\frac{k}{2}\right]} & \text{if } k \neq 3 \\ -4\pi + 4\pi\ln(2\alpha) & \text{if } k = 3 \end{cases} \tag{3.136}$$

$$C_1^{\text{2D}} = \begin{cases} \frac{2\pi\alpha^{k-2}}{(k-2)\Gamma\left[\frac{k}{2}\right]} & \text{if } k \neq 2 \\ 2\pi\ln(\alpha) & \text{if } k = 2 \end{cases} \tag{3.137}$$

$$C_2 = -\frac{\alpha^k}{\Gamma(\frac{k}{2}+1)} \tag{3.138}$$

$$L_0 = \begin{cases} (L_x L_y L_z)^{1/3} & \text{in 3D} \\ (L_x L_y)^{1/2} & \text{in 2D} \end{cases} \tag{3.139}$$

$$\boldsymbol{n}_r = (\boldsymbol{n}\cdot\boldsymbol{L})/L_0, \text{ with } \boldsymbol{L} = (L_x, L_y, L_z) \tag{3.140}$$

$$\boldsymbol{m}_k = (\boldsymbol{m}\cdot\boldsymbol{L}')L_0, \text{ with } \boldsymbol{L}' = (1/L_x, 1/L_y, 1/L_z)\ . \tag{3.141}$$

Alternatively, by performing a momentum space sum the above set of equations become

$$U^{\mathrm{gen}} = \frac{1}{L_0^k}\sum_{i<j} q_i q_j \tilde{\psi}(r_{ij}/L_0) + \frac{1}{2L_0^k}\sum_{\boldsymbol{m}_k\neq 0} \varkappa(\boldsymbol{m}_k)|\tilde{S}_q(\boldsymbol{m}_k)|^2 + \frac{\sum q_i^2}{2L_0^k}\tilde{\xi} \tag{3.142}$$

$$U^{\mathrm{jel}} = \frac{q_-^2}{L_0^k}\sum_{i<j} \tilde{\psi}(r_{ij}/L_0) + \frac{1}{2L_0^k}\sum_{\boldsymbol{m}_k\neq 0} \varkappa(\boldsymbol{m}_k)|\tilde{S}_{\mathrm{equal}}(\boldsymbol{m}_k)|^2 + \frac{Nq_-^2}{2L_0^k}\tilde{\xi} \tag{3.143}$$

$$\tilde{\psi}(\boldsymbol{r}) = \sum_{\boldsymbol{n}} R(\boldsymbol{n}_r, \boldsymbol{r}) + C_1 \tag{3.144}$$

$$\tilde{\xi} = \sum_{\boldsymbol{n}\neq\boldsymbol{0}} \rho(\boldsymbol{n}_r) + C_1 + C_2 \tag{3.145}$$

$$\tilde{S}_{\mathrm{equal}} = q_- \sum_j \exp(2\pi \mathrm{i}\boldsymbol{m}_k\boldsymbol{r}_j/L) \tag{3.146}$$

$$\tilde{S}_q = \sum_j q_j \exp(2\pi \mathrm{i}\boldsymbol{m}_k\boldsymbol{r}_j/L)\ . \tag{3.147}$$

In accordance with considerations discussed in preceding sections, the simulation cell has to fulfil the charge neutrality condition ($\sum_{i=1}^N q_i = 0$) for long-range potentials. Also, notice that in the particular case of a cubic simulation cell, $\boldsymbol{n}_r = \boldsymbol{n}$, $\boldsymbol{m}_k = \boldsymbol{m}$.

Explicit expressions of the coefficients $\rho(\boldsymbol{n})$ and $\varkappa(\boldsymbol{m})$ for the most relevant interactions are summarized for 3D and 2D systems in Table 3.1 and Table 3.2, respectively.

Table 3.1: Coefficients $\rho(\boldsymbol{n})$ and $\varkappa(\boldsymbol{n})$ taken from Eqs (3.37) and (3.18) for 3D geometry. LR and SR stand for long range and short range, respectively.

	$\rho(\boldsymbol{n})$	$\varkappa(\boldsymbol{m})$
LR $\frac{1}{\lvert r\rvert}$	$\frac{\mathrm{erfc}(\alpha\lvert\boldsymbol{n}\rvert)}{\lvert\boldsymbol{n}\rvert}$	$\frac{1}{\pi m^2} e^{-\frac{\pi^2 m^2}{\alpha^2}}$
LR $\frac{1}{\lvert r\rvert^2}$	$\frac{e^{-\alpha^2 n^2}}{n^2}$	$\frac{\pi}{\lvert\boldsymbol{m}\rvert}\mathrm{erfc}\frac{\pi\lvert\boldsymbol{m}\rvert}{\alpha}$
SR $\frac{1}{\lvert r\rvert^4}$	$\frac{\alpha^2 n^2+1}{n^4} e^{-\alpha^2 n^2}$	$2\pi\left(\sqrt{\pi}\alpha e^{-\frac{\pi^2 m^2}{\alpha^2}} - \pi^2\lvert\boldsymbol{m}\rvert\mathrm{erfc}\frac{\pi\lvert\boldsymbol{m}\rvert}{\boldsymbol{\alpha}}\right)$
SR $\frac{1}{\lvert r\rvert^5}$	$\frac{\mathrm{erfc}(\alpha\lvert\boldsymbol{n}\rvert)}{\lvert\boldsymbol{n}\rvert^5} + \frac{4e^{-\alpha^2 n^2}}{3\sqrt{\pi}\lvert\boldsymbol{n}\rvert^5}\left(\frac{3\alpha\lvert\boldsymbol{n}\rvert}{2} + (\alpha\lvert\boldsymbol{n}\rvert)^3\right)$	$\frac{4\pi\alpha^2}{3}\left(e^{-\frac{\pi^2 m^2}{\alpha^2}} - \frac{\pi^2 m^2}{\alpha^2}E_1\left(\frac{\pi^2 m^2}{\alpha^2}\right)\right)$
SR $\frac{1}{\lvert r\rvert^6}$	$\left(\frac{\alpha^4}{2n^2} + \frac{\alpha^2}{n^4} + \frac{1}{n^6}\right)e^{-\alpha^2 n^2}$	$\frac{\pi^{3/2}\alpha^3}{3}\left(e^{-\frac{\pi^2 m^2}{\alpha^2}}\left(1 - \frac{2\pi^2 m^2}{\alpha^2}\right) + \frac{2\pi^{7/2}\lvert\boldsymbol{m}\rvert^3}{\alpha^3}\mathrm{erfc}\frac{\pi\lvert\boldsymbol{m}\rvert}{\alpha}\right)$
SR $\frac{1}{\lvert r\rvert^{12}}$	$\sum_{i=0}^{5}\frac{(\alpha n)^{2i}}{i!}\frac{e^{-\alpha^2 n^2}}{n^{12}}$	$-\sum_{i=0}^{4}(-2)^{i+1}(7-2i)!!\left(\frac{\pi m}{\alpha}\right)^{2i}\frac{e^{-\frac{\pi^2 m^2}{\alpha^2}}}{945}$ $-\frac{32\sqrt{\pi}\left(\frac{\pi m}{\alpha}\right)^9}{945}\mathrm{erfc}\frac{\pi m}{\alpha}$

The expressions of the Ewald summation components are consistent in appropriate limits with the earlier published results by M. Mazars [Maz10, Maz11] (inverse power-law potentials in 2D and 3D geometries), by C. Mora *et al.* [MPW07] (2D dipolar bosons), by N. Karasawa *et al.* [KI89] and W.-Z. Ou-Yang *et al.* [OYLS+05] (Lennard–Jones potential).

3.8 Practical application and optimizations in the Ewald technique

3.8.1 Optimization scheme with N^2 dependence

The basic idea of the Ewald method is to calculate slowly decaying sums in a rapid manner by means of the Fourier transform of the slowly converging part. Although conceptually it provides an exact result, the number of terms which has to be summed in order to reach the needed convergence is *a priori* unknown. Once we choose the interaction potential, this fixes the exact form of the sums to calculate, and the practical remaining question is the proper choice of the free parameter α and the numbers of terms to be calculated in the sums, originated from coordinate and momentum spaces. The total computer time T is obtained from the time needed to evaluate different sums

$$T = (t_r N_r + t_k N_k) N^2/2, \tag{3.148}$$

with the constants t_r and t_k depending on the complexity of the coefficients in the sums and the factor $N^2/2$ approximating the number of pairs. Here N_r and N_k are numbers of terms which are summed for each pair $\boldsymbol{r}_{ij}$, in particular the case $N_r = 1$ corresponds to the so called minimum image convention. One can notice that t_k is usually much less then t_r, since in the Jacobi-transformed sum we only calculate cosine functions, which is generally far less time-consuming than the complicated functions appearing in R. It is clear that the parameter α affects only the resulting error in the energy. In fact, the value of α being very small or very large eliminates errors in one of the sums, but amplifies them in the other, so there is an "optimal" point for α, yielding a minimum error in the total energy.

Table 3.2: The coefficients $\rho(\boldsymbol{n})$ and $\varkappa(\boldsymbol{m})$ taken from Eqs (3.37) and (3.77) for 2D geometry. LR and SR stand for long range and short range, respectively.

	$\rho(\boldsymbol{n})$	$\varkappa(\boldsymbol{m})$
LR $\frac{1}{\lvert r\rvert}$	$\frac{\mathrm{erfc}(\alpha\lvert\boldsymbol{n}\rvert)}{\lvert\boldsymbol{n}\rvert}$	$\frac{1}{\lvert\boldsymbol{m}\rvert}\mathrm{erfc}\frac{\pi\lvert\boldsymbol{m}\rvert}{\alpha}$
SR $\frac{1}{\lvert r\rvert^3}$	$\frac{2\alpha}{\sqrt{\pi}n^2}e^{-\alpha^2n^2} + \frac{\mathrm{erfc}(\alpha\lvert\boldsymbol{n}\rvert)}{\lvert\boldsymbol{n}\rvert^3}$	$4\left(\sqrt{\pi}\alpha e^{-\frac{\pi^2m^2}{\alpha^2}} - \pi^2\lvert\boldsymbol{m}\rvert\mathrm{erfc}\frac{\pi\lvert\boldsymbol{m}\rvert}{\boldsymbol{\alpha}}\right)$
SR $\frac{1}{\lvert r\rvert^4}$	$\frac{\alpha^2n^2+1}{n^4}e^{-\alpha^2n^2}$	$\pi\alpha^2\left(e^{-\frac{\pi^2m^2}{\alpha^2}} - \frac{\pi^2m^2}{\alpha^2}E_1(\frac{\pi^2m^2}{\alpha^2})\right)$
SR $\frac{1}{\lvert r\rvert^5}$	$\frac{\mathrm{erfc}(\alpha\lvert\boldsymbol{n}\rvert)}{\lvert\boldsymbol{n}\rvert^5} + \frac{4e^{-\alpha^2n^2}}{3\sqrt{\pi}\lvert\boldsymbol{n}\rvert^5}(\frac{3\alpha\lvert\boldsymbol{n}\rvert}{2} + (\alpha\lvert\boldsymbol{n}\rvert)^3)$	$\frac{8\sqrt{\pi}\alpha^3}{9}\left(e^{-\frac{\pi^2m^2}{\alpha^2}}(1-\frac{2\pi^2m^2}{\alpha^2}) + \frac{2\pi^{7/2}\lvert\boldsymbol{m}\rvert^3}{\alpha^3}\mathrm{erfc}\frac{\pi\lvert\boldsymbol{m}\rvert}{\alpha}\right)$
SR $\frac{1}{\lvert r\rvert^6}$	$(\frac{\alpha^4}{2n^2} + \frac{\alpha^2}{n^4} + \frac{1}{n^6})e^{-\alpha^2n^2}$	$\frac{\pi\alpha^4}{4}\left(e^{-\frac{\pi^2m^2}{\alpha^2}}(1-\frac{\pi^2m^2}{\alpha^2}) + \frac{\pi^4m^4}{\alpha^4}E_1(\frac{\pi^2m^2}{\alpha^2})\right)$
SR $\frac{1}{\lvert r\rvert^{12}}$	$\sum_{i=0}^{5}\frac{(\alpha n)^{2i}}{i!}\frac{e^{-\alpha^2n^2}}{n^{12}}$	$\sum_{i=0}^{4}(-1)^i(4-i)!\left(\frac{\pi m}{\alpha}\right)^{2i}\frac{e^{-\frac{\pi^2m^2}{\alpha^2}}}{120}$ $-\frac{(\frac{\pi m}{\alpha})^{10}}{120}E_1\left(\frac{\pi^2m^2}{\alpha^2}\right)$

In the following, we discuss a way for error (δE) minimization assuming the calculation time T fixed. From our point of view, a useful approach for practical implementation is represented by the following scheme

- We determine a time law $T = (t_r N_r + t_k N_k)N^2/2$ in a preliminary calculation and fix the values of t_r and t_k.
- We take a set of configurations, corresponding to the equilibrated state using an initial Ewald summation. Then, we calculate the exact energies $E_{\rm ex}$ (as a converged result of the Ewald summation) and the energies $E(\alpha, N_r, N_k)$ biased by a choice of N_r and N_k. For each pair (N_r, N_k), we find an optimal value of $\alpha = \alpha_{\rm opt}(N_r, N_k)$.
- We choose the goal accuracy $\delta E_{\rm acc}$ (normally, well below the statistical error). We plot the error as a function of the computer time spent and choose the less time consumption case among the points that lie below $\delta E_{\rm acc}$, therefore obtaining all the parameters required: α, N_r and N_k. From now on, these parameters are used in actual simulations.

3.8.2 Example of optimization

Let us illustrate the scheme proposed in the preceding subsection taking as an example the problem of two-dimensional zero-temperature Bose gas of particles, interacting through the pairwise repulsive $C_3/|\boldsymbol{r}|^3$ potential. The model corresponds to the dipole-dipole interaction with all dipole moments aligned perpendicularly to the plane of motion. The simulation is performed with $N = 108$ particles in a quadratic box ($L_x = L_y = L = 1$). The dimensionless Hamiltonian in the present example is taken to be $\hat{H} = -\sum_{i=1}^{N} \nabla_i^2/2 + \sum_{i<j} 1/|\boldsymbol{r}_{ij}|^3$ with the unit of energy being $\hbar^2/mL^2$. To describe the ground-state properties of the system we use the variational Monte Carlo (VMC) method and a Jastrow wave function with a two-body correlation factor which is solution of the two-body scattering problem [McM65].

The optimization is done by averaging over $N_{\rm conf} = 50$ uncorrelated VMC configurations, sampled according to the chosen probability distribution. We define the error $\delta E(\alpha)$ as a sum over $N_{\rm conf}$ configurations of the difference of the Ewald energy $E(i_{\rm conf}, \alpha, N_r, N_k)$, calculated for a given set of parameters (α, N_r, N_k) and the converged energy $E_{\rm ex}(i_{\rm conf}) = \lim_{N_k\to\infty} \lim_{N_r\to\infty} E(i_{\rm conf}, \alpha, N_r, N_k)$. The dependence of the computer time T, needed for the evaluation of Ewald sums, on the parameter set is shown in Figs 3.1 and 3.2. In Fig. 3.1, we show the dependence of T on the number of terms N_r in real space for different fixed numbers of terms N_k in the momentum space. The computation time is proportional to the number of terms and the resulting dependence is linear in N_r. A fixed number of terms N_k requires a certain amount of calculations which results in a constant shift. Similarly, keeping N_r fixed and varying N_k produces a linear dependence in N_k with a constant shift which depends on N_r, as shown in Fig. 3.2.

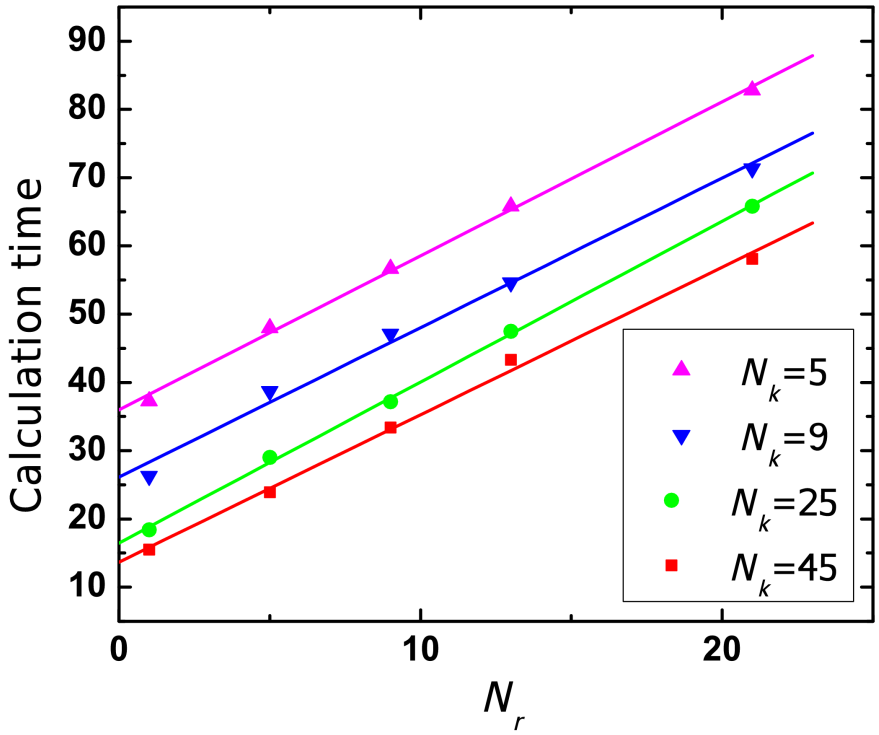

Figure 3.1: Dependence of the calculation time T on the number of terms N_r in the coordinate space for fixed numbers of terms in the momentum space $N_k = 5, 9, 25, 45$. Symbols are calculation times. Lines are linear fits for the data.

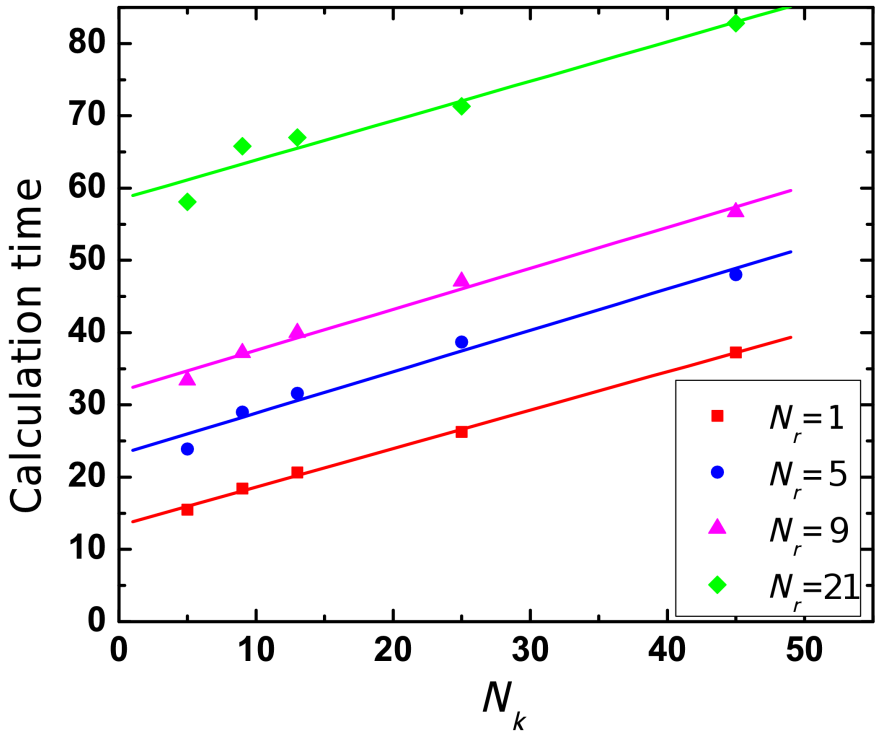

Figure 3.2: Dependence of the calculation time T on the number of terms N_k in the momentum space for fixed numbers of terms in the coordinate space $N_r = 1, 5, 9, 21$. Symbols are calculation times. Lines are linear fits for the data.

As one sees in Figs.3.1 and 3.2, the time dependence is linear both on N_k and N_r, although the point corresponding to (0,0) in (N_r, N_k) does not necessarily gives $T = 0$, since the reported time also contains some initializing calculations. The total error in the potential, as it is defined above, is given by

$$\delta E(\alpha) = \sqrt{\sum_{i_{\rm conf}=1}^{N_{\rm conf}} \frac{\left(E(\alpha, i_{\rm conf}) - E_{\rm ex}(i_{\rm conf})\right)^2}{N_{\rm conf}}} \,. \tag{3.149}$$

According to our previous considerations, in the case of very small or very large values of α the error coming from one of two sums, that is in the real or momentum space, grows and dominates over the error coming from the other sum; for a certain "optimal" range of α these two errors are of the same order. Notice that for each particular configuration, and each pair (N_r, N_k), it is possible to find $\alpha_{\rm opt}(i_{conf})$, such that $E(\alpha_{\rm opt}(i_{conf}), i_{conf}) - E_{\rm ex}(i_{conf}) = 0$. Instead, our task is to obtain a "universal" parameter α_0, minimizing the total error (3.149). The mean over the configuration set of the biased energies $\bar{E}(\alpha_0, i_{\rm conf})$ is used as an estimation for the mean of the exact energies $\bar{E}_{ex}$, introducing an inevitable systematic error. As it appears in typical calculations, this error is at least one order of magnitude smaller than the statistical error (3.149) given by the minimization of $\delta E(\alpha)$. In our benchmark calculations we also checked the dependence of the total energy on the value α for different pairs (N_r, N_k), which revealed characteristic plateaus for certain ranges of α (of the order of 1). It means that the Ewald summation indeed converges fast to a universal result. Nevertheless, the optimum value of the parameter α, minimizing the cumulative error, depends on the cut-off numbers in the sums in the range from $\alpha = 1.45$ ($N_r = 21$, $N_k = 5$) to $\alpha = 5.25$ ($N_r = 1$, $N_k = 45$).

A second step is the study of the dependence of the error and time on different pairs (N_r, N_k). The calculation time can be split as the sum of times for summing up in coordinate and momentum spaces, $T = (N_r t_r + N_k t_k)N^2/2$ as in Eq. (3.148), with N_r, N_k being the numbers of terms in each sum for a single pair. Every one of these sums converges when N_r, $N_k \to \infty$ to a certain value, depending on α, while the sum of the limiting values is a constant. We can take into account the errors, corresponding to each of the sums separately. For $\alpha \to 0$ the error for the real space term is zero and the other one tends to infinity (and vice versa as $\alpha \to \infty$). The minimum total error should therefore correspond to the value of α, satisfying the relation $\mathrm{d}(\delta E_r + \delta E_k)/\,\mathrm{d}\alpha = 0$.

Focusing on the 2D system of our example, we note that the long-range expansions of the terms in (3.37) and (3.77) are similar, in a sense that the leading terms in both expressions are Gaussians,

$$\frac{\Gamma(k/2, \alpha^2 n^2)}{\Gamma(k/2) n^k} = \exp(-\alpha^2 n^2)\left[\frac{C_r}{n^2} + O\left(\frac{1}{|\boldsymbol{n}|^3}\right)\right] \tag{3.150}$$

$$\frac{\pi^{\frac{3}{2}}\alpha^{k-3}}{\Gamma(k/2)} E_{\frac{k-1}{2}}\left(\frac{\pi^2 m^2}{\alpha^2}\right) = \exp\left(-\frac{\pi^2 m^2}{\alpha^2}\right)\left[\frac{C_k}{m^2} + O\left(\frac{1}{|\boldsymbol{m}|^3}\right)\right] \,. \tag{3.151}$$

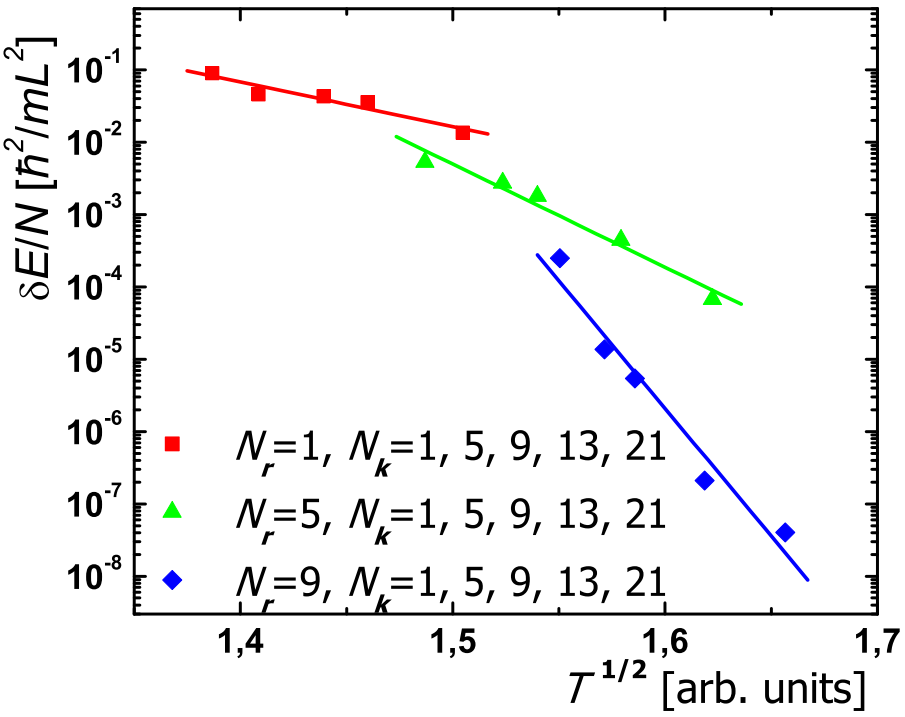

Figure 3.3: Resulting error of the energy per particle as a function of the computer time for different parameter sets. Symbols are the errors, related to truncation in the Ewald method. Lines are exponential fits for the data.

The power-law terms in $\boldsymbol{n}$, $\boldsymbol{m}$ and the constants C_r, C_k may be neglected since the leading behavior is driven by the Gaussian. The cut-off errors due to finite numbers of elements in the sums can be evaluated by ignoring the discrete structure of the images and approximating the sums by uniform integrals,

$$\begin{aligned} \delta E &= \frac{N^2}{2}\int_R^\infty \exp(-\alpha^2 r^2) 2\pi r \,\mathrm{d}r + \frac{N^2}{2}\int_K^\infty \exp\left(-\frac{\pi^2 k^2}{\alpha^2}\right) 2\pi k \,\mathrm{d}k \\ &= \frac{\pi N^2}{2}\left[\frac{\exp(-\alpha^2 N_r/\pi)}{\alpha^2} + \frac{\alpha^2 \exp\left(-\pi N_k/\alpha^2\right)}{\pi^2}\right] \end{aligned} \tag{3.152}$$

with $R \simeq \sqrt{N_r/\pi}$ and $K \simeq \sqrt{N_k/\pi}$ the approximate cut-off lengths in real and momentum spaces, respectively. The optimal value for α can be obtained by solving the equation $\mathrm{d}\delta E_r/\,\mathrm{d}\alpha = -\,\mathrm{d}\delta E_r/\,\mathrm{d}\alpha$. The first-order approximation of this equation is found by taking logarithms of both sides and omitting constants and terms, depending on α logarithmically, that is

$$A_k/\alpha^2 - A_r\alpha^2 = 0 \tag{3.153}$$

with $A_k = \pi N_k$ and $A_r = N_r/\pi$, which yields

$$\alpha = (A_k/A_r)^{1/4} = \left(\pi^2 N_k/N_r\right)^{1/4} \ . \tag{3.154}$$

Then, at lowest order one finds (3.152),

$$\delta E \sim \frac{N^2}{2}\exp(-\alpha^2 N_r/\pi) = \frac{N^2}{2}\exp(-\sqrt{N_k N_r}) \ . \tag{3.155}$$

Since the calculation time is linear with the numbers of elements N_r and N_k, we may conclude that with N_k fixed and comparatively large N_r, $\ln(\delta E) \sim \sqrt{N_r} \sim \sqrt{T}$ and vice versa, with N_r fixed and large N_k, $\ln(\delta E) \sim \sqrt{N_k} \sim \sqrt{T}$. This power law may be easily checked in our calculations, as it is shown in Fig. (3.3). Note that for the obtained value of α the errors of the real- and momentum-space cutoffs are of the same order of magnitude, that is $\delta E_r \approx \delta E_k$, which may serve as a rough criterion to optimize the parameter α.

3.8.3 Optimization scheme with $N^{3/2}$ dependence

A more advanced procedure for optimization of the parameters, proposed by Perram *et al.* [PPdL88], yields an asymptotic scaling $N^{3/2}$, with N the number of particles. It is based on the form of Ewald summation with the rearranged momentum space sum, linear in N (3.142). Note that here the linear N dependence is obtained after a summation over particle coordinates, while in Sections (3.8.1) and (3.8.2) the momentum space sum was evaluated over the pairs of the particles and had N^2 dependence. Suppose the values of the calculation time t_r, t_k to perform unit computations in both sums are known and the target

error level $\exp(-p)$ is fixed. Then, the total execution time in the real and momentum spaces is

$$T = T_r + T_k = N^2 \pi R^2 t_r + N \pi K^2 t_k \tag{3.156}$$

with $p = \alpha^2 R^2 = \pi^2 K^2 / \alpha^2$. Expressing K as $K = p/(\pi R)$ we can see that the minimum of the total time T corresponds to

$$R_{\text{opt}} = \left(\frac{p}{\pi}\right)^{1/2} \left(\frac{t_k}{t_r}\right)^{1/4} N^{-1/4} \tag{3.157}$$

$$K_{\text{opt}} = \left(\frac{p}{\pi}\right)^{1/2} \left(\frac{t_k}{t_r}\right)^{-1/4} N^{1/4} \tag{3.158}$$

$$\alpha_{\text{opt}} = \sqrt{\pi} \left(\frac{t_k}{t_r}\right)^{-1/4} N^{1/4} \,. \tag{3.159}$$

The computation time is equally divided between the real and momentum space parts (this was also stated in our simple optimization scheme), with a scaling of the whole summation given by

$$T = 2N^2 \pi R^2 t_r = 2p\sqrt{t_r t_k} N^{3/2} \tag{3.160}$$

Notice that the values of the free parameters change very slowly when the simulation cell is enlarged, and in particular α is not affected by the choice of the precision. Similar formulas for the optimized parameters in three-dimensional systems, with a discussion of different techniques to improve performance of the Ewald summation, are given by Fincham [Fin94]. A more precise and detailed analytic study of the cut-off errors with verifications of the analytic results in actual calculations can be found in the work of Kolafa and Perram [KP92]. An optimized method for treating the truncation error in Ewald sums with generic potentials was proposed by Natoli and Ceperley [NC95]. While the needed CPU time scales as $\mathcal{O}(N \ln N)^{3/2}$, it was shown that in the example of the Coulomb potential the method resulted in greatly improved accuracy compared to that of standard Ewald technique for a comparable computational effort. This method is based on an expansion of the real space function in an arbitrary radial basis with a parametric set of numbers in place of the k-dependent prefactors of $\exp(2\pi \mathrm{i} \boldsymbol{mr})$. The subsequent minimization of χ^2 with respect to the whole set of parameters yields a final optimal solution, that is the real space expansion coefficients and the k-space factors. This technique was also applied to derive the optimized summation formulas for the two-dimensional Coulomb system [HB05].

In general, the unit computation time in momentum space is 2–4 times faster than the one in real space. Taking the following reasonable assumptions $p = 4\pi$, $t_k/t_r = 3$, we find $R_{\text{opt}} \approx 2.6/N^{1/4}$ (the box size is taken to be 1). We want R to be below 0.5, since in this case the summation in the real space reduces to the accumulation of the single component $\boldsymbol{n} = 0$ ("minimum image convention"). This condition $R_{\text{opt}} = 0.5$, with our previous assumptions, corresponds to

$$N_{\text{opt}} = 770, \;\; K_{\text{opt}} = 8.0, \;\; \alpha_{\text{opt}} = 7.1 \tag{3.161}$$

In smaller systems, the other components of the real sum, starting from $|\boldsymbol{n}| = 1$, should be considered.

It is worth pointing out that if the interaction is very strong at short distances (as for the Lennard-Jones potential), then in principle the real-space cut-off R can be chosen below the "hard core radius" with a large enough value of α. This leads to the possibility of dropping completely the real-space part of the total sum and treat the k-space only. This can be advantageous in different aspects, especially with the current progress in the development of efficient FFT-based methods. Nonetheless, we are not aware of any present application of a similar technique.

3.9 Conclusions

In the present Chapter, we have applied the Ewald summation method to $1/|\boldsymbol{r}|^k$ polytropic potentials in three-, two- and one-dimensional geometries in a simulation box with periodic boundary conditions. We have found the explicit functional forms for all the components of the sums in both real and momentum spaces, with special attention being paid to the cases of long-range interactions, that is conditionally convergent or divergent potentials (corresponding to $k < D$, with D standing for the dimensionality), "marginal" interactions ($k = D$), and short-range interactions (with $k > D$). For the latter case of short-range interaction potentials, where in principle a straightforward summation of the initial sum (3.1) is possible, the Ewald method is shown to be useful, as it yields the faster (Gaussian) convergence rate. A condition of charge neutrality of the simulation cell is stated to be necessary for conditionally convergent and divergent potentials; a homogeneous positive charge background ("jellium" model) is introduced as the most relevant and frequently used kind of neutralization. The conditionality of the convergence for a charge-neutral system, governed by the Coulomb interaction, is discussed with a justification of the use of a specific periodicity-preserving convergence factor. The derivation technique, presented in our work, is consistent with the arguments of de Leeuw *et al.* [dLPS80].

The results are first presented for the case of a 3D system in a cubic simulation box in order to explain the general mathematical procedure, which for the specific case of the Coulomb potential recovers well-known results [AT89]. Later on, the same mathematical technique is applied to 2D and 1D geometries. For the one-dimensional case the initial sum for the potential energy is explicitly evaluated (3.96), nonetheless the Ewald summation is developed for this case too and may be used as a mathematical equality. The special representations of the reciprocal space sums, linear in the number of particles N and hence more efficient in actual modeling, are presented for 3D and 2D systems. The explicit expressions for the terms of the Ewald sums are given in a tabular form for physically relevant potentials with small integer power indexes k, as dipole-dipole interaction potential, Lennard-Jones potential and others in both three- and two-dimensional geometries (see Tables 1 and 2).

When the simulation box cannot be chosen cubic, for example in a modeling of a three-dimensional hcp crystal structure, the Ewald method can also be applicable after a certain modifications. Formally, it consists in the choice of an appropriate rectangular simulation box and a substitution of the vector $\boldsymbol{n}$ by $\boldsymbol{n}_r = (\boldsymbol{n}_x L_x + \boldsymbol{n}_y L_y + \boldsymbol{n}_z L_z)/L_0$ and $\boldsymbol{m}_k = (\boldsymbol{m}_x/L_x + \boldsymbol{m}_y/L_y + \boldsymbol{m}_z/L_z)L_0$ in the real and momentum space sums, respectively [see (3.102) and (3.103)].

The optimization of the involved parameters, that is cut-off numbers in both sums and the integration parameter α, is a necessary operation in order to improve the convergence rates and avoid excessive calculations. The main idea of the optimization, proposed in the present work, is to perform a benchmark calculation, minimizing the variance of the result. A particular example of the application of the technique is presented for a calculation of the potential energy of a two-dimensional gas of dipoles, aligned perpendicular to the plane of motion. This practical optimization technique is thought to be efficient for stationary and nearly uniform systems that appear, for instance, in Monte Carlo simulations. In spite of being very simple, it allows to find rather quickly adequate parameter ranges. The analytical estimations of the parameters are given as well and are proven to be consistent with the results, obtained in our method. A more sophisticated method to optimize the calculation parameters, taking advantage of the $\mathcal{O}(N)$ representation of the Fourier transform sum, is also presented with explicit estimations of the parameters for a typical system simulated by Quantum Monte Carlo methods.

Chapter 4

Phase diagram of a Yukawa system

4.1 Introduction

Recent advances in trapping and controlling ultracold dilute gases have permitted to realize highly tunable and extremely pure Fermi systems [DGPS99, GPS08]. This has provided new insight in the study of fundamental problems in condensed matter physics. For example, the original BCS theory [BCS57] was developed to explain superconductivity in metals, where the control over interactions and densities is very limited. However, in recent experiments with ultracold Fermi gases in the BCS-BEC crossover the strength of the interactions is controlled by external magnetic fields in the vicinity of a Feshbach resonance, while the geometry is tuned by means of magnetic or optical confinement. This has allowed, for instance, to measure the equation of state in the BCS-BEC crossover in high precision experiments [NNCS10, KSCZ12]. Numerically, the best calculation of the zero-temperature equation of state is obtained in quantum Monte Carlo simulations [CCPS03, CPCS04, ABCG04, FGG11, CGSZ11]

After the big success achieved with single species there is nowadays a growing interest in fermionic mixtures. Quite recently, fermionic mixtures consisting of atoms with different masses have been realized experimentally [TVA+08, IKH+11] and studied theoretically [GGSC09, BRS09, BD10]. Novel physical phenomena like Efimov states [Pet03, HHP10, LP11, YZZ11, WLvSE12], trimer and cluster formation might be observed [KMW+06, KFM+09, ZDD+09, BWR+09, WHH+09, WLO+09, KFB+09, NHM+10] in these systems. The case of large mass imbalance is especially interesting, and mixtures of ^{6}Li and ^{40}K are being investigated experimentally [TVA+08, WSK+08, VTC+09, STN+09, TGL+10, CBV+10, TKZ+11, RCS+11]. Even larger mass ratios are reached in mixtures of ^{6}Li and ^{173}Yb [IKH+11, HTY+11]. In this chapter we present results for the phase diagram of Fermi mixtures as a function of the mass ratio using quantum Monte Carlo methods and determine how crystallization of this system can be realized.

From the theoretical point of view, it was proposed in Ref. [PAP+07] that an effective Yukawa interaction, induced between heavy-light pairs of fermions, might lead to crystallization in quasi-two-dimensional systems. In this work we extend that discussion and analyze the possibility of realizing a gas-crystal phase transition at zero temperature in three-dimensional systems. We obtain the phase diagram and discuss how large mass ratios have to be for reaching crystallization.

The interest in the phase diagram of quantum Yukawa particles is rather old as the Yukawa potential has long been used, for instance, as a model for neutron matter [BP75,

Kaw81]. The Yukawa potential also describes interactions in dusty plasmas where charged dust particles are surrounded by plasma which introduces screening [HFD96, HFD97, SA11]. The Yukawa potential is often used as well as a model for suspensions of charged colloidal particles [KRG86, RKG88, RT87, MF91, HHBN11, GNP12]. The classical finite temperature phase diagram has been extensively studied [HFD96, HFD97, SA11, KRG86, RKG88, RT87, MF91, HHBN11, GNP12] while much less is known about the full quantum phase diagram.

In the 70's, Ceperley and collaborators [CCK76, CCK78] used the diffusion Monte Carlo algorithm to estimate the zero-temperature phase diagram of the Yukawa Bose fluid. In their work the phase diagram was built assuming that the Lindemann ratio remains constant along the solid-gas coexistence curve, with the explicit value being evaluated only at a single point. In the present Chapter we carry out a full study of the transition curve and present the phase diagram in terms of experimentally relevant densities and mass ratios of heavy to light fermions. The Lindemann criterion prediction has turned out to be quite precise apart from the region of high densities.

4.2 Model Hamiltonian

Mixtures of fermions with different masses have been realized recently in a new generation of experiments [TVA+08, WSK+08, VTC+09, STN+09, TGL+10, CBV+10, TKZ+11, RCS+11, IKH+11, HTY+11]. The interactions can be tuned to allow the formation of two-component molecules. The s-wave interactions within a single component are prohibited due to Pauli principle. Yet, an effective interaction between same-spin fermions can be induced by the presence of the other component. The limit of large mass ratio has been analytically addressed in Ref. [PAP+07]. The effective interaction between heavy particles, which was obtained in the limit of large distances within first Born approximation, has the form of a screened Coulomb (Yukawa) potential. This leads to a description of the system in terms of a composite (molecular) bosonic gas interacting with an effective potential.

We study a system of heavy fermions of mass M interacting among themselves and moving on a background of light fermions of mass m. The net effect induced by the movement of the light fermions can be characterized by a Yukawa potential, leading to the following effective Hamiltonian [PAP+07] describing the interaction between composite bosons formed by pairs of heavy and light atoms

$$\hat{H} = -\frac{\hbar^2}{2M}\sum_i \Delta_i + \sum_{i<j} \frac{2\hbar^2}{m} \frac{\exp(-2|\mathbf{r}_i - \mathbf{r}_j|/a)}{a|\mathbf{r}_i - \mathbf{r}_j|}, \tag{4.1}$$

where a is the atom-atom s-wave scattering length between two atomic species and $\mathbf{r}_i$ are positions of heavy atoms while the positions of light atoms have been integrated out. The ground-state properties of the system are then governed by two dimensionless parameters, namely the gas parameter na^3 and the mass ratio M/m. Equivalently, Hamiltonian (4.1) describes a bosonic system interacting via the screened Coulomb potential

$V_{\text{int}}(r) = q\exp(-\lambda r)/r$ by mapping the charge to $q = 2\hbar^2/ma$ and the screening length to $\lambda^{-1} = a/2$.

We calculate the ground-state properties corresponding to the Hamiltonian (4.1) by means of the diffusion Monte Carlo (DMC) algorithm [BCN94]. This method solves stochastically the Schrödinger equation in imaginary time providing the exact energy within controllable statistical errors. The coexistence curves can then be traced by direct comparison of the energies of the solid and gas phases. The efficiency of the DMC method is greatly enhanced when importance sampling is used. This is done by multiplying the (unknown) ground-state wave function $\psi(\mathbf{r}_1, \ldots, \mathbf{r}_N)$ by a guiding wave function $\psi_T(\mathbf{r}_1, \ldots, \mathbf{r}_N)$ and solving the equivalent Schrödinger equation for the product. As a result, the points in phase space where the guiding function is large get sampled more frequently and this improves convergence to the ground state (see Section 2 of this Thesis).

The properties of the gas phase are studied by constructing the guiding function in a Jastrow two-body product form $\psi_T(\mathbf{r}_1, \ldots, \mathbf{r}_N) = \prod_{i<j} f_2(|\mathbf{r}_i - \mathbf{r}_j|)$. We determine the optimal two-body Jastrow term $f_2(r)$ by solving the corresponding Euler–Lagrange hypernetted-chain equations [Kro98] (HNC/EL), discussed previously in Section 2.4.3.4, discarding the contribution of the elementary diagrams. The resulting wave function captures basic ingredients coming both from the two- and many-body physics of the problem. On the other hand, the energy of the solid phase is obtained by using a Nosanow-Jastrow guiding wave function $\psi_T(\mathbf{r}_1, \ldots, \mathbf{r}_N) = \prod_{i=1}^{N} f_1(\mathbf{r}_i - \mathbf{r}_i^{\text{latt.}}) \prod_{i<j} f_2(|\mathbf{r}_i - \mathbf{r}_j|)$ with Gaussian one-body terms $f_1(\mathbf{r}_i - \mathbf{r}_i^{\text{latt.}}) = \exp(-\alpha(\mathbf{r} - \mathbf{r}_i^{\text{latt.}})^2)$ describing the localization of particles close to the lattice sites $\mathbf{r}_i^{\text{latt.}}$. The parameter α controls the localization strength and is optimized by minimizing the variational energy.

In order to find the energy in the thermodynamic limit, we carry out simulations of a system of N particles in a box with periodic boundary conditions, and take the limit $N \to \infty$ while keeping the density fixed. In the simulation of the crystal the number of particles should be commensurate with the box which restricts the allowed number of particles. For fcc packing the simulation box supports $N = 4i^3 = 4, 32, 108, 256, \ldots$. In order to add more values we also use periodic boundary conditions on a truncated octahedron (see Appendix B), which allows simulations with $N = 2i^3 = 2, 16, 54, 128, 250, 432, \ldots$ particles with a larger effective volume of the simulation box and reduced anisotropy effects. Finally, the convergence is further improved by the Ewald summation technique [Ewa21, OAB12] in the cubic box, which we use in the calculations at large densities.

In Fig. 4.1 we show two characteristic examples of the finite-size dependence of the energy at two different densities. For large enough system sizes, the energy is well fitted by a linear dependence in $1/N$. For small number of particles the behavior is no longer linear, especially at large densities due to strong interparticle correlations. We find that system sizes of $N > 100$ have to be used in order to ensure the linear regime at considered densities. The thermodynamic energy is then obtained as a result of a linear extrapolation $1/N \to 0$.

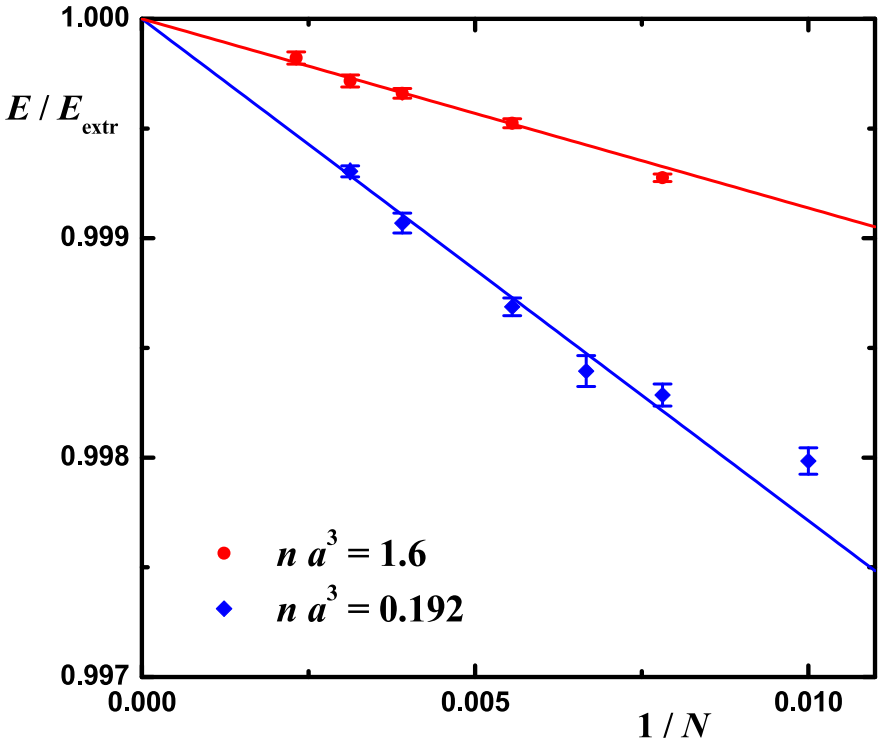

Figure 4.1: An example of finite-size dependence of the energy in the gas with periodic boundary conditions in truncated octahedron for $M/m = 187$ at two different densities $na^3 = 1.6$ (upper set of data points) and $na^3 = 0.192$ (lower set of data points). Symbols, DMC energy; lines, linear fit to energy for large system sizes. Energies are scaled with the thermodynamic value E_{extr}, obtained in $1/N \to 0$ extrapolation.

.

4.3 Phase diagram

An intrinsic property of Coulomb particles is to self-assemble into a Wigner crystal at low densities and to remain in a gaseous phase in the opposite limit, due to the long-range character of the interaction [Wig34]. The Yukawa potential is similar to the Coulomb one at densities large enough for the interparticle distance to be much smaller than the screening length, which is fixed by the s-wave scattering length a between two different species of atoms. One then concludes that the Yukawa system stays in a gaseous phase at large densities. In the opposite regime of small densities, $na^3 \ll 1$, the interaction potential decays exponentially fast showing a short-range behavior that leads the system to a gaseous phase. For example, the fcc crystal of hard-sphere bosons of diameter a_s melts at density $na_s^3 \approx 0.24$ [HLS71, KLV74, DNRA90]. The intermediate regime $na^3 \approx 1$ is the most interesting one, as crystallization may or may not take place depending on the strength of the interaction, which in the current case of the Hamiltonian in Eq. (4.1) is governed by the mass ratio M/m. A relevant question then is what is the minimal mass ratio at which crystallization can be observed.

In order to obtain an accurate description of the phase diagram, we study the finite size dependence and extrapolate the energy to the thermodynamic limit. As we mentioned in the sections, devoted to the methodology, the diffusion Monte Carlo method is also generally biased by the average size of the population of walkers N_w (sets of N_p particle configurations), that can be controlled in the simulation. In practice the results of different calculations converge to a stable value, when N_w is large enough, although the convergence can be achieved with much less N_w with a better trial wave. Usually the population of walkers, when the convergence is reached, is between 250 and 500 and is not affected much by the size of a system, therefore a preliminary simulation can be carried out fast with a small number of particles. Figure (4.2) demonstrates the analysis of N_w convergence for the Yukawa system of 64 particles in a liquid phase (no size correction added). The convergence is seen to be reached for $N_w \approx 200$.

Throughout all the DMC simulations that we run we use the second-order in time step approximation of the Green's function of the Hamiltonian, which means that the time step bias in the results is also $\mathcal{O}(\tau^2)$. This dependence can be observed by performing a set of trial calculations in order to find a value of $\Delta\tau$, when the time-related error complies with our accuracy goal. In Figure (4.3) we plotted the energy per particle versus time step and extrapolated the data to 0 by a parabola. Here we can suggest that the acceptable time step is approximately 1000 (the required accuracy level is around the statistical noise for each single calculation).

The resulting energies of the gas and solid phases are then analyzed using the double-tangent Maxwell construction which provides the melting and freezing densities. The zero-temperature phase diagram parameterized in terms of the dimensionless density na^3 and the mass ratio, is shown in Fig. 4.4. We find that for mass ratios smaller than the critical value $M/m \approx 180$ the gas phase is energetically preferable at any density. On the

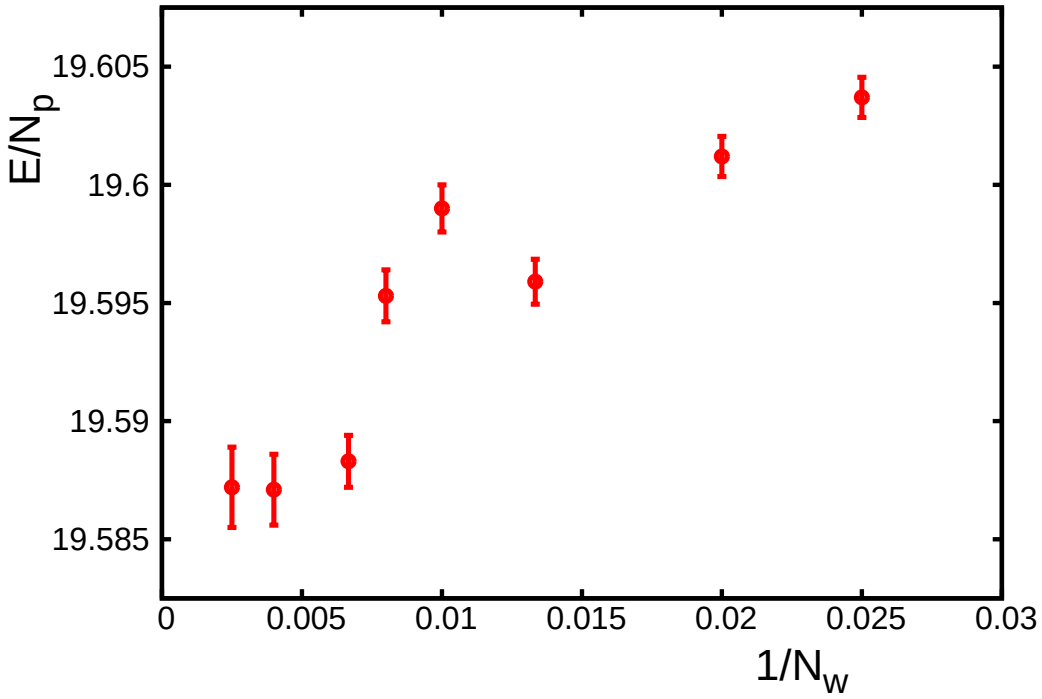

Figure 4.2: Dependence of the energy per particle E/N_p on the inverse number of walkers $1/N_w$ for the Yukawa system in a liquid phase, 64 particles.

other hand, for larger mass ratios there is always a gas-solid transition at low densities and a solid-gas transition at large ones. Energetically, both the fcc and bcc lattices are possible in the solid phase. It is very difficult to discern numerically which packing is preferred as the energies in different crystalline phases are extremely close. Still, in the large potential energy limit, corresponding to a mass ratio $M/m \gg 1$, it is enough to compare the potential energy of the classical crystals with different packings. A simple, geometrical construction assuming that particles are tightly tied to their equilibrium positions leads to a transition density $na^3 \approx 1.58$. This prediction is depicted as a blue dashed line in Fig. 4.4. In the low-density limit we numerically find the value of the s-wave scattering length a_s of the Yukawa potential (4.1) and fit it as $a_s/a = 0.436\ln(M/m)$ with accuracy below 1% in the region of interest. Note that a is the s-wave scattering length of fermionic particles which lead to the effective bosonic Hamiltonian (4.1) while a_s is the s-wave scattering length between bosonic Yukawa particles. For the sake of comparison we also plot in Fig. 4.4 the gas-solid transition line of hard spheres of size a_s given by $M/m = \exp(1.424/(n^{1/3}a))$.

The figure also shows the results of Ceperley *et al.* [CCK76, CCK78] which were obtained by doing DMC calculations for three characteristic points in the phase diagram close to the solid-gas transition line. Overall, the agreement between that prediction and our results is good, the main differences affecting the region of large density where Coulomb effects are strong. To our best knowledge this is the first time that the high-density quantum

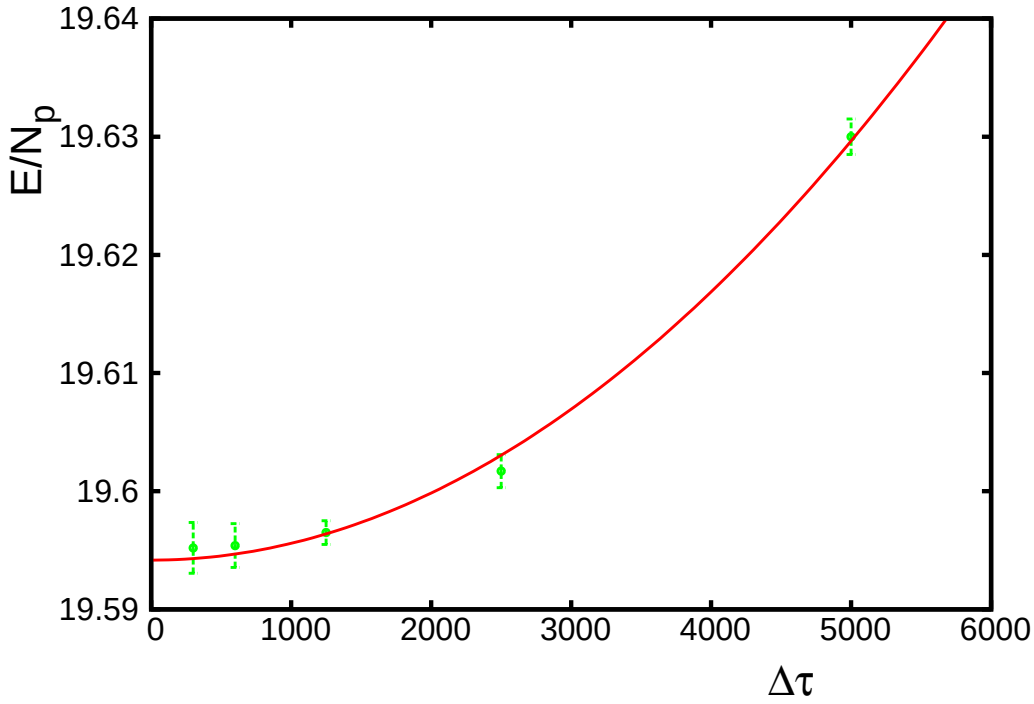

Figure 4.3: Energy per particle E/N_p (green points with errorbars) versus the time step $\Delta\tau$ for the Yukawa system in a liquid phase, 64 particles; red solid line for a quadratic fit. Energy units are $E_1 = \hbar^2/ma^2$, time units are $\hbar/E_1 \cdot 10^{-6}$.

solid-gas phase transition is observed in a simulation of Yukawa systems.

In the case of the fermionic molecules, the resulting critical mass ratio is much larger than $M/m \approx 13.6$ for which the system is unstable due to formation of Efimov states [Pet03, HHP10, LP11, YZZ11, WLvSE12]. The obtained phase diagram describes properties of metastable fermionic molecules while the true ground state corresponds to a many-body bound state. The stronger the effective interaction is (that is, the larger the mass ratio), the more distant are heavy fermions and the smaller the overlap with localized Efimov states is.

4.4 Large mass ratios

According to our results, the minimal mass ratio for which the crystalline phase can exist is $M/m \approx 180$ and it is achieved at the somewhat large value of the gas parameter $na^3 \approx 0.3$. At these densities the fermionic nature of the molecules becomes important as the Hamiltonian (2.65) is derived under the assumption that $na^3 \lesssim 1/8$ [PAP+07]. Our bosonic model is expected to be reliable at smaller densities where the critical mass ratio is further increased.

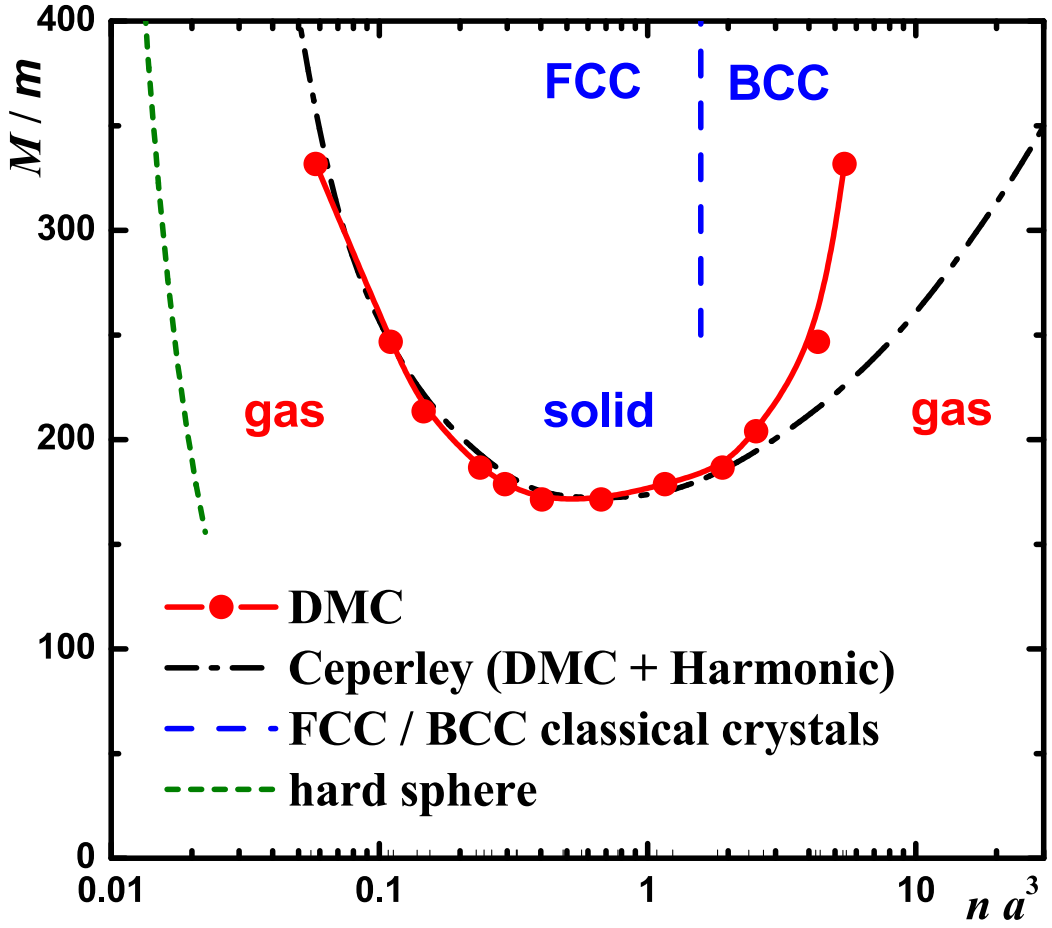

Figure 4.4: Zero-temperature phase diagram of the Yukawa potential corresponding to the Hamiltonian in Eq. (4.1) in terms of the gas parameter na^3 and the mass ratio M/m. Red symbols: transition point as obtained from the double-tangent Maxwell construction applied to the Monte Carlo data energies extrapolated to the thermodynamic limit; dashed line: critical density $na^3 = 1.58\ldots$ at which the energy of perfect fcc and bcc packings are equal; dash-dotted line: prediction of Ceperley *et al.* [CCK76, CCK78] obtained by imposing a constant Lindemann ratio; short-dashed line: $na_s^3 = 0.24$ [HLS71, KLV74, DNRA90].

The mixtures of different fermionic atoms have already been successfully realized in experiments [IKH+11, HTY+11] but at significantly smaller mass ratios. Probably, the largest directly achievable mass ratio currently is that of Yb and Li atoms, $M/m = 29$, which is still much smaller than the critical mass ratio needed to observe the formation of an ultracold crystal.

An alternative way to realize a fermionic mixture with a large and variable mass ratio is to confine one of the components to an optical lattice. At low filling fraction the distances between atoms are large compared with the lattice spacing, and the separation of length scales allows the description of the movement of a particle in the lattice as that of a quasiparticle with an effective mass moving in a medium where the lattice is absent. In a deep lattice interactions between particles are much weaker than the confining energy and so, to a first approximation, one can consider that as the problem of a single particle diffusing in the lattice.

An optical lattice created by counter-propagating laser beams imposes an external potential $V_{\text{latt.}}(x, y, z) = V_0 \left(\sin^2 kx + \sin^2 ky + \sin^2 kz\right)$ on every particle. The diffusion of a particle over a large distance is then governed by the tunneling rate between neighboring sites. The diffusion is largely suppressed (and the effective mass greatly increased) when the amplitude of the optical lattice is large, i.e. when $V_0 \gg E_r$ with $E_r = \hbar^2 k^2/2m$ the recoil energy. The excitation spectrum in the lowest band can be described by Bloch waves of quasi-momentum $\mathbf{q}$ and energy $\varepsilon_0(\mathbf{q}) = \frac{3}{2}\hbar\omega_0 - 2J\left(\cos q_x d + \cos q_y d + \cos q_z d\right) + \ldots$ with $d = \pi/k$ the lattice constant [BDZ08]. At small momenta the spectrum is quadratic in q and can be interpreted as the spectrum $\varepsilon_0(q) = E_0 + \hbar^2 q^2/2m^*$ of a free quasiparticle with an effective mass m^*. Within the lowest band approximation the effective mass is inversely proportional to the hopping parameter J,

$$\frac{m^*}{m} = \frac{1}{\pi^2}\frac{E_r}{J} \,. \tag{4.2}$$

The tunneling is greatly suppressed in the deep optical lattice limit $V_0 \gg E_r$. To better understand the contribution of the tunneling term in the present case, a semiclassical treatment within the Wentzel-Kramers-Brillouin(WKB) approximation can be used to calculate the tunneling probability p. One finds that it is proportional to

$$p \sim J^2 \propto \exp\{-2\int_{x_1}^{x_2} dx\, \sqrt{2m(V(x) - E)}/\hbar\} \,, \tag{4.3}$$

where x_1 and x_2 are the classical turning points. In the deep optical lattice limit one can assume $V(r) - E \approx V(r)$, with x_1 and x_2 corresponding to the positions of two neighboring minima. The resulting integral can be easily evaluated and predicts an exponential form $J \propto \exp(-\sqrt{V_0/E_r})$. A more precise expression can be obtained from the width of the lowest band in the 1D Mathieu-equation [BDZ08], yielding

$$J = \frac{4}{\sqrt{\pi}} E_r \left(\frac{V_0}{E_r}\right)^{3/4} \exp\left\{-2\left(\frac{V_0}{E_r}\right)^{1/2}\right\} \,. \tag{4.4}$$

This expression, together with Eq. (4.2), provides an analytic approximation for the effective mass m^*.

In order to determine the dependence of m^* on the lattice parameters in a non-perturbative way we evaluate the diffusion constant D of a real particle moving on the lattice and compare it to the diffusion constant $D_0 = \hbar^2/2m^*$ of a free quasiparticle of effective mass m^*. The diffusion constant is obtained by means of DMC propagation in imaginary time by measuring the mean-square displacement $\langle(\mathbf{r}(\tau) - \mathbf{r}(0))^2\rangle = \langle(x(\tau) - x(0))^2\rangle + \langle(y(\tau) - y(0))^2\rangle + \langle(z(\tau) - z(0))^2\rangle$ where $\mathbf{r} = (x, y, z)$ denote particle coordinates. The diffusion constant is then extracted as $D = \lim_{\tau\to\infty} \hbar\langle(\mathbf{r}(\tau) - \mathbf{r}(0))^2\rangle/(2\tau d)$, where $d = 3$ is the system dimensionality. The resulting dependence of m^* on the lattice amplitude is shown in Fig. 4.5. The figure shows the Monte Carlo prediction (solid line) compared with the approximation of Eq. (4.2) with J taken from Ref. [BDZ08] (circles) and from Eq. (4.4) (dashed line). As it can be seen, there is an almost constant shift between m^* obtained in the Monte Carlo simulation and Ref. [BDZ08] compared to Eqs. (4.2-4.4). We have found that the description in the relevant region of interest is very much improved by subtracting a constant shift $E^{(1)} = -3/4E_r$ from V_0 in the argument of Eq. (4.4). This last prediction is shown by a thin line in Fig. 4.5 and provides a good approximation for $V_0 \gtrsim 10E_r$.

One can understand these results in the following way: in the absence of the optical lattice the effective mass and the bare mass coincide, so $m^* = m$. As the amplitude V_0 of the lattice is increased, the particle movement is slowed down and the effective mass increases. In the deep optical lattice limit the effective mass grows as $m^*/m \propto \exp(\sqrt{V_0/E_r})$ and so the ratio can be made arbitrarily large by increasing the amplitude V_0 (for instance $m^*/m \sim 1000$ at $V_0/E_r = 40$; see the inset in Fig. 4.5). This mechanism allows for increasing the mass of one of the two components while keeping the other one unaltered, so that the ratio M/m of the fermionic mixture can be made as large as desired when the mass of the heavy component is identified with the effective mass m^*. Consequently, and according to the phase diagram shown in Fig. 4.4, there is a wide range of densities where one could find the system in the crystalline superlattice phase. Heights of optical lattices as large as $(35 - 60)E_r$ are readily achieved in current experiments [WTL+06, TWL+06] and correspond to sufficiently large effective mass ratios for the crystallization to be realized.

Both small density and large density transition lines are accessible for Yukawa interaction caused by screening in dusty plasma, colloids and neutron matter. On the contrary, in two-component Fermi gas only the left part of the phase diagram can be realized since the effective Yukawa interaction is valid only at low densities. In fact, the validity criterion for the interaction potential in Eq. (2.65) was studied in Ref. [PAP+07] and was found to be well satisfied for distances larger then $r \approx 2a$ which leads to the condition $\rho a^3 \lesssim 1/8$ when r is identified with the mean interparticle distance. In this way, for example, for $\rho a^3 = 0.1$ and mass ratio $M/m = 300$ the system is expected to be in a crystalline form. Much larger effective mass ratios can be achieved for realistic [WTL+06, TWL+06] lattice heights of $(35 - 60)E_r$. We thus conclude that by using an optical lattice, a fermionic mixture of

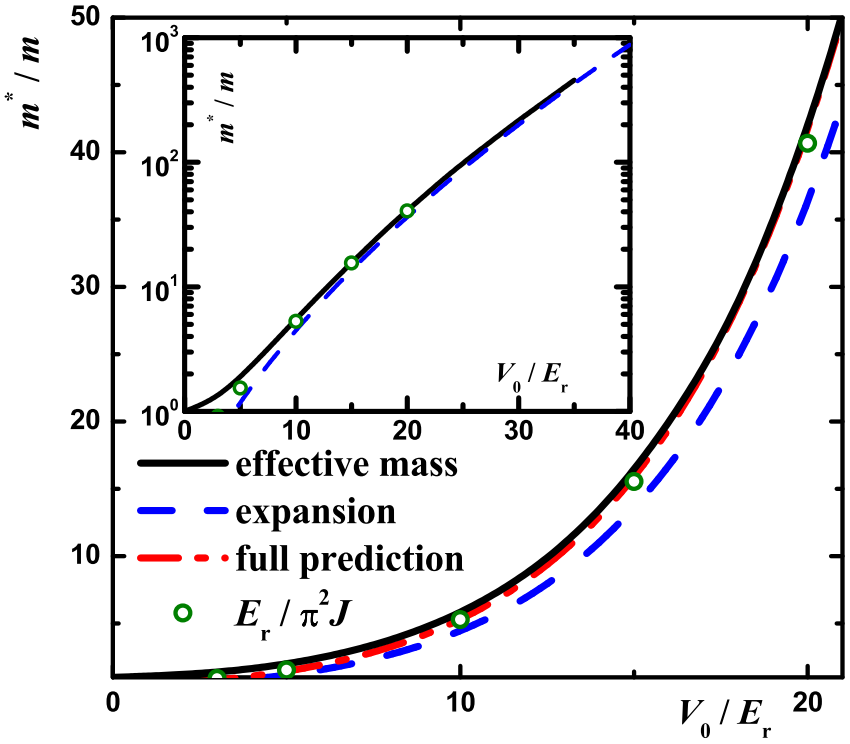

Figure 4.5: Effective mass as a function of the lattice amplitude V_0 in units of the recoil energy E_r. Solid line: results obtained from the diffusion constant evaluated by propagation in imaginary-time; circles: lowest band approximation of Eq. (4.2) with values of J taken from [BDZ08]; dashed line: same results with J from the expansion in Eq. (4.4); dash-dotted line, same expansion with V_0 shifted by $-3/4E_r$. Inset: same results on a semi-logarithmic scale.

very different mass components can be used to test the phase diagram of the equivalent Yukawa model.

4.5 Conclusions

To summarize, in this Chapter we have obtained the zero-temperature phase diagram of bosons interacting through Yukawa forces. We have used a diffusion Monte Carlo simulation starting from a very good approximation to the optimal variational ground-state wave function obtained by solving the corresponding Euler–Lagrange hypernetted chain equations. The resulting phase diagram is very similar to the one originally obtained by Ceperley and collaborators [CCK76, CCK78], although significant differences arise at large densities. The phase diagram shows that any fermionic mixture of pure elements will always be seen in gaseous form, as the mass ratios required for crystallization of weakly

bound fermionic molecules are far beyond the ones that can be achieved in nature. Finally, we investigate an alternative mechanism based on the confinement of one of the species to a deep optical lattice which exponentially increases its effective mass as a function of the confining amplitude. The resulting mass ratio of the mixture created in this way can then be tuned at will and could be used to check experimentally the predicted phase diagram both in the gas and crystal (superlattice) phases.

Chapter 5

Phase diagram of Rydberg atoms

5.1 Introduction

Rydberg atoms have one electron excited to a high energy level. Such atoms exhibit strong and highly tunable interactions which may have an extraordinarily long range. Optically excited from suspended clouds of cold atoms, Rydberg atoms interact both between themselves and with the surrounding unexcited atoms, resulting in a rich behavior of the Rydberg systems.

Due to the strong interactions, a Rydberg atom shifts the levels of nearby atoms sufficiently to prevent their subsequent excitation. A large number of studies deal with a *local* blockade regime. In such a regime a Rydberg atom blocks excitations in its vicinity, and the atomic clouds may be injected with well over 10^3 Rydberg excitations before the existing excitations block any further ones [HRB+07, TFS+04, SRLA+04]. Unfortunately, the arrangement of the excited atoms in such experiments is not directly accessible and has been a subject of intense investigation. Understanding the ordering of Rydberg atoms may be important for interpretation of the experimental results, for example for the antiblockade effect predicted in [APPR07]. It was also suggested that a spatially ordered state may allow for a better control over quantum states in such experiments [PDL10]. Finally, there is an exciting possibility of observing phase transitions in these versatile systems, especially to states with long-range ordering [WLPB08, LWK+09].

Quantum many-body treatments attempting modelling of realistic Rydberg systems have been developed in the past [TFS+04, RH05, APPR07, SC10, PDL10, YRP+09], and were successful in reproducing a number of important experimental features [TFS+04, YRP+09, LWK+09, AGHW10, SGH+10]. Due to complexity, it is often difficult to consider long-range order with such calculations. Nonetheless, strong short-range spatial correlations between Rydberg atoms were obtained in the calculations of Refs. [RH05, AGHW10, SC10], as the atoms avoid each other due to the blockade. Successful observation of the antiblockade effect was also a demonstration of a creation of the strong short-range correlations [AGHW10]. Possibility of long-range ordering (crystallization) of Rydberg atoms was recently predicted for systems coupled to specially selected chirped laser pulses [PDL10, vBSvL+11]. Ordering was also considered, and crystalline phase found, in theoretical calculations of both one and two-dimensional optical lattices [SLMD10, WB10, JAL11, SPG11]. Remarkable non-commensurate crystalline phases in optical lattices emerged in Ref. [WB10].

Given the complex nature of the interactions in the Rydberg systems, it is important to know how much of the behavior of large assemblies of Rydberg atoms stems directly from the pair potential of the interaction between the atoms. For this reason we aim to study ordering in the simplest model of the Rydberg systems. Because of the large number of Rydberg-excited atoms in the experiments, we consider the thermodynamic limit. While the results are established in the thermodynamic equilibrium, many present experiments with Rydberg atoms are too short to reach equilibrium. Thus comparison in such cases must be made cautiously.

5.2 Model and methods

The dominant interactions in the Rydberg systems are usually the Förster-resonant dipole-dipole interactions between the excited atoms. It was shown by Walker and Saffman [WS05, WS08] that, given a pair of Rydberg atoms in the same state, the interaction will not have zeroes as a result of the hyperfine structure or alignment of the atoms only if the resonant coupling is from the s to p states. Furthermore, interactions in the $s+s \to p+p$ channels depend only weakly on the hyperfine structure of the p states, resulting in a nearly isotropic interaction, to within 10^{-2}. This perhaps in part motivates the use of the ns Rydberg states in current experiments [HRB+07, HRB+08, LWK+09, SGH+10]. Neglecting the hyperfine structure, the interaction for this resonance is isotropic and its matrix element is given in terms of the Förster defect δ as [WS05]

$$V(r) = \frac{\delta}{2} - \operatorname{sign}(\delta)\sqrt{\left(\frac{C_3}{r^3}\right)^2 + \frac{\delta^2}{4}}, \tag{5.1}$$

which changes from $V = C_3/r^3$ to van der Waals' $V = C_6/r^6$ (with $C_6 = -C_3^2/\delta$) for distances much larger than the crossover $R_{3\to 6} \sim (-C_6/\delta)^{1/6}$. In the case of a strong local blockade, the blockade radius is often larger than the crossover distance. In such a case, the excited atoms are more likely to be found at distances where the interaction is already of the van der Waals type.

The above arguments motivate the repulsive van der Waals model for the Rydberg atoms in the local blockade regime. We disregard any energy transfer or interactions with the underlying gas of the ground-state atoms, and particles are treated as spinless bosons in three-dimensional space with the many-body Hamiltonian

$$\mathcal{H} = -\frac{\hbar^2}{2m}\sum_i \nabla_i^2 + \sum_{i<j} \frac{C_6}{|\boldsymbol{r}_i - \boldsymbol{r}_j|^6}. \tag{5.2}$$

Defining the reduced units of length and energy as

$$r_0 = \left(\frac{mC_6}{\hbar^2}\right)^{\frac{1}{4}}, \quad E_0 = \frac{\hbar^3}{m^{3/2}C_6^{1/2}} \tag{5.3}$$

allows to describe the properties of this model universally in terms of just two parameters, the dimensionless density ρr_0^3 and temperature $k_B T/E_0$. The units are selected to satisfy $E_0 = \hbar^2/mr_0^2 = C_6/r_0^6$. The mass m in Eq. (5.3) is the mass of the atom.

It is important to establish the applicability of the bulk phase diagram to finite systems. For a cloud of size R and number density ρ, the tail potential energy per particle can be estimated as $\rho C_6/R^3$. In order for the phase transition to occur at the same parameters in the limited system as in a bulk one, it is sufficient that the missing potential energy is much smaller than the kinetic energy. In the case $Tk_B \gg E_0$, this reduces to $R \gg \sqrt[3]{\rho C_6/Tk_B}$. When $Tk_B \ll E_0$, kinetic energy is estimated as $\hbar^2\rho^{2/3}/m$ and thus $R \gg r_0(\rho r_0^3)^{1/9}$.

5.3 Results for the phase diagram

The phase diagram of the model includes a solid at high densities and, at lower densities, a gas phase that Bose-condenses at sufficiently low temperatures [OAL+11]. To locate these phase regions, we employed a number of methods, each suitable in a certain area of the phase diagram. At zero temperature, the model was treated with the diffusion Monte Carlo (DMC), a projector method which provides an exact ground-state energy for bosonic systems (see Section 2 of this Thesis). DMC has been used successfully in the past to calculate the equations of state and locate quantum phase transitions for a variety of systems. Transitions at non-zero temperature were studied with path integral Monte Carlo (PIMC) [Gil90, Cha97, Cep95, SCB09], a first principles method which allows to compute the averages of quantum operators by summing over the quantum partition function of the system. Both DMC and PIMC methods allow to treat systems with several hundred particles under periodic boundary conditions, with thermodynamic limits obtained by a suitable extrapolation. Additionally, classical limits were established with classical Monte Carlo calculations. In two regimes the location of phase transitions could be expressed in a semi-analytical form. In the first case, the transition between superfluid and normal gas was expressed in terms of the scattering length of the potential by means of a known relationship. In the second, the solid-to-gas transition was located at low temperatures with the harmonic theory. The results are summarized in the phase diagram shown in Fig. 5.3.

At sufficiently high density, the atoms are expected to form a crystalline solid. Summing the potential energy of the *perfect* lattice structures, we conclude that the preferred symmetry is fcc. While other structures may be excluded on the energetic grounds, the energy of the hcp structure is very close to that of the fcc. The difference between the perfect crystal energies, $E_{hcp} - E_{fcc} = 2 \times 10^{-4}(\rho r_0^3)^2 E_0$, is small enough to be comparable to or even swamped by the temperature effects in present experiments (for example, in works [TFS+04, HRB+08, SGH+10]). The hcp phase is anticipated to be metastable with respect to the transition to the fcc phase. Zero-point motion and temperature effects are expected to keep the fcc symmetry preferred to hcp. If the dressed interaction [LHL12, HNP10] in

the form $V_{g-g} = 1/(\xi_0^2 + r^6)$ between the ground-state atoms is considered (ξ stands for a blockade radius), the preferable crystal packing can change, as shown in Fig. (5.1).

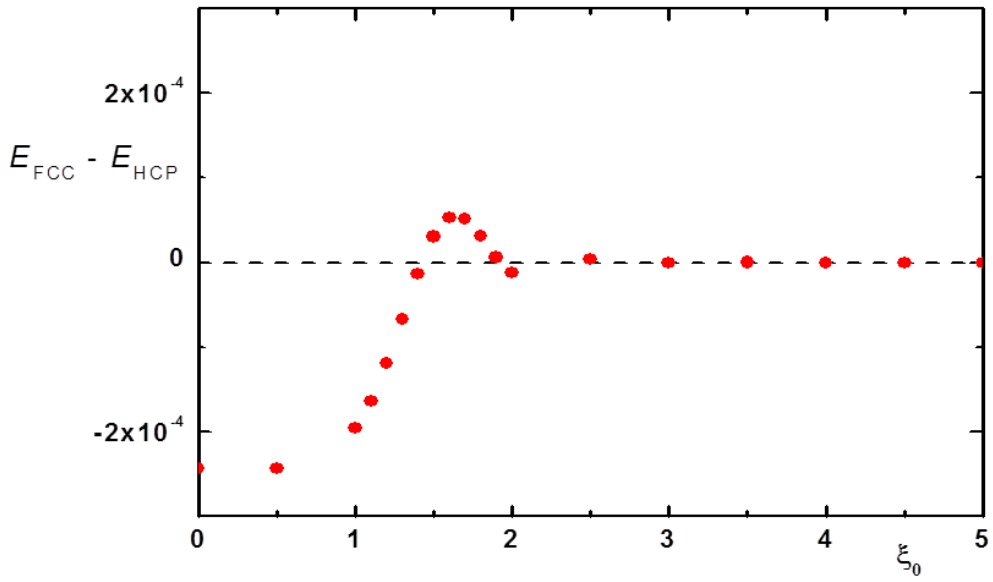

Figure 5.1: Dependence of the difference of the Madelung energies of ideal fcc and hcp crystals in the units of E_0 on blockade radius ξ_0.

In the rest, we assume the system crystallizes in the fcc structure.

Investigation on the zero-temperature line was done with the DMC method [HJR94, BC94]. For importance sampling in the gas phase we used a Jastrow form

$$f_{ij}(r) = \prod_{i<j} \{\exp\left[-1/2(b/r_{ij})^2\right] + \exp\left[-1/2(b/(L-r_{ij}))^2\right]\}\,, \tag{5.4}$$

$r_{ij} < L/2$, for a periodic box of size L. The second power in $1/r$ arises from the cusp condition of the scattering problem with the repulsive $1/r^6$ potential and is also compatible with the presence of long-wavelength phonons [RC67]. The parameter b was variationally optimized beforehand. The Nosanow–Jastrow wave function was used for importance sampling in the solid phase [Nos64, CB08b]. It consists of the product of the above Jastrow term and a site-localizing Nosanow term $\prod_i \exp\left[-(\boldsymbol{r}_i - \boldsymbol{l}_i)^2/2\gamma\right]$, where $\boldsymbol{r}_i$ and $\boldsymbol{l}_i$ denote correspondingly the coordinates of the atoms and lattice sites, and γ is the second optimized parameter (for the detailed discussion see Section 2.4.2). The breaking of exchange symmetry between particles in the solid affects the energy only negligibly [CACB09]. Within the statistical errors of the DMC, results for the energies of the fcc and hcp lattices are indistinguishable and both are lower than the energies derived using bcc configuration.

While the phase transitions are conventionally reported as a function of pressure rather than density, density of the Rydberg atoms is more accessible and controllable experimentally. We therefore choose to express the transition locations in terms of density, even for the first-order solidification transition (in this case one needs to specify the coexistence region). We find that the equations of state for the fcc solid and gas phases cross at the *transition density*

$$\rho_c \, r_0^3 = 3.9 \pm 0.2, \tag{5.5}$$

expressed in the reduced units with the help of Eq. (5.3). The coexistence region of the solid and gas phase at zero temperature, determined using the double-tangent Maxwell construction, is narrow and is in fact smaller than the above error for the transition density (which arises mostly from the extrapolation to the thermodynamic limit; calculations were performed with up to 256 particles). The double-tangent Maxwell construction[1] is a standard procedure to describe the phase transitions. It relies on equality of chemical potentials of two phases at the same pressure in the coexistence region. Alternatively it can be presented as a linear dependence of the Helmholtz free energy A on the volume $V = 1/\rho$ in the coexistence region:

$$\frac{\partial A_1}{\partial V}(V_1) = \frac{A_2 - A_1}{V_2 - V_1} \tag{5.6}$$

and a demand of a constant pressure

$$\frac{\partial A_1}{\partial V}(V_1) = \frac{\partial A_2}{\partial V}(V_2) \tag{5.7}$$

that is equivalent to finding of a common tangent of the equations of two states (at $T = 0$ free energy is equal to the total energy of the system). The Maxwell construction at zero temperature is given in Fig. (5.2). The lines cubic polynomial fits to the Monte Carlo data. The

Although the coexistence region is relatively narrow, its width can be obtained with a satisfactory accuracy. Let us explain how it is done in our case. First of all we need to evaluate the effect of the statistical uncertainty on these results. The Monte Carlo data for the equation of state of the liquid and crystalline phases, with the statistic errors for each point (it is convenient to work with volume $V = 1/\rho$ as an argument), is approximated with a cubic polynomial. On the first step, the value of energy at each point is moved by a random Gaussian shift with the variation, equal to the corresponding statistical error. Then, the coefficients of the optimal polynomial approximations for $E_{\text{liquid}}(V)$ and $E_{\text{solid}}(V)$ are recalculated, and therefore one finds new positions of the melting and crystallization points, the intersection point and the width of the coexistence zone. If this procedure is carried out many times, one can obtain the variance of each of the values. In this case the error is approximately 1.5%. A separate source of the error in the estimation of the width

[1] For a detailed discussion on the topic see, for instance, [Hua05]

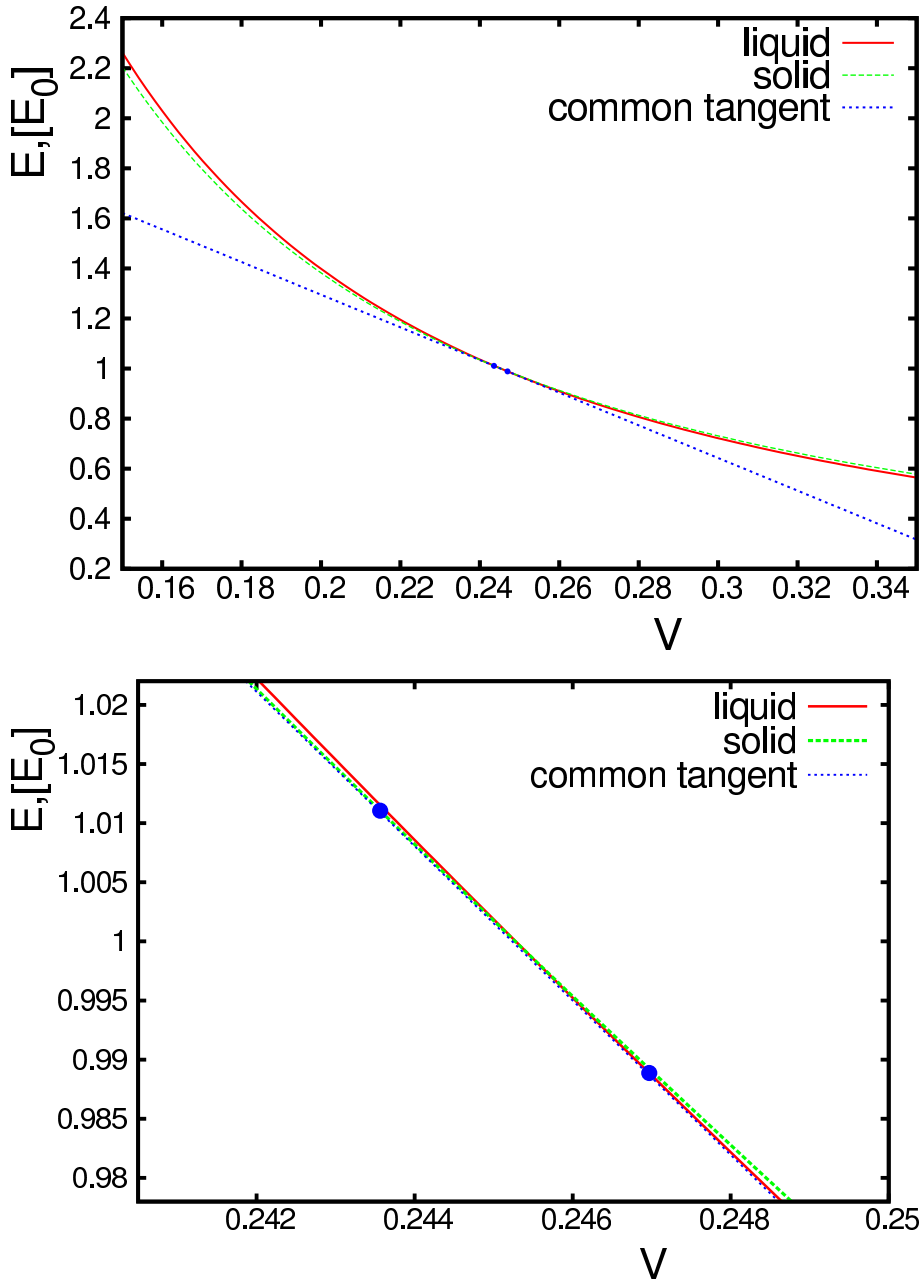

Figure 5.2: Study of double-tangent Maxwell construction. Equations of states $E(V)$ (the volume $V = 1/\rho$, dimensionless) calculated with DMC for the system of 256 particles for liquid (red solid line) and solid (green dashed line) phases of the Rydberg system, normalized by the intersection energy E_0. The common tangent is a blue dotted line, blue circles stand for two tangent points. The upper and lower plots demonstrate the same data with diffenerent ranges of the inverse density.

of the coexistence zone is the finite-size dependence of the results, that may be estimated by extrapolating the data to $N_p \to \infty$. The relative error of this estimation is of the same order, as for the phase transition density, given above, that is $\sim 5\%$. The overall result for the width of the coexistence region can be evaluated as

$$\Delta\rho = 0.056 \pm 0.003\,. \tag{5.8}$$

The transition line between solid and gas phases at small temperatures can be determined with the harmonic theory [AM76], assuming the Lindemann ratio remains unchanged on the transition line. The value of the Lindemann parameter at melting may be extracted from the DMC calculations of the transition density at zero temperature. The resulting low-temperature dependence of the gas-to-solid transition density is given by

$$T_c^{\text{harmonic}} = C\sqrt{(\rho - \rho_c)\, r_0^3}\frac{E_0}{k_\text{B}}, \tag{5.9}$$

where ρ_c is the transition density at zero temperature, Eq. (5.5), and the constant $C = 8.0$ is determined numerically from the dispersion curves of the solid and depends on the interactions and geometry of the fcc lattice.

A quantum solid melts at lower temperatures than the classical one due to the zero-point motion of the atoms. The classical transition was located in the canonical ensemble by Metropolis sampling of the Boltzmann factor. As the potential energy C_6/r^6 is exactly proportional to the square of the density, the transition temperature for the classical system also scales exactly as $T \propto \rho^2$. We find that

$$T_c^{\text{classical}} = 0.22\left(\rho r_0^3\right)^2 \frac{E_0}{k_\text{B}}. \tag{5.10}$$

As expected, such scaling removes the Planck constant from the classical transition temperature, which in fact simplifies to $T_c^{\text{classical}} k_\text{B} = 0.22\rho^2 C_6$.

To fully account for quantum effects, the gas-to-solid transition at $T \neq 0$ was also located with PIMC calculations. We used a decomposition of the action operator that is accurate beyond the fourth order [Chi04]. For details of the method and implementation, see Ref. [SCB09]. The transition was located by observing melting or solidification while working in the canonical ensemble, beginning with configurations of atoms placed on a randomly distorted lattice. Used in this way, the calculations determine a range in which the transition density is located. PIMC results confirm the validity of the harmonic approximation at low temperatures. At higher temperatures the transition density follows the classical melting curve (5.10).

The above results establish the solidification transition of the repulsive van der Waals model. Additionally, the dynamic nature of the Rydberg gas raises a possibility for the spatial ordering to be induced kinetically, as the combination of decay and strong blockade will favor supplanting excitations to be equidistant from their immediate neighbors. We

modelled such a process and observed that replacement of decaying excitations in local blockade regime indeed creates a short-distance order, but not a true long-distance crystalline ordering. These finding are consistent with much more elaborate dynamic models of Refs. [RH05, AGHW10, SC10].

At low temperature, the gas phase of the model is expected to form a Bose–Einstein condensate (BEC). Transition between the BEC and normal gas phases at low densities lies slightly above the ideal Bose gas condensation temperature,

$$T_{\mathrm{BEC}}^{\mathrm{ideal}} = 2\pi \left(\frac{\rho r_0^3}{2.612\ldots} \right)^{2/3} \frac{E_0}{k_{\mathrm{B}}}, \tag{5.11}$$

due to the repulsive interaction between particles [PGP08]. The correction is governed by the scattering length of the potential a_s, which can be found to be equal to $a_s = 2\,\Gamma\left(3/4\right)/\Gamma\left(1/4\right) r_0 = 0.676\ldots r_0$. The transition temperature is then given by $T_{\mathrm{BEC}} = T_{\mathrm{BEC}}^{\mathrm{ideal}} \left(1 + c a_s \rho^{1/3}\right)$, where c is a positive constant of the order of unity (for details, see Ref. [PGP08] and references therein). In the present case this expression is only valid at very low densities (one needs to satisfy at least $\rho r_0^3 < 5 \times 10^{-2}$ to make the description in terms of the zero-momentum scattering length meaningful), where the magnitude of the correction is not significant.

At higher densities the BEC-to-normal gas transition is no longer universal and depends on the form of the potential. We determined the location of this second-order transition with the PIMC method by calculating the superfluid transition from the winding number estimator [PC87b]. The PIMC calculations show that at higher densities the interactions deplete the condensate and the transition temperature is lower than for the ideal Bose gas. Combining the PIMC results, the region in which the triple point is located was determined as $4.5 < T/(E_0/k_{\mathrm{B}}) < 6.5$ and $4 < \rho r_0^3 < 5$, which we consider sufficiently narrow for practical considerations.

5.4 Comparison with experimental conditions

Because the interaction constant C_6 enters the reduced units [Eq. (5.3)], the effective temperature and density can be varied over many orders of magnitude. Most of the present experiments are deeply in the "classical" region of the phase diagram (Fig. 5.3). As an example, we consider the conditions of the experiments presented in Ref. [HRB+08]. For the excitation with 170 ns laser pulses, the system parameters at 4 μK are $T/(E_0/k_{\mathrm{B}}) \approx 33 \times 10^5$ and $\rho r_0^3 \approx 1.9 \times 10^3$, which in fact correspond to the gas phase of the equilibrium phase diagram. For 320 ns excitation pulses and $T = 1$ μK, $T/(E_0/k_{\mathrm{B}}) \approx 8.2 \times 10^5$ and $\rho r_0^3 \approx 7.4 \times 10^3$, well below the gas-to-solid transition. Therefore, the achievable temperature and density are already in the range suitable for investigating the equilibrium phase diagram. Increasing the excitation number increases the interaction constant C_6 and moves the system deeper into the classical regime where the gas and solid phases are

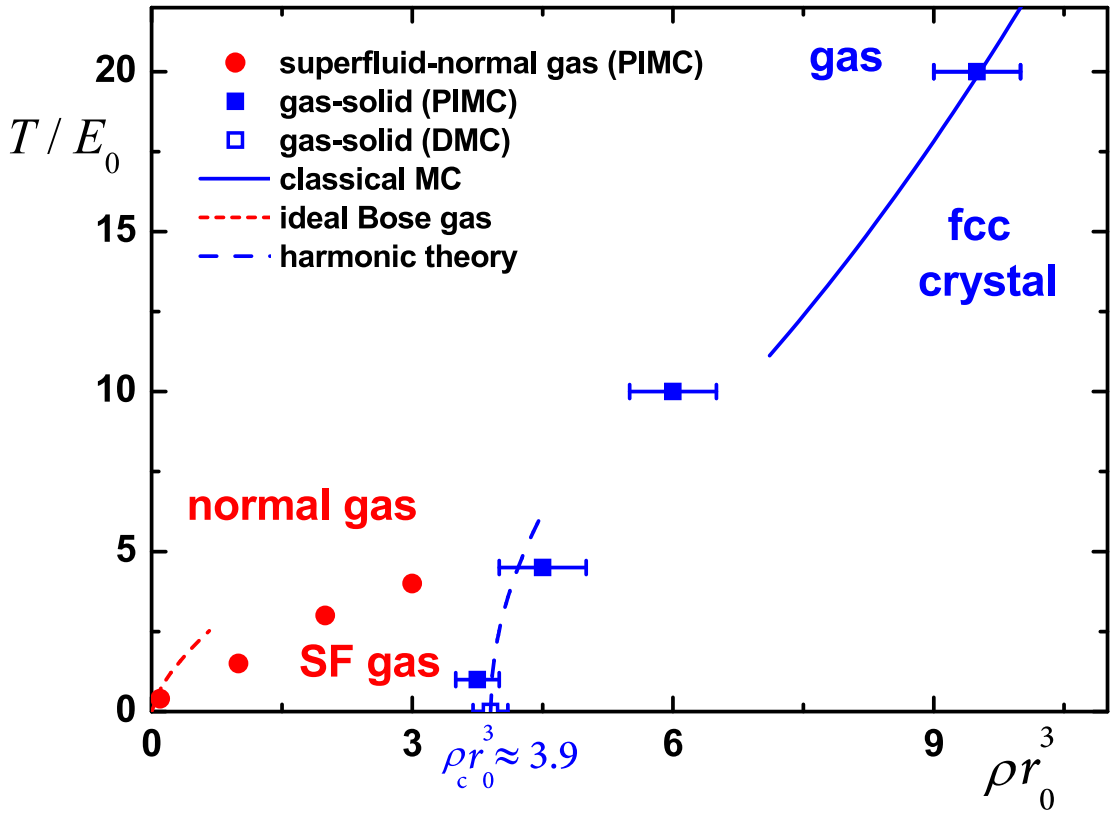

Figure 5.3: Phase diagram of the repulsive C_6/r^6 interaction, scaled to units given in Eq. (5.3). Location of the gas-to-solid transition at zero temperature, determined with DMC, is shown with an open blue square on the $T = 0$ axis. Dashed blue line shows gas-to-solid transition as found with harmonic theory [Eq. (5.9)]. Solid blue line shows classical gas-to-solid transition [Eq. (5.10)]. Solid blue squares show location of the gas-to-solid transition as determined with PIMC. Red short-dashed line marks the Bose–Einstein condensation of the ideal gas [Eq. (5.11)]. Filled red bullets show Bose–Einstein condensation temperatures found with PIMC.

separated by the simple condition of Eq. (5.10). The quantum regime of the phase diagram may be accessed by decreasing the excitation numbers or increasing the Förster defect δ.

Whether Rydberg atoms in actual experiments will reach or even approach an equilibrium phase depends on their lifetime, the experiment's duration and availability of a relaxation mechanisms. Because of the short lifetimes of the Rydberg states, most current experiments are performed on such short timescales as to make the thermal motion negligible. It is therefore said that the experiments are performed with Rydberg excitations of a frozen gas. If the experiments are extended closer to the currently achievable lifetimes of the Rydberg states, which can be as large as 100 μs [vDKH+08, LWK+09], some degree of thermal equilibration will already be achieved. Besides the thermal motion there are, however, at least two other kinds of motion that may need to be considered. The first one is the motion of the excited atoms due to the strong forces between them. The characteristic timescale associated with such a motion is the time that it takes for a Rydberg atom to travel the mean distance between Rydberg atoms. Given the mean distance $\xi \approx \rho^{-1/3}$ and the imbalance force of the order of C_6/ξ^6, this time is given by

$$t_{\text{ballistic}} \sim \sqrt{\frac{m}{C_6 \rho^{8/3}}} \,. \tag{5.12}$$

For a small fixed number of Rydberg excitations time (5.12) decreases rapidly with the excitation number n as $n^{-11/2}$; as the local blockade is reached, $\rho \propto C_6^{-1/2}$, and $t_{\text{ballistic}}$ instead grows as $n^{11/6}$. For example, Rydberg systems created by the 1.970 μs pulses from $1\mu K$ gas in the experiment of Ref. [HRB+08] have $t_{\text{ballistic}} \approx 12$ μs. For the setup of Ref. [LWK+09], $t_{\text{ballistic}} \approx 60$ μs while the clouds could be successfully studied for as long as 20 μs. Collisional ionization and heating could potentially hamper such relaxation [ARLGW07].

5.5 Excitation spectrum of a classical crystal

In the previous parts of this Section the properties of a quantum system comprised of Rydberg atoms at zero and finite temperature were investigated, and the quantum phase diagram was presented.

In the present subsection, we consider a classical system, governed by the van der Waals interaction $1/r^6$ and look for its excitation spectrum in the low temperature regime (or equivalently in the regime of very strong interactions). In accordance with the comparison of classical potential energies of different kinds of crystal lattice, for $T = 0$ we chose the face-centered cubic (fcc) lattice as preferable, with the Madelung energy of the hexagonal close pack (hcp) being only slightly higher. In practice the fcc packing is also advantageous, since its elementary cell is "cubic", and its first Brillouin zone has central, plane and axis symmetry.[1] The first Brillouin zone of fcc formation is known to be a truncated octahedron

[1]The first Brillouin zone is a primitive cell, not reducible to a smaller one by translations of the lattice

with the critical points K,L,U,W,X (see Fig. 5.4).

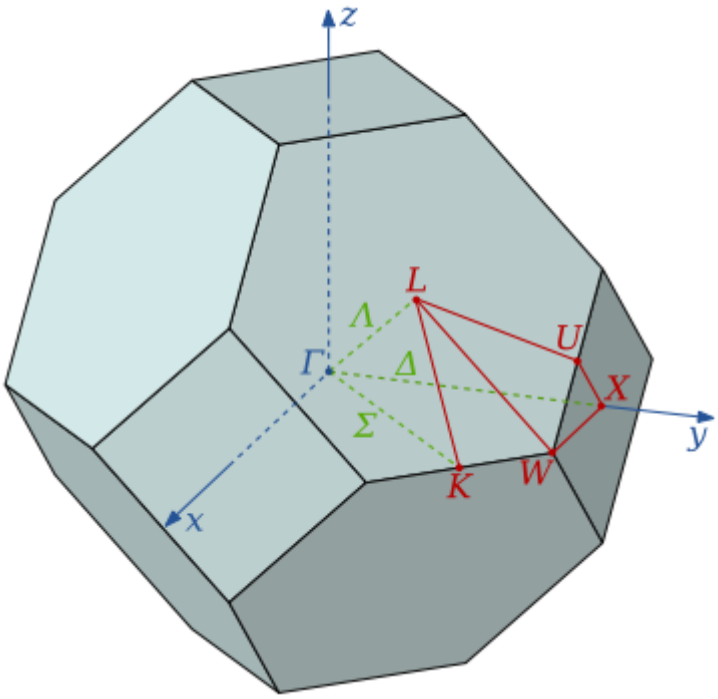

Figure 5.4: Brillouin zone of fcc crystal packing. Figure is taken from Wikipedia webpage *http://en.wikipedia.org/wiki/Brillouin_zone*.

The Hamiltonian of the system takes the form

$$H = -\sum_{i=1}^{N} \nabla^2 + \sum_{i>j} \frac{C_6}{|\boldsymbol{r}_i - \boldsymbol{r}_j|^6} \,. \tag{5.13}$$

We consider the case of low kinetic energy, that is when the interaction strength constant C_6 is large enough, and the system may be treated in a perturbative manner within a harmonic approximation. The positions of the crystal nodes can be fixed at $\boldsymbol{R}_i$. In order to find the excitation spectrum of this system we can follow the procedure of Refs. [BM77, MPW07]. First of all, we give to the particles small arbitrary displacements $\boldsymbol{u}_i$ from the nodes. The potential energy is then represented by

$$E_p = \frac{C_6}{2} \sum_{i \neq j} \frac{1}{|\boldsymbol{r}_{ij} + \boldsymbol{u}_{ij}|^k} \tag{5.14}$$

with the notations $\boldsymbol{r}_{ij} = \boldsymbol{r}_i - \boldsymbol{r}_j$, $\boldsymbol{u}_{ij} = \boldsymbol{u}_i - \boldsymbol{u}_j$ and $k = 6$.

in reciprocal space

Then, we perform an expansion of the potential energy E_p in powers of the displacements u_i^α, where α labels the Cartesian coordinates $\alpha = x, y, z$ and U stands for the Madelung energy of a chosen crystal packing.

$$E_p = U + \frac{1}{2}\sum_{i\alpha}\sum_{j\beta}\Phi_{\alpha\beta}(\boldsymbol{r}_{ij})u_i^\alpha u_j^\beta + ... \tag{5.15}$$

The first-order term here vanishes due to the fact that $\{\boldsymbol{R}_i\}$ is a minimum-energy configuration. The Hessian matrix $\Phi_{\alpha\beta}(\boldsymbol{r}_{ij})$ is obtained through a simple double differentiation:

$$\Phi_{\alpha\beta}(\boldsymbol{r}_{ij}) = -\frac{C_k}{2}\left(\frac{k(k+2)r_{ij}^\alpha r_{ij}^\beta}{r_{ij}^{k+4}} - \frac{k\delta_{\alpha\beta}}{r_{ij}^{k+2}}\right), \text{ if } \quad i \neq j, \tag{5.16}$$

$$\Phi_{\alpha\beta}(\boldsymbol{r}_{ii}) = \frac{C_k}{2}\sum_{j\neq i}\left(\frac{k(k+2)r_{ij}^\alpha r_{ij}^\beta}{r_{ij}^{k+4}} - \frac{k\delta_{\alpha\beta}}{r_{ij}^{k+2}}\right). \tag{5.17}$$

The Fourier transformed dynamical matrix $C_{\alpha\beta}(\boldsymbol{q})$ is related to $\Phi_{\alpha\beta}(\boldsymbol{r}_{ij})$ by the expression

$$C_{\alpha\beta}(\boldsymbol{q}) = \frac{1}{m}\sum_{i,j}\Phi_{\alpha\beta}(\boldsymbol{r}_{ij})\exp[-\mathrm{i}\boldsymbol{q}\boldsymbol{r}_{ij}] \tag{5.18}$$

where m stands for the mass of a particle in the kinetic term of the Hamiltonian. In order to simplify the treatment and get rid of the conditional definitions for $\Phi_{\alpha\beta}$, we introduce the matrix $S_{\alpha\beta}(\boldsymbol{q})$ such that

$$S_{\alpha\beta}(\boldsymbol{q}) = \sum_{i\neq j}\left(\frac{k(k+2)r_{ij}^\alpha r_{ij}^\beta}{r_{ij}^{k+4}} - \frac{k\delta_{\alpha\beta}}{r_{ij}^{k+2}}\right)\exp[-\mathrm{i}\boldsymbol{q}\boldsymbol{r}_{ij}] \tag{5.19}$$

then it can be seen that

$$C_{\alpha\beta}(\boldsymbol{q}) = -\frac{C_k}{2m}(S_{\alpha\beta}(\boldsymbol{q}) - S_{\alpha\beta}(0)) \tag{5.20}$$

The dynamical matrix can be used to obtain the normal mode frequencies by solving the eigenvalue problem

$$C_{\alpha\beta}(\boldsymbol{q})\boldsymbol{e}(\boldsymbol{q}) = \omega^2\boldsymbol{e}(\boldsymbol{q}). \tag{5.21}$$

Since $C_{\alpha\beta}$ is a real symmetric 3x3 matrix, there exists a complete and orthonormal set of three eigenvectors, written in which the Hamiltonian is diagonal. The wave vectors $\boldsymbol{q}$ are taken from the irreducible Brillouin zone.

For our case of the chosen model potential between Rydberg atoms $k = 6$, one has to evaluate the following sums

$$S_{\alpha\beta}(\boldsymbol{q}) = \sum_{i\neq j}\left(\frac{48r_{ij}^\alpha r_{ij}^\beta}{r_{ij}^{10}} - \frac{6\delta_{\alpha\beta}}{r_{ij}^{8}}\right)\exp[-\mathrm{i}\boldsymbol{q}\boldsymbol{r}_{ij}] \tag{5.22}$$

$$S_{\alpha\beta}(0) = \sum_{i\neq j}\left(\frac{48r_{ij}^\alpha r_{ij}^\beta}{r_{ij}^{10}} - \frac{6\delta_{\alpha\beta}}{r_{ij}^{8}}\right) \tag{5.23}$$

The Hamiltonian is rewritten in dimensionless form as

$$H = -\frac{1}{2r_s}\sum_{i=1}^{N}\Delta_i^2 + \sum_{i<j}\frac{1}{|\mathbf{r}_i - \mathbf{r}_j|^6} \tag{5.24}$$

where distance and energy units are

$$r_0 = 1/\rho^{1/3} \tag{5.25}$$

$$E_0 = C_6/r_0^6\,, \tag{5.26}$$

and the following form for the dimensionless parameter r_s

$$\frac{1}{r_s} = \frac{\hbar^2}{mr_0^2E_0} = \frac{\hbar^2}{mC_6\rho^{4/3}} \tag{5.27}$$

which characterizes the ratio between the kinetic and potential energies. It can be noticed that the parameter r_s plays the role of the mass m in Eq. (5.18). The units of frequency of the normal modes are taken as

$$\omega_0 = \frac{1}{\sqrt{r_s}} = \frac{\hbar}{(mC_6)^{1/2}\rho^{2/3}}\,. \tag{5.28}$$

In reduced units the problem can be rewritten as

$$\omega^2(\boldsymbol{q})\boldsymbol{u} = \Phi_{\alpha\,\beta}(\boldsymbol{q})\boldsymbol{u} \tag{5.29}$$

with

$$\Phi_{\alpha\,\beta}(\boldsymbol{q}) = \frac{\partial^2}{\partial u_\alpha \partial u_\alpha}\left(\sum_{j\neq 0}\frac{1-\exp(\mathrm{i}\boldsymbol{q}\mathbf{r}_j)}{|\boldsymbol{r}_j+\boldsymbol{u}|^6}\right)|_{\boldsymbol{u}\to 0}\ . \tag{5.30}$$

The kernel $\Phi_{\alpha\,\beta}(\boldsymbol{q})$ can be calculated by means of the Ewald summation technique.

The excitation spectrum in this units is shown in Fig. 5.5. In our description the three distinct branches of the spectrum can be degenerate (the second and the third coincide on the path GX). For small values of momentum $\boldsymbol{q}$ the excitations are in phononic (linear) regime modes with the sound velocity $c = \omega/|\boldsymbol{q}|$, which is dependent on a direction in a crystal. For GX direction in the crystal two sound velocities (of two coinciding transverse modes and one longitudinal mode) are equal to

$$\begin{aligned} c_1 &= 19.41 \\ c_{2,3} &= 10.04 \end{aligned}$$

in the units of $\omega_0 r_0$. It can be noticed that the longitudinal mode is also phononic unlike the case of the three-dimensional Wigner crystal, where a typical long-wavelength behavior of the frequency is $\omega_l(q) \sim \sqrt{q}$. The spectrum is periodic as one reaches a border of the first Brillouin zone, the values of the frequencies are also continuous, as seen in Fig. 5.5, when a momentum vector approaches the point X from different directions. At finite temperature the spectrum is expected to be smeared.

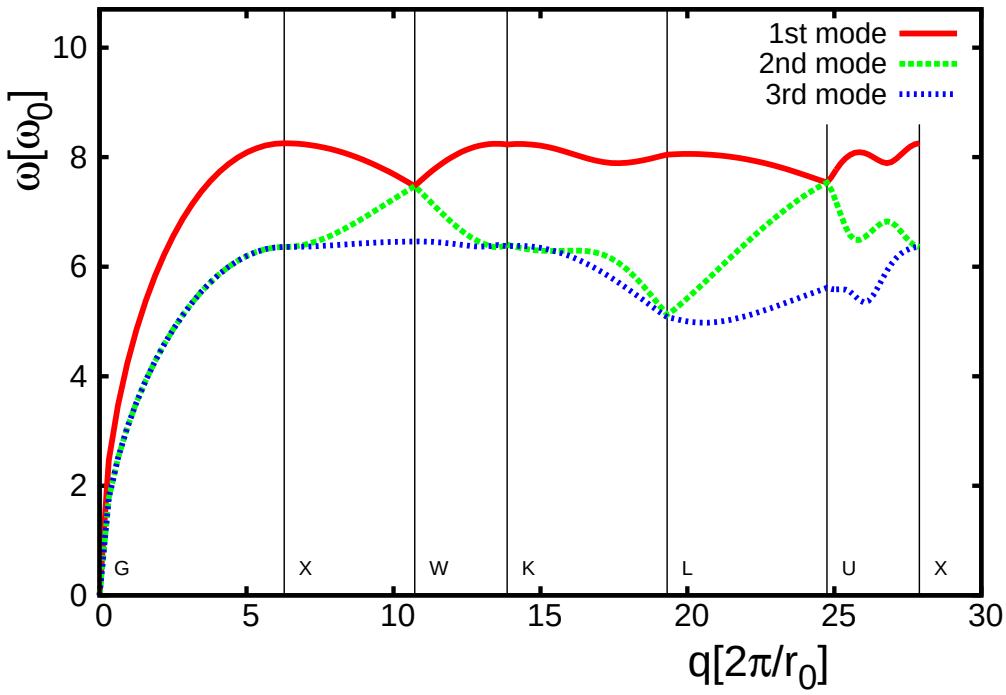

Figure 5.5: Excitation spectrum of the van der Waals $1/r^6$ interaction. The wave vector $\boldsymbol{q}$ follows the path G,X,K,L,U,W,X in the first Brillouin zone with the metrics of the vector preserved. The units for frequency and wave vector are ω_0 and $2\pi/r_0$ respectively, see Eqs. (5.25) and (5.28).

5.6 Discussion and conclusions

A very interesting and open question is the possibility of supersolidity in Rydberg systems. Ground state atoms dressed in Rydberg states exhibit weak van der Waals interactions at large distances, as described in [HNP10]. The question of supersolidity of such atoms was addressed in Refs. [CJB+10, HNP10]. Here, we consider an alternative scenario in which the gas is additionally allowed to have a lattice of Rydberg excitations. Such a lattice would in turn impose weak but long-ranged spatial correlations onto the ground state atoms. At the same time, the ground-state atoms may be Bose condensed [HRB+08]. However, it may be impossible to identify which of the atoms was excited within a certain proximity, as was demonstrated, for example, by the superatom analysis of the experimental results in Refs. [HRB+07, TFS+04]. However, motion will lead to dephasing of this state [HLW+11]. If the atoms are indeed prepared in such a mixed state, combining the ground $|g\rangle$ and excited $|e\rangle$ states as $|g\rangle + \alpha|e\rangle$, $\bar{N}_g^{-1} \ll \alpha \ll 1$, then both the lattice-forming and the BEC components are indistinguishable and may be said to be formed by the same atoms. Therefore, such a system would consist of particles which would simultaneously break translational symmetry and possess off-diagonal long-range order, which is a realization of

supersolid. While our model does not include the light field, the conditions for the phases of both excited and ground state atoms may be immediately extracted from Fig. 5.3, just with different reduced units for the two species.

In conclusion, it is possible to parameterize a model with isotropic van der Waals interactions into a universal phase diagram. We have characterized the phase diagram of Rydberg atoms by considering a model of bosons with repulsive van der Waals interaction, and determined solidification and Bose–Einstein condensation conditions. Relaxation mechanisms other than thermal motion should be considered if one considers Rydberg systems on timescales of several tenth of microseconds. We have also studied the excitation spectrum within the approximation of a classical harmonic crystal. Finally, it is worth mentioning that interactions between Rydberg excitations open a possibility of new supersolid scenarios.

Chapter 6

Para-hydrogen at low temperature

6.1 Introduction

Superfluidity and Bose-Einstein condensation (BEC) have been stunningly shown in metastable dilute alkali gases, magnetically confined at ultralow temperatures. [PS03] The extreme diluteness of these gases allows for the achievement of BEC with an almost full occupation of the zero-momentum state that has been possible to observe and measure quite easily. This contrasts with the difficulties encountered in the measure of the condensate fraction in liquid ^{4}He, which amounts only 8% at the equilibrium density. [GDA+11] However, liquid ^{4}He is a stable superfluid below the lambda transition $T_\lambda = 2.17$ K and therefore a system more easily accessible. Before the blowup produced in the field of quantum fluids by the first experimental realization of BEC gases, liquid helium was the only paradigm of a superfluid. From long time ago, there has been great interest in the search of superfluid condensed phases other than liquid helium. Spin-polarized atomic deuterium and tritium are predicted to be fermionic and bosonic liquids, respectively, in the limit of zero temperature. [PC87a, BMVB09] However, its experimental study has proven to be very elusive due to its high recombination rate, and only the case of atomic hydrogen, whose ground state is a gas, has been experimentally driven to its BEC state. [FKW+98] The next candidate for superfluidity is molecular hydrogen, which has been studied for a long time. [Sil80] This seems a priori an optimal system due to its very light mass but it crystallizes at relatively high temperature as a consequence of the intensity of its intermolecular attraction, without exhibiting any superfluid transition in the liquid phase. In the present work, we study the properties of metastable liquid or glass molecular hydrogen at very low temperatures using quantum Monte Carlo methods.

In 1972, Ginzburg and Sobyanin [GS72] proposed that any Bose liquid should be superfluid below a certain temperature T_λ, unless it solidifies at temperature T_f higher than T_λ. To give a first estimation of T_λ, they used the ideal Bose gas theory, obtaining

$$T_\lambda = 3.31 \frac{\hbar^2}{g^{2/3} m k_B} \rho^{2/3} , \tag{6.1}$$

where m is the atomic mass, g is the spin degeneracy, k_B is the Boltzmann constant and ρ is the density of the system. Ginzburg and Sobyanin proposed molecular *para*-hydrogen (p-H_2) as a plausible candidate for superfluidity: being a spinless boson ($g = 1$) with a small mass, p-H_2 should undergo a superfluid transition at a relatively high temperature (according to Eq. (6.1), $T_\lambda \simeq 6$ K).

The estimation of T_λ, given by Eq. (6.1), is clearly inaccurate in the case of dense liquids because it cannot account for the observed dependence of T_λ with the density. In fact, T_λ slightly decreases in liquid ^{4}He when ρ increases, a manifestly opposite behavior to the increase with $\rho^{2/3}$ given by the ideal gas formula (6.1). In order to provide a more reasonable estimation of T_λ, Apenko [Ape99] proposed a phenomenological prescription for the superfluid transition, similar to the Lindemann criterion for classical crystal melting. In this way, he was able to take into account quantum decoherence effects due to the strong interatomic potential and to relate the critical temperature for superfluidity with the mean kinetic energy per particle above the transition. For p-H_2, he concluded that T_λ should vary between 1.1 K and 2.1 K, depending on the density of the system.

Superfluid p-H_2 is not observed in a stable form because it crystallizes at temperature $T_f = 13.8$ K, which is significantly higher than the expected T_λ. Several studies about crystal nucleation in p-H_2 have been performed in order to understand if the liquid can enter a supercooled phase, i.e., a metastable phase in which the liquid is cooled below its freezing temperature without forming a crystal. Maris *et al.* [MSH83] calculated the rate $\Gamma(T)$ of homogeneous nucleation of the solid phase from the liquid as a function of the temperature T, showing a maximum of Γ around $T = 7$ K and a rapid decrease at lower temperature. This suggests that, if it would be possible to supercool the liquid through the range where Γ is large, one might be able to reach a low-temperature region where the liquid is essentially stable. However, recent experiments have indicated that, even at $T \sim 9$ K, the rate of crystal growth is so high that the liquid phase freezes quickly into a metastable polymorph crystal. [KFT+11]

Even though several supercooling techniques have been proposed to create a metastable liquid phase in bulk p-H_2, [MSW87, VM00, GFP+06] none of them has proven so far to be successful and no direct evidence of superfluidity has been detected. However, there are evidences of superfluidity in several spectroscopic studies of small doped p-H_2 clusters. In 2000, Grebenev *et al.* [GSTV00] analyzed the rotational spectra of a linear carbonyl sulfide (OCS) molecule surrounded by 14 to 16 p-H_2 molecules absorbed in a larger helium droplet, which fixes the temperature of the cluster. When p-H_2 is immersed in a ^{4}He droplet ($T = 0.38$ K), the measured spectra shows a peak indicating the excitation of angular momentum around the OCS axis. On the other hand, if the small p-H_2 cluster is put inside a colder ^{4}He-^{3}He droplet ($T = 0.15$ K), the peak disappears: the OCS molecule is then able to rotate freely inside the hydrogen cluster, pointing to the superfluidity of the surrounding p-H_2 molecules. These results have been confirmed in a later experiment on small p-H_2 clusters doped with carbon dioxide. [LLRRM10] From a precise analysis of the rotational spectra, it has been possible to measure the effective momentum of inertia of these small systems, and thus of their superfluid fraction ρ_s, providing a clear evidence of superfluidity in clusters made up of $N \leq 18$ p-H_2 molecules. These clusters are too small for extracting reliable predictions of a metastable liquid phase and larger clusters would be desirable. To this end, Kuyanov-Prozument and Vilesov [KPV08] have been able to stabilize liquid clusters with an average size of $N \approx 10^4$ p-H_2 molecules down to

temperature $T = 2$ K, but they do not see any evidence of superfluidity. Other attempts of producing liquid p-H_2 well below T_f ($T = 1.3$ K) are based on the generation of continuous hydrogen filaments of macroscopic dimensions. [GFP+06]

The search for a superfluid p-H_2 phase has been intense also from the theoretical point of view. The rather simple radial form of the p-H_2-p-H_2interaction and the microscopic accuracy achieved by quantum Monte Carlo methods have stimulated a long-standing effort for devising possible scenarios where supercooled p-H_2 could be studied. In practically all the cases, the search is focused on systems of reduced dimensionality or in finite systems. PIMC simulations of p-H_2 films adsorbed on a surface with impurities observed superfluidity for some arrangements of these impurities, [GC97] but these results were posteriorly questioned by other PIMC studies. [Bon05] In a one-dimensional channel, like the one provided experimentally by narrow carbon nanotubes, it has been predicted a stable liquid phase in the limit of zero temperature. [GBC00] The largest number of theoretical works are devoted to the study of small clusters, both pure [SCK91, MB06, MB07, KSCT07, MB08, SB11, GN08] and doped with impurities. [KW02, PZKW05, KW05] All these simulations show that p-H_2 becomes superfluid below a certain temperature T = 1-2 K and that the superfluid fraction depends on the number of molecules of the cluster. When the cluster becomes larger than a certain molecular number ($N >$ 18-25), solid-like structures are observed and the superfluidity vanishes.

We address the calculation of the equation of state of the metastable liquid p-H_2 phase in the limit of zero temperature using the diffusion Monte Carlo (DMC) method. The simulation of the liquid phase in this limit is easier than at finite temperature and therefore it is able to provide accurate information on its main energetic and structure properties.

The rest of the chapter is organized as follows. In Sec. 6.2, we introduce the quantum Monte Carlo methods used in the study and report specific details on how the simulations are carried out. Sec. 6.3 contains the results of the equation of state, structure properties, and condensate fraction of metastable liquid p-H_2 at zero temperature. and finally the main conclusions of the present work are discussed in Sec. 6.4.

6.2 Methodology and construction of trial wave functions

The H_2 molecule, which is composed of two hydrogen atoms linked by a covalent bond, is spherically symmetric in the *para*-hydrogen state (total angular momentum zero). The energy scale involved in electronic excitations ($\sim 10^5$ K) is orders of magnitude larger than the intermolecular one ($\sim 10^1$ K), thus to model the p-H_2-p-H_2interaction by means of a radial pair-potential and to consider the molecules as point-like turns out to be justified upon the condition of low or moderate pressures. In this work, we have chosen the well-known and commonly used semiempirical Silvera-Goldman pair potential. [SG78] This potential has proved to be accurate at low temperature and at the pressure regimes in

which we are interested.

The study in the limit of zero temperature has been performed with the DMC method. DMC is a first-principles method which can access exactly the ground state of bosonic systems. It is a form of Green's Function Monte Carlo which samples the projection of the ground state from the initial configuration with the operator $\exp[-(\mathcal{H}-E_0)\tau]$. Here, $\mathcal{H}$ is the Hamiltonian

$$\mathcal{H} = -\frac{\hbar^2}{2m}\sum_{i=1}^{N}\boldsymbol{\nabla}_i^2 + \sum_{1=i<j}^{N} V(r_{ij}) \ , \tag{6.2}$$

E_0 is a norm-preserving adjustable constant and τ is the imaginary time. The simulation is performed by advancing in τ via a combination of diffusion, drift and branching steps on walkers $\boldsymbol{R}$ (sets of $3N$ coordinates) representing the wavefunction of the system. [BCN94] The imaginary-time evolution of the walkers is "guided" during the drift stage by a guiding wavefunction ϕ_G, which is usually a good guess for the wavefunction of the system. This function contains basic ingredients of the system as its symmetry, phase and expected behaviors at short and long distances according to its Hamiltonian. Technically, ϕ_G allows importance sampling and thus reduces the variance of the ground-state estimations. It is straightforward to show that for the Hamiltonian $\mathcal{H}$ and any operator commuting with it, the expectation value is computed exactly within statistical error. Other diagonal operators which do not fulfill this condition require of a special treatment, known as pure estimation, [CB95b] which leads also for this case to unbiased results (for details see Section 2.5 of this Thesis).

The phase of the system is imposed within the typical imaginary-time length by the guiding wave function. This property of the DMC method is here a key point if we are pursuing a prospection on the properties of the metastable liquid p-H_2 phase. Then, for the liquid phase ϕ_G is taken in a Jastrow form

$$\phi_G(\boldsymbol{R}) = \prod_{1=i<j}^{N} f(r_{ij}) \ , \tag{6.3}$$

with a two-body correlation function [Rea79]

$$f(r) = \exp\left[-\frac{1}{2}\left(\frac{b}{r}\right)^5 - \frac{L}{2}\exp\left[-\left(\frac{r-\lambda}{\Lambda}\right)^2\right]\right] \ . \tag{6.4}$$

In order to compare the results obtained for the liquid phase with the ones corresponding to the stable hcp solid we have carried out some simulations with a guiding wave function of Nosanow-Jastrow type

$$\phi_G^s(\boldsymbol{R}) = \prod_{1=i<j}^{N} f(r_{ij}) \prod_{i=1}^{N} g(r_{iI}) \ , \tag{6.5}$$

the set $\{\boldsymbol{r}_I\}$ being the lattice points of a perfect hcp lattice. Optimal values for the parameters entering Eq. (6.4) are $b = 3.68$Å, $L = 0.2$, $\lambda = 5.24$Å, and $\Lambda = 0.89$Å for the

liquid phase, and $b = 3.45$Å, $L = 0.2$, $\lambda = 5.49$Å, and $\Lambda = 2.81$Å for the solid one. The Nosanow term is chosen in Gaussian form, $g(r) = \exp(-\gamma r^2)$. The density dependence of the parameters in the Jastrow term is small, and neglected in practice when used in DMC, whereas the Nosanow term parameter γ is optimized for the whole range of densities. We have used 256 and 180 particles per simulation box for the liquid and hcp solid phases, respectively. The number of walkers and time-step have been adjusted to reduce any bias coming from them to the level of the statistical noise.

6.3 Results at zero temperature

We have calculated the main properties of the metastable liquid and stable hcp solid phases of p-H_2. Our main goal has been to know the properties of a hypothetical bulk liquid phase and compare them with the ones of the stable solid. In order to achieve reliable estimations of liquid p-H_2 it is crucial to work with a guiding wave function of liquid type, as we have discussed in the preceding Section. Within the typical imaginary-time length of our simulations we have not seen the formation of any crystal structure, i.e., no signatures of Bragg peaks in the structure function $S(k)$ have been registered so far.

In Fig. 6.1, we plot the DMC energies per particle of metastable liquid p-H_2 as a function of the density. For comparison, we also report the results obtained for the hcp crystal phase. Our hcp energies are in close agreement with the ones reported in Ref. [OP06] using the same Silvera-Goldman potential. In the figure, we also show the experimental estimation at $T = 0$ K from Ref. [Sch70], $E/N = -89.9$ K, that lies a bit below of our results. This is again in agreement with previous DMC results [OP06] which show that the experimental energy is, in absolute value, underestimated and overestimated by the Silvera-Goldman and Buck potential, [BHK+83] respectively. Our results for both phases are well reproduced by the polynomial law

$$\frac{E}{N} = \left(\frac{E}{N}\right)_0 + A\left(\frac{\rho-\rho_0}{\rho_0}\right)^2 + B\left(\frac{\rho-\rho_0}{\rho_0}\right)^3 , \tag{6.6}$$

$(E/N)_0$ and ρ_0 being the equilibrium energy per particle and equilibrium density, respectively. These equations of state are shown in Fig. 6.1 with lines. The optimal parameters of the fits are: $\rho_0 = 0.026041(20)$Å^{-3}, $(E/N)_0 = -86.990(37)$ K, $A = 232(2)$ K, $B = 156(11)$ K for the solid, and $\rho_0 = 0.023386(40)$Å^{-3}, $(E/N)_0 = -76.465(51)$ K, $A = 188(1)$ K, $B = 131(10)$ K for the liquid. As expected, our DMC results shows that the solid phase is the stable one with a difference in energy per particle at the respective equilibrium points of ~ 10 K, the equilibrium density of the liquid being ~ 10 % smaller than the solid one. The same trend was observed in a DMC simulation of two-dimensional p-H_2, but there the differences were significantly smaller. [CB08a] It is worth noticing that about one half of the energy difference in the bulk systems comes from the decrease of the kinetic energy

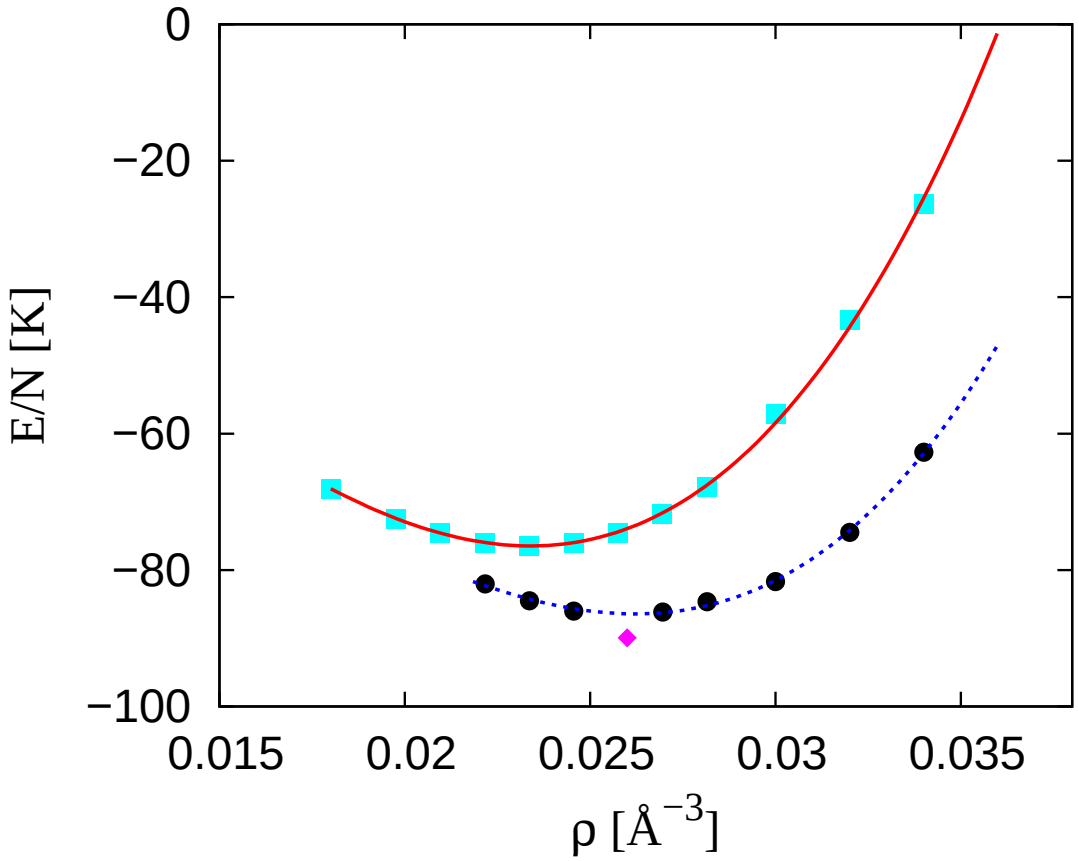

Figure 6.1: DMC energies per particle as a function of the density. Squares and circles correspond to the liquid and solid phases, respectively. Solid and dashed lines are the polynomial fits to the DMC energies for the liquid and solid, respectively. The diamond is the experimental energy of hcp molecular hydrogen from Ref. [Sch70]

per particle going from the liquid to the solid: at density $\rho = 0.03\,\text{Å}^{-3}$, it amounts 93.3(1) and 89.1(1) K for the liquid and solid, respectively.

From the equations of state (6.6), it is easy to know the pressure of the system at any density using the relation $P(\rho) = \rho^2[d(E/N)/d\rho]$. The results obtained for metastable liquid and stable solid phases are shown in Fig. 6.2. As one can see, at a given density the pressure of the liquid is larger than the one of the solid mainly due to the different location of the equilibrium densities ($P = 0$). The results for the solid are compared with experimental data from Ref. [DdWS79] showing a good agreement especially for not very large pressures. The density at which the function $P(\rho)$ has a zero slope defines the spinodal point; beyond this limit the system is no more thermodynamically stable as a homogeneous phase. At this point, the speed of sound $c(\rho) = [m^{-1}(dP/d\rho)]^{1/2}$ becomes zero. Results for $c(\rho)$ are shown for both phases in Fig. 6.3. The speed of sound decreases when the density is reduced and drops to zero at the spinodal point: ($\rho_c = 0.0176(1)\,\text{Å}^{-3}$, $P_c = -12.6(5)$ MPa) and ($\rho_c = 0.0195(1)\,\text{Å}^{-3}$, $P_c = -17.5(5)$ MPa) for liquid and solid, respectively.

DMC produces also accurate results for the structure of the bulk system. In Fig. 6.4, we show results for the two-body radial distribution function $g(r)$ of the liquid p-H_2 phase for a set of densities. This function is proportional to the probability of finding two molecules separated by a distance r. Increasing the density, the main peak becomes higher and moves to shorter interparticle distances; at least three peaks are observed. All these features point to the picture of a very dense quantum liquid, with much more structure than in stable liquid ^{4}He. In the same Fig. 6.4, we show results for the static structure factor $S(k)$, related to $g(r)$ by a Fourier transform. As one can see, the main peak increases quite fast with the density suggesting a highly structured metastable liquid. Nevertheless, we have not observed within the scale of the simulations the emergence of any Bragg peak which would point to formation of crystallites in the simulation box. In Fig. 6.5, we illustrate the comparison between $S(k)$ for the liquid and solid systems at a density $\rho = 0.0245\ \mathbf{r}\text{A}^{-3}$, close to the equilibrium density of the liquid. The difference is the one expected between a liquid and a solid: oscillating function towards one at large k for the liquid and a sequence of Bragg peaks, corresponding to the hcp lattice, for the solid.

One of the most relevant properties of a superfluid is the mean occupation of the zero-momentum state, i.e., the condensate fraction n_0. As it is well known, n_0 can be obtained from the asymptotic behavior of the one-body density matrix $\rho(r)$,

$$n_0 = \lim_{r\to\infty} \rho(r)\ , \tag{6.7}$$

with $\rho(r)$ being obtained as the expectation value of the operator

$$\left\langle \frac{\Phi(\mathbf{r}_1, \ldots, \mathbf{r}_i + \mathbf{r}, \ldots, \mathbf{r}_N)}{\Phi(\mathbf{r}_1, \ldots, \mathbf{r}_N)} \right\rangle\ . \tag{6.8}$$

DMC results for the condensate fraction of liquid p-H_2 as a function of the density, obtained using the extrapolated estimator (there are no reliable pure estimators for non-diagonal

operators), are shown in Fig. 6.6. The decrease of n_0 with the density is well described by an exponential decay (line in the figure). The strong interactions induced by the deep attractive potential well produce a big depletion of the condensate state. At the equilibrium density, our estimation for the condensate fraction is $n_0 = 0.0037(7)$. This value is more than one order of magnitude smaller than the measured condensate fraction [GDA+11] of liquid ^{4}He at equilibrium (0.08).

6.4 Conclusions

A possible observation of superfluidity in bulk or clustered systems of para-hydrogen atoms p-$H_2$was a subject of an extensive study in the last decades ([GS72], [SCK91]) due to a variety of advantageous properties of such atoms. Nevertheless the experimental observation has not been performed yet, mostly because of a relatively high solidification temperature of p-H_2, that can bring a perspective superfluid transition deeply into the metastable phase.

Our Group performed a multifold study of the system of para-hydrogen atoms p-H_2at low temperatures deeply below the point of crystallization by means of Quantum Monte Carlo methods. The zero-temperature simulation was performed in order to investigate the properties of a metastable liquid phase and to find the fraction of the Bose-Einstein condensate in the relevant range of densities. The methods of choice for the zero-temperature simulations of the p-H_2system were the Variational Monte Carlo and the diffusion Monte Carlo techniques. The latter is an efficient and versatile instrument to calculate the quantum properties of the system, including the non-local ones. The results of the zero-temperature simulations suggest that the metastable liquid para-hydrogen is a strongly correlated liquid, that again might be a sign of instability of this hypothetical system. The calculation of the Bose-Einstein condensate show that the condensate fraction is substantially lower than in the liquid helium ^{4}He.

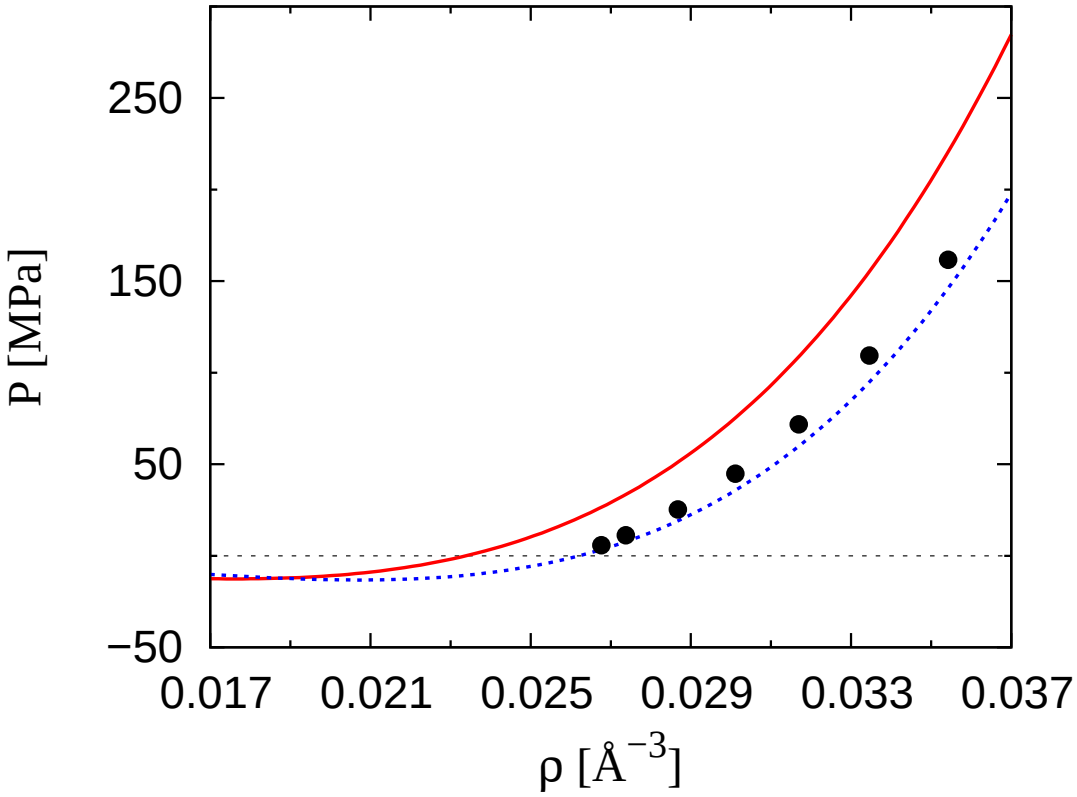

Figure 6.2: Pressure of the liquid (solid line) and solid (dashed line) p-H_2 phases as a function of the density. Experimental points for the solid phase [DdWS79] are show as solid circles.

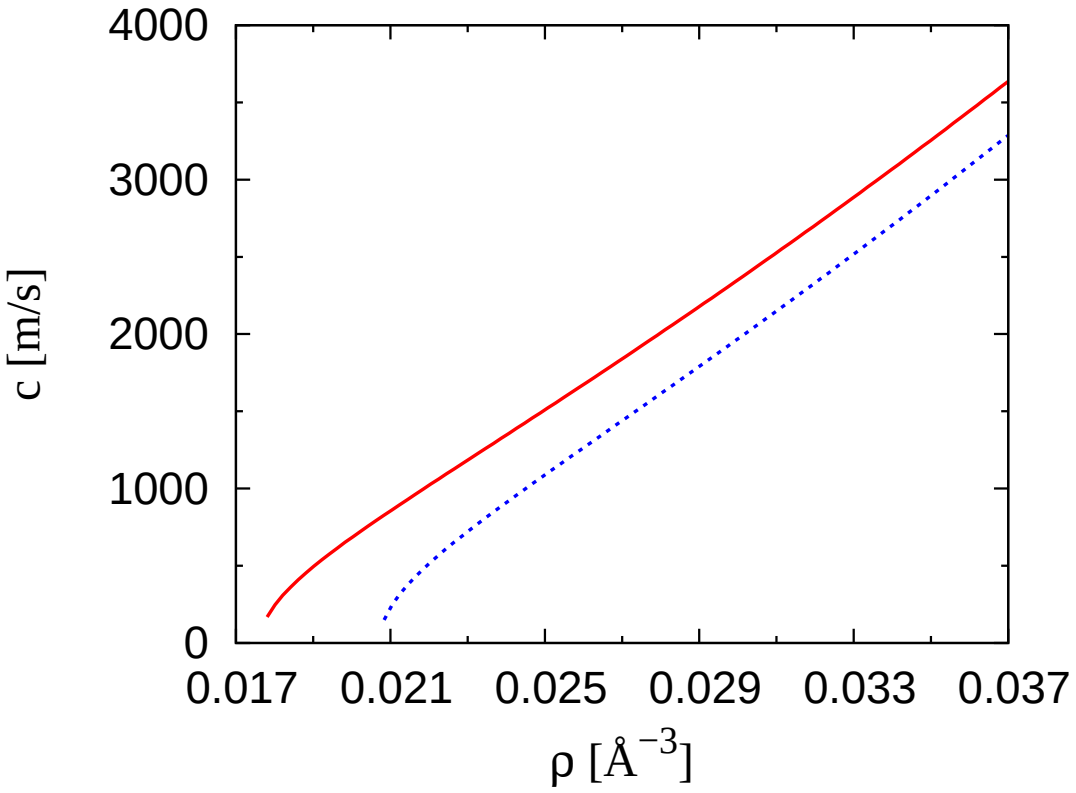

Figure 6.3: Speed of sound of the liquid (solid line) and solid (dashed line) p-H_2 phases as a function of the density.

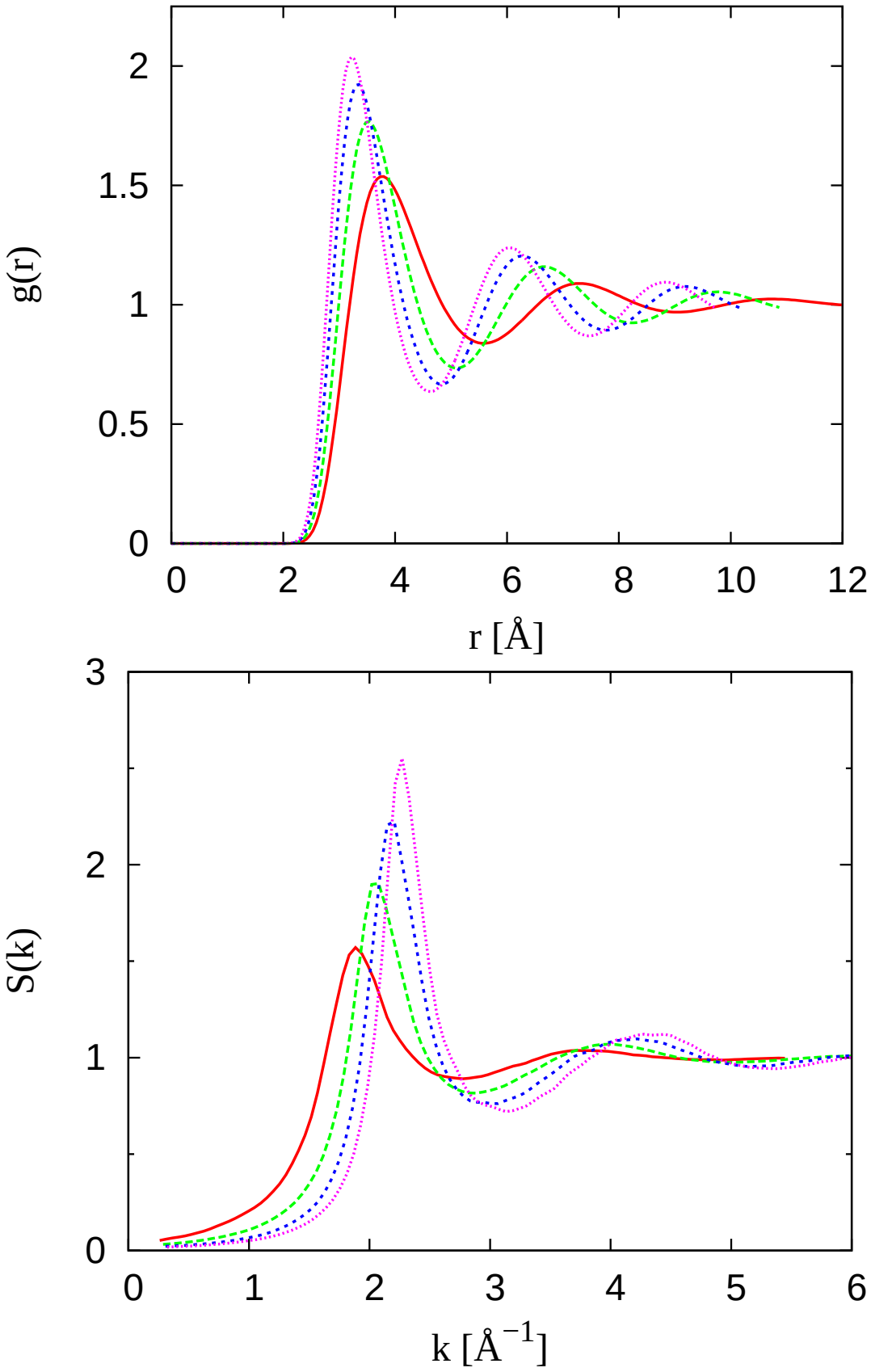

Figure 6.4: *Top panel:* Two-body radial distribution function of the liquid p-H_2 phase at different densities: solid, long-dashed, short-dashed, and dotted lines stand for densities $\rho = 0.0180$, 0.0245, 0.0300, and 0.0340 Å^{-3}, respectively. *Bottom panel:* Static structure factor of the liquid phase. Same densities and notation than in the top panel.

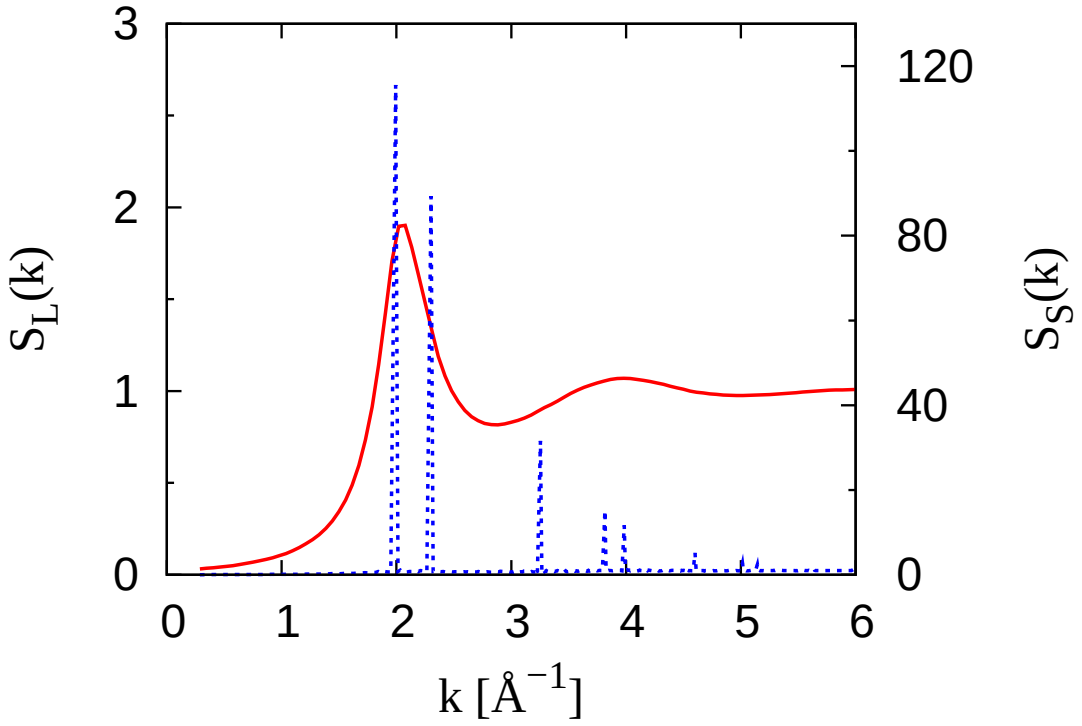

Figure 6.5: Static structure function of liquid and solid p-H_2 at density $\rho = 0.0245\,\text{Å}^{-3}$. The result for the liquid $S_L(k)$ (left scale) is shown with a solid line; the one for the hcp solid $S_S(k)$ (right scale) with a dashed line.

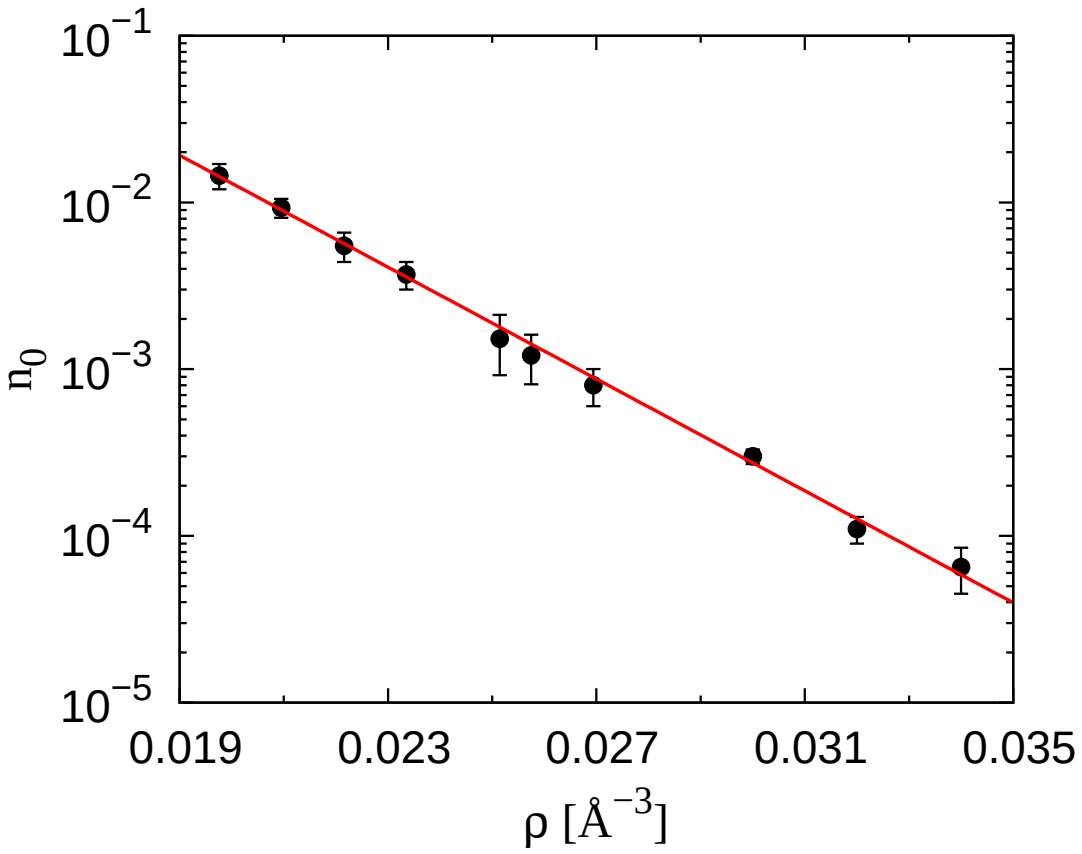

Figure 6.6: Condensate fraction of metastable liquid p-H_2 as a function of the density. The points are the DMC results and the line is an exponential fit to them.

Chapter 7

Conclusions and list of publications

Here we summarize the results, presented in the Thesis.

In Chapter 3, devoted to the generalization of the Ewald summation technique, we derived explicit expressions for the Ewald sums in three-dimensional systems, governed by a generic $1/|\boldsymbol{r}|^k$ power-law interaction, with periodic boundary conditions applied. We also extended the derivation to the cases of two-dimensional and one-dimensional geometry. The importance of these generalizations can be seen, as they apply to many physically important interaction potentials as the dipole-dipole interaction, van der Waals interaction etc. In this Thesis we give the functional forms for the terms of the Ewald sums (both in momentum and coordinate space), ready for implementation in actual calculations. The derivation and the functional form of the results differs in the cases of short-ranged ($k > D$), long-ranged ($k < D$) and "marginal" ($k = D$) forces, where D is the system dimensionality. The cases of long-range forces require separate calculations because of the divergence of the potential energy. This unphysical divergence disappears when demanding a charge-neutrality of the system, which can be restored within the "jellium" model. The resulting expressions in the jellium model are explicitly given. It is argued that in the case of some short-range potentials the Ewald method can be advantageous with respect to a direct summation due to a faster convergence rate, typically, of a Gaussian kind versus a certain power-law rate. We also give a discussion of the convergence properties of a quasi-neutral Coulomb system.

The results are first presented for the case of a 3D system in a cubic simulation box in order to explain the general mathematical procedure, which for the specific case of the Coulomb potential recovers well-known results [AT89]. Later on, the same mathematical technique is applied to 2D and 1D geometries. For the one-dimensional case the initial sum for the potential energy is explicitly evaluated in Eq. (3.96), nonetheless the Ewald summation is developed as well for this case and may be used as a mathematical equality. The more efficient representations of the reciprocal space sums, which have a complexity $\mathcal{O}(N)$ instead of $\mathcal{O}(N^2)$ with the number of particles N, are presented for 3D and 2D systems. The explicit expressions for the terms of the Ewald sums are given in a tabular form for physically relevant potentials with small integer power indices k, as dipole-dipole interaction potential, Lennard-Jones potential and others in both three- and two-dimensional geometries (refer to Tables 3.1 and 3.2).

When the simulation box cannot be chosen cubic, for example in a modelling of a three-dimensional hcp crystal structure, the Ewald method can also be applied after certain modifications. Formally, it consists in the choice of an appropriate rectangular simulation

box and a substitution of the vector $\boldsymbol{n}$ by $\boldsymbol{n}_r = (\boldsymbol{n}_x L_x + \boldsymbol{n}_y L_y + \boldsymbol{n}_z L_z)/L_0$ and $\boldsymbol{m}_k = (\boldsymbol{m}_x/L_x + \boldsymbol{m}_y/L_y + \boldsymbol{m}_z/L_z)L_0$ in the real and momentum space sums, respectively [see Eqs. (3.102) and (3.103)].

The optimization of the involved parameters, that is the integration parameter α and the cut-off lengths in coordinate and momentum space, is a necessary operation in order to improve the convergence rates and to avoid excessive calculations. The main idea of the optimization, that we propose in the this Thesis, is to perform a benchmark calculation, minimizing the variance in the energy. We show how this optimization technique works on the example of a two-dimensional gas of dipoles, aligned perpendicularly to the plane of motion. This proposed optimization technique is mostly efficient in simulations of gases and crystals. In spite of being very simple, it allows to find rather quickly adequate parameter ranges. The analytical estimations of the optimal parameters are given as well and are proven to be consistent with the results, obtained in an explicit optimization. A more sophisticated method to optimize the calculation parameters, taking advantage of the $\mathcal{O}(N)$ representation of the Fourier transform sum, is also presented with explicit estimations of the parameters for a typical system simulated by Quantum Monte Carlo methods.

Another problem studied is the phase diagram of Yukawa systems. The Coulomb potential is probably one of the most basic and widespread interactions in the nature as it describes forces between charges. In a charge neutral system, the presence of a second component introduces screening. The Yukawa potential as well appears in the problem of mass-imbalanced two-component Fermi gas. It is known that in the case of a large mass imbalance, the light fermions introduce an effective Yukawa potential between the heavy fermions. It was predicted in [PAP+07] that this effective interaction might lead to crystallization in two-dimensional systems, although no estimations were done in three-dimensional case. The study of Ceperley *et al.* [CCK76] partially addresses the problem of the zero-temperature phase diagram. In their work the transition line was drawn by using approximate Lindemann melting criterion. For the first time a fully quantum mechanical calculation is done in order to find the zero-temperature phase diagram of Yukawa particles. The diffusion Monte Carlo method is expected to give a ground state energy exactly, so the phase diagram should be exact. The melting and solidification points are found by using the double-tangent Maxwell construction. The Lindemann criterion indeed applies in a large part of the phase diagram apart from the high density regime where notable differences compared to the prediction of Ceperley *et al.* are visible.

We discovered that an improvement to the efficiency of the diffusion Monte Carlo method can be obtained by using the hypernetted chain (HNC) method (based on a solution of the corresponding Euler-Lagrange hypernetted chain equations) in a construction of Jastrow guiding wave functions. The HNC method allows to find a very good numerical approximation for the two-body Jastrow terms provides a result, which is already optimized in a many-body sense. The HNC solutions are also advantageous, since they do not require cumbersome multiparametric optimizations, and are quite precise and very fast.

The phase diagram of Yukawa particles has a peculiar shape. That is, a double transition is possible, when for a fixed interaction strength, a change in the density might cause reentrant gas-solid-gas transition. This unusual behavior is caused by a competition between long-range Coulomb part of the Yukawa potential (melts at large densities) and exponential screening (melts at small densities). To the best of our knowledge this is the first time that the high-density melting was observed in this system in a quantum simulation.

Based on our calculations we find that the mass ratios in achievable fermionic mixtures of pure elements are too small to undergo a transition to a crystal phase regardless of the density of the bulk. Nonetheless, larger effective mass ratios can be reached if the heavier component is confined by an optical lattice, that enhances strongly the strength of the lattice. This alternative procedure of obtaining large effective mass ratios is discussed in the Thesis, and based on the available data on the current and perspective experimental set-ups the principal feasibility to produce experimental conditions for observation of the crystallization is argued. The heights of optical lattices are typically tunable by the intensity of laser beams, so that the correctness of our theoretical predictions for the phase transition can be checked.

In order to localize more accurately the phase transition point in the high density regime we applied the Ewald summation technique, that yields the potential energy of the simulation cell, replicated infinitely in the space. This method proved to be efficient in enhancing the rate of the convergence of the DMC energy with the number of particles in spite of introducing additional calculation costs. The specific Ewald summation for the case of a Yukawa system was implemented in the simulation code, used in our research Group. The idea to apply the HNC method to produce highly optimized Jastrow terms of trial wave functions can be used in future Monte Carlo simulations of other physical systems.

In the next part of the work, given in the Thesis, we presented a quantum Monte Carlo study of a bulk system of bosonic Rydberg atoms, that is alkali atoms with a single electron residing on a very high orbital, interacting through van der Waals interaction potential $1/|\mathbf{r}|^6$. A perspective utilization of Rydberg atomic clouds as quantum gates or for an observation of Bose–Einstein condensation, requires an utmost stable and predictable system, that often implies that the interaction is repulsive and independent on spacial directions, hence our simple model should be physically relevant. The asymptotic van der Waals $C_6/|\mathbf{r}|^6$ is a common leading term of the interaction of Rydberg atoms, derived by virtue of the perturbation theory. One of the aims that we pursue in the study is to understand how much of the behavior of a real system comes from this leading term, and to which extent the $1/|\mathbf{r}|^6$ interaction of the excited atoms in the cloud can describe crucial properties of experimentally relevant systems like mixtures of excited and ground state atoms.

The zero-temperature properties of a system of Rydberg atoms, as presented in Section 5, are controlled by a unified dimensionless parameter ρr_0^3, which depends on the

density ρ and the interaction strength $r_0 = (mC_6/\hbar^2)^{1/4}$. The behaviors of distinct systems with different parameters like particle mass and interaction strength constant, are therefore identical, if they possess the same value of ρr_0^3, for instance, the systems solidify and melt at the same dimensionless density. Making use of the diffusion Monte Carlo method, we found that for a system, governed by a model Hamiltonian

$$\mathcal{H} = -\frac{\hbar^2}{2m}\sum_i \nabla_i^2 + \sum_{i<j}\frac{C_6}{|\boldsymbol{r}_i - \boldsymbol{r}_j|^6}.$$

rewritten in a proper dimensionless form, the zero-temperature transition point happens in the density range

$$\rho_c\, r_0^3 = 3.9 \pm 0.2\,.$$

The position of the phase transition is obtained by applying the double-tangent Maxwell construction technique implying that the pressure and the free energy stay unchanged along the melting curve. Possible types of the crystal packing, preferred by the system in its solid state, have been discussed. The calculations of the Madelung energy for different lattices suggest that face-centered cubic (fcc) and hexagonal close-packed (hcp) are the preferable packings with a slight advantage of fcc, although the introduction of a quantum defect correction δ in the interaction potential can give the advantage to hcp. We stick to the fcc lattice, which was used throughout our quantum Monte Carlo simulations as a preferable crystal formation in the solid phase.

The finite temperature properties of the system were studied both with classical and quantum Monte Carlo methods. First of all we applied the classical Monte Carlo technique, based on the evolution of the system in accordance with its classical partition function. The estimates for the liquid-solid phase transition curve in case of high temperatures, where the classical approach is valid, have been found. The region of low temperatures, where the quantum description is required, was studied with the path integral Monte Carlo (PIMC) method. This technique allowed to find the region of the solid-gas phase transition as well as to localize the transition between normal fluid and superfluid phases. The results of the PIMC simulations completed the phase diagram of the system as a function of dimensionless density and dimensionless temperature, on the other hand confirming the correctness of the DMC and classical calculations, as the PIMC data came as a smooth transition between the two.

We also present a discussion of a possible treatment of the crystallized Rydberg atom clouds as a model for perspective research of the supersolid phase.

In Section 6 we performed extensive quantum Monte Carlo calculations of atomic para-hydrogen p-H_2 at zero temperature below its solidification curve in a range of densities. In this study our principal motivation was to understand better the properties of the metastable liquid/glass phase at low temperatures. In the limit of zero temperature we have used the DMC method, which is a very efficient tool to sample this metastable phase through the use of a trial wave function with a corresponding symmetry. The data provided

by diffusion Monte Carlo method suggests that the Bose-Einstein condensate fraction is subject to a large depletion compared to that of the stable liquid ^{4}He.

In conclusion in this Thesis we successfully applied quantum Monte Carlo techniques for studying the quantum phase diagrams in a number of physical systems which are relevant to current and future experiments. Our research Group

- learned to carry out the Ewald summation for different physical systems and to use it for solving the finite size correction problem;
- studied and implemented in the code the modified periodic boundary conditions (truncated tetrahedron), which might be used to enhance the efficiency of our Monte Carlo calculations;
- realized the usefullness the hypernetted chain (HNC) method for constructing optimized Jastrow terms of trial wave functions;
- improved the understanding of the ways to study quantum phase transitions by virtue of quantum and classic Monte Carlo method.

As a consequence of this work, and as a result of this Thesis, we published the following articles:

1. O. N. Osychenko, G. E. Astrakharchik, Y. Lutsyshyn, Yu. E. Lozovik, and J. Boronat: "*Phase diagram of Rydberg atoms with repulsive van der Waals interaction*", Phys. Rev. A **84**, 063621 (2011).
2. O. N. Osychenko, G. E. Astrakharchik, and J. Boronat: "*Ewald method for polytropic potentials in arbitrary dimensionality*", Mol. Phys. **110**, 4, 227-247 (2012).
3. O. N. Osychenko, G. E. Astrakharchik, F. Mazzanti, and J. Boronat: "*Zero-temperature phase diagram of Yukawa bosons*", Phys. Rev. A **85**, 063604 (2012).
4. O. N. Osychenko, R. Rota, and J. Boronat: "*Superfluidity of metastable glassy bulk para-hydrogen at low temperature*", Phys. Rev. B **85**, 224513 (2012).

Appendix A

Ewald method for polytropic potentials

We prove that the sums S_{-+} and S_{++} (3.46–3.47) vanish on average, allowing to calculate the potential energy over the negatively charged particles' positions only.

- First, let us show that the integral of ψ over the cell is zero. Since the distances are in the units of L, consider the cubic cell $\Omega = (x, y, z) \in [-1/2, 1/2]^3$, that yields

$$\int_\Omega \psi(\boldsymbol{r})\,\mathrm{d}\boldsymbol{r} = J_1 + J_2 + C_1 \tag{A.1}$$

where

$$J_1 = \int_\Omega \mathrm{d}\boldsymbol{r} \sum_{\boldsymbol{n}} R(\boldsymbol{n}, \boldsymbol{r}) \tag{A.2}$$

$$J_2 = \int_\Omega \mathrm{d}\boldsymbol{r} \sum_{\boldsymbol{m}\neq\boldsymbol{0}} K(\boldsymbol{m}, \boldsymbol{r})\ . \tag{A.3}$$

It can be easily seen, that the second integral J_2 is zero,

$$\begin{aligned} J_2 &= \sum_{\boldsymbol{m}\neq\boldsymbol{0}} \varkappa(\boldsymbol{m}, \boldsymbol{r}) \int_\Omega \cos(2\pi \boldsymbol{m}\boldsymbol{r})\,\mathrm{d}\boldsymbol{r} \\ &= \sum_{\boldsymbol{m}\neq\boldsymbol{0}} \varkappa(\boldsymbol{m}) \frac{\sin(2\pi m_x + m_y + m_z))}{(2\pi)^3 m_x m_y m_z} = 0 \end{aligned} \tag{A.4}$$

As far as the integral J_1 is concerned, we can notice that the regions $\Omega'(\boldsymbol{n}) = \boldsymbol{r} + \boldsymbol{n}$, where $\boldsymbol{r} \in \Omega$, $\boldsymbol{n} \in \mathbb{Z}^3$ are the same cubic unit cells, displaced by an integer vector, thus covering all the coordinate space with only zero-measure intersections. It means that the summation of the integrals in (A.2) over the cell Ω can be substituted by the integration over the whole coordinate space,

$$\begin{aligned} J_1 &= \sum_{\boldsymbol{n}} \int_{\Omega'(\boldsymbol{n})} R(\boldsymbol{n}, \boldsymbol{r})\,\mathrm{d}\boldsymbol{r} = \sum_{\boldsymbol{n}} \int_{\Omega'(\boldsymbol{n})} \frac{\Gamma(\frac{k}{2}, \alpha^2|\boldsymbol{r}+\boldsymbol{n}|^2)}{\Gamma(\frac{k}{2})|\boldsymbol{r}+\boldsymbol{n}|^k} \\ &= \alpha^{k-3} \int_{\mathbb{R}^3\setminus 0} \frac{\Gamma(\frac{k}{2}, \boldsymbol{\rho}^2)}{\Gamma(\frac{k}{2})\boldsymbol{\rho}^k}\,\mathrm{d}\boldsymbol{\rho} = -\frac{2\pi^{\frac{3}{2}}\alpha^{k-3}}{(k-3)\Gamma\left[\frac{k}{2}\right]} = -C_1\ , \end{aligned} \tag{A.5}$$

and thus the whole integral (A.1) is equal to zero.

- Consider two species of the particles: negative charges q_i on positions $\boldsymbol{r}_i$ and a positively charged and uniformly distributed background with a total charge $q_+N_+ = -q_iN_i$, ensuring the neutrality of the cell. Let us demonstrate that S_{-+} is equal to zero, when the number of background charges tends to infinity. In this case the sum (3.46) for S_{-+} may be rewritten as an integral over the background charges' positions

$$S_{-+} = \sum_i q_i \int_\Omega \psi(\boldsymbol{r}_p - \boldsymbol{r}_i)\sigma \, \mathrm{d}\boldsymbol{r}_p = \sum_i q_i \int_{\Omega_i} \psi(\boldsymbol{r})\sigma \, \mathrm{d}\boldsymbol{r} \ , \tag{A.6}$$

where we did the change of variables $\boldsymbol{r} = \boldsymbol{r}_p - \boldsymbol{r}_i$. The regions Ω and Ω_i refer to the original simulation cell and the same cell, moved by the vector $\boldsymbol{r}_i$, and σ stands for the background charge density $\sigma = -q_iN_i/V(\Omega)$. It is clear that every vector $\boldsymbol{r} = (x, y, z) \in \Omega_i$ can be displaced into the cell Ω by the corresponding shift $\tilde{\boldsymbol{r}} = (\tilde{x}, \tilde{y}, \tilde{z}) = (x - aL, y - bL, z - cL) \in \Omega$ with integers a, b, c. The Jacobian J of the change of variables $\boldsymbol{r} \to \tilde{\boldsymbol{r}}$ is obviously 1. On the other hand, due to the periodicity of ψ,

$$\psi(\boldsymbol{r}) = \psi(\tilde{\boldsymbol{r}}) \ , \tag{A.7}$$

and $\tilde{\boldsymbol{r}}$ runs over the whole region Ω due to the conservation of the volume with $J = 1$. Finally, Eq. (A.6) can be written as

$$S_{-+} = \sum_i q_i \int_\Omega \psi(\tilde{\boldsymbol{r}})\sigma \, \mathrm{d}\tilde{\boldsymbol{r}} = 0 \ . \tag{A.8}$$

In the similar manner, the interaction between the charges of the background S_{++} in the limit $N_+ \to \infty$ is given by the double integral

$$S_{++} = \frac{1}{2} \int_\Omega \mathrm{d}\boldsymbol{r}_1 \int_\Omega \mathrm{d}\boldsymbol{r}_2 \psi(\boldsymbol{r}_1 - \boldsymbol{r}_2)\sigma^2 = 0 \ , \tag{A.9}$$

since $\int_\Omega \psi(\boldsymbol{r}_1 - \boldsymbol{r}_2) \, \mathrm{d}\boldsymbol{r}_2 = 0$, following the same arguments as for the case of S_{-+}.

Appendix B

Truncated octahedron boundary conditions

Apart from the standard cubic periodic boundary conditions we expored a possibility to apply the truncated octahedron periodic boundary conditions. This kind of periodic conditions has an advantage to reduce effects of anisotropy as well as enhance the overall efficiency of the simulation.

The truncated octahedron simulation cell, represented by a cube with removed angles, possesses a periodicity with the steps $\{\boldsymbol{L}\}_p = (\pm L/2, \pm L/2, \pm L/2)$, which means that only a crystal formation of a cubic class (simple cubic, bcc, fcc) with a composition, corresponding to even values of L/a ($a = (N_{cell}/\rho)^{1/3}$ stands for a size of the elementary cell) is commensurate with the cell. It means that the simulation in periodic boundary conditions is only possible for a certain reduced set of particles in the box. In practice it is equivalent to the exclusion of the crystal configurations with odd values of L/a; for instance, in case of fcc lattice one has to omit $N_p = 2(2i+1)^3 = 2,\ 64,\ 250,\ 686....$

The situation regarding hcp formation is similar, with the only difference that as it always happens in the case of hcp the simulation should be performed in a cell with unequal size lengths L_x, L_y, L_z. If the truncation of the interaction (minimum image convention) is to be applied, one takes the distance from the center to the nearest plane, that is the plane with the equation $X/L_x + Y/L_y + Z/L_z = 3/4$. The spherical cut-off radius in this case is equal to

$$r_{\text{cut}} = \frac{3/4}{\sqrt{1/L_x^2 + 1/L_y^2 + 1/L_z^2}}\,. \tag{B.1}$$

The values of L_x, L_y, L_z are chosen such that the cell is commensurate with the lattice. We also require that an arbitrary periodic translation $\boldsymbol{r} \to \boldsymbol{r} + \{\boldsymbol{L}\}$ brings a lattice site again to a site. This condition results in a demand of having all numbers L_x/a_x, L_y/a_y, L_z/a_z even, that again reduces the variety of options for a number of particles in a cell to $N_p = 32, 256, 864, ...$

The number of particles N_p in a simulation in a truncated octahedron cell corresponds to a cut-off radius

$$r_c = \frac{\sqrt{3}}{4}(2N_p/\rho)^{1/3} \tag{B.2}$$

which is a distance to the nearest plane of the cell. The same distance in the cubic p.b.c. is obtained by $3\sqrt{3}/4N_p \approx 1.3$ or, as diffusion Monte Carlo technique is $\mathcal{O}(N_p^2)$, by about 68%

of additional calculation time. This effect is hindered by a more complex implementation of a particle motion, but in practice the overall efficiency gap is never below 30%.

As it was mentioned above, a truncated octahedron cell replicated periodically with the displacements from the set $\{\boldsymbol{L}\}$ fills entirely the coordinate space. This makes the application of the Ewald technique theoretically possible, once the original potential energy sum is rewritten in a suitable form, compatible with the standard x, y, z-axis periodicity, required by the Ewald method. Indeed, as one can easily notice, the total set of cell images can be classified into two groups: the images, produced by an even number steps with a resulting cell displacement (iL, jL, kL) (i, j, k are arbitrary integers) and by an odd number of step with a displacement $(iL, jL, kL)+(L/2, L/2, L/2)$. If one thinks of a simulation cell as a compound of the original cell Ω and the displaced cell $\Omega_d = (L/2, L/2, L/2) + \Omega$, the total space will be covered again by its replications along the axis x, y, z with the period L. This allows to apply the Ewald summation technique directly to this complex cell with the number of particles equal to $2N_p$, but due to the similarity of Ω and Ω_d, the sums may be simplified in the following way:

$$\begin{aligned}
\frac{1}{2}\sum_{i\neq j}^{2N_p}\sum_{\boldsymbol{n}} R(\boldsymbol{r}_{ij}) &= \frac{1}{2}\sum_{\boldsymbol{n}}\left[\sum_{i,j=1;i\neq j}^{N_p} + \sum_{i,j=N_p+1;i\neq j}^{2N_p} + \sum_{i=1}^{N_p}\sum_{j=N+1}^{2N_p} + \sum_{i=N_p+1}^{2N_p}\sum_{j=1}^{N_p}\right] R(\boldsymbol{r}_{ij}) \\
&= \sum_{\boldsymbol{n}}\left[\sum_{i,j=1;i\neq j}^{N_p} + \sum_{i=1}^{N_p}\sum_{j=N+1}^{2N_p}\right] R(\boldsymbol{r}_{ij}) \\
&= \sum_{\boldsymbol{n}}\left[\sum_{i,j=1;i\neq j}^{N_p} R(\boldsymbol{r}_{ij}) + \sum_{i,j=1}^{N_p} R(\boldsymbol{r}_{ij}+\boldsymbol{L}/2)\right] \\
&= \sum_{\boldsymbol{n}}\left[\sum_{i,j=1;i\neq j}^{N_p} (R(\boldsymbol{r}_{ij}) + R(\boldsymbol{r}_{ij}+\boldsymbol{L}/2)) + \sum_{i=1}^{N_p} R(\boldsymbol{L}/2)\right]. \qquad \text{(B.3)}
\end{aligned}$$

where we place the points $1, ..., N_p$ to the cell Ω and their corresponding images $1 + Np, ..., 2Np$ to Ω_d. In a similar line of thought we can represent the Fourier-transformed part of the Ewald sum:

$$\frac{1}{2}\sum_{i\neq j}^{2N_p}\sum_{\boldsymbol{m}\neq 0} K(\boldsymbol{r}_{ij}) = \sum_{\boldsymbol{m}\neq 0}\Big(\sum_{i,j=1;i\neq j}^{N_p} (K(\boldsymbol{r}_{ij}) + K(\boldsymbol{r}_{ij}+\boldsymbol{L}/2))\Big) + \sum_{i=1}^{N_p} K(\boldsymbol{L}/2)\Big). \qquad \text{(B.4)}$$

The constants ξ, C_1, C_2 (refer to Eqs. (3.36,3.38,3.39)) stay clearly unchanged, as they characterize the self-image interactions, not biased by a specific cell geometry. Notice that the number of particles, appearing as a factor of ξ in the expression for the total energy is now $2N_p$.

Bibliography

[ABCG04] G. E. Astrakharchik, J. Boronat, J. Casulleras, and S. Giorgini. *Phys. Rev. Lett.*, 93:200404, 2004.

[AEM+95] M. H. Anderson, J. R. Ensher, M. R. Matthews, C. E. Wieman, and E. A. Cornell. Observation of bose-einstein condensation in a dilute atomic vapor. *Science*, 269:198, 1995.

[AGHW10] T. Amthor, C. Giese, C. S. Hofmann, and M. Weidemüller. *Phys. Rev. Lett.*, 104:013001, 2010.

[AGLS06] G. E. Astrakharchik, D. M. Gangardt, Y. E. Lozovik, and I. A. Sorokin. *Phys. Rev. E*, 74:021105, 2006.

[AM38] J. F. Allen and A. D Misener. *Nature*, 141:75, 1938.

[AM76] N. W. Ashcroft and D. N. Mermin. *Solid State Physics*. Thomson Learning, Toronto, 1976.

[Ape99] S. M. Apenko. Critical temperature of the superfluid transition in bose liquids. *Phys. Rev. B*, 60:3052–3055, Aug 1999.

[APPR07] C. Ates, T. Pohl, T. Pattard, and J. M. Rost. *Phys. Rev. A*, 76:013413, 2007.

[ARLGW07] Thomas Amthor, Markus Reetz-Lamour, Christian Giese, and Matthias Weidemüller. Modeling many-particle mechanical effects of an interacting rydberg gas. *Phys. Rev. A*, 76:054702, Nov 2007.

[AT89] M. P. Allen and D. J. Tildesley. *Computer simulation of liquids*. Oxford University Press, 1989.

[BC94] J. Boronat and J. Casulleras. Monte carlo analysis of an interatomic potential for he. *Phys. Rev. B*, 49:8920–8930, Apr 1994.

[BCLH08] V. Ballenegger, J. J. Cerda, O. Lenz, and Ch. Holm. *J. Chem. Phys.*, 128:034109, 2008.

[BCN94] J. Boronat, J. Casulleras, and J. Navarro. *Phys. Rev. B*, 50:3427, 1994.

[BCS57] J. Bardeen, L. N. Cooper, and J. R. Schrieffer. Theory of superconductivity. *Phys. Rev.*, 108:1175–1204, Dec 1957.

[BD10] D. Blume and K. M. Daily. Breakdown of universality for unequal-mass fermi gases with infinite scattering length. *Phys. Rev. Lett.*, 105:170403, Oct 2010.

[BDZ08] I. Bloch, J. Dalibard, and W. Zwerger. *Rev. Mod. Phys.*, 80:885, 2008.

[BHK+83] U. Buck, F. Huisken, A. Kohlhase, D. Otten, and J. Schaefer. *J. Chem. Phys.*, 78:4439, 1983.

[Bij40] A. Bijl. *Physica*, 7:869, 1940.

[BLdL98] J. Beckers, C. Loewe, and S. de Leeuw. *Mol. Simul.*, 6:369, 1998.

[BM77] Lynn Bonsall and A. A. Maradudin. Some static and dynamical properties of a two-dimensional wigner crystal. *Phys. Rev. B*, 15:1959–1973, Feb 1977.

[BMVB09] I. Bešlić, L. Markić Vranješ, and J. Boronat. Quantum monte carlo simulation of spin-polarized tritium. *Phys. Rev. B*, 80:134506, Oct 2009.

[Bon05] M. Boninsegni. *New J. Phys.*, 7:78, 2005.

[BP75] G. Baym and C. J. Pethick. *Ann. Rev. Nucl. Sci.*, 25:27, 1975.

[BRL91] R. N. Barnett, P. J. Reynolds, and W. A. Lester. *J. Comput. Phys.*, 96:258, 1991.

[BRS09] I. Bausmerth, A. Recati, and S. Stringari. Chandrasekhar-clogston limit and phase separation in fermi mixtures at unitarity. *Phys. Rev. A*, 79:043622, Apr 2009.

[BST66] S. Brush, H. Sahlin, and E. Teller. *J. Chem. Phys.*, 45:2102, 1966.

[BSTH95] C. C. Bradley, C. A. Sackett, J. J. Tollett, and R. G. Hulet. Evidence of bose-einstein condensation in an atomic gas with attractive interactions. *Phys. Rev. Lett.*, 75:1687–1690, Aug 1995.

[BW08] R. Blatt and D. Wineland. Entangled states of trapped atomic ions. *Nature (London)*, 453:1008., 2008.

[BWR+09] G. Barontini, C. Weber, F. Rabatti, J. Catani, G. Thalhammer, M. Inguscio, and F. Minardi. Observation of heteronuclear atomic efimov resonances. *Phys. Rev. Lett.*, 103:043201, Jul 2009.

[CACB09] C. Cazorla, G. E. Astrakharchik, J. Casulleras, and J. Boronat. Bose-einstein quantum statistics and the ground state of solid ^{4}he. *New Journal of Physics*, 11(1):013047, 2009.

[CB95a] J. Casulleras and J. Boronat. Unbiased estimators in quantum monte carlo methods: Application to liquid ^{4}He. *Phys. Rev. B*, 52:3654–3661, Aug 1995.

[CB95b] J. Casulleras and J. Boronat. Unbiased estimators in quantum monte carlo methods: Application to liquid ^{4}He. *Phys. Rev. B*, 52:3654–3661, Aug 1995.

[CB08a] C. Cazorla and J. Boronat. Two-dimensional molecular *para* -hydrogen and *ortho* -deuterium at zero temperature. *Phys. Rev. B*, 78:134509, Oct 2008.

[CB08b] C. Cazorla and J. Boronat. Zero-temperature equation of state of solid 4 he at low and high pressures. *Journal of Physics: Condensed Matter*, 20(1):015223, 2008.

[CBV+10] L. Costa, J. Brachmann, A.-C. Voigt, C. Hahn, M. Taglieber, T. W. Hänsch, and K. Dieckmann. *s*-wave interaction in a two-species fermi-fermi mixture at a narrow feshbach resonance. *Phys. Rev. Lett.*, 105:123201, Sep 2010.

[CCK76] D. M. Ceperley, G. V. Chester, and M. H. Kalos. Exact calculations of the ground state of model neutron matter. *Phys. Rev. D*, 13:3208–3213, Jun 1976.

[CCK78] D. Ceperley, G. V. Chester, and M. H. Kalos. Monte carlo study of the ground state of bosons interacting with yukawa potentials. *Phys. Rev. B*, 17:1070–1081, Feb 1978.

[CCPS03] J. Carlson, S.-Y. Chang, V. R. Pandharipande, and K. E. Schmidt. *Phys. Rev. Lett.*, 91:050401, 2003.

[Cep95] D. M. Ceperley. Path integrals in the theory of condensed helium. *Reviews of Modern Physics*, 67:279, 1995.

[CGJT10] Cheng Chin, Rudolf Grimm, Paul Julienne, and Eite Tiesinga. Feshbach resonances in ultracold gases. *Rev. Mod. Phys.*, 82:1225–1286, Apr 2010.

[CGSZ11] J. Carlson, S. Gandolfi, K. E. Schmidt, and S. Zhang. *Phys. Rev. A*, 84:061602 (R), 2011.

[Cha97] C. Chakravarty. *Int. Rev. Phys. Chem.*, 16:421, 1997.

[Chi90] Siu A. Chin. Quadratic diffusion monte carlo algorithms for solving atomic many-body problems. *Phys. Rev. A*, 42:6991–7005, Dec 1990.

[Chi04] Siu A. Chin. Quantum statistical calculations and symplectic corrector algorithms. *Phys. Rev. E*, 69:046118, Apr 2004.

[Chu98] Steven Chu. Nobel lecture: The manipulation of neutral particles. *Rev. Mod. Phys.*, 70:685–706, Jul 1998.

[CJB+10] F. Cinti, P. Jain, M. Boninsegni, A. Micheli, P. Zoller, and G. Pupillo. Supersolid droplet crystal in a dipole-blockaded gas. *Phys. Rev. Lett.*, 105:135301, Sep 2010.

[CP79] C. E. Campbell and F. J. Pinski. *Nucl. Phys.*, A328:210, 1979.

[CPCS04] S. Y. Chang, V. R. Pandharipande, J. Carlson, and K. E. Schmidt. Quantum monte carlo studies of superfluid fermi gases. *Phys. Rev. A*, 70:043602, 2004.

[CSPS07] B. Capogrosso-Sansone, N. V. Prokof'ev, and B. V. Svistunov. Phase diagram and thermodynamics of the three-dimensional bose-hubbard model. *Phys. Rev. B*, 75:134302, Apr 2007.

[CT98] Claude N. Cohen-Tannoudji. Nobel lecture: Manipulating atoms with photons. *Rev. Mod. Phys.*, 70:707–719, Jul 1998.

[CTGO11] Claude Cohen-Tanoudji and David Guéry-Odelin. *Advances in Atomic Physics*. World Scientific, 2011.

[CW08] J. Clarke and F. K. Wilhelm. Superconducting quan- tum bits. *Nature (London)*, 453:1031, 2008.

[DdWS79] A. Driessen, J. A. de Waal, and I. F. Silvera. *J. Low Temp. Phys.*, 34:255, 1979.

[DGPS99] Franco Dalfovo, Stefano Giorgini, Lev P. Pitaevskii, and Sandro Stringari. Theory of bose-einstein condensation in trapped gases. *Rev. Mod. Phys.*, 71:463–512, Apr 1999.

[dLB47] F. V. der Lage and H. Bethe. *Phys. Rev.*, 71:612, 1947.

[dLPS80] S. W. de Leeuw, J. W. Perram, and E. R. Smith. *Proc. R. Soc. Lon. A*, 373:27, 1980.

[DMA+95] K. B. Davis, M.-O. Mewes, M. R. Andrews, N. J. van Druten, D. S. Durfee, D. M. Kurn, and W. Ketterle. Bose-einstein condensation in a gas of sodium atoms. *Phys. Rev. Lett.*, 75:3969, 1995.

[DNRA90] A. R. Denton, P. Nielaba, K. J. Runge, and N. W. Ashcroft. Freezing of a quantum hard-sphere liquid at zero temperature: A density-functional approach. *Phys. Rev. Lett.*, 64:1529–1532, Mar 1990.

[DYP93] T. Darden, D. York, and L. Pederson. *J. Chem. Phys.*, 98:10089, 1993.

[EGA10] H. D. E. Eleftherios, E. Gdoutos, and R. Agrawal. *Int. J. Numer. Meth. Engng*, 84:1541, 2010.

[Ehr33] P. Ehrenfest. Phasenumwandlungen im ueblichen und erweiterten sinn, classifiziert nach den entsprechenden singularitaeten des thermodynamischen potentiales. *Proceedings Koninklijke Akademie van Wetenschappen*, 36:153–157, 1933.

[Ein24] A. Einstein. *Sitzber. Kgl. Preuss. Akad. Wiss.*, 261, 1924.

[Ein25] A. Einstein. *Sitzber. Kgl. Preuss. Akad. Wiss.*, 3, 1925.

[EPB+95] U. Essmann, L. Perera, M. L. Berkowitz, T. Darden, H. Lee, and L. G. Pedersen. *J. Chem. Phys.*, 103:8577, 1995.

[Ewa21] P. P. Ewald. *Annalen der Physik*, 369:253, 1921.

[Fee67] Eugene Feenberg. *Theory of Quantum Fluids.* Academic Press, 1967.

[FF96] L. M. Fraser and W. M. C. Foulkes. *Phys. Rev. B*, 53:1814, 1996.

[FGG11] M. M. Forbes, S. Gandolfi, and A. Gezerlis. *Phys. Rev. Lett.*, 106:235303, 2011.

[Fin94] D. Fincham. *Mol. Simul.*, 13:1, 1994.

[FKW+98] Dale G. Fried, Thomas C. Killian, Lorenz Willmann, David Landhuis, Stephen C. Moss, Daniel Kleppner, and Thomas J. Greytak. Bose-einstein condensation of atomic hydrogen. *Phys. Rev. Lett.*, 81:3811–3814, Nov 1998.

[FWGF89] M. P. A. Fisher, P. B. Weichman, G. Grinstein, and D. S. Fisher. *Phys. Rev. B*, 40:546, 1989.

[GBC99] S. Giorgini, J. Boronat, and J. Casulleras. Ground state of a homogeneous bose gas: A diffusion monte carlo calculation. *Phys. Rev. A*, 60:5129, 1999.

[GBC00] M. C. Gordillo, J. Boronat, and J. Casulleras. Zero-temperature equation of state of quasi-one-dimensional H_2. *Phys. Rev. Lett.*, 85:2348–2351, Sep 2000.

[GC97] M. C. Gordillo and D. M. Ceperley. Superfluidity in H_2 films. *Phys. Rev. Lett.*, 79:3010–3013, Oct 1997.

[GDA+11] H. R. Glyde, S. O. Diallo, R. T. Azuah, O. Kirichek, and J. W. Taylor. Bose-einstein condensation in liquid ^{4}He under pressure. *Phys. Rev. B*, 83:100507, Mar 2011.

[GFP+06] R. E. Grisenti, R. A. Costa Fraga, N. Petridis, R. Dörner, and J. Deppe. *Europhys. Lett.*, 73:540, 2006.

[GGSC09] Alexandros Gezerlis, S. Gandolfi, K. E. Schmidt, and J. Carlson. Heavy-light fermion mixtures at unitarity. *Phys. Rev. Lett.*, 103:060403, Aug 2009.

[Gil90] M. J. Gillan. *Computer Modelling of Fluids, Polymers and Solids*. Kluwer, Dodrecht, 1990.

[Gir60] M. Girardeau. *J. Math. Phys. (N.Y.)*, 1:516, 1960.

[Gla63] Roy J. Glauber. The quantum theory of optical coherence. *Phys. Rev.*, 130:2529, 1963.

[GME+02] Markus Greiner, Olaf Mandel, Tilman Esslinger, Theodor W. Hänsch, and Immanuel Bloch. *Nature*, 415:39, 2002.

[GN08] R. Guardiola and J. Navarro. *Cent. Eur. J. Phys.*, 6:33, 2008.

[GNP12] J. Gapinski, G. Nägele, and Adam Patkowski. *J. Chem. Phys.*, 136:024507, 2012.

[GPS08] Stefano Giorgini, Lev P. Pitaevskii, and Sandro Stringari. Theory of ultracold atomic fermi gases. *Rev. Mod. Phys.*, 80:1215–1274, Oct 2008.

[GR87] L. Greengard and V. Rokhlin. *J. Comput. Phys.*, 73:325, 1987.

[GR97] L. Greengard and V. Rokhlin. *Acta Numerica*, 6:229, 1997.

[GS72] V. L. Ginsburg and A. A. Sobyanin. *JETP Letters*, 15:242, 1972.

[GS03] D. M. Gangardt and G. V. Shlyapnikov. Local correlations in a strongly interacting one-dimensional bose gas. *New Journal of Physics*, 5:79, 2003.

[GSTV00] S. Grebenev, B. Sartakov, J. P. Toennies, and A. F. Vilesov. *Sci*, 289:1532, 2000.

[Gua98] R. Guardiola. *Microscopic Quantum Many-Body Theories and Their Applications*. Springer, Berlin, 1998.

[GZW97] G. T. Gao, X. C. Zeng, and W. Wang. *J. Chem. Phys.*, 106:3311, 1997.

[Han73] J.-P. Hansen. *Phys. Rev. A*, 8:3096, 1973.

[HB05] M. Holzmann and B. Bernu. *J. Comput. Phys.*, 206:111, 2005.

[HE88] R. W. Hockney and J. W. Eastwood. *Computer Simulation Using Particles*. Institute of Physics, 1988.

[HFD96] S. Hamaguchi, R. T. Farouki, and D. H. E. Dubin. *J. Chem. Phys.*, 105:7641, 1996.

[HFD97] S. Hamaguchi, R. T. Farouki, and D.H.E. Dubin. *Phys. Rev. E*, 56:4671, 1997.

[HGE73] R. W. Hockney, S. P. Goel, and J. W. Eastwood. *Chem. Phys. Lett.*, 21:589, 1973.

[HHBN11] M. Heinen, P. Holmqvist, A. J. Banchio, and Gerhard Nägele. *J. Chem. Phys.*, 134:044532, 2011.

[HHP10] K. Helfrich, H.-W. Hammer, and D. S. Petrov. Three-body problem in heteronuclear mixtures with resonant interspecies interaction. *Phys. Rev. A*, 81:042715, Apr 2010.

[HJR94] B. L. Hammond, W. Lester Jr., and P. J. Reynolds. *Monte Carlo Methods in Ab Initio Quantum Chemistry*. World Scientific, Singapore, 1994.

[HLS71] Jean-Pierre Hansen, Dominique Levesque, and Daniel Schiff. Fluid-solid phase transition of a hard-sphere bose system. *Phys. Rev. A*, 3:776–780, Feb 1971.

[HLW+11] Jens Honer, R. Löw, Hendrik Weimer, Tilman Pfau, and Hans Peter Büchler. Artificial atoms can do more than atoms: Deterministic single photon subtraction from arbitrary light fields. *Phys. Rev. Lett.*, 107:093601, Aug 2011.

[HNP10] N. Henkel, R. Nath, and T. Pohl. Three-dimensional roton excitations and supersolid formation in rydberg-excited bose-einstein condensates. *Phys. Rev. Lett.*, 104:195302, May 2010.

[HRB+07] R. Heidemann, U. Raitzsch, V. Bendkowsky, L. Santos B. Butscher, R. Löw, and T. Pfau. *Phys. Rev. Lett.*, 99:163601, 2007.

[HRB+08] Rolf Heidemann, Ulrich Raitzsch, Vera Bendkowsky, Björn Butscher, Robert Löw, and Tilman Pfau. Rydberg excitation of bose-einstein condensates. *Phys. Rev. Lett.*, 100:033601, Jan 2008.

[HTY+11] Hideaki Hara, Yosuke Takasu, Yoshifumi Yamaoka, John M. Doyle, and Yoshiro Takahashi. Quantum degenerate mixtures of alkali and alkaline-earth-like atoms. *Phys. Rev. Lett.*, 106:205304, May 2011.

[Hua05] K. Huang. *Lectures On Statistical Physics And Protein Folding*. World Scientific, Singapore, 2005.

[IKH+11] Vladyslav V. Ivanov, Alexander Khramov, Anders H. Hansen, William H. Dowd, Frank Münchow, Alan O. Jamison, and Subhadeep Gupta. Sympathetic cooling in an optically trapped mixture of alkali and spin-singlet atoms. *Phys. Rev. Lett.*, 106:153201, Apr 2011.

[Jac21] C. G. J. Jacobi. *J. reine angew. Math.*, 3:403, 1921.

[JAL11] S. Ji, C. Ates, and I. Lesanovsky. Two-dimensional rydberg gases and the quantum hard-squares model. *Phys. Rev. Lett.*, 107:060406, Aug 2011.

[Jas55] R. Jastrow. *Phys. Rev.*, 98:1479, 1955.

[JBC+98] D. Jaksch, C. Bruder, J. I. Cirac, C. W. Gardiner, and P. Zoller. Cold bosonic atoms in optical lattices. *Phys. Rev. Lett.*, 81:3108–3111, Oct 1998.

[JR07] R. E. Johnson and S. Ranganathan. *Phys. Rev. E*, 75:056706, 2007.

[Kap38] P. Kapitza. *Nature*, 141:74, 1938.

[Kaw81] Hikaru Kawamura. *Prog. Theor. Phys.*, 66:772, 1981.

[Kee42] W. H. Keesom. *Helium.* Elsevier, 1942.

[KFB+09] S. Knoop, F. Ferlaino, M. Berninger, M. Mark, H.-C. Nägerl, and R. Grimm. *Journal of Physics Conference Series*, 194:012064, 2009.

[KFM+09] S. Knoop, F. Ferlaino, M. Mark, M. Berninger, H. Schöbel, H.-C. Nägerl, and R. Grimm. *Nature Phys.*, 5:227, 2009.

[KFT+11] Matthias Kühnel, José M. Fernández, Guzmán Tejeda, Anton Kalinin, Salvador Montero, and Robert E. Grisenti. Time-resolved study of crystallization in deeply cooled liquid parahydrogen. *Phys. Rev. Lett.*, 106:245301, Jun 2011.

[KI89] N. Karasawa and W. A. Goddard III. *J. Phys. Chem.*, 93:7320, 1989.

[KKP] J. Keiner, S. Kunis, and D. Potts. *C subroutine library for computing the non equispaced discrete Fourier transform (NDFT) in one or more dimensions.* http://www.tu-chemnitz.de/ potts/nfft.

[KLV74] M. H. Kalos, D. Levesque, and L. Verlet. Helium at zero temperature with hard-sphere and other forces. *Phys. Rev. A*, 9:2178–2195, May 1974.

[KMJ99] E. Krotscheck, M.D.Miller, and J.Wojdylo. Variational approach to the many-boson problem in one dimension. *Phys. Rev. B*, 60:13028, 1999.

[KMN+07] P. Kok, W. J. Munro, K. Nemoto, T. C. Ralph, J. P. Dowling, and G. J. Milburn. Linear optical quantum computing with photonic qubits. *Rev. Mod. Phys.*, 79:135, 2007.

[KMW+06] T. Kraemer, M. Mark, P. Waldburger, J. G. Danzl, C. Chin, B. Engeser, A. D. Lange, K. Pilch, A. Jaakkola, H.-C. Nägerl, and R. Grimm. *Nature*, 440:315, 2006.

[KP92] J. Kolafa and J. Perram. *Mol. Simul.*, 9:351, 1992.

[KPV08] Kirill Kuyanov-Prozument and Andrey F. Vilesov. Hydrogen clusters that remain fluid at low temperature. *Phys. Rev. Lett.*, 101:205301, Nov 2008.

[KRG86] Kurt Kremer, Mark O. Robbins, and Gary S. Grest. Phase diagram of yukawa systems: Model for charge-stabilized colloids. *Phys. Rev. Lett.*, 57:2694–2697, Nov 1986.

[Kro98] E. Krotscheck. *Microscopic Quantum Many-Body Theories and Their Applications*. Springer, 1998.

[KSCT07] S. A. Khairallah, M. B. Sevryuk, D. M. Ceperley, and J. P. Toennies. Interplay between magic number stabilities and superfluidity of small parahydrogen clusters. *Phys. Rev. Lett.*, 98:183401, May 2007.

[KSCZ12] Mark J. H. Ku, Ariel T. Sommer, Lawrence W. Cheuk, and Martin W. Zwierlein. Revealing the superfluid lambda transition in the universal thermodynamics of a unitary fermi gas. *Science*, 335(6068):563–567, 2012.

[KW02] Yongkyung Kwon and K. Birgitta Whaley. Nanoscale molecular superfluidity of hydrogen. *Phys. Rev. Lett.*, 89:273401, Dec 2002.

[KW05] Y. Kwon and K. B. Whaley. *J. Low Temp. Phys.*, 140:227, 2005.

[LHL12] Weibin Li, Lama Hamadeh, and Igor Lesanovsky. Probing the interaction between rydberg-dressed atoms through interference. *Phys. Rev. A*, 85:053615, May 2012.

[LKC74] K. S. Liu, M. H. Kalos, and G. V. Chester. Quantum hard spheres in a channel. *Phys. Rev. A*, 10:303–308, Jul 1974.

[LL80] L. Landau and E. Lifshitz. *Statistical Physics, part 1.* Butterworth–Heinemann, 1980.

[LLRRM10] Hui Li, Robert J. Le Roy, Pierre-Nicholas Roy, and A. R. W. McKellar. Molecular superfluid: Nonclassical rotations in doped *Para* -hydrogen clusters. *Phys. Rev. Lett.*, 105:133401, Sep 2010.

[LP11] Guan-Qiang Li and Ping Peng. Formation of a heteronuclear tetramer A_3b via efimov-resonance-assisted stimulated raman adiabatic passage. *Phys. Rev. A*, 83:043605, Apr 2011.

[LW93] Jia Ling Lin and J. P. Wolfe. Bose-einstein condensation of paraexcitons in stressed cu_2o. *Phys. Rev. Lett.*, 71:1222–1225, Aug 1993.

[LWK+09] R. Löw, H. Weimer, U. Krohn, R. Heidemann, V. Bendkowsky, B. Butscher, H. P. Büchler, and T. Pfau. *Phys. Rev. A*, 80:033422, 2009.

[LWS+03] X. Li, Y. Wu, D. Steel, D. Gammon, T. H. Stievater, D. S. Katzer, D. Park, C. Piermarocchi, and L. J. Sham. An all-optical quantum gate in a semiconductor quantum dot. *Science*, 301:809, 2003.

[Mah00] Gerald D. Mahan. *Many-Particle Physics, 3rd edition.* Kluwer Academic / Plenum Publishers, New York, 2000.

[Maz07a] M. Mazars. *Mol. Phys.*, 105:1909, 2007.

[Maz07b] M. Mazars. *J. Chem. Phys.*, 126:056101, 2007.

[Maz10] M. Mazars. *J. Phys. A: Math. Theor.*, 43:425002, 2010.

[Maz11] M. Mazars. *Phys. Rep.*, 500:43, 2011.

[MB06] Fabio Mezzacapo and Massimo Boninsegni. Superfluidity and quantum melting of p-h_2 clusters. *Phys. Rev. Lett.*, 97:045301, Jul 2006.

[MB07] Fabio Mezzacapo and Massimo Boninsegni. Structure, superfluidity, and quantum melting of hydrogen clusters. *Phys. Rev. A*, 75:033201, Mar 2007.

[MB08] Fabio Mezzacapo and Massimo Boninsegni. Local superfluidity of parahydrogen clusters. *Phys. Rev. Lett.*, 100:145301, Apr 2008.

[McM65] W. L. McMillan. *Phys. Rev.*, 138:442, 1965.

[MF91] E. J. Meijer and D. Frenkel. *J. Chem. Phys.*, 94:2269, 1991.

[MP95] G. Makov and M. Payne. *Phys. Rev. B*, 51:4014, 1995.

[MPLW08] A. Micheli, G. Pupillo, Xin Lu, and Chang-Qin Wu. *Phys. Rev. B*, 78:024108, 2008.

[MPW07] C. Mora, O. Parcollet, and X. Waintal. *Phys. Rev. B*, 76:064511, 2007.

[MRR+53] N. Metropolis, A. W. Rosenbluth, M. N. Rosenbluth, A. H. Teller, and E. Teller. *J. Chem. Phys.*, 21:1087, 1953.

[MSH83] H. J. Maris, G. M. Seidel, and T. E. Huber. *J. Low Temp. Phys.*, 51:471, 1983.

[MSW87] H. J. Maris, G. M. Seidel, and F. I. B. Williams. Experiments with supercooled liquid hydrogen. *Phys. Rev. B*, 36:6799–6810, Nov 1987.

[NC95] V. Natoli and D. M. Ceperley. *J. Comput. Phys.*, 117:171, 1995.

[Ner07] Walther Nernst. *Experimental and Theoretical Applications of Thermodynamics to Chemistry.* New York: Charles Scribner's Sons, 1907.

[NG99] M. Naraschewski and R. J. Glauber. *Phys. Rev. A*, 59:4595, 1999.

[NHM+10] Shuta Nakajima, Munekazu Horikoshi, Takashi Mukaiyama, Pascal Naidon, and Masahito Ueda. Nonuniversal efimov atom-dimer resonances in a three-component mixture of ^{6}Li. *Phys. Rev. Lett.*, 105:023201, Jul 2010.

[NNCS10] N. Navon, S. Nascimbène, F. Chevy, and C. Salomon. The equation of state of a low-temperature fermi gas with tunable interactions. *Science*, 328(5979):729–732, 2010.

[Nos64] L. H. Nosanow. Theory of crystalline he^3 at 0k. *Phys. Rev. Lett.*, 13:270–272, Aug 1964.

[OAB12] O.N. Osychenko, G.E. Astrakharchik, and J. Boronat. Ewald method for polytropic potentials in arbitrary dimensionality. *Molecular Physics*, 110(4):227–247, 2012.

[OAL+11] O. N. Osychenko, G. E. Astrakharchik, Y. Lutsyshyn, Yu. E. Lozovik, and J. Boronat. Phase diagram of rydberg atoms with repulsive van der waals interaction. *Phys. Rev. A*, 84:063621, Dec 2011.

[OP06] Francesco Operetto and Francesco Pederiva. Diffusion monte carlo study of the equation of state of solid para-h_2. *Phys. Rev. B*, 73:184124, May 2006.

[OTF+01] C. Orzel, A. K. Tuchman, M. L. Fenselau, M. Yasuda, and M. A. Kasevich. *Science*, 291:2386, 2001.

[OYLS+05] Wen-Ze Ou-Yang, Zhong-Yuan Lu, Tong-Fei Shi, Zhao-Yan Sun, and Li-Jia An. *J. Chem. Phys.*, 123:234502, 2005.

[PAP+07] D. S. Petrov, G. E. Astrakharchik, D. J. Papoular, C. Salomon, and G. V. Shlyapnikov. Crystalline phase of strongly interacting fermi mixtures. *Phys. Rev. Lett.*, 99:130407, Sep 2007.

[Par75] D. E. Parry. *Surf. Sci.*, 49:433, 1975.

[Par76] D. E. Parry. *Surf. Sci.*, 54:195, 1976. (erratum).

[PC87a] R. M. Panoff and J. W. Clark. Ground-state phases of polarized deuterium species. *Phys. Rev. B*, 36:5527–5539, Oct 1987.

[PC87b] E. L. Pollock and D. M. Ceperley. Path-integral computation of superfluid densities. *Phys. Rev. B*, 36:8343–8352, Dec 1987.

[PDL10] T. Pohl, E. Demler, and M. D. Lukin. *Phys. Rev. Lett.*, 104:043002, 2010.

[Pet95] H. G. Petersen. *J. Chem. Phys.*, 103:3668, 1995.

[Pet03] D. S. Petrov. Three-body problem in fermi gases with short-range interparticle interaction. *Phys. Rev. A*, 67:010703, Jan 2003.

[PG96] E. L. Pollock and J. Glosli. *Comp. Phys. Commun.*, 95:93, 1996.

[PGP08] S. Pilati, S. Giorgini, and N. Prokof'ev. Critical temperature of interacting bose gases in two and three dimensions. *Phys. Rev. Lett.*, 100:140405, Apr 2008.

[Phi98] William D. Phillips. Nobel lecture: Laser cooling and trapping of neutral atoms. *Rev. Mod. Phys.*, 70:721–741, Jul 1998.

[PPdL88] J. Perram, H. Petersen, and S. W. de Leeuw. *Mol. Phys.*, 65:875, 1988.

[PS03] L. P. Pitaevskii and S. Stringari. *Bose-Einstein Condensation*. Oxford University Press, Oxford, 2003.

[PZKW05] F. Paesani, R. E. Zillich, Y. Kwon, and K. B. Whaley. *J. Chem. Phys.*, 122:181106, 2005.

[RBHL86] P. Reynolds, R. Barnett, B. Hammond, and W. Lester. Molecular physics and chemistry applications of quantum monte carlo. *Journal of Statistical Physics*, 43:1017–1026, 1986. 10.1007/BF02628327.

[RC67] L. Reatto and G.V. Chester. Phonons and the properties of a bose system. *Phys. Rev.*, 155:88, 1967.

[RCS+11] Ridinger, A., Chaudhuri, S., Salez, T., Eismann, U., Fernandes, D.R., Magalhães, K., Wilkowski, D., Salomon, C., and Chevy, F. Large atom number dual-species magneto-optical trap for fermionic 6li and 40k atoms. *Eur. Phys. J. D*, 65(1-2):223–242, 2011.

[Rea79] L. Reatto. *Nucl. Phys.*, A328:253, 1979.

[RH05] F. Robicheaux and J. V. Hernández. *Phys. Rev. A*, 72:063403, 2005.

[RKG88] O. Robbins, K. Kremer, and G. S. Grest. *J. Chem. Phys.*, 88:3286, 1988.

[RR90] K.J. Runge and R.J. Runge. *Quantum Simulations of Condensed Matter Phenomena*. World Scientific, Singapore, 1990.

[RT87] R. O. Rosenberg and D. Thirumalai. Order-disorder transition in colloidal suspensions. *Phys. Rev. A*, 36:5690–5700, Dec 1987.

[Run92] Karl J. Runge. Quantum monte carlo calculation of the long-range order in the heisenberg antiferromagnet. *Phys. Rev. B*, 45:7229–7236, Apr 1992.

[SA11] P. K. Shukla and K. Avinash. Phase coexistence and a critical point in ultracold neutral plasmas. *Phys. Rev. Lett.*, 107:135002, Sep 2011.

[SB11] E. Sola and J. Boronat. *J. Phys. Chem. A*, 115:7071, 2011.

[SC00] G. Salin and J.-M. Caillol. *J. Chem. Phys.*, 113:10459, 2000.

[SC10] J. Stanojevic and R. Côté. *Phys. Rev. A*, 81:053406, 2010.

[SCB09] K. Sakkos, J. Casulleras, and J. Boronat. *J. Chem. Phys.*, 130:204109, 2009.

[Sch70] O. Schnepp. One-phonon excited states of solid h_2 and d_2 in the ordered phase. *Phys. Rev. A*, 2:2574–2574, Dec 1970.

[SCK91] Philippe Sindzingre, David M. Ceperley, and Michael L. Klein. Superfluidity in clusters of p -h_2 molecules. *Phys. Rev. Lett.*, 67:1871–1874, Sep 1991.

[SD76] M. Sangester and M. Dixon. *Adv. Phys.*, 25:247, 1976.

[SD01] C. Sagui and T. Darden. *J. Chem. Phys.*, 114:15, 2001.

[SG78] I. F. Silvera and V. V. Goldman. *J. Chem. Phys.*, 69:4209, 1978.

[SGH$^+$10] H. Schempp, G. Gunter, C. S. Hofmann, C. Giese, S. D. Saliba, B. D. DePaola, T. Amthor, M. Weidemüller, S. Sevincli, and T. Pohl. *Phys. Rev. Lett.*, 104:173602, 2010.

[Sil80] I. F. Silvera. *Rev. Mod. Phys.*, 52:393, 1980.

[SKE$^+$05] Y. Shan, J. L. Klepeis, M. P. Eastwood, R. O. Dror, and D. E. Shaw. *J. Chem. Phys.*, 122:054101, 2005.

[SLMD10] J. Schachenmayer, I. Lesanovsky, A. Micheli, and A. J. Daley. *New J. Phys.*, 12:103044, 2010.

[SMCP07] M. R. Shirts, D. L. Mobley, J. D. Chodera, and V. S. Pande. *J. Phys. Chem. B*, 111:13052, 2007.

[Smi94] E. R. Smith. *J. Stat. Phys.*, 77:449, 1994.

[SPD04] C. Sagui, L. Pedersen, and T. Darden. *J. Chem. Phys.*, 120:73, 2004.

[SPG11] Eran Sela, Matthias Punk, and Markus Garst. Dislocation-mediated melting of one-dimensional rydberg crystals. *Phys. Rev. B*, 84:085434, Aug 2011.

[Spo97] E. Spohr. *J. Chem. Phys.*, 107:6342, 1997.

[SRLA+04] K. Singer, M. Reetz-Lamour, T. Amthor, L. G. Marcassa, and M. Weidemuller. *Phys. Rev. Lett.*, 93:163001, 2004.

[Ste98] G. Steidl. *Adv. Comput. Math.*, 9:337, 1998.

[STN+09] F. M. Spiegelhalder, A. Trenkwalder, D. Naik, G. Hendl, F. Schreck, and R. Grimm. Collisional stability of $^{40}\mathbf{K}$ immersed in a strongly interacting fermi gas of ^{6}Li. *Phys. Rev. Lett.*, 103:223203, Nov 2009.

[Sut71] B. Sutherland. *Phys. Rev. A*, 4:2019, 1971.

[SW71] ElÃas M. Stein and Guido L. Weiss. *Introduction to Fourier Analysis on Euclidean Spaces*. Princeton University Press, 1971.

[SWM10] M. Saffman, T. G. Walker, and K. Mølmer. Quantum information with rydberg atoms. *Rev. Mod. Phys.*, 82:2313–2363, Aug 2010.

[TCF+11] S. Trotzky, Y.-A. Chen, A. Flesch, I. P. McCulloch, U. Schollwock, J. Eisert, and I. Bloch. *Phys. Rev. Lett.*, 106:235304, 2011.

[TFS+04] D. Tong, S. M. Farooqi, J. Stanojevic, S. Krishnan, R. Cote Y. P. Zhang, E. E. Eyler, and P. L. Gould. *Phys. Rev. Lett.*, 93:063001, 2004.

[TGL+10] T. G. Tiecke, M. R. Goosen, A. Ludewig, S. D. Gensemer, S. Kraft, S. J. J. M. F. Kokkelmans, and J. T. M. Walraven. Broad feshbach resonance in the ^{6}Li-$^{40}\mathbf{K}$ mixture. *Phys. Rev. Lett.*, 104:053202, Feb 2010.

[TJ96] A. Y. Toukmaji and J. A. Board Jr. *Comp. Phys. Commun.*, 95:73, 1996.

[TKZ+11] A. Trenkwalder, C. Kohstall, M. Zaccanti, D. Naik, A. I. Sidorov, F. Schreck, and R. Grimm. Hydrodynamic expansion of a strongly interacting fermi-fermi mixture. *Phys. Rev. Lett.*, 106:115304, Mar 2011.

[TOPK06] A. K. Tuchman, C. Orzel, A. Polkovnikov, and M. A. Kasevich. *Phys. Rev. A*, 74:051601, 2006.

[TTHK99] Eddy Timmermans, Paolo Tommasini, Mahir Hussein, and Arthur Kerman. Feshbach resonances in atomic bose-einstein condensates. *Physics Reports*, 315(1-3):199 – 230, 1999.

[TVA+08] M. Taglieber, A.-C. Voigt, T. Aoki, T. W. Hänsch, and K. Dieckmann. Quantum degenerate two-species fermi-fermi mixture coexisting with a bose-einstein condensate. *Phys. Rev. Lett.*, 100:010401, Jan 2008.

[TWL+06] G. Thalhammer, K. Winkler, F. Lang, S. Schmid, R. Grimm, and J. Hecker Denschlag. Long-lived feshbach molecules in a three-dimensional optical lattice. *Phys. Rev. Lett.*, 96:050402, Feb 2006.

[vBSvL+11] R. M. W. van Bijnen, S. Smit, K. A. H. van Leeuwen, E. J. D. Vredenbregt, and S. J. J. M. F. Kokkelmans. *J. Phys. B*, 44:184008, 2011.

[vDKH+08] C. S. E. van Ditzhuijzen, A. F. Koenderink, J. V. Hernández, F. Robicheaux, L. D. Noordam, and H. B. van Linden van den Heuvell. Spatially resolved observation of dipole-dipole interaction between rydberg atoms. *Phys. Rev. Lett.*, 100:243201, Jun 2008.

[vGd59] J. M. J. van Leeuwen, J. Groeneveld, and J. de Boer. New method for the calculation of the pair correlation function. I. *Physica*, 25:792–808, January 1959.

[VM00] V. S. Vorob'ev and S. P. Malyshenko. *J. Phys.: Condens. Matter*, 12:5071, 2000.

[VTC+09] A.-C. Voigt, M. Taglieber, L. Costa, T. Aoki, W. Wieser, T. W. Hänsch, and K. Dieckmann. Ultracold heteronuclear fermi-fermi molecules. *Phys. Rev. Lett.*, 102:020405, Jan 2009.

[War98] A. F. Ware. *SIAM Rev.*, 40:838, 1998.

[WB05] X. Wu and B. R. Brooks. *J. Chem. Phys.*, 122:044107, 2005.

[WB10] Hendrik Weimer and Hans Peter Büchler. Two-stage melting in systems of strongly interacting rydberg atoms. *Phys. Rev. Lett.*, 105:230403, Nov 2010.

[WHH+09] J. R. Williams, E. L. Hazlett, J. H. Huckans, R. W. Stites, Y. Zhang, and K. M. O'Hara. Evidence for an excited-state efimov trimer in a three-component fermi gas. *Phys. Rev. Lett.*, 103:130404, Sep 2009.

[Wig34] E. Wigner. On the interaction of electrons in metals. *Phys. Rev.*, 46:1002–1011, Dec 1934.

[WKPE99] D. Wolf, P. Keblinski, S. R. Phillpot, and J. Eggebrecht. *J. Chem. Phys.*, 110:8254, 1999.

[WLO+09] A. N. Wenz, T. Lompe, T. B. Ottenstein, F. Serwane, G. Zürn, and S. Jochim. Universal trimer in a three-component fermi gas. *Phys. Rev. A*, 80:040702, Oct 2009.

[WLPB08] H. Weimer, R. Löw, T. Pfau, and H. P. Büchler. *Phys. Rev. Lett.*, 101:250601, 2008.

[WLvSE12] Yujun Wang, W. Blake Laing, Javier von Stecher, and B. D. Esry. Efimov physics in heteronuclear four-body systems. *Phys. Rev. Lett.*, 108:073201, Feb 2012.

[WS05] Thad G. Walker and Mark Saffman. *J. Phys. B: At. Mol. Opt. Phys.*, 38:S309, 2005.

[WS08] Thad G. Walker and M. Saffman. Consequences of zeeman degeneracy for the van der waals blockade between rydberg atoms. *Phys. Rev. A*, 77:032723, Mar 2008.

[WSK+08] E. Wille, F. M. Spiegelhalder, G. Kerner, D. Naik, A. Trenkwalder, G. Hendl, F. Schreck, R. Grimm, T. G. Tiecke, J. T. M. Walraven, S. J. J. M. F. Kokkelmans, E. Tiesinga, and P. S. Julienne. Exploring an ultracold fermi-fermi mixture: Interspecies feshbach resonances and scattering properties of ^{6}Li and ^{40}K. *Phys. Rev. Lett.*, 100:053201, Feb 2008.

[WTL+06] K. Winkler, G. Thalhammer, F. Lang, R. Grimm, J. Hecker Denschlag, A. J. Daley, A. Kantian, H. P. Büchler, and P. Zoller. *Nature (London)*, 441:050402, 2006.

[WW] E. T. Whittaker and G. N. Watson. *A Course in Modern Analysis*. Cambridge University Press, Cambridge, 4th edition edition.

[YB99] In-Chul Yeh and Max L. Berkowitz. *J. Chem. Phys.*, 111:3155, 1999.

[YJ06] Q. L. Wen Yang and Xigao Jin. *J. Chem. Theory Comput.*, 6:1618, 2006.

[YRP+09] K. C. Younge, A. Reinhard, T. Pohl, P. R. Berman, and G. Raithel. *Phys. Rev. A*, 79:043420, 2009.

[YZZ11] Tao Yin, Peng Zhang, and Wei Zhang. Stable heteronuclear few-atom bound states in mixed dimensions. *Phys. Rev. A*, 84:052727, Nov 2011.

[ZDD+09] M. Zaccanti, B. Deissler, C. D'Errico, M. Fattori, Jona-Lasinio M., S. Müller, G. Roati, M. Inguscio, and G. Modugno. *Nature Phys.*, 5:586, 2009.

Acknowledgements

I acknowledge the financial support of DGI and Generalitat de Catalunya (Spain) through the grants, that allowed to bring this work to life. I would like to express my deep gratitude to my advisers, Jordi and Grigory, and all my other collaborators, for I learned a lot from them both professionally and personally. I dare to hope that working at the University I found not only colleagues, but also good friends. I would like to thank Yaroslav Lutsyshyn for his careful reading of the manuscript. Finally, I can't forget to mention my family, that despite being far from me, was always very caring and supportive.